Física Quàntica i Astrofísica
Universitat de Barcelona

Study of b-hadron decays into two hadrons and a photon at LHCb and first observation of b-baryon radiative decays

Vicente José Rives Molina
Directors: Dra. Miriam Calvo Gómez i Dr. Albert Puig Navarro
Tutor: Domènec Espriu Climent
Programa de Doctorat de Física, Juliol 2016

Acknowledgements

A lo largo del doctorado he conocido a una serie de gente que me han hecho crecer tanto como investigador como persona. De la misma manera, toda la gente que ya formaba parte de mi vida al empezar me influenciaron y me siguen influenciando hoy en día para ser lo que soy. Es imposible acordarse de todas esas personas pero lo intentaré en estas líneas.

En primer lugar, quiero agradecer a Albert y Miriam su ayuda, su apoyo, sus correcciones, sus ideas y, en definitiva, su guía, sin la que habría sido imposible hacer nada de esto.

No puedo olvidarme de Rosón, el profesor por el cual decidí hacer física en la Universidad de Salamanca, así como de Alfredo Valcarce, que, ya en la universidad, supo transmitirnos su pasión por la física de partículas y motivarnos para ir más allá en el mundo de la investigación y aportar nuestro granito de arena. Además, quiero agradecer a todos los miembros del grupo de física de altas energías del LHCb de Barcelona por darme la oportunidad de unirme a ellos y poder desarrollar los proyectos en los que hemos trabajado juntos estos años. A Carla, porque con ella las horas en el despacho no se hacen tan largas. A todos los *sexy lunchers* porque los parones a mediodía son muy necesarios.

No me quiero olvidar de la gente que conocí nada más llegar a Barcelona y que aún sigue en mi vida: a Clara, a Garo, a Javi y Anna, Alex, Camille y todos los que hemos vivido y convivido en el piso de Lesseps, que siempre nos quedará ahí y seguro que nunca olvidaremos.

A Cayetano y a Montejo, que ya hace mil años que nos conocimos y aún así nunca nos hemos aburrido.

A los omnívoros, porque nos conocimos todos en Ginebra y estamos por ahí dando vueltas, pero siempre con ganas de saber qué tal estamos todos.

A Clarilla, porque las casualidades a veces pasan cuando más necesario es que pasen y son las pequeñas cosas de cada día las que nos pueden hacer recuperar una sonrisa que estaba perdida entre tinieblas.

Y, sobre todo, quiero agradecer a mi familia que siempre me hayan apoyado, que siempre hayan estado ahí, que siempre me hayan demostrado que están siempre conmigo aunque estén un poco lejos. Todo lo que soy es gracias a ellos y todo lo que puedo llegar a ser será gracias a lo que ellos me han enseñado. Por eso lo único que puedo hacer es daros las gracias y deciros que siempre estáis conmigo, que sois un ejemplo a seguir y

que os quiero. Muchas gracias a mis abuelas, a mi hermana, a Ciarán, a Archie, a mi padre y a mi madre.

To Archie, and our secret words.

I am the Alpha and the Omega
Book of Revelation 1:8

Contents

Resumen

El Modelo Estándard de la física de partículas (ME) es la teoría que describe las partículas elementales y sus interacciones. Fue formulada durante el siglo XX y ha sido puesta a prueba a través de un gran número de experimentos, que han confirmado sus predicciones. A pesar de su éxito, el ME no es una teoría completa ya que no incluye la gravedad, la energía y la materia oscura, entre otros aspectos.

En el ME las partículas elementales que forman la materia se pueden dividir en quarks y leptones, que, en ambos casos, se dividen en tres familias, mientras que las interacciones entre las partículas tienen lugar a través de bosones.

Los hadrones B, en cuya composición podemos encontrar un quark b (o antiquark $\overline{b}$), y sus desintegraciones, constituyen un lugar excelente para la puesta a prueba del ME a través de la medida de algunos de sus parámetros, como son los elementos de la matriz CKM (matriz que describe la rotación de los estados de masa y de sabor de los quarks) o los parámetros relacionados con la violación de la simetría *CP*.

Uno de los lugares más prometedores a la hora de la medida de parámetros del ME son las corrientes neutras de cambio de sabor (FCNC), en las que, a través de la interacción débil, se produce un cambio en la generación de uno de los quarks que componen el hadrón de forma que la carga eléctrica entre el quark del estado final y el del estado inicial es la misma. Este tipo de procesos, en el ME, no puede producirse a través de *diagramas de árbol* y, por tanto, son muy sensibles a la presencia de nuevas partículas (no incluidas en el ME), que podrían alterar el valor predicho por el ME de observables físicos relacionados con la desintegración. Las desintegraciones radiativas (en las que un fotón forma parte del estado final de la desintegración) son un ejemplo de este tipo de corrientes.

En este trabajo se presenta el análisis de datos recogidos por el experimento LHCb sobre desintegraciones radiativas durante el Run 1, que corresponden a un total de 3 fb^{-1} recogidos durante los años 2011 y 2012. En concreto, la medida de la frecuencia relativa de desintegración entre los canales de desintegración $B_s^0 \to \phi\gamma$ y $\Lambda_b^0 \to \Lambda^{*0}\gamma$ con respecto a $B^0 \to K^{*0}\gamma$ así como la medida de la asimetría *CP* para los canales $B^0 \to K^{*0}\gamma$ y $\Lambda_b^0 \to \Lambda^{*0}\gamma$. Los resultados obtenidos son compatibles con las predicciones del ME y con las medidas realizadas anteriormente.

Desintegraciones radiativas de hadrones B

Los procesos FCNC, dentro del ME, sólo pueden ocurrir a través de transiciones electromagnéticas con (al menos) un *loop*. Las desintegraciones radiativas que se estudian en este trabajo corresponden a procesos FCNC del tipo $b \to s$. Estos procesos están dominados por un quark t virtual que se empareja, tal como señala la Fig. 2.2, con un bosón W. Extensiones del ME predicen nuevas partículas que podrían entrar en el *loop*,

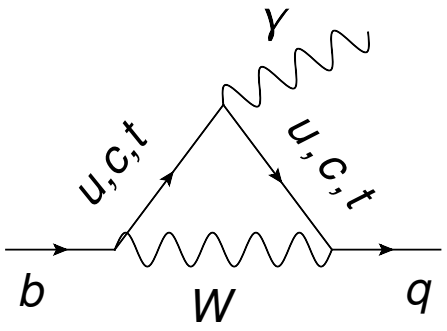

Figure 1: *Loop* radiativo tal como permite el ME, en el que los procesos FCNC no pueden ocurrir a nivel de *árbol*.

modificando los valores de observables físicos predichos por el ME. Algunos de estos observables son la frecuencia de desintegración (*branching fraction*) y la asimetría de *CP*. La predicción para la fracción de frecuencias de desintegración entre $B^0 \to K^{*0}\gamma$ y $B_s^0 \to \phi\gamma$ es 1.0 ± 0.2 [1] y para la $\mathcal{A}^{CP}$ de $B^0 \to K^{*0}\gamma$ es de $(-0.61 \pm 0.43)\%$ [2]. Estas dos magnitudes han sido ya medidas por el experimento LHCb [3] y este trabajo constituye una actualización de dicha medida, haciendo uso de una cantidad mayor de datos y alcanzando un resultado más preciso. Respecto de las magnitudes relacionadas con $\Lambda_b^0 \to \Lambda^{*0}\gamma$, las predicciones relacionadas con la frecuencia de desintegración sitúan esta magnitud, dependiendo de la resonancia intermedia, alrededor de 10^{-5} [4], mientras que desde el punto de vista experimental ninguna de las medidas presentadas en este trabajo se ha llevado a cabo con anterioridad.

El CERN y el LHC

La Organización Europea para la Investigación Nuclear (CERN) es el laboratorio de física de partículas más grande del mundo. Está situado en la frontera franco-suiza, cerca de la ciudad de Ginebra. Un total de 22 países europeos son miembros, aunque otros muchos países del mundo participan en los experimentos que allí se llevan a cabo, haciendo que sean más de 10.000 el número total de científicos que trabajan en el CERN. Varios hitos de la ciencia se han producido en el CERN, desde la invención de la *World Wide Web* hasta el descubrimiento de los bosones Z y W, responsables de la interacción débil.

En la actualidad, el CERN acoge el mayor acelerador de partículas del mundo, el

LHC, que está diseñado para acelerar protones hasta una energía de 7 TeV por haz, haciendo posible que se pueda trabajar con una energía del centro de masas de 14 TeV. El LHC está dispuesto en un anillo circular de unos 27 km de longitud en un túnel a unos 100 m de profundidad en el que en anterioridad se encontraba el acelerador LEP, en el que se aceleraban y colisionaban electrones y positrones y que estuvo en funcionamiento hasta el año 2000.

Un total de siete experimentos están dispuestos a lo largo del LHC.

- ALICE, dedicado al estudio de la interacción entre el plasma quark-gluón y la materia a través de colisiones de núcleos pesados.
- ATLAS, dedicado a la comprobación del ME y la búsqueda de nuevas partículas y nuevas teorías más allá del ME.
- CMS, dedicado, al igual que ATLAS, a la comprobación del ME y búsqueda de nuevas partículas y física más allá del ME.
- LHCb, dedicado al estudio de la violación de *CP* paridad y las desintegraciones raras de hadrones con un quark b.
- LHCf, dedicado a la medida de la sección eficaz de partículas neutras en la dirección cercana al haz de protones.
- MoEDAL, dedicado a la búsqueda del monopolo magnético y otras partículas masivas estables ionizantes.
- TOTEM, dedicado a la medida de la sección eficaz (con un método independiente de la luminosidad), *scattering* elástico (para la mejor comprensión de la estructura interna del protón) y procesos difractivos.

El experimento LHCb

El experimento LHCb, situado en el punto de interacción 8 del LHC, está dedicado al estudio de la física de quarks masivos, siendo su principal objetivo la medida de la asimetría *CP* y los observables relacionados con las desintegraciones raras de hadrones con quarks b y c.

A diferencia de la mayoría de los detectores de partículas, la geometría del LHCb consiste en un espectrómetro de brazo único que cubre un ángulo de 10–300 mrad en el plano horizontal y 10–250 mrad en el plano vertical, debido a que los pares $b\bar{b}$ se producen en direcciones muy próximas al haz de protones. La Fig. 2 muestra la geometría del LHCb, donde se destacan los distintos sub-detectores, que se describen a continuación.

Vertex Locator (VELO): Es el detector más próximo al punto de choque de los protones y su objetivo es la correcta reconstrucción de los puntos de interacción entre los haces así como los puntos de desintegración de los hadrones B.

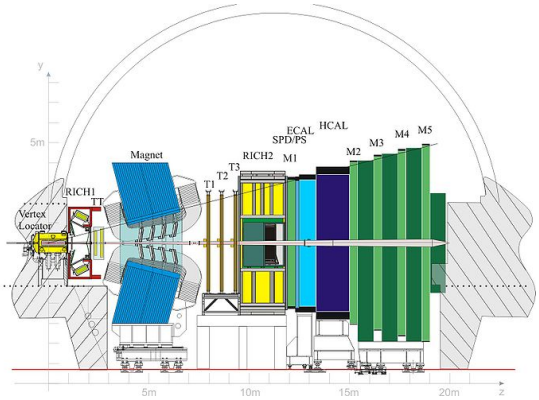

Figure 2: Geometría del LHCb, donde se han destacado los distintos sub-detectores.

Cámara de trazas: Está formada por tres sub-detectores: el tracker turicensis (TT), el inner tracker (IT) y el outer tracker (OT). El primero de ellos se encuentra antes del imán mientras que los otros dos están situados después. El objetivo de los tres sub-detectores en su conjunto es el de determinar de forma precisa el momento de las partículas que se generan en las colisiones o en las posteriores deintegraciones.

Detectores Cherenkov (RICH): Son dos sub-detectores, denominados RICH1 y RICH2, encargados de la identificación de partículas a través de la medida de su velocidad y de la luz Cherenkov que emiten al atravesar cada uno de ellos.

Sistema de Calorímetros: Compuesto por un total de cuatro sub-detectores (SPD, PS, ECAL y HCAL), se encarga de la identificación de partículas electromagnéticas y la medida de la energía de éstas así como la de partículas hadrónicas. Otra de las funciones del calorímetro es su funcionamiento como sistema de trigger, la selección de eventos con partículas de alto momento transverso o el veto de eventos con alta multiplicidad.

Cámara de muones: Formada por un total de cinco cámaras (M1–M5), se encarga de la identificación de los muones. La primera cámara se encuentra antes del sistema de calorímetros mientras que el resto están después.

La frecuencia de las colisiones en el LHC es de $\sim$ 10 MHz, haciendo imposible el almacenamiento de todos los eventos. El sistema de *trigger* del LHCb se encarga de reducir el número de eventos que se almacenan para un posterior análisis a $\sim$ 3 kHz a través de dos fases: el L0 y el HLT.

El L0 reduce la frecuencia de eventos a $\sim$ 1 MHz a través de información extraída del sistema de calorímetros y las cámaras de muones. El HLT se divide a su vez en dos partes, HLT1 y HLT2, y consiste en un conjunto de algoritmos que se ejecuta y que seleccionan los eventos reconstruyéndolos de forma completa.

El sistema *online* se encarga de la transferencia de datos entre el detector y el sistema de almacenamiento permanente. Se divide en tres sub-sistemas: la adquisición de datos (DAQ), que transporta los datos seleccionados por el L0 al sistema de almacenamiento, el sistema de *timing and fast control* (TFC), que controla el flujo de datos entre el detector y la granja de ordenadores que lleva a cabo el proceso del HLT y el sistema de control del experimento (ECS), que controla y monitoriza el detector, los sistemas de trigger, el DAQ y el TFC.

Calibración del SPD

El SPD es uno de los sub-detectores que forman parte del sistema de calorímetros. Su función es ayudar a la diferenciación entre partículas electromagnéticas cargadas y neutras. Está formado por celdas cuadradas de plástico centelleantes de 1.5 cm de grosor y lado variable (4 cm, 6 cm y 12 cm), dependiendo de la parte del detector (más pequeñas cuanto más cerca de los haces de protones, ya que es la zona de mayor densidad de partículas).

El funcionamiento del SPD se basa en el hecho de que al atravesar un medio centelleante, una partícula cargada deposita una cierta cantidad de energía. Si esta energía depositada es mayor que cierto umbral (presente debido a la presencia de ruido electrónico, que podría simular la presencia de señal), el SPD determina la presencia de una partícula electromagnética cargada, cuya energía será depositada en el ECAL. Si, por el contrario, una deposición de energía en el ECAL no va asociada a señal en el SPD, se considera que esa partícula es una partícula electromagnética neutra.

La eficiencia de cada una de las celdas del SPD se define como la fracción de veces que la energía medida es mayor que el umbral respecto del número de veces que una traza reconstruída por el sistema de trazas apunta a esa celda. A lo largo del Run 1 se observó una caída en las eficiencias para celdas de las tres partes que componen el SPD (parte interior, media y exterior). Con el fin de recuperar el rendimiento del SPD de cara al Run 2, se llevó a cabo la calibración del mismo, a través de una modificación de los valores de los umbrales para cada celda afectada. Esta calibración se produjo de dos formas distintas: a través de la toma de datos de rayos cósmicos, como se hizo antes del Run 1 y a través de datos de colisiones de protones.

La calibración con rayos cósmicos se llevó a cabo al inicio del Long Shutdown 1 (periodo de apagado del LHC y sus detectores) con el fin de utilizar candelas estándar para la medida de eficiencias del SPD anteriormente al inicio del Run 2 y comprobar de ese modo si el efecto de caídas de eficiencia seguía presente o no, ya que, a través del proceso de *annealing*, el SPD podía recuperar su rendimiento, ya que se confirmó que la caída de eficiencias era consecuencia de la radiación a la cual las celdas estuvieron sometidas durante el Run 1. Debido al estado radiactivo del SPD y el PS, la calibración del SPD sólo pudo hacerse de forma cualitativa y no cuantitativa, con lo que una calibración posterior al inicio del Run 2 era necesaria, haciendo uso de datos procedentes de colisiones.

La calibración con trazas procedentes de colisiones se llevó a cabo al inicio del Run 2 y consistió en la medida de la eficiencia para cada celda. Una vez comprobada la presencia

del efecto de caída de la eficiencia, se llevó a cabo una redefinición de los valores de los umbrales de las celdas, haciendo posible así una distribución uniforme de las eficiencias a lo largo de todo el SPD. La Fig. 3 muestra el mapa de eficiencias del SPD antes y después de la calibración.

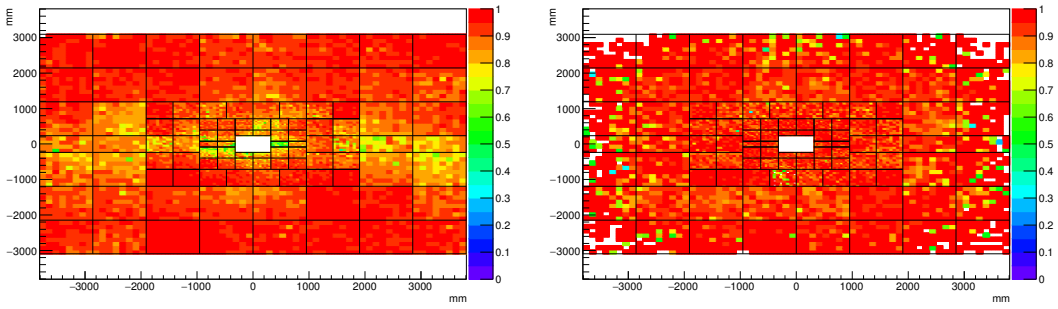

Figure 3: Mapa de eficiencias del SPD al final del Run 1 (izquierda) y al inicio del Run 2 (derecha), una vez aplicada la calibración. La cantidad de datos presente para el mapa de eficiencias del Run 2 es limitada, pero es posible observar que el efecto de caída de eficiencias ha desaparecido.

Herramienta para la separación de γ/π^0

Los piones neutros se desintegran un $\sim$ 99% de las veces en un par de fotones. Si la desintegración se produce suficientemente lejos del ECAL, los dos fotones darán lugar a dos *clusters* en el ECAL. Sin embargo, si la desintegración se produce cerca del ECAL, los dos fotones no dispondrán de suficiente tiempo como para separarse y podrían confundirse con uno solo. Una variable basada en la forma y propiedades del *cluster* ha sido construida con el fin de diferenciar piones neutros y fotones.

Las variables de identificación no están bien reproducidas en el software del LHCb y, por lo tanto, para conseguir un mismo rendimiento en datos reales y en simulación, es necesaria la calibración de estas variables. En este caso, se han desarrollado dos herramientas distintas que, a través del uso de datos reales, permiten una correcta extracción del valor de la eficiencia para un requerimiento concreto en la variable de separación γ/π^0.

Las dos herramientas se basan en el principio de que en bines suficientemente pequeños de momento transverso (p_{T}) y pseudo-rapidez (η), la eficiencia asociada a un corte en la variable de separación es la misma tanto para datos reales como para simulación. La herramienta de tabla de eficiencias (*Efficiency table tool*) ofrece, para un corte determinado en γ/π^0, un valor de la eficiencia del corte para cada uno de los bines bi-dimensionales, dando lugar a una tabla de eficiencias. Por otro lado, la herramienta de *Resampling* genera una nueva variable de separación γ/π^0 a partir de histogramas de calibración (producidos con muestras puras de datos seleccionados offline) como el que puede verse en Fig. 4, habiendo uno por cada bin bidimensional. La herramienta selecciona el bin determinado a partir de los valores de η y p_{T} de la partícula en el

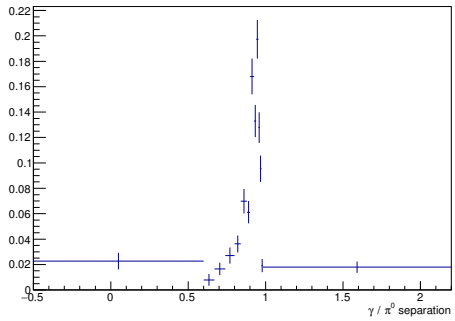

Figure 4: Distribución de la variable de separación γ/π^0 para el caso de fotones definido por el intervalo de momento transverso [2600, 3700] MeV y pseudo-rapidez [2.80, 3.25] para $B^0 \to K^{*0}\gamma$.

evento de simulación y asigna un valor aleatorio dentro del histograma, entendido como una distribución de probabilidad (PDF). En el caso de disponer de grandes muestras de simulación, la distribución de valores asignados aleatoriamente tiende a recuperar la distribución original extraída a partir de la muestra con el fondo sustraído de datos seleccionados. Las dos herramientas permiten la calibración de la variable γ/π^0 para fotones y para piones neutros.

Estudios de desintegraciones $b \to hh\gamma$

El objetivo principal de este trabajo es doble: por un lado, medir la relación de frecuencias de desintegración de los procesos radiativos $B_s^0 \to \phi\gamma$ y $\Lambda_b^0 \to \Lambda^{*0}\gamma$ con respecto a $B^0 \to K^{*0}\gamma$ y, por otro lado, medir la asimetría de *CP* directa para los procesos $B^0 \to K^{*0}\gamma$ y $\Lambda_b^0 \to \Lambda^{*0}\gamma$.

Los estados finales estudiados se definen por las desintegraciones $K^* \to K^{\pm}\pi^{\mp}$, $\phi \to K^+K^-$ y $\Lambda^{*0} \to K^-p$ (y sus complejos conjugados).

Selección de datos

La selección de datos para los tres canales de desintegración tratan de ser lo más parecidos posibles con el fin de maximizar la cancelación de incertidumbres sistemáticas asociadas a cada uno de los procesos de selección. En este sentido, los procesos de reconstrucción y el de una suave selección son lo más similares posibles: los mesones B^0 y B_s^0 y el barión Λ_b^0 se construyen a partir de un fotón y una resonancia intermedia (K^*, ϕ, Λ^{*0}, respectivamente), que se construye a partir de pares de trazas de cargas opuestas (un kaón y un pión, dos kaones, un kaón y un protón, dependiendo del canal).

La selección de datos se lleva a cabo en varios pasos: una suave preselección, seguida de una selección simultánea en las variables de identificación de partículas (PID), aislamiento del vértice y una variable construida a través de un método multivariante que es usada para eliminar la contaminación procedente del fondo combinatorio. Esta herramienta sólo

se usa para los canales relativos a B^0 y B_s^0. La optimización del valor del corte para todas las variables en todos los pasos de la selección está determinada por la maximización de la figura de mérito, definida como

$$FOM = \frac{S}{\sqrt{S+B}}, \tag{1}$$

donde S y B hacen referencia al número de eventos de señal y ruido (calculados a partir de un fit a la distribución de la masa invariante de la partícula con sabor b resultante de cada corte).

Composición del fondo

Una vez que la selección está fijada, las contaminaciones de distintos procesos se analizan: contaminaciones en un canal de señal procedentes de los otros dos canales de desintegración, la contaminación procedente del fondo combinatorio, la contaminación procedente de desintegraciones reconstruidas totalmente pero en las que se ha producido una incorrecta identificación de las partículas del estado final y la contaminación procedente de desintegraciones que se reconstruyen de forma parcial.

La Tabla 1 recoge los canales de desintegración que se han estudiado en la descripción del fondo para los canales de señal, así como si su presencia relativa esperada para cada canal de señal en caso de ser considerada como relevante (la contaminación relativa esperada debe ser mayor del 0.1%).

Extracción de observables físicos

Una vez que la composición del fondo es descrita, se lleva a cabo un fit simultáneo que consiste en un total de cinco fits: uno para el canal $B_s^0 \to \phi\gamma$ y dos para $B^0 \to K^{*0}\gamma$ y $\Lambda_b^0 \to \Lambda^{*0}\gamma$, uno para cada sabor ($B^0$ y $\overline{B}^0$ por un lado y Λ_b^0 y $\overline{\Lambda}_b^0$ por otro). Un total de 30 parámetros se extraen del fit, cuyos resultados se pueden ver en la Fig. 5. Entre ellos, el número de eventos para canal de señal y el valor de la asimetría de CP sin corregir para $B^0 \to K^{*0}\gamma$ y $\Lambda_b^0 \to \Lambda^{*0}\gamma$. Estas cinco cantidades son la clave para el cálculo de los observables objeto de esta tesis: la medida relativa de la frecuencia de desintegración para $B_s^0 \to \phi\gamma$ y $\Lambda_b^0 \to \Lambda^{*0}\gamma$ respecto de $B^0 \to K^{*0}\gamma$ y la medida de $\mathcal{A}^{CP}$ para $B^0 \to K^{*0}\gamma$ y $\Lambda_b^0 \to \Lambda^{*0}\gamma$.

En términos generales, la frecuencia de desintegración para una determinada desintegración $A \to B\ C$ viene dada por:

$$\mathcal{B}(A \to BC) = \frac{N}{2 \times \sigma \times f \times \epsilon}, \tag{2}$$

donde N corresponde al número de eventos de esa desintegración en concreto, σ es la sección eficaz correspondiente a ese proceso, f es el factor de hadronización y ϵ es la eficiencia de selección para esa desintegración. El resultado del fit corresponde a los valores de N para cada desintegración, los valores de f y de σ son extraídos de medidas

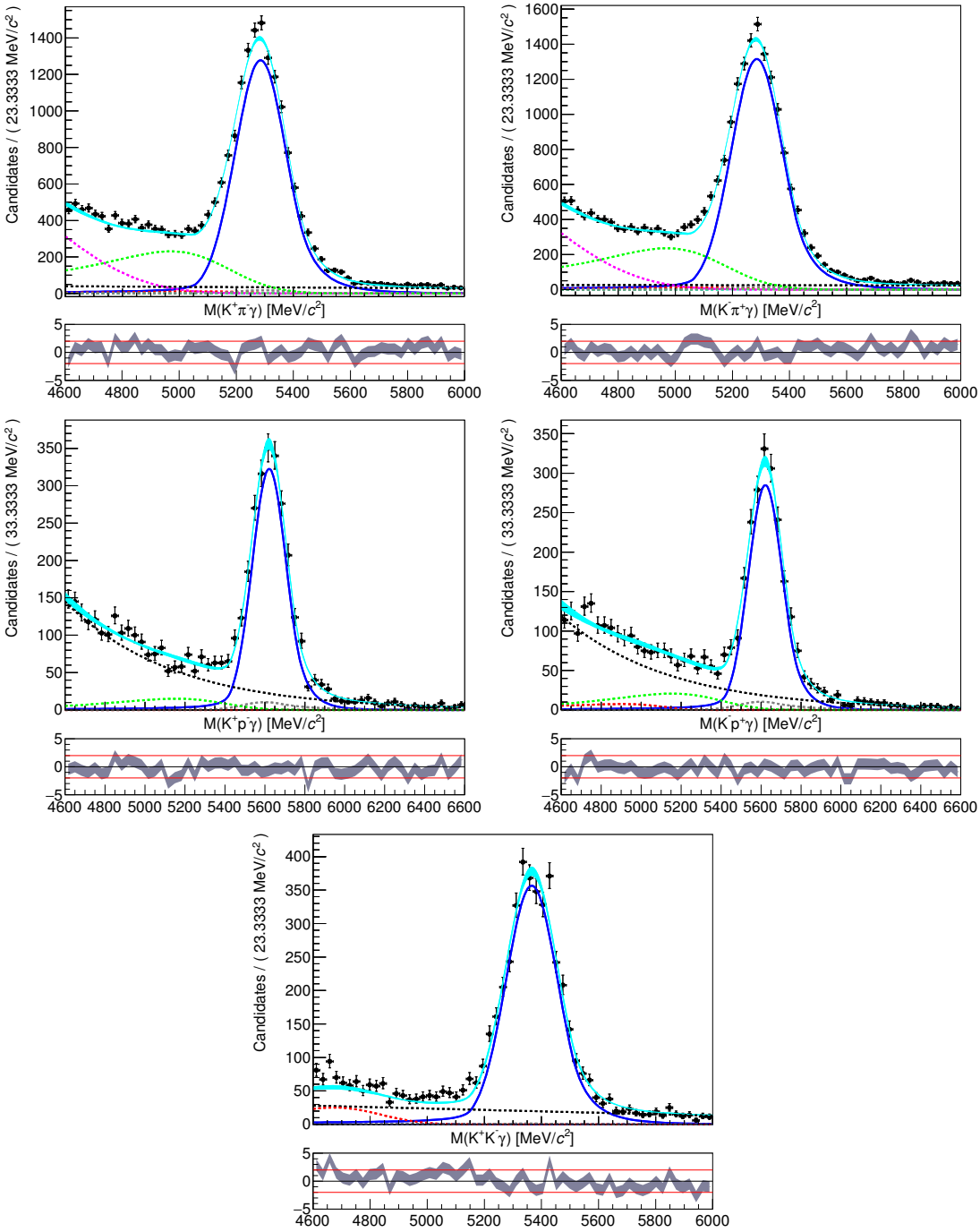

Figure 5: Resultado de los cinco fits simultáneos que definen las cantidades físicas utilizadas para la extracción de los observables objeto de esta tesis para $B^0 \to K^{*0}\gamma$ (parte superior, izquierda y derecha para cada posible sabor), $\Lambda_b^0 \to \Lambda^{*0}\gamma$ (parte media, izquierda y derecha para cada posible sabor) y $B_s^0 \to \phi\gamma$ (parte inferior).

Table 1: Lista de canales de desintegración estudiados para la descripción del fondo. También se detalla si los distintos canales son relevantes (contaminación mayor del 0.1%) o despreciable (N, contaminación menor del 0.1%) para cada canal de señal.

Decay Channel	$B^0 \to K^{*0}\gamma$	$B_s^0 \to \phi\gamma$	$\Lambda_b^0 \to \Lambda^{*0}\gamma$
$B^0 \to J/\psi\, K^{*0}$	N	N	N
$B^0 \to K_1^0\gamma$	$(8.15 \pm 0.15)\%$	$(2.23 \pm 0.21)\%$	$(0.36 \pm 0.07)\%$
$B^0 \to \rho^0\gamma$	$(1.40 \pm 0.06)\%$	N	N
$B^0 \to K\pi\pi^0$	$(0.25 \pm 0.03)\%$	$(0.18 \pm 0.06)\%$	-
$B_s^0 \to J/\psi\,\phi$	N	N	N
$B^+ \to D^{*0}\pi^+\pi^-\pi^0$	N	N	N
$B^+ \to \eta' K^+$	N	N	N
$B^+ \to K_1^+\gamma$	$(12.98 \pm 0.26)\%$	$(1.27 \pm 0.16)\%$	-
$B^+ \to K_2^*\gamma$	$(1.54 \pm 0.07)\%$	N	N
$B^+ \to K^{*+}\phi$	N	N	-
$B^+ \to \phi K^+\gamma$	N	$(0.83 \pm 0.13)\%$	$(0.19 \pm 0.01)\%$
$B^+ \to D^0\rho^+$	$(4.87 \pm 0.12)\%$	$(7.37 \pm 0.37)\%$	-
$B^+ \to K_1(1270)\eta$	N	N	-
$B^+ \to K^+K^-\pi^+\pi^0$	N	N	-
$B^+ \to K^+\pi^-\pi^+\pi^0$	N	N	-
$B^+ \to K^*\pi^+\gamma$	N	N	-
$B^+ \to \rho^+\rho^0$	$(1.63 \pm 0.07)\%$	N	-
$B^0 \to D^0(\to K^+K^-)\pi^0$	-	-	N
$B^0 \to D^0(\to K^+\pi^-)\pi^0$	-	-	N
$B^0 \to K^*\eta'$	$(2.04 \pm 0.03)\%$	N	-
$B_s^0 \to \phi\pi^0$	-	Tomada de referencia	-

realizadas por el LHCb y la eficiencia es calculada de forma separada para cada uno de los pasos de la selección. En este trabajo se estudia la relación de una frecuencia de desintegración de un canal respecto de otro con el fin de reducir los errores sistemáticos, ya que el proceso de selección se intenta que sea lo más parecido posible (teniendo en cuenta la distinta topología y cinemática de cada canal) con el fin de minimizar los errores sistemáticos.

En cuanto a la asimetría $\mathcal{A}^{CP}$, se define, para $B^0 \to K^{*0}\gamma$, como

$$\mathcal{A}^{CP} = \frac{N(\overline{B}^0) - N(B^0)}{N(\overline{B}^0) + N(B^0)}, \tag{3}$$

y de forma similar para Λ_b^0. El resultado extraído del fit corresponde al valor de la $\mathcal{A}^{CP}$ sin corregir, a la que ciertas correcciones han de ser aplicadas. Estas correcciones están relacionadas con la asimetría de producción de B^0 (Λ_b^0) y $\overline{B}^0$ ($\overline{\Lambda}_b^0$) en el LHC debido a que las partículas que se hacen colisionar son protones (y por tanto el contenido quark no es simétrico) y con la dilución de B^0 en $\overline{B}^0$ debido a la oscilaciones de es-

tos mesones (este efecto no aparece en el cálculo de la $\mathcal{A}^{CP}$ para Λ_b^0 ya que éstos no oscilan).

Conclusiones

En este documento se ha presentado el trabajo realizado en relación a la calibración del sub-detector SPD necesaria debido a la caída de eficiencias del mismo debido al envejecimiento de los fototubos, centelleador y fibras después de un largo período de funcionamiento (por radiación acumulada). Gracias a esta calibración, la eficiencia del SPD volvió a ser la misma que al inicio del Run 1, alrededor del 95%.

Además, se ha desarrollado una herramienta de software que permite una mejor separación entre fotones y π^0 a nivel de análisis *offline* y que se basa en la forma de los *clusters* en el calorímetro electrónico así como el uso de variables topológicas y cinemáticas para una mejor descripción de la variable de separación en la simulación.

Por último, y haciendo uso de los datos recogidos por el experimento LHCb durante los años 2011–2012, se ha procedido al cálculo de la frecuencia relativa de desintegración de los procesos relativos $B_s^0 \to \phi\gamma$ y $\Lambda_b^0 \to \Lambda^{*0}\gamma$ respecto a $B^0 \to K^{*0}\gamma$ así como el cálculo de la asimetría $\mathcal{A}^{CP}$ para $B^0 \to K^{*0}\gamma$ y $\Lambda_b^0 \to \Lambda^{*0}\gamma$. Los resultado encontrados para estos observables físicos son, para las frecuencias de desintegración,

$$\begin{aligned} \frac{\mathcal{B}(B^0 \to K^{*0}\gamma)}{\mathcal{B}(B_s^0 \to \phi\gamma)} &= 1.350 \pm 0.031\,(\text{stat}) \pm 0.041\,(\text{syst}) \pm 0.107(f_s/f_d \\ \frac{\mathcal{B}(B^0 \to K^{*0}\gamma)}{\mathcal{B}(\Lambda_b^0 \to \Lambda^{*0}\gamma)} &= 1.279 \pm 0.027\,(\text{stat}) \pm 0.059\,(\text{syst}) \pm 0.171(f_{\Lambda_b}/f_d, \end{aligned} \tag{4}$$

y, para la medida de $\mathcal{A}^{CP}$

$$\begin{aligned} \mathcal{A}^{CP}(B^0 \to K^{*0}\gamma) &= (0.54 \pm 0.81\,(\text{stat}) \pm 0.30\,(\text{syst}))\% \\ \mathcal{A}^{CP}(\Lambda_b^0 \to \Lambda^{*0}\gamma) &= (0.11 \pm 1.8\,(\text{stat}) \pm 1.22\,(\text{syst}))\%. \end{aligned} \tag{5}$$

Este análisis supone una mejora en la medida ya realizada por el LHCb de la frecuencia de desintegración de $B_s^0 \to \phi\gamma$ respecto de $B^0 \to K^{*0}\gamma$ y de la medida de la asimetría $\mathcal{A}^{CP}$ para $B^0 \to K^{*0}\gamma$ así como la primera observación de $\Lambda_b^0 \to \Lambda^{*0}\gamma$ y la medida, en el LHCb, de la frecuencia de desintegración respecto de $B^0 \to K^{*0}\gamma$ y de la asimetría $\mathcal{A}^{CP}$.

A partir de la relación de frecuencias entre $B_s^0 \to \phi\gamma$ y $\Lambda_b^0 \to \Lambda^{*0}\gamma$ respecto de $B^0 \to K^{*0}\gamma$, es posible determinar sus frecuencias de desintegración:

$$\begin{aligned} \mathcal{B}(B_s^0 \to \phi\gamma) &= (3.21 \pm 0.28) \times 10^{-5} \\ \mathcal{B}(\Lambda_b^0 \to \Lambda^{*0}\gamma) &= (3.39 \pm 0.48) \times 10^{-5}, \end{aligned} \tag{6}$$

que corresponde, para el caso de $\Lambda_b^0 \to \Lambda^{*0}\gamma$, a la primera medida de la frecuencia de desintegración radiativa de un barión con un quark b.

1

Introduction

The Standard Model (SM) of particle physics, a set of theories that were developed during the 20^{th} century, aims to explain three of the four fundamental forces of nature: electromagnetism, strong and weak interactions. From a theoretical point of view, the SM was finished during the 1970s, but it was not until 2012 when its last piece, the Higgs boson, was experimentally confirmed [5, 6].

Despite having been proved to be a very successful theory with many experimental observations, the SM fails to explain crucial phenomena that would make it a complete theory. Its main shortcomings are the inclusion of gravity as described by general relativity, the existence and properties of dark matter and dark energy and neutrino oscillations. It also fails to explain the different abundances of matter and antimatter that are observed in the Universe.

In particular, *CP* violation is related to the last of these problems [7] as it is a necessary condition to the asymmetrical matter-antimatter abundances to appear from a symmetrical initial state. However, the SM prediction for *CP* violation [8] is not enough to explain the large asymmetry observed [9].

From the experimental point of view, *CP* violation was first observed in neutral kaon decays [10]. The Belle and BaBar experiments observed *CP* violation in the b-sector in 2001 [11, 12]. There are many physical observables in the b sector related to *CP* violation. These observables are predicted with high precision by the SM so any large deviation in these parameters would mean the existence of *new* physics. As a consequence, b-physics is an ideal place to test the SM predictions.

The LHCb experiment, one of the experiments of the Large Hadron Collider, is specialized in the study of heavy flavour hadrons. One of the topics of interest is flavour-changing neutral currents, which can only happen via loop processes within the SM, making them a very sensitive place for the search of contributions from new particles entering the loop. Radiative decays (decays where there is a photon in the final state) are one of this kind of processes.

This thesis will verse about the measurement of the ratio of branching fractions between the $B_s^0 \to \phi\gamma$ and $\Lambda_b^0 \to \Lambda^{*0}\gamma$ decays with respect to the $B^0 \to K^{*0}\gamma$ decay as well as the direct *CP* asymmetry for the $B^0 \to K^{*0}\gamma$ and $\Lambda_b^0 \to \Lambda^{*0}\gamma$ decays. In addition,

the $\Lambda_b^0 \to \Lambda^{*0}\gamma$ decay corresponds to the first observation of b-baryon radiative decay. This work corresponds to the analysis of the whole LHCb Run 1 dataset, collected in the years 2011–2012, which amounts to a total of 3 fb^{-1}. The ratio of branching fractions between $B_s^0 \to \phi\gamma$ and $B^0 \to K^{*0}\gamma$ and the *CP* for the latter were already measured by the LHCb with data collected in 2011 [3] and therefore this thesis superseeds those measurements.

The photon reconstruction and identification is done with information from the Calorimeter detector. The SPD detector, the part of the calorimeter in charge of the discrimination of photons and electrons at the first level of trigger, suffered from ageing problems during the Run 1 period. This thesis includes detailed studies on the monitorization of the ageing effect on the SPD efficiencies as well as the description of the calibration process that followed.

One of the main sources of background for radiative decays is the misidentification of neutral pions and photons. The thesis introduces an offline tool that improves the simulation description of the γ/π^0 separation variable.

Chapter 2 gives a complete description of the Standard Model as a general framework to describe fundamental particles and their interactions, a deep explanation of *CP* violation and its different types, *CP* violation within B decays and radiative decays.

Chapter 3 gives a brief description of the European Organization for Nuclear Research (CERN), the Large Hadron Collider, the largest particle accelerator of the world, and the experiments placed along it, giving a more deep insight of the LHCb experiment.

Chapter 4 explains the observed ageing of the SPD and the steps that followed in order to perform a complete calibration of it for the Run 2 data-taking period.

Chapter 5 presents a software tool designed to distinguish between photons and neutral pions given their different signature in the calorimeter. A detailed description of the separation variable is given, followed by a data-driven method that allows an evaluation of efficiencies when performing an offline requirement on the variable.

Chapter 6, which corresponds to the main topic of this thesis, presents the measurement of the relative branching fractions of $B_s^0 \to \phi\gamma$ and $\Lambda_b^0 \to \Lambda^{*0}\gamma$ with respect to $B^0 \to K^{*0}\gamma$ and of the *CP* asymmetry of the $\Lambda_b^0 \to \Lambda^{*0}\gamma$ and $B^0 \to K^{*0}\gamma$ decays for the full Run I LHCb dataset. Moreover, this work reports the first observation of a b-baryon radiative decay.

The conclusions of this work are discussed in Chapter 7.

2

Theoretical framework

This chapter summarises the theoretical basis related to the study of B mesons and their decays and, in particular, the case of radiative decays. It is divided in different sections: a description of the SM, followed by a discussion of CP violation in the context of b-hadron decays, including neutral meson oscillation; finally, radiative decays of b-hadrons are described in further detail.

2.1 The Standard Model

Three of the fundamental interactions are considered within the SM framework: the electromagnetic force, the weak nuclear force and the strong nuclear force, leaving gravity out because it has not been possible to find a quantum description for it. It is based on the local gauge invariance principle of the groups [13–16]:

$$SU(3)_C \times SU(2)_L \times U(1)_Y, \tag{2.1}$$

where Y and C represent the *weak hypercharge* and the *colour charge*, respectively. The $SU(2)$ part of this group affects only to left-handed fermions (noted specifically by the L subindex). This gauge group is spontaneously broken to $SU(3)_C \times U(1)_Q$, where Q represents the electric charge generator, defined as

$$Q = \frac{Y}{2} - T_3, \tag{2.2}$$

where T_3 corresponds to the third component of the weak isospin, one of the three generators of $SU(2)$.

The SM includes three fermion generations that can be represented as Dirac spinors. These fermions are split into quarks and leptons, depending on whether they interact strongly (quarks) or not (leptons). Both types of fermions can interact weakly and electromagnetically. There are six types (flavours) of quarks: up (u), down (d), charm (c), strange(s), top (t) and bottom (b). The left-handed quarks and leptons are represented as $SU(2)_L$ doublets and their corresponding right-handed fields are represented as $SU(2)_R$ singlets, which translates into the fact that right-handed particles do not interact weakly

Table 2.1: Left-handed doublets and right-handed singlets in the SM for the first (top row), second (middle row) and third (bottom row) generations.

$\begin{pmatrix} \nu_e \\ e^- \end{pmatrix}_L$,	$\begin{pmatrix} u \\ d \end{pmatrix}_L$	e^-_R, u_R, d_R
$\begin{pmatrix} \nu_\mu \\ \mu^- \end{pmatrix}_L$,	$\begin{pmatrix} c \\ s \end{pmatrix}_L$	μ^-_R, c_R, s_R
$\begin{pmatrix} \nu_\tau \\ \tau^- \end{pmatrix}_L$,	$\begin{pmatrix} t \\ b \end{pmatrix}_L$	τ^-_R, t_R, b_R

within the SM. Table 2.1 gathers SM fermions into singlets or doublets depending on their chirality while Table 2.2 summarizes some of their properties.

The only difference among the different fermion generations is their masses, that increases as we move from one generation to the next. Quarks are usually referred to as *up*-type (that includes u, c and t quarks) or *down*-type quarks (that includes d, s and b quarks), depending on their electromagnetic charge. Each of these particles has its corresponding antiparticle.

In the SM, forces are mediated through the exchange of gauge bosons. These particles include a total of 8 *gluons* (g, carriers of the strong interaction) and three *weak bosons* ($W^\pm$, Z) that, along with the photon (γ), are the carriers of the electroweak interaction. Table 2.3 summarizes the SM boson properties.

Although the SM accounts for all the ordinary matter observed, it is known to be an incomplete theory: only $\sim 5\%$ of all the forces and matter known to exist in the Universe are explained through the SM. Dark matter ($\sim 24\%$ of the Universe) and dark energy ($\sim 71\%$) can't be explained making use of the SM. In addition, the fact that gravity can't be accommodated into the same formalism suggests that the SM could be an effective field theory. Theories *beyond the SM* try to find a more complete framework that could explain all the phenomena that are observed [17]. During the LHC Run 1 (which corresponds to the period of time during which the data used for this work were collected, 2011–2012), no evidence for any of these theories was found and, in fact, measurements have dismissed or strongly constrained many of these theories [18–27].

2.1.1 The Standard Model Lagrangian

The SM Lagrangian can be written as the combination of two different terms: the quantum chromodynamics sector (QCD) [13] and the electroweak sector (EW) [14–16]. The QCD term is given by:

$$\mathcal{L}_{\text{QCD}} = \sum_i \bar{\psi}_i \gamma^\mu (i\partial_\mu - g_s G^a_\mu T^a)\psi_i \tag{2.3}$$

where G^a_μ is the $SU(3)$ gauge field that contains the gluons, T^a are the $SU(3)$ generators, $\gamma\ _\mu$ are the Dirac matrices, ψ_i are the spinors related to the quarks and g_s is the strong

Table 2.2: Table of quark and lepton families with their mass and charge according to the Particle Data Group [4].

Generation	Name	Symbol	Mass	Charge
		Quarks		
1st	Up	u	2.3 MeV	$+2/3$
	Down	d	4.8 MeV	$-1/3$
2nd	Charm	c	1.275 GeV	$+2/3$
	Strange	s	95 MeV	$-1/3$
3rd	Top	t	173.21 GeV	$+2/3$
	Beauty	b	4.18 GeV	$-1/3$
		Leptons		
1st	Electron	e	0.51 MeV	-1
	Electron neutrino	ν_e	$< 2\,\text{eV}$	0
2nd	Muon	μ	105.66 MeV	-1
	Muon neutrino	ν_μ	< 0.19 MeV	0
3rd	Tau	τ	1.78 GeV	-1
	Tau neutrino	ν_τ	< 18.2 MeV	0

Table 2.3: Standard Model bosons, electric charge and mass.

Particle	Force carrier	Electric charge	Mass (GeV)
γ	Electromagnetic	0	0
W^+/W^-	Weak	+1/-1	80.39
Z	Weak	0	91.19
g	Strong	0	0

coupling constant.

The EW sector is a Yang-Mills gauge theory with the symmtery group $SU(2) \times U(1)_Y$ [28]:

$$\mathcal{L}_{\text{EW}} = \sum_i \bar{\psi}_i \gamma^\mu (i\partial_\mu - g' \frac{1}{2} Y B_\mu - g \frac{1}{2} \vec{\tau} \cdot \vec{W}_\mu) \psi_i, \tag{2.4}$$

where B_μ is the $U(1)$ gauge field, $\vec{W}_\mu$ is the three-component $SU(2)_L$ gauge field, $\vec{\tau}$ are the Pauli matrices (that only act on left-handed fermions), Y is the weak hyper-charge,

g and g' are the coupling constants and ψ_i are the spinors related to the fermions.

The previous Lagrangians do not include any mass terms. However, the SM particles are measured to be massive (as can be seen in Table 2.2), so a mechanism that makes this possible needs to be added. The *Englert-Brout-Higgs mechanism* offers this possibility via the spontaneous breakdown of symmetry [29–34]. If a scalar field of the form

$$V(\Phi) = \frac{1}{2}\mu^2\Phi^2 + \frac{1}{4}\lambda\Phi^4 \tag{2.5}$$

is introduced, where $\mu^2 < 0$, λ is a positive parameter and Φ is an external field, there is more than one possible minimum for the potential with non-zero vacuum expectation value $v = \sqrt{-\mu^2/\lambda}$. The field Φ (*Higgs field*) is a scalar doublet field of the $SU(2)_L$ group, that can be written as

$$\Phi = \frac{1}{\sqrt{2}} \begin{pmatrix} \phi^+ \\ \phi^0 \end{pmatrix}, \tag{2.6}$$

where the superindices indicate the electromagnetic charge of the field. With this term, the electroweak gauge fields acquire a mass without breaking the gauge symmetry, also providing mass term to the fermions through Yukawa mass terms of the form

$$\mathcal{L}(x) = g\bar{\psi}(x)\phi(x)\psi(x). \tag{2.7}$$

The Higgs field itself also acquires a mass that is given by

$$M_H = \sqrt{-2\mu^2} \tag{2.8}$$

The general purpose detectors at the LHC (ATLAS and CMS) have reported the observation of a new particle compatible with the SM Higgs boson (with a mass of $125 \pm 0.21 \pm 0.11$ GeV), which would confirm the Higgs mechanism [5, 6].

2.2 B physics in the Standard Model

B decays in the SM are described by the *low-energy effective Hamiltonian* [35], which is an effective field theory [36] built using the operator product expansion formalism [37]. The element that connects the initial and the final states ($\mathcal{H}_{\text{eff}}$) can be written as

$$\langle f|\mathcal{H}_{\text{eff}}|i\rangle \propto \sum_k C_k(\mu)\langle f|\mathcal{O}_k(\mu)|i\rangle, \tag{2.9}$$

where μ is appropriate renormalisation scale, which for B decays is usually chosen as the mass of the bottom quark (m_b), $\mathcal{O}_k(\mu)$ are the local operators that form a complete set for a given transition, and the $C_k(\mu)$ correspond to the Wilson coefficients.

This formalism allows the separation of the contribution from "long-distance" effects (encoded in the hadronic matrix elements $\langle f|\mathcal{O}_k(\mu)|i\rangle$, due to non-perturbative strong interactions) and "short-distance" effects (that can be computed perturbatively and are described by the Wilson coefficients, $C_k(\mu)$). Since the perturbative part encodes physics

at larger scales than μ, it carries information of particles heavier than that scale (which may be SM or beyond SM particles).

The complete basis of operators that describe the effective Hamiltonian of weak decays of the b quark to a quark q (where q can be either the d or the s quarks), with $\Delta B = 1$ (where the varying property is the *bottom quantum number*, related to the number of *bottom* quarks in the particle) can be divided in five categories [38].

1. Current-current operators

$$\begin{aligned} \mathcal{O}_1^{qq'} &= (\bar{q}_\alpha q'_\beta)_{V-A}(\bar{q}'_\beta b_\alpha)_{V-A} \\ \mathcal{O}_2^{qq'} &= (\bar{q}_\alpha q'_\alpha)_{V-A}(\bar{q}'_\beta b_\beta)_{V-A}, \end{aligned} \tag{2.10}$$

2. QCD-penguin operators

$$\begin{aligned} \mathcal{O}_3^q &= (\bar{q}_\alpha b_\alpha)_{V-A} \sum_{q'} (\bar{q}'_\beta q'_\beta)_{V-A} \\ \mathcal{O}_4^q &= (\bar{q}_\alpha b_\beta)_{V-A} \sum_{q'} (\bar{q}'_\beta q'_\alpha)_{V-A} \\ \mathcal{O}_5^q &= (\bar{q}_\alpha b_\alpha)_{V-A} \sum_{q'} (\bar{q}'_\beta q'_\beta)_{V+A} \\ \mathcal{O}_6^q &= (\bar{q}_\alpha b_\beta)_{V-A} \sum_{q'} (\bar{q}'_\beta q'_\alpha)_{V+A}, \end{aligned} \tag{2.11}$$

3. Electroweak-penguin operators

$$\begin{aligned} \mathcal{O}_7^q &= \frac{3}{2}(\bar{q}_\alpha b_\alpha)_{V-A} \sum_{q'} e_{q'} (\bar{q}'_\beta q'_\beta)_{V+A} \\ \mathcal{O}_8^q &= \frac{3}{2}(\bar{q}_\alpha b_\beta)_{V-A} \sum_{q'} e_{q'} (\bar{q}'_\beta q'_\alpha)_{V+A} \\ \mathcal{O}_9^q &= \frac{3}{2}(\bar{q}_\alpha b_\alpha)_{V-A} \sum_{q'} e_{q'} (\bar{q}'_\beta q'_\beta)_{V-A} \\ \mathcal{O}_{10}^q &= \frac{3}{2}(\bar{q}_\alpha b_\beta)_{V-A} \sum_{q'} e_{q'} (\bar{q}'_\beta q'_\alpha)_{V-A}, \end{aligned} \tag{2.12}$$

4. Magnetic-penguin operators

$$\begin{aligned} \mathcal{O}_{7\gamma}^q &= \frac{e}{8\pi^2} m_b \bar{q}_\alpha \sigma^{\mu\nu}(1+\gamma^5) b_\alpha F_{\mu\nu} \\ \mathcal{O}_{8G}^q &= \frac{g}{8\pi^2} m_b \bar{q}_\alpha \sigma^{\mu\nu}(1+\gamma^5) T^a_{\alpha\beta} b_\beta G^a_{\mu\nu}, \end{aligned} \tag{2.13}$$

5. Semi-leptonic operators

$$\begin{aligned}
\mathcal{O}^q_{9V} &= \frac{3}{2}(\bar{q}_\alpha b_\alpha)_{V-A}(\bar{l}l)_V \\
\mathcal{O}^q_{10A} &= \frac{3}{2}(\bar{q}_\alpha b_\alpha)_{V-A}(\bar{l}l)_A \\
\mathcal{O}^q_{\nu\bar{\nu}} &= \frac{3}{2}(\bar{q}_\alpha b_\alpha)_{V-A}(\bar{\nu}\nu)_{V-A} \\
\mathcal{O}^q_{\mu\bar{\mu}} &= \frac{3}{2}(\bar{q}_\alpha b_\alpha)_{V-A}(\bar{\mu}\mu)_{V-A},
\end{aligned} \tag{2.14}$$

where $V \pm A$ represents the Lorentz structures $\gamma_\mu(1 \pm \gamma_5)$, α and β represent the $\mathrm{SU}(3)_C$ colour indices, q' runs over all the different quark flavours active at this scale (m_b) and $e_{q'}$ is the corresponding electromagnetic charge of the quark.

2.3 *CP* violation in the Standard Model

The Cabibbo-Kobayashi-Maskawa matrix (V_{CKM}) describes the relation between particle mass eigenstates and particle weak eigenstates. This is a 3×3 matrix that is usually expressed as [39]:

$$\begin{pmatrix} V_{ud} & V_{us} & V_{ub} \\ V_{cd} & V_{cs} & V_{cb} \\ V_{td} & V_{ts} & V_{tb} \end{pmatrix}. \tag{2.15}$$

The CKM matrix elements can be described by three angles and one complex phase. Following the most common parameterisation for the matrix [4], one can write:

$$V_{\mathrm{CKM}} = \begin{pmatrix} c_{12}c_{13} & s_{12}c_{13} & s_{13}e^{-i\delta} \\ -s_{12}c_{23} - c_{12}s_{23}s_{13}e^{i\delta} & c_{12}c_{23} - s_{12}s_{23}s_{13}e^{i\delta} & s_{23}c_{13} \\ s_{12}s_{23} - c_{12}c_{23}s_{13}e^{i\delta} & -s_{23}c_{12} - s_{12}c_{23}s_{13}e^{i\delta} & c_{23}c_{13} \end{pmatrix} \tag{2.16}$$

where s_{ij} and c_{ij} mean $\sin\theta_{ij}$ and $\cos\theta_{ij}$ respectively, and i and j are the generation labels ($i, j = 1, 2, 3$). The δ phase is the only source of *CP* violation in the SM.

Since the CKM matrix elements are complex numbers, we can express them as a modulus and a phase, making it possible for a generic element to be written as $V_{ij} = |V_{ij}|e^{i\gamma}$. The matrix elements V_{13} and V_{31} are the only ones that have significant phase.

The CKM matrix must be unitary, which implies:

$$\sum_j |V_{ij}|^2 = 1, \qquad \sum_i |V_{ij}|^2 = 1, \tag{2.17}$$

where the first sum is over the down-type quarks and the second one is over the up-type quarks. Another consequence of unitarity is [40]:

$$\sum_k V_{ik}V_{jk}^* = 0, \qquad \sum_k V_{ki}V_{kj}^* = 0, \tag{2.18}$$

where again the first sum is over the down-type quarks and the second one is over the up-type quarks.

There are six equations that comply this last condition. Each of these equations can be represented geometrically in the complex plane as a triangle (each of the sides of the triangle would be one of the terms in the sum). All of them have the same area ($J/2$, where J stands for the Jarlskog invariant, which is defined as $\mathrm{Im}(V_{ij}V_{kl}V_{il}^*V_{kj}^*)$ for $i, j, k, l \in \{1, 2, 3\}$, with a value of approximately 4×10^{-5}). Describing *CP* violation in terms of unitarity triangles is advantageous because they are convention-independent, *i.e.*, if the parameterisation of the CKM matrix is changed, that only implies a rotation of the whole triangle within the complex plane but the side lengths and internal angles do not vary. This property makes the unitarity triangles a fundamental way of parametrising *CP* violation in the SM.

As stated before, the V_{ub} and V_{td} elements are the ones with significant imaginary parts, which translates, in terms of the unitary triangles, in the fact that the sides of the triangles are of similar sizes for the triangle involving those CKM elements (this is not the case for the other triangles, where typically one of the sides is much smaller than the other two). Therefore, this is what is usually called the Unitary Triangle. The triangle angles (usually denoted α, β and γ) are defined as [41]:

$$\alpha = \arg\left[-\frac{V_{td}V_{tb}^*}{V_{ud}V_{ub}^*}\right] \qquad \beta = \arg\left[-\frac{V_{cd}V_{cb}^*}{V_{td}V_{tb}^*}\right] \qquad \gamma = \arg\left[-\frac{V_{ud}V_{ub}^*}{V_{cd}V_{cb}^*}\right], \tag{2.19}$$

where the relation $\alpha + \beta + \gamma = \pi$ is to be preserved. The current values for the three angles introduced previously are presented in Table 2.4. Figure 2.1 shows the current knowledge of the parameters of the unitary triangle [42].

Table 2.4: Current values for the Unitary Triangle angles [42].

Angle	Value
α	$(90.4^{+2.0}_{-1.0})^\circ$
β	$(22.62^{+0.44}_{-0.42})^\circ$
γ	$(73.2^{+6.3}_{-7.0})^\circ$

2.4 Neutral meson oscillation

The concept of *CP* violation is directly related to the observed phenomenon of neutral meson oscillation. One of the possible ways for *CP* violation to take place is by happening

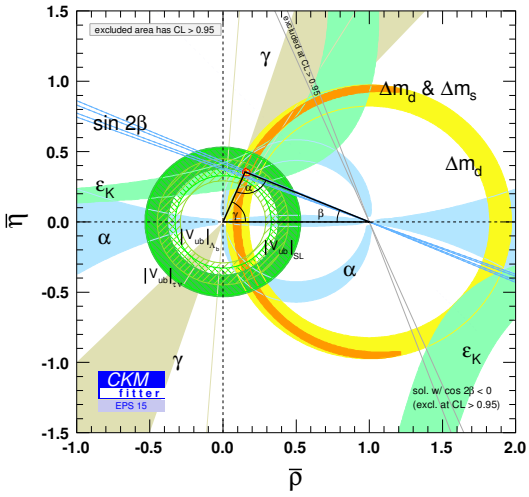

Figure 2.1: Current constrains to the Unitary Triangle.

at the mixing of the two oscillating states.

Let us consider an arbitrary linear combination of a neutral flavour state and its self-conjugate (which will correspond to a particle and its antiparticle), that we can write as

$$a|B^0\rangle + b|\bar{B}^0\rangle, \tag{2.20}$$

where, in general, a and b are two complex parameters. The time evolution of this state will be given by the time dependent Schrödinger equation

$$i\frac{d}{dt}\begin{pmatrix} a \\ b \end{pmatrix} = \mathcal{H}\begin{pmatrix} a \\ b \end{pmatrix} \equiv \left(\mathcal{M} - \frac{i}{2}\Gamma\right)\begin{pmatrix} a \\ b \end{pmatrix}, \tag{2.21}$$

where $\mathcal{M}$ and Γ represent, respectively, the mass and the decay widths of the states and are two 2×2 hermitian matrices. CPT invariance ensures the diagonal elements for such matrices to be equal, and therefore $\mathcal{H}_{11} = \mathcal{H}_{22}$ [43] and $\Gamma_{11} = \Gamma_{22}$, which means that the mass and the decay width of the particle and the antiparticle are the same

$$\begin{aligned} \mathcal{M}_{11} &= \mathcal{M}_{22} \equiv \mathcal{M} \\ \Gamma_{11} &= \Gamma_{22} \equiv \Gamma. \end{aligned} \tag{2.22}$$

Weak-interaction eigenstates and mass eigenstates are not the same and therefore, even if, as stated before, $H_{11} = H_{22}$, there are two mass eigenstates. We will refer to them as the light state ($|B_L\rangle$) and the heavy state ($|B_H\rangle$).

These two states can be written as a function of the particle-antiparticle states $|B^0\rangle$ and $|\bar{B^0}\rangle$:

$$\begin{aligned} |B_L\rangle &= p|B^0\rangle + q|\bar{B^0}\rangle \\ |B_H\rangle &= p|B^0\rangle - q|\bar{B^0}\rangle, \end{aligned} \tag{2.23}$$

where p and q are two parameters normalised to unity in the following way:

$$|p|^2+|q|^2= 1. \tag{2.24}$$

Defining I as the 2×2 unitary matrix and solving the characteristic equation

$$|\mathcal{H} - EI|= 0, \tag{2.25}$$

two eigenvalues ($E_{1,2}$) can be found:

$$\begin{aligned} E_1 &= M - \frac{i}{2}\Gamma + \sqrt{(M_{12} - \frac{i}{2}\Gamma_{12})(M^*_{12} - \frac{i}{2}\Gamma_{12})} \equiv M_1 - \frac{i}{2}\Gamma_1 \\ E_2 &= M - \frac{i}{2}\Gamma + \sqrt{(M_{12} - \frac{i}{2}\Gamma_{12})(M^*_{12} - \frac{i}{2}\Gamma_{12})} \equiv M_2 - \frac{i}{2}\Gamma_2. \end{aligned} \tag{2.26}$$

The relation between p and q can be found making use of the eigenvector equations

$$(\mathcal{H} - EI) \begin{pmatrix} p \\ \pm q \end{pmatrix} = 0, \tag{2.27}$$

from where it is possible to find:

$$\frac{q}{p} = \sqrt{\frac{M^*_{12} - \frac{i}{2}\Gamma^*_{12}}{M_{12} - \frac{i}{2}\Gamma_{12}}}. \tag{2.28}$$

The Schrödinger equation describes the time evolution of the *light* and the *heavy* initial states in the following way:

$$\begin{aligned} |B_L(t)\rangle &= e^{-i(M_1 - \frac{i}{2}\Gamma_1)t}|B_L\rangle \\ |B_H(t)\rangle &= e^{-i(M_2 - \frac{i}{2}\Gamma_2)t}|B_H\rangle. \end{aligned} \tag{2.29}$$

Going back to the weak eigenstates ($|B^0\rangle$ and $|\bar{B^0}\rangle$) and using Eq. (2.23) and Eq. (2.29), we can write:

$$\begin{aligned} |B^0(t)\rangle &= \frac{1}{2}\Big[(e^{-i(M_1 - \frac{i}{2}\Gamma_1)t} + e^{-i(M_2 - \frac{i}{2}\Gamma_2)t})|B^0\rangle \\ &+ \frac{q}{p}\,(e^{-i(M_1 - \frac{i}{2}\Gamma_1)t} - e^{-i(M_2 - \frac{i}{2}\Gamma_2)t})|\bar{B^0}\rangle\Big] \\ &\equiv f_+(t)|B^0\rangle + f_-|\bar{B^0}\rangle, \end{aligned} \tag{2.30}$$

and

$$\begin{aligned}|\bar{B}^0(t)\rangle &= \frac{1}{2}\Big[\frac{p}{q}(e^{-i(M_1-\frac{i}{2}\Gamma_1)t} - e^{-i(M_2-\frac{i}{2}\Gamma_2)t})|B^0\rangle \\ &\quad + (e^{-i(M_1-\frac{i}{2}\Gamma_1)t} + e^{-i(M_2-\frac{i}{2}\Gamma_2)t})|\bar{B}^0\rangle\Big] \\ &\equiv \frac{p}{q}f_-(t)|B^0\rangle + f_+|\bar{B}^0\rangle,\end{aligned} \tag{2.31}$$

where the $f_\pm(t)$ function has been introduced to simplify the notation.

With all this, the probability to find a state $|B^0\rangle$ or $|\bar{B}^0\rangle$ at a time t is:

$$\begin{aligned}\mathcal{P}(|B^0\rangle) &= |\langle B^0|B^0(t)\rangle|^2 = \frac{1}{4}\Big(e^{-\Gamma_1 t} + e^{-\Gamma_2 t} + 2e^{-\bar{\Gamma}t}\cos(\Delta M t)\Big) \\ \mathcal{P}(|\bar{B}^0\rangle) &= |\langle \bar{B}^0|\bar{B}^0(t)\rangle|^2 = \frac{1}{4}\Big(e^{-\Gamma_1 t} + e^{-\Gamma_2 t} - 2e^{-\bar{\Gamma}t}\cos(\Delta M t)\Big),\end{aligned} \tag{2.32}$$

where $\bar{\Gamma}$ is the average decay width ($\bar{\Gamma} = (\Gamma_1 + \Gamma_2)/2$) and ΔM is the mass difference between the two eigenstates, $\Delta M = M_2 - M_1$.

All this implies that the states $|B^0\rangle$ and $|\bar{B}^0\rangle$ oscillate naturally from an initial pure state $|B^0\rangle$ or $|\bar{B}^0\rangle$. This oscillation depends on a parameter related to their mass and their decay width, $\Delta M/\bar{\Gamma}$.

2.5 Types of *CP* violation for B-meson decays

The probability of finding a state $|B^0\rangle$ or $|\bar{B}^0\rangle$ at a time t is specified in Eq. (2.32). For the decay amplitude evolution with time of those states as initial states to reach the same (*CP* eigenstate) final state, $|f\rangle$ can be written as:

$$\begin{aligned}\Gamma_f(t) &= |\langle f|\mathcal{H}|B^0(t)\rangle|^2 \\ &= |A_f|^2\Big[|f_+(t)|^2 + \Big(\frac{q\bar{A}_f}{pA_f}\Big)^2|f_-(t)|^2 + 2\,\mathrm{Re}\,\Big(f_+^*(t)f_-(t)\frac{q}{p}\frac{\bar{A}_f}{A_f}\Big)\Big] \\ \bar{\Gamma}_f(t) &= |\langle f|\mathcal{H}|\bar{B}^0(t)\rangle|^2 \\ &= |A_f|^2\Big[|\frac{\bar{A}_f}{A_f}|^2|f_+(t)|^2 + \Big(\frac{p}{q}\Big)^2|f_-(t)|^2 + 2\Big(\frac{p}{q}\Big)^2\,\mathrm{Re}\,\Big(f_+^*(t)f_-(t)\frac{q}{p}\frac{\bar{A}_f^*}{A_f}\Big)\Big],\end{aligned} \tag{2.33}$$

where $A_f = \langle f|\mathcal{H}|B^0(t)\rangle$ and $\bar{A}_f = \langle f|\mathcal{H}|\bar{B}^0(t)\rangle$ are the instantaneous decay amplitudes. Since in both cases we end up in the same final state, any difference between the two rates Γ_f and $\bar{\Gamma}_f$ will be proof of *CP* violation.

Three different types of *CP* violation can arise:

1. *CP* violation in the decay, if $|\frac{\bar{A}_f}{A_f}|^2 \neq 1$.
2. *CP* violation in the mixing, if $|\frac{p}{q}|^2 \neq 1$.
3. *CP* violation in the interference, if $\mathrm{Im}(\frac{q\bar{A}_f}{pA_f}) \neq 0$.

In the B^0 meson sector, $\Delta\Gamma$ is small. This fact makes it convenient to rewrite Eq. (2.33) as a function of $\Delta\Gamma$ and ΔM. This leads to:

$$\begin{aligned}\Gamma_f(t) &= \frac{|A_f|^2}{2}e^{-\bar{\Gamma}t}\Big[(1+|\lambda|^2)\cosh(\frac{\Delta\Gamma t}{2}) + 2\,\mathrm{Re}(\lambda)\sinh(\frac{\Delta\Gamma t}{2}) \\ &\quad + (1-|\lambda|^2)\cos(\Delta M t) + 2\,\mathrm{Im}(\lambda)\sin(\Delta M t)\Big] \\ \bar{\Gamma}_f(t) &= \frac{|\bar{A}_f|^2}{2|\lambda|^2}e^{-\bar{\Gamma}t}\Big[(1+|\lambda|^2)\cosh(\frac{\Delta\Gamma t}{2}) - 2\,\mathrm{Re}(\lambda)\sinh(\frac{\Delta\Gamma t}{2}) \\ &\quad - (1-|\lambda|^2)\cos(\Delta M t) + 2\,\mathrm{Im}(\lambda)\sin(\Delta M t)\Big]\end{aligned} \tag{2.34}$$

where the amount of *CP* violation is quantified by the complex parameter λ, defined as $\lambda = \frac{p\bar{A}_f}{qA_f}$. In the case in which the final self-conjugate state is considered ($\bar{f}$), the time dependent decay widths can be written as:

$$\begin{aligned}\Gamma_{\bar{f}}(t) &= \frac{|A_{\bar{f}}|^2}{2|\bar{\lambda}|^2}e^{-\bar{\Gamma}t}\Big[(1+|\bar{\lambda}|^2)\cosh(\frac{\Delta\Gamma t}{2}) + 2\,\mathrm{Re}(\bar{\lambda})\sinh(\frac{\Delta\Gamma t}{2}) \\ &\quad - (1-|\bar{\lambda}|^2)\cos(\Delta M t) - 2\,\mathrm{Im}(\bar{\lambda})\sin(\Delta M t)\Big] \\ \bar{\Gamma}_{\bar{f}}(t) &= \frac{|A_{\bar{f}}|^2}{2}e^{-\bar{\Gamma}t}\Big[(1+|\bar{\lambda}|^2)\cosh(\frac{\Delta\Gamma t}{2}) + 2\,\mathrm{Re}(\bar{\lambda})\sinh(\frac{\Delta\Gamma t}{2}) \\ &\quad - (1-|\bar{\lambda}|^2)\cos(\Delta M t) + 2\,\mathrm{Im}(\bar{\lambda})\sin(\Delta M t)\Big]\end{aligned} \tag{2.35}$$

where $\bar{\lambda} = \frac{pA_{\bar{f}}}{q\bar{A}_{\bar{f}}}$.

2.5.1 *CP* violation in the decay

CP violation in the decay happens when the decay width of a B meson to a final state f is different from the decay width of a $\bar{B}$ meson to the self-conjugate of that final state, $\bar{f}$. This implies:

$$\frac{\Gamma(B\to f)}{\Gamma(\bar{B}\to\bar{f})} \neq 1 \tag{2.36}$$

This type of *CP* violation is the only one that can take place for charged mesons (other sources of *CP* violation are possible in the case of neutral mesons, as will be discussed). The amount of *CP* violation can be quantified and expressed in terms of the asymmetry:

$$\frac{\Gamma_f - \bar{\Gamma}_{\bar{f}}}{\Gamma_f + \bar{\Gamma}_{\bar{f}}} = \frac{1-|\frac{\bar{A}_{\bar{f}}}{A_f}|^2}{1+|\frac{\bar{A}_{\bar{f}}}{A_f}|^2}. \tag{2.37}$$

2.5.2 *CP* violation in the mixing

This kind of CP violation takes place when $|\frac{q}{p}| \neq 1$ in Eq. (2.33). This implies that the off-diagonal elements in the mass and decay matrices in Eq. (2.28) are not equal, which translates into the fact that the mixing rate between $|B^0\rangle \to |\bar{B^0}\rangle$ and $|\bar{B^0}\rangle \to |B^0\rangle$ is not the same. This is the result of the mass eigenstates not being *CP* eigenstates. A way to see *CP* violation in the mixing within the B system is by looking into semi-leptonic decays, where the following asymmetry can be built:

$$A_{sl} = \frac{\Gamma(\bar{B} \to l^- \nu X) - \Gamma(B \to l^+ \nu X)}{\Gamma(\bar{B} \to l^- \nu X) + \Gamma(B \to l^+ \nu X)} = \frac{1 - |\frac{q}{p}|^4}{1 + |\frac{q}{p}|^4} \tag{2.38}$$

The reason to choose semileptonic decays is that the charge of the lepton in the final state determines the flavour of the b quark (i.e., if it is a quark b or an antiquark $\bar{b}$) and therefore it is possible to know if the B-hadron has oscillated or not.

2.5.3 *CP* violation in the interference

Reaching the same CP-eigenstate (f) from a neutral B meson is possible via two different ways: B decays and $\bar{B}$ decays. It is possible to quantify the amount of *CP* violation if we use the time-dependent *CP* asymmetry:

$$A(t) = \frac{\Gamma_f - \bar{\Gamma}_f}{\Gamma_f - \bar{\Gamma}_f} = \frac{(1 - |\lambda|^2)\cos(\Delta M t) + 2\,\mathrm{Im}(\lambda)\sin(\Delta M t)}{(1 + |\lambda|^2)\cosh(\frac{\Delta\Gamma t}{2}) + 2\,\mathrm{Re}(\lambda)\sinh(\frac{\Delta\Gamma t}{2})}. \tag{2.39}$$

As pointed out earlier, $\Delta\Gamma$ is small in the B^0 system, so the asymmetry can be re-written in the following fashion:

$$A(t) = \frac{1 - |\lambda|^2}{1 + |\lambda|^2}\cos(\Delta M t) + \frac{2\,\mathrm{Im}(\lambda)}{1 + |\lambda|^2}\sin(\Delta M t). \tag{2.40}$$

The first term coefficient is due to direct *CP* violation in the decay and the second term coefficient is due to *CP* violation in the interference between the decay and the mixing. Therefore, *CP* violation in the interference will be present when $\mathrm{Im}(\lambda) \neq 0$.

2.6 Measuring *CP* violation in B decays

The condition for *CP* violation to occur is the existence of two or more contributions to a decay process with different weak and strong phases. In completely leptonic and in semi-leptonic B decays, the contribution from one of these possible diagrams is much larger than the rest, which leaves little room for clear direct *CP* violation. On the other hand, completely non-leptonic decays often have similar contributions in size from two diagrams, so the size of direct *CP* violation to be observed is more significant.

B decays are usually grouped into five different categories depending on the different processes involved. These groups would be:

- Decays where there is only tree contribution or where other categories can be considered as negligible. The SM predicts zero or very small *CP* violation due to Cabibbo suppression. An example of this type of processes would be the $B^+ \to \phi K^+$ decay.
- Decays in which non-tree contributions are small but sizable. These modes imply small values for direct *CP* violation. An example of this type of processes would be the $B^0 \to D^+ D^-$ decay.
- Decays where the tree contribution is comparable to non-tree contributions (that may even dominate). This is usually due to small CKM matrix elements and usually provokes large interference effects. An example of this type of processes would be the $B^0 \to \rho K$ decay.
- Decays where there is no tree contribution. The interference then takes place between the two penguin diagrams with different down-type quarks in the loop. An example of this type of decay would the $B^0 \to K^+ K^-$ decay.
- Radiative decays, which are penguin processes with different down-type quarks in the loop interfere with the leading contributions coming from electromagnetic penguins. An example of this type of decay would be the $B^0 \to K^{*0}\gamma$ decay.

2.7 Radiative B decays

Radiative B decays are a type of Flavour Changing Neutral Currents (FCNC). These processes are forbidden at tree-level within the SM but allowed at one-loop level. At quark level, radiative B decays are described by the process $b \to q\gamma$ where $q = \{d, s\}$, in the way shown in Fig. 2.2.

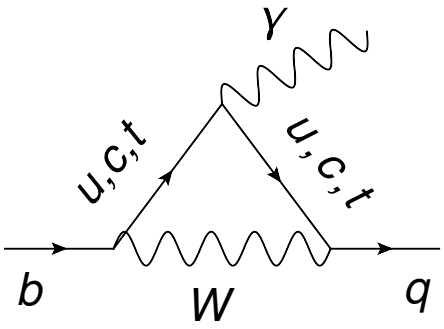

Figure 2.2: Radiative loop as allowed in the SM, where FCNC are forbidden at tree-level.

The large mass of the t quark compared to that for the other quarks (as stated in Table 2.2) reduces the effect of the GIM mechanism [44][1], offering a unique place to test

[1]Mechanism by which processes with the same Feynmann diagram cancel out their contributions for the case in which the propagators have equal mass.

the SM at high energy scales due to the domination of the top quark contribution in the virtual loop.

From a mathematical formalism, radiative B decays can be expressed, in an inclusive way, as $B \to X_s\gamma$, which represents the $b \to s\gamma$ transition. The effective Hamiltonian that describes these decays includes only eight operators

$$\begin{aligned}\mathcal{H}_{\text{eff}}(b \to s) = \frac{G_F}{\sqrt{2}} V_{ts}^* V_{tb} \Big(\sum_{i=1}^{6} C_i(\mu)\mathcal{O}_i^q(\mu) + \\ C_{7\gamma}(\mu)\mathcal{O}_{7\gamma}(\mu) + \\ C_{8G}(\mu)\mathcal{O}_{8G}(\mu)\Big),\end{aligned} \tag{2.41}$$

where G_F is the Fermi constant, V_{ij} are the Cabibbo-Kobayashi-Maskawa (CKM) matrix elements and μ is the normalisation scale, which is of the order of the mass of the bottom quark, m_b. Equation (2.41) does not include the term proportional to $V_{us}^* V_{ub}$ since it is about two orders of magnitude lower than the one expressed and, therefore, negligible.

Radiative decays are sensitive to the existence of particles not-described by the SM since they could have a non-zero contribution to different observables if they entered in the loop. Due to the challenges involved in the measurement of inclusive decays ($B \to X_s\gamma$), exclusive decays are studied at LHCb. These decays are not so clean from a theoretical point of view [2] but are easier to identify at experimental level and allow the study of many physical observables: branching fractions, CP, forward-backward and isospin asymmetries, as well as measurements of the photon polarization.

The LHCb role regarding radiative B decays is the measurement of those physical observables in order to compare these measured values to the ones given by prediction, to confirm or discard models in which contributions from beyond the SM are predicted.

[2] In comparison with inclusive decays, dominated by partonic, perturbatively calculable, contributions with small non-perturbative corrections.

3

CERN, LHC and the LHCb experiment

This chapter introduces the experimental environment to the data analysis. It is divided in different sections, where the Conseil Européen pour la Recherche Nucleaire (CERN), the LHC accelerator and the different experiments placed along the accelerator are presented.

3.1 The European Organization for Nuclear Research

The European Organization for Nuclear Research (CERN) is the world's largest particle physics laboratory. It was founded in 1954 and it is located in the Franco-Swiss border, near the city of Geneva.

CERN has housed many different particle physics experiments in which large international collaborations have worked. It currently hosts the largest and most energetic particle accelerator ever built, the LHC, and the experiments that are located along its ring, such as ALICE, ATLAS, CMS, LHCb, TOTEM, MoEDAL and LHCf.

CERN was founded by eleven European countries (Belgium, Denmark, France, Germany, Greece, Italy, Netherlands, Norway, Sweden, Switzerland and United Kingdom) on September 29th, 1954 although now a total of 22 countries are considered as CERN members. Additional members, listed in chronological order of membership, are: Austria, Spain, Portugal, Finland, Poland, Hungary, Czech Republic, Slovakia, Bulgaria, Israel and Romania. All CERN members, apart from Israel, are European countries.

Other countries collaborate at CERN. Some of them have *observer* status and other non-member countries are involved in CERN programs. All these collaborators add up to a total of over 10,000 visiting scientists from 608 institutes and universities from 113 countries around the world [45].

3.2 The Large Hadron Collider

The Large Hadron Collider (LHC) is the largest and most powerful tool for particle physicists in the world [46]. It consists of two superconducting rings placed in the tunnel built to host the Large Electron-Positron Collider (LEP). This accelerator, running from 1989 to 2000, was the one in which, among other successes, the W and Z bosons were observed for the first time (discoveries made by the UA1 and UA2 experiments [47]). Its tunnel is about 27 Km long and is underground, at an average of 100 m under the Franco-Swiss border, next to CERN. A schematic view of the LHC tunnel underground is shown in Fig. 3.1.

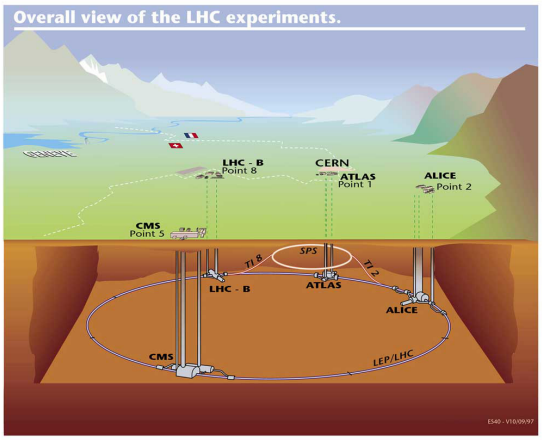

Figure 3.1: Schematic view of the LHC ring under the Franco-Swiss border and its four main experiments. The CERN label represents the headquarters of the organization, located in Meyrin (Switzerland).

The LHC is constructed with 1232 15 m-long superconducting dipole magnets which bend the beams along the ring. Moreover, 392 superconducting quadrupoles 5–7 m long are placed in between dipoles to focus the beams. Additional types of magnets move and squeeze the beams at the collision points. Protons are accelerated at LHC by 16 superconducting radio-frequency cavities, 8 for each beam, placed between the CMS and ALICE collision points. All these superconducting material operates at a temperature of 1.9 K, maintained with liquid helium, in order to keep the conditions necessary for superconductivity.

Usually, the term LHC is used for the whole accelerator complex, in which protons are accelerated into very large energies, but it is the last part of a multiple-step process: protons are extracted from hydrogen gas; they are then injected into a linear accelerator (LINAC2), where they get accelerated to an energy of 50 MeV; once the protons reach that energy, they enter into the Proton Synchrotron Booster (PSB), where the energy gets to 1.4 GeV and where the bunches are formed (the protons do not travel on their own but in bunches where the capacity can be modulated); they are then injected into

the Proton Synchrotron (PS), where their energy is increased to 25 GeV to then enter the Super Proton Synchrotron (SPS), where the energy rise is up to 450 GeV; finally, the protons are injected into the LHC, where they can reach energies of the TeV scale. All these steps are carried out in the *CERN accelerator complex*, inside the CERN facilities. A schematic view of all the different accelerators can be found in Fig. 3.2.

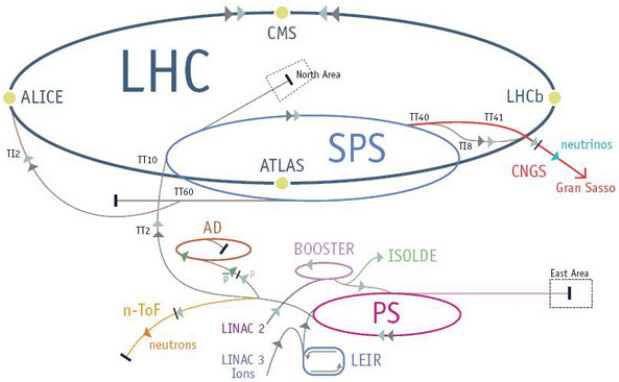

Figure 3.2: The CERN accelerator complex. The size of the different accelerators is not to scale.

During the data taking, the centre-of-mass energy reached at the LHC was 7 TeV for 2011 and 8 TeV for 2012. The highest expected energy to reach for the Run 2, started in May 2015, is of 14 TeV for the centre-of-mass energy.

The LHC also allows the study of heavy ions collision physics by accelerating lead nuclei to an energy of 2.76 TeV/nucleon when it is running in Pb-Pb mode as well as proton-ion collisions, ranging from 115 GeV to 8 TeV for p-Ar and p-Pb, respectively.

3.3 The experiments of the LHC

A total of seven experiments are placed along the LHC accelerator, situated at the four interaction points of the LHC ring. In this section a short description of six of them is given: ALICE, ATLAS, CMS, LHCf, TOTEM and MoEDAL. LHCb, as it is the detector that collected the data used in this work, is described in detail in Sec. 3.4.

3.3.1 ALICE

Standing for *A Large Ion Collider Experiment*, ALICE [48] is dedicated to the study of strongly interacting matter and quark-gluon plasma. To do so, ALICE works in different conditions than the rest of the experiments; mainly focusing on the study of the collisions of heavy nuclei (Pb-Pb).

Designed typical particle physics detector, ALICE covers the interaction point almost completely (as shown in the ALICE layout in Fig. 3.3), in order to be able to detect all the different particles produced at the interaction point.

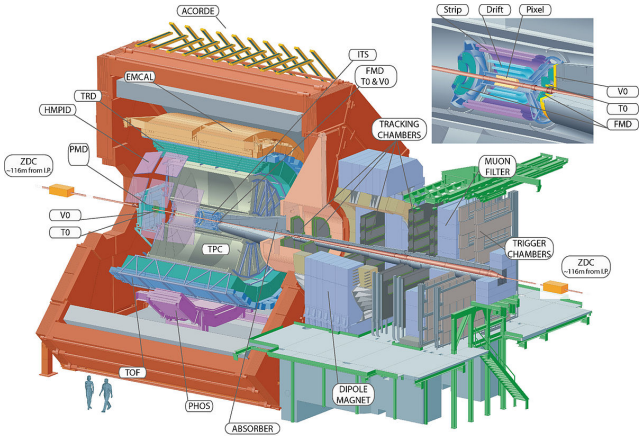

Figure 3.3: ALICE detector layout. The different sub-detectors are marked.

3.3.2 ATLAS and CMS

The ATLAS (standing for *A Toroidal LHC ApparatuS*) [49] and CMS (standing for *Compact Muon Solenoid*) [50] detectors are both general purpose detectors, which means that their task is to test the SM at the TeV scale and to search for new particles. To do so, and following the same strategy than ALICE, they have almost 4π coverage around their interaction points. As a remarkable note, it was in these detectors where the Higgs boson was discovered in July 2012 [5, 6].

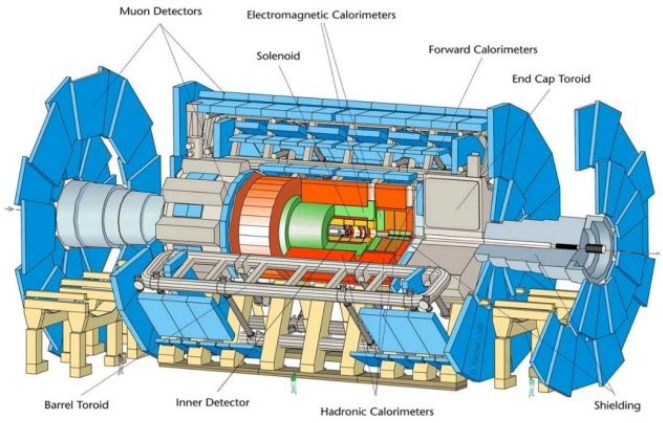

Figure 3.4: ATLAS detector layout. The different sub-detectors are marked.

ATLAS and CMS share the same goals but they were built following different approaches in order for them to be complementary. Figures 3.4 and 3.5 show the ATLAS and CMS detector layouts, respectively. ATLAS is the biggest particle physics experiment ever built and CMS is the heaviest one.

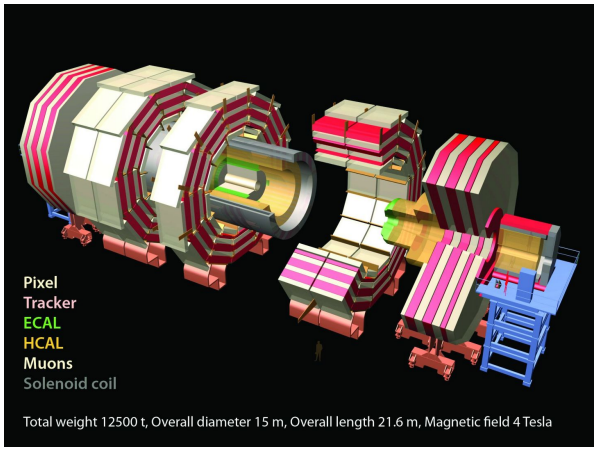

Figure 3.5: CMS detector layout. The different sub-detectors are marked.

3.3.3 LHCf

The *Large Hadron Collider forward* (LHCf) experiment [51] consists of two sub-detectors (one of them shown in Fig. 3.6), one in each side of the ATLAS detector. Each of these detectors is made out of a series of interleaved scintillators and absorbers.

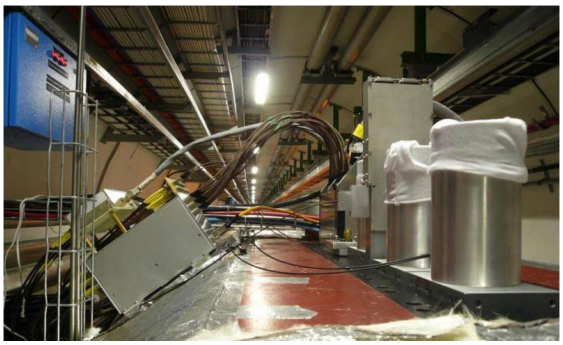

Figure 3.6: Picture of one of the LHCf detectors. Being the smallest detector at the LHC, its size is 80 cm × 30 cm × 10 cm.

The LHCf detector intends to measure the amount of π^0 created in the proton collisions in the LHC as well as their energy, to help explaining the origin of very high-energy cosmic rays. In particular, LHCf is tasked is to provide data for calibrating the hadron interaction models that describe these cosmic rays.

3.3.4 MoEDAL

The *Monopole and Exotics Detector at the LHC* (MoEDAL) [52] is dedicated to the search for the Magnetic Monopole or Dyon and other highly ionizing Stable (or pseudo-stable) Massive Particles (SMPs). If any evidence of these particles was observed, it would mean

the presence of physics beyond the SM. The MoEDAL experiment is located in the LHCb cavern, shown in Fig. 3.7.

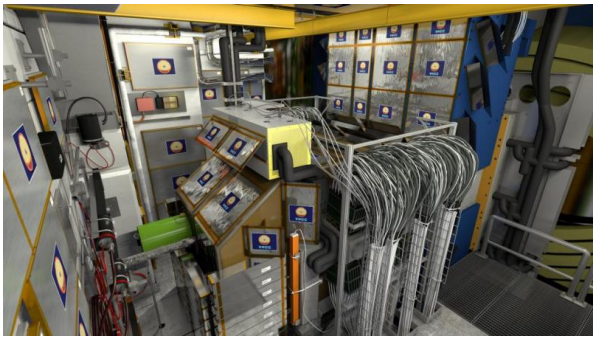

Figure 3.7: Picture of the MoEDAL layout.

3.3.5 TOTEM

The *Total Elastic and diffractive cross section Measurement* (TOTEM) experiment [53] is dedicated to the measurement of the total proton-proton cross-section with the luminosity-independent method based on the Optical Theorem, which requires a detailed study of the elastic scattering cross-section and the measurement of the total inelastic rate. Furthermore, TOTEM's physics program aims at a deeper understanding of the proton structure by studying elastic scattering with large momentum transfers, and via a comprehensive menu of diffractive processes. One of the TOTEM stations is shown in Fig. 3.8.

Figure 3.8: Picture of one of the TOTEM stations. There are a few stations at both sides of the CMS experiment.

3.4 The LHCb experiment

The LHCb (standing for *Large Hadron Collider beauty*) experiment [54–56] is dedicated to the study of heavy flavour physics at the LHC. Its main aim is to make precise measurements of *CP* violation and rare decays of beauty and charm hadrons. Unlike the rest of the large experiments at the LHC (i.e., ALICE, ATLAS and CMS) and since at LHC energies b-hadrons from pp collisions are produced boosted in the forward (or backward) direction, the LHCb experiment does not require 4π coverage around the interaction point. This can be seen in Fig. 3.9, where the polar angle correlation of the b-quark and its antiparticle is represented.

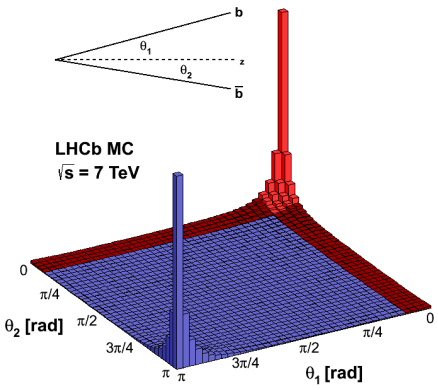

Figure 3.9: Polar angle correlation for the b-hadron and $\bar{b}$-hadron produced by a $b\bar{b}$ pair, as calculated by simulation for a centre-of-mass energy of 7 TeV. The light red area marks the LHCb acceptance region.

The LHCb is a single-arm spectrometer with an angular forward acceptance from about 10 mrad to 300 mrad (in the bending plane) or to 250 mrad (in the non-bending plane), as shown in Fig. 3.10. In terms of pseudo-rapidity, the LHCb acceptance is in the $2 < \eta < 5$ interval. The sub-detectors of which the LHCb experiment is made of are grouped in three independent systems: tracking system, particle identification system and trigger system. The online and offline systems are in charge of the data treatment.

3.4.1 Tracking sub-detectors

A total of four sub-detectors are included in this group. In increasing distance from the interaction point, they are: the vertex locator (VELO), the tracking turicensis (TT), the magnet and the T1–T3 tracking stations. All these sub-detectors are used in order to perform an accurate measurement of the position and momentum of the charged particles produced at the interaction point or the ones produced after their decay.

The **Vertex Locator** (VELO) [57] surrounds the interaction region and is made out of a series of silicon modules that provide information about the position of particles as

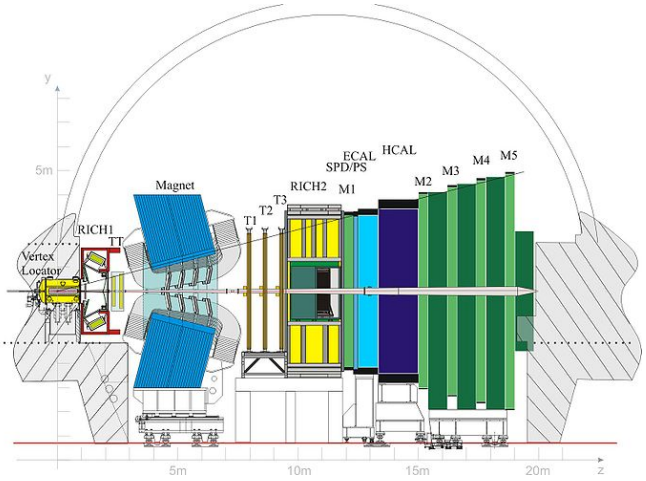

Figure 3.10: LHCb detector layout. The different sub-detectors are marked.

they travel through it, shown in Fig. 3.11. The VELO goal is to distinguish between the *pp* interaction point (also known as primary vertex, PV) and the point where the *b*- or *c*-hadron decays (secondary vertex, SV).

The VELO is moved during the process of stabilization of the LHC beams to protect it from radiation. Once the VELO is in the *closed* position (the VELO stays at a distance of about 8 mm from the beam line), the LHCb experiment starts taking data. The spatial resolution on the primary vertex depends on the number of tracks, but on average it is found to be 42 µm on the z-axis direction and 10 µm in the $r - \phi$ plane. Each of the 21 VELO stations is composed by one r-sensor and one ϕ-sensor, with the configuration shown in Fig. 3.12. The r-sensors are made of concentric semicircular strips (4×512 strips) centered on the nominal LHC beam position. To minimize the occupancy, each strip is subdivided into four 45 ° regions. The minimum pitch at the innermost radius is of 32 µm, increasing linearly to 101.6 µm at the outer radius. The ϕ-sensors are subdivided into two regions, inner and outer, with 683 and 1365 strips, respectively. This avoids unacceptably high strip occupancies in the innermost edge and too large strip pitch at the outer edge of the sensor. A skew of 20 ° (10 °) is introduced in the inner (outer) region to improve pattern recognition, with reversed skew between the inner and the outer regions. Furthermore, the modules are placed so that adjacent ϕ-sensors have opposite skew with respect to each other, achieving a traditional stereo configuration.

The **Tracking Turicensis** (TT) [58,59] is situated right after the VELO sub-detector. It is about 150 cm wide and 130 cm high and is a high planar station made of silicon micro-strip sensors arranged in four stations separated along the beam axis. In the first and in the last station the strips are perpendicular to the beam axis (i.e., they are vertical) while in the case of the second and the third stations, the strips have been rotated -5 ° and +5 ° with respect to the vertical direction, respectively. Figure 3.13 shows the TT detection layers.

The dipole **Magnet** [60–62] allows the measurement of the momentum of charged

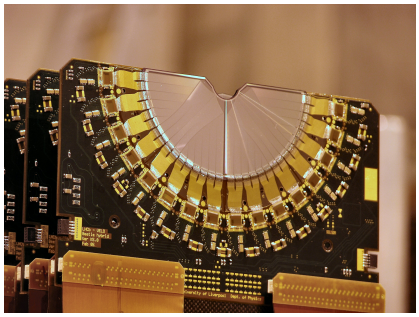

Figure 3.11: VELO sensor.

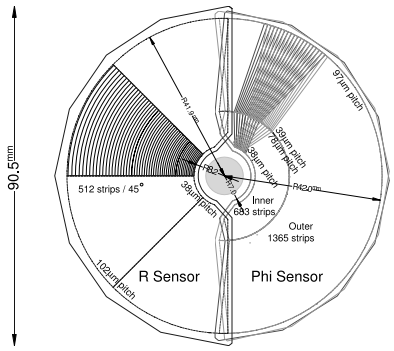

Figure 3.12: Schema of the $r\phi$ geometry of a VELO sensor, showing one portion of the strips. Strips of the two adjacent modules to the ϕ sensor to highlight the stereo angle.

particles, since their trajectories bend when exposed to a magnetic field. In the case of the LHCb magnet, the adopted design was a warm magnet with saddle-shaped coils in a window-frame yoke with sloping poles to match the required detector acceptance. The coils are of conical saddle and are placed face-to-face, separated by the magnet yoke. Each coil consists of fifteen pancakes arranged in five triplets and produced of pure Al-99.7 hollow conductor in an annealed state. The magnet produces a vertical magnetic field so charged particles trajectories bend in the horizontal plane. The magnet polarity can be switched from *up* to *down*, which is done to reduce systematic effects that may be produced by the magnetic field as well as other detector asymmetries. For tracks originating near the *pp* interaction point the integrated magnetic field is of 4 Tm. Figure 3.14 shows a picture of the LHCb magnet right after its installation.

The three **T stations** (T1-T3) [63, 64] are located right after the dipole magnet and are segmented into two different regions, the inner tracker (IT) and the outer tracker

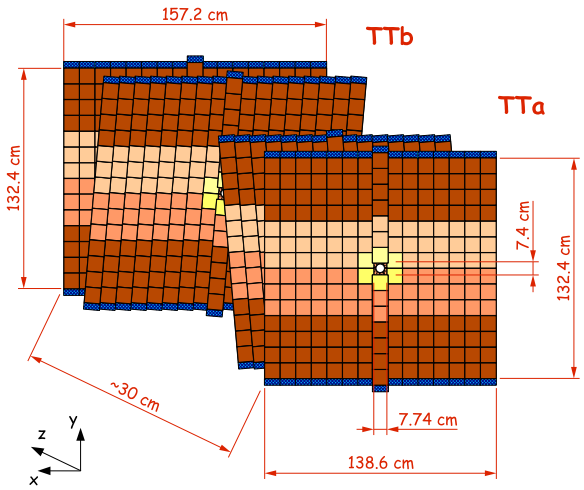

Figure 3.13: Layout of the four TT stations.

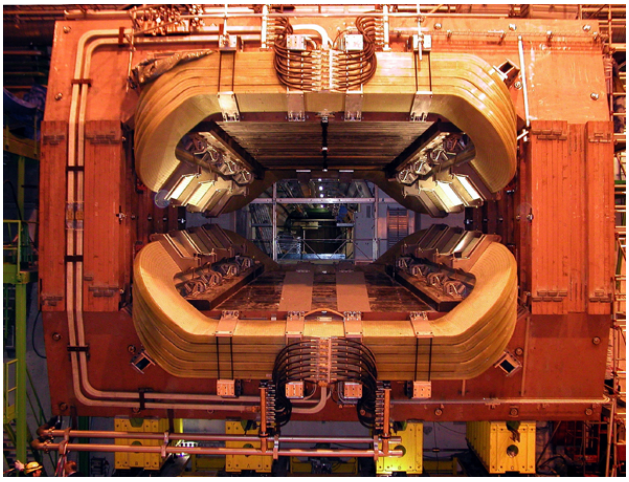

Figure 3.14: LHCb magnet.

(OT), which cover the innermost part and the large area around it, respectively. The technology used for the IT is the same used for the TT, while the OT uses drift-tubes. The OT drift-tubes are filled with a mixture of Argon and CO_2, giving a fast drift-time below 50 ns and a drift-coordinate resolution of 200 µm. A layout of the OT, IT and TT system is given in Fig. 3.15.

Tracks can be divided in different types depending on the amount of sub-detectors involved in their reconstruction:

- **Long tracks** are those which cross the full tracking system. They have the most precise momentum determination and therefore are the most commonly used set of

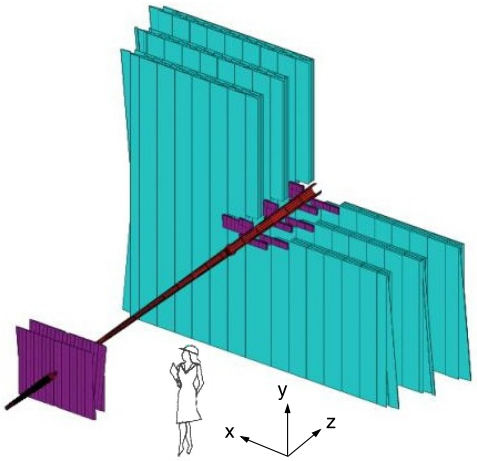

Figure 3.15: OT (blue), IT and TT (purple) stations.

tracks for physics analyses.

- **Upstream tracks** only transverse the VELO and the TT and correspond to low momentum tracks that are bent out of acceptance by the magnetic field, so they usually have poor momentum resolution. These tracks can be used for background studies in the RICH particle identification algorithms since they may generate Cherenkov photons in the RICH1.
- **Downstream tracks** only traverse the TT and the T stations and are relevant in the study of long-lived particles, where the decay point is outside the VELO acceptance.
- **VELO tracks** only leave signal in the VELO. They usually correspond to particles with large angle or backward tracks (so they leave the LHCb acceptance) and are useful for primary vertex reconstruction.
- **T-tracks** are only measured in the T stations and are usually produced in secondary interactions. They are also used, along with long and downstream tracks, to classify ECAL clusters as charged (*i.e.* the cluster can be associated to a track) or neutral (*i.e.* the cluster cannot be associated to any track). These tracks are useful in the RICH2 global pattern recognition.

A sketch of the different types of tracks, and the intensity of the magnetic field on them, depending on their relative position to the interaction point, is shown in Fig. 3.16.

3.4.2 LHCb calorimeters

The LHCb calorimeter system [65] consists of a total of four sub-detectors: the Scintillator Pad Detector (SPD), the Pre-Shower (PS), the Electromagnetic Calorimeter (ECAL) and the Hadronic Calorimeter (HCAL). The goal for the LHCb calorimeter

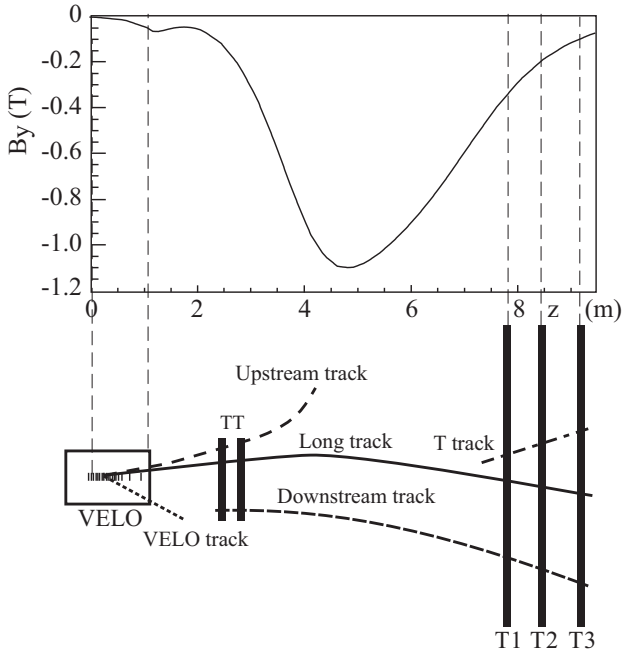

Figure 3.16: Schematic illustration of the various track types [54]. The main magnetic field component (B_y) is plotted above as a function of the z coordinate.

system is to select high transverse energy (E_{T}) candidates for hadrons, electrons and photons at the first level of the trigger system, provide the identification of hadrons, photons and electrons and measure the energy of electrons and photon candidates as well as the photon candidate position. Each calorimeter sub-detector is made up of cells

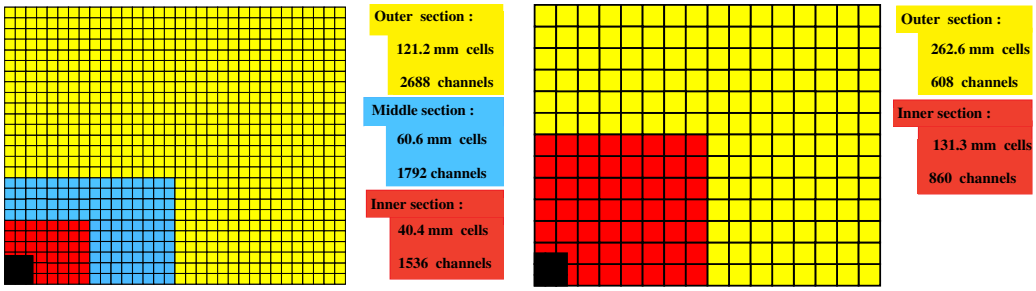

Figure 3.17: Lateral segmentation of the SPD, PS and ECAL (left) and the HCAL (right). One quarter of the detector front face is shown. In the left figure the cell dimensions are given for the ECAL.

(6016 for the SPD, PS and ECAL and 1488 for the HCAL) which independently provide information about the energy and the position of the particles. Due to the dependence of occupancy for the different parts of the sub-detectors with the angle with respect to the beam pipe, cells have different sizes. The SPD, the PS and the ECAL sub-detectors

are segmented projectively into three different regions, while the HCAL is segmented into two regions, as shown in Fig. 3.17.

The Scintillator Pad Detector and Pre-Shower sub-detectors

These two sub-detectors have a very similar layout: they are both divided in three different regions (inner, middle and outer parts, where cell sizes of roughly 4×4, 6×6 and 12×12 cm^2, respectively) that make up to 6016 scintillating plastic cells with a depth of 1.5 cm, with a fragmentation that matches the one for the ECAL. A lead plane, with a thickness of 2.5 X_0, separates the two sub-detectors. The sensitive area of the detector is 7.6 m wide and 6.2 m high.

The SPD is a binary detector that accounts for charged particles hits and plays two roles: the SPD multiplicity (number of hits collected in the detector) is part of the first level of trigger (L0) and, on the other hand, it is used to separate photons from electrons. For a particle that leaves an energy deposition in the PS and forms an ECAL cluster, the SPD determines it being a photon or an electron by comparing the energy left at the SPD with a pre-set cell-to-cell threshold. It has been shown that photons arriving at the SPD with an energy between 20 and 50 GeV have a misidentification probability of 0.8% when applying a threshold of 0.7 Minimum Ionizing Particles (MIPs).

After traversing the SPD, particles interact with the interlaying lead layer between the SPD and the PS, which makes them produce an electromagnetic shower. The distinction between charged pions and electrons is done by measuring the dispersion of this electromagnetic shower in the PS. With a threshold set at about 4 MIPs, it has been measured that both the pion rejection and the electron selection are well above 90% for energies between 10 and 50 GeV.

The Electromagnetic Calorimeter

The ECAL is placed at about 12.5 m away from the interaction point and is used to measure the energy carried by the particles that are stopped inside it. A depth of 25 X_0 was chosen to ensure the full continence of electromagnetic showers. It uses *shashlik* technology, which is a scintillator/lead structure read by fibres perpendicular to the scintillator that leads to fast response time and good resistance to radiation. Its design energy resolution was studied in a test beam [66, 67] is given by

$$\frac{\sigma_E}{E} = \frac{(9.368 \pm 0.018)\%}{\sqrt{E}} \oplus (0.833 \pm 0.025)\% \oplus \frac{0.145 \pm 0.013}{E}, \tag{3.1}$$

where the third parameter value is smaller than the pedestal values for the ECAL cells and therefore can be neglected. As an example, the results of the test for an outer module can be found in Fig. 3.18.

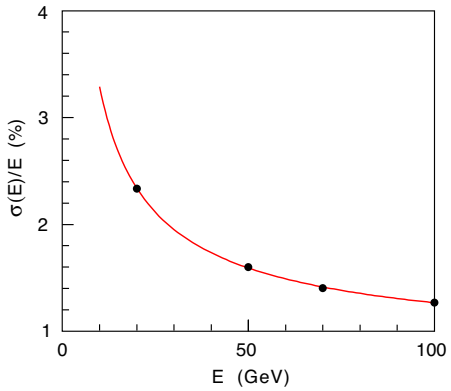

Figure 3.18: The ECAL energy resolution as measured with electrons over a surface of (±15 mm, ±30 mm) in an outer module.

The Hadronic Calorimeter

The HCAL, made from iron and scintillating tiles (as absorber and active material, respectively), is mainly used for triggering and particle identification. The scintillating tiles of this sampling structure run parallel to the beam axis. In the lateral direction, the distance between tiles is of 1 cm of iron, while in the longitudinal direction the length of tiles and iron spacers corresponds to the hadron interaction length in steel.

The HCAL is placed at about 13.3 m from the interaction point, right after the ECAL and its dimensions are of 8.4 m in height, 6.8 m in width and 1.65 m in length. As pointed out before, the HCAL is segmented in just two regions into squares with sides of 13.13 cm and 26.26 cm for the inner and outer regions, respectively. Due to space limitations inside the cavern, the HCAL cannot completely contain hadronic showers, and therefore the measured energy is an estimation of the total hadron energy. The HCAL resolution [68], written in the same way as Eq. (3.1), was measured in test beams to be

$$\frac{\sigma_E}{E} = \frac{(69 \pm 5)\%}{\sqrt{E}} \oplus (9 \pm 2)\%, \tag{3.2}$$

where the energy is to be expressed in GeV. Figure 3.19 shows the dependence of the HCAL resolution with the energy of the particles for different simulation models and for real data.

3.4.3 The Muon System

The LHCb muon system [69–71] is composed of five different stations (M1–M5) with an inner angular acceptance of ±20 mrad for the bending plane and ±16 mrad for the non-bending plane while the outer angular acceptance is of ±306 mrad and ±258 mrad for the bending and non-bending plane, respectively. The first station is placed before the calorimeter system while the four last stations are placed after it, being the furthest sub-detectors from the interaction point. The reason for this is the long muon lifetime

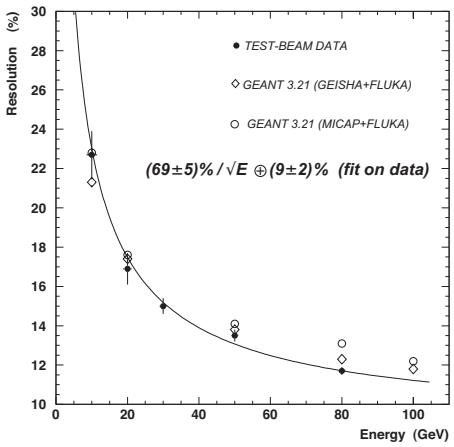

Figure 3.19: HCAL energy resolution measured for real data and simulation with three different hadronic simulation codes. The curve is the fit to the data.

($\tau_\mu \sim 2.2\,\mu$s), with a low interaction probability which means that they fly through the whole detector.

The muon stations consist of Multi-Wire Proportional Chambers (MWPC) with their planes perpendicular to the beam axis. Station M1 is placed before the calorimeter system and is used for the improvement of the p_{T} measurement in the trigger. The rest of the stations are placed after the calorimeter system. In between M2–M5 there are 80 cm thick iron layers that play the role of absorber, in order to select highly penetrating muons, as shown in Fig. 3.20.

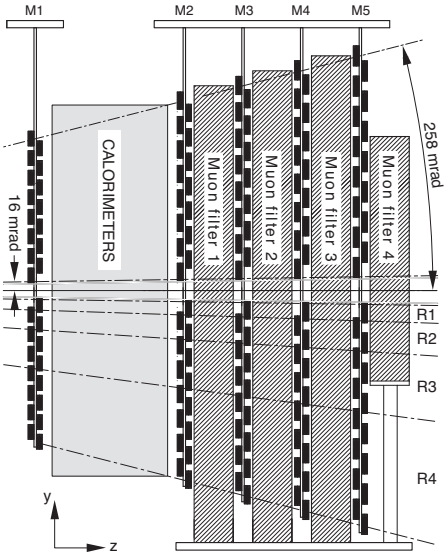

Figure 3.20: Side view of the muon system.

The detectors provide space point measurements of the track and information is

passed on by partitioning the detector into rectangular logical pads, whose dimensions define the spatial resolution. Figure 3.21 shows the front view of a quadrant of a muon station, where the logical pads are marked.

As in the case of the calorimeters, the muon stations geometry is projective and they are also segmented; there are four segments in this case (R1–R4), where each pad is twice as big as the previous one.

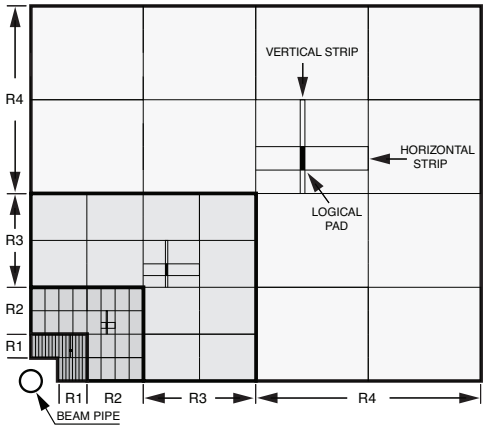

Figure 3.21: Front view of one quadrant of stations M2 and M3 showing the partitioning into sectors. In one sector of each region a horizontal and a vertical strip are shown. The intersection of a horizontal and vertical strip defines a logical pad.

The muon system plays a key role for the LHCb collaboration due to its physics program, where b-hadron decays into final states where muons are observed and their study is expected to shed light on some beyond SM theoretical predictions. The muon system also provides useful information at the Level-0 and at the High Level Trigger, such as p_{T} information and muon identification, respectively.

3.4.4 LHCb Particle Identification sub-detectors

Most of the particle decays that take place at LHCb have a final state containing kaons or pions. Their correct identification is key to a correct description of the decay chain, which is mandatory to access to the study of Cabbibo suppressed modes. To achieve this purpose, the LHCb experiment has two RICH (Ring Imaging Cherenkov) detectors, which allow the identification of these hadrons within a wide momentum range.

The Cherenkov light produced by the charged particles when they travel through the radiators is deflected by a series of spherical and flat mirrors, to Hybrid Photo Detector (HPD) photo-cathodes. The aperture of the light cone emitted by the particles depends on their speed. Making use of the information provided by the tracking system and the magnetic field it is possible to compute the particle mass as well as its charge, which identify the particle. Once the Cherenkov rings are constructed, different likelihoods for particle hypotheses are built. For a given particle mass, the Cherenkov angle is dependent on the particle momentum. Figure 3.22 shows this dependency for different types of

particles. Figure 3.23 shows an sketch of the layout of both RICH detectors where the different parts are noted.

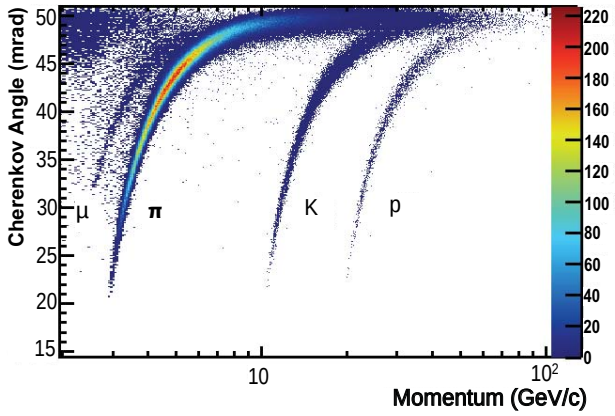

Figure 3.22: Reconstructed Cherenkov angle for *isolated* tracks, as a function of track momentum in the C_4F_{10} radiator [72]. The Cherenkov bands for muons, pions, kaons and protons are clearly visible.

The **RICH1** [73] sub-detector is placed before the dipole magnet and covers low momentum particles (1–60 GeV) within the whole LHCb acceptance. Its radiators are aerogel and C_4F_{10}. On the other had, the **RICH2** sub-detector [74, 75] is placed after the dipole magnet and covers particles with large momentum (15-100 GeV), having an acceptance that corresponds to ± 120 mrad in the horizontal plane and ± 100 mrad in the vertical one. In this case, the radiator is CF_4.

3.4.5 LHCb Trigger System

The LHC is designed to provide proton-proton collisions with a rate of 40 MHz. In order to reduce this rate, which is too high to be recorded, the LHCb trigger [55, 76, 77] selects those events that are considered interesting for further analysis. The trigger output rate is nominally of 2 kHz, although it was increased to 3 kHz [78] during the 2011 data taking period and 5 kHz [79] for the 2012 data taking period.

The LHCb trigger system consists of two different levels, the Level-0 (L0) trigger and the High Level trigger (HLT). The L0 is implemented in custom electronics and operates synchronously with the LHC bunch-crossing frequency of 40 MHz. Its purpose is to reduce the rate from 10-15 MHz (which is the actual rate of visible *pp* collisions, i.e., those event with at least two charged particles with enough hits in the VELO and T stations to be reconstructible) to 1 MHz, at which the entire detector can be read out [79]. The HLT is implemented in software and is divided in two different stages: HLT1 and HLT2. In HLT1 there is a partial event reconstruction, with strong requirements on the particles momentum and their impact parameter (IP). If the event is accepted, the HLT2 then performs a full event reconstruction. The output from the HLT2 stage is

Figure 3.23: RICH1 and RICH2 layouts (left and right, respectively).

then recorded for further offline analysis. A single computer node is in charge of the application of the HLT1 and HLT2 on data. Figure 3.24 corresponds to a sketch of the complete LHCb trigger chain.

The different requirements that make up the set of cuts that the different levels of the LHCb trigger applies on the data as well as the algorithms configuration are put together in what is called the Trigger Configuration Key (TCK). This makes it possible to fully reproduce the LHCb trigger at software level.

The L0 Trigger

The L0 trigger corresponds to the first of the steps in the trigger chain and is required to provide its output as fast as possible. This implies that the LHCb sub-detectors used at this level are the ones that give a fast response. The L0 trigger has therefore three different components:

- Pile-up system L0 trigger.
- Calorimeter L0 trigger.
- Muon L0 trigger.

The **pile-up** system is related to the occupancy of the event, in particular, with the number of observed interactions per bunch-crossing. It consists of two planes perpendicular to the beam line and located after the VELO. Each plane is made out

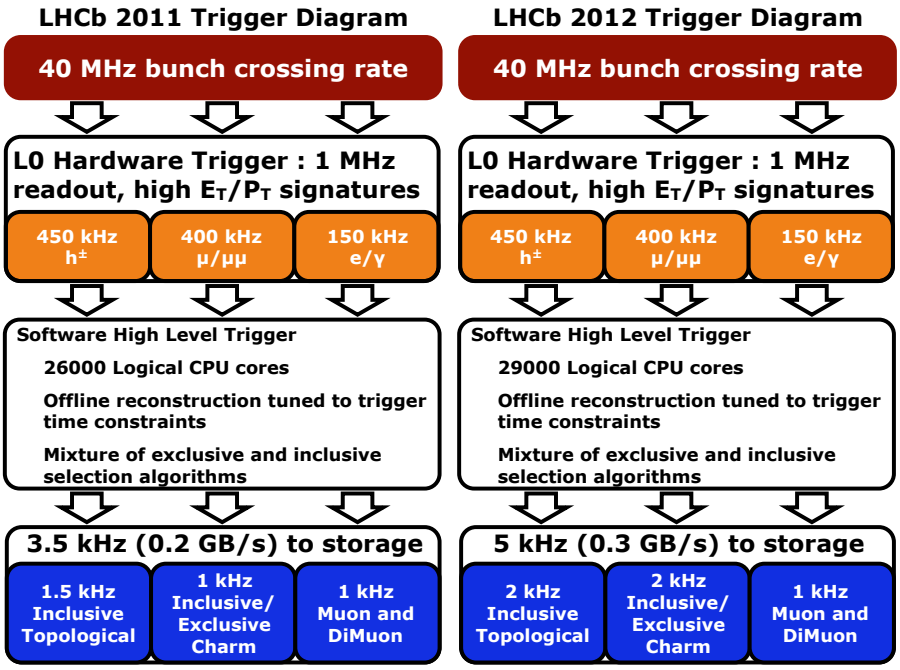

Figure 3.24: Schema of the event flow in the LHCb trigger system for 2011 (left) and 2012 (right).

of two overlapping VELO r-sensors. It provides the position of the primary vertices along the beam axis and the total backward charged-track multiplicity. However, this component was not used during Run 1.

The **calorimeter** L0 trigger measures the transverse energy (E_{T}) of hadrons, electrons, photons and neutral pion candidates, built by reconstructing 2×2 cell clusters. It then selects the one with the highest E_{T} for each category. The total charged track multiplicity of the event is obtained from the SPD sub-detector and a cut on this value is applied to veto events with a large number of primary vertices. As shown in Fig. 3.25, requiring a maximum of 600 hits keeps about 100% of the events with a single interaction point while a large fraction of events with more than one interaction are left out [80]. Also, events with high multiplicity take a long time to reconstruct, which is to be avoided at this level.

The **muon** L0 trigger selects the two muons with highest p_{T} for each quadrant of the muon detector. The standalone muon reconstruction allows a resolution of 20% on the p_{T} of muons.

Information from the calorimeter and the muon components are combined and analysed. The decision unit then accepts or rejects the event.

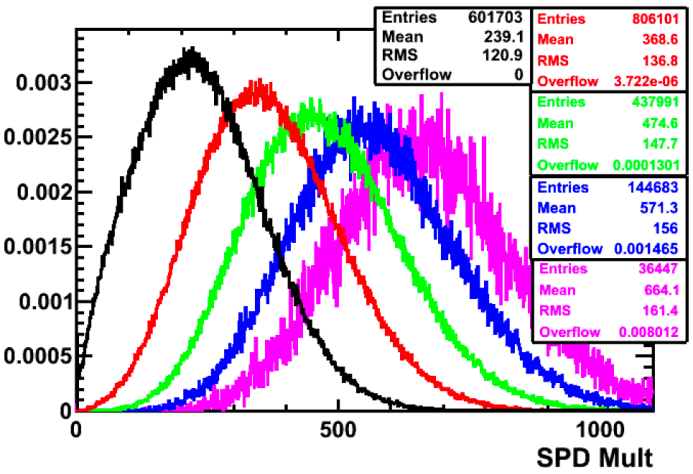

Figure 3.25: SPD charged-track multiplicity for events with one (black), two (red), three (green), four (blue) or five (magenta) primary vertices.

The HLT Trigger

Unlike the L0 trigger, the HLT is a software application. It runs over events that have satisfied any of the requirements at the L0 trigger and in a specialized computer farm, on the Event Filter Farm (EFF), which is composed of 1000 multi-core computing nodes.

The main purpose of the **HLT1** stage is to reduce the background rate independently of the conditions at which the data is taken. The HLT1 looks for high quality tracks with large p_{T} and large impact parameter, which are the signature of B and D meson decays. The selection efficiency for signal events has been measured to be larger than 80% for most of the LHCb benchmark channels [81]. In addition to this, lifetime unbiased muon and electron triggers are used for analysis that are sensitive to the presence of biases in the lifetime [82].

When events reach the **HLT2** stage, the rate is low enough to perform full reconstruction, which means that secondary vertices can be looked for. Global Event Cuts (GEC), such as charged-track multiplicity, are usually applied to discard those events that present too much trouble to reconstruct in terms of CPU-time. The HLT2 trigger stage is a combination of exclusive lines (those designed for a decay or small amount of decays in particular, with specific requirements to the aimed analysis) and inclusive lines (those designed for a broad number of particle decays, so general properties are required).

3.4.6 Online and Offline Systems

The online system is in charge of the correct transfer of data from the electronics to the permanent storage as well as ensure the correct synchronization of all detector channels (among themselves and with respect to the LHC clock). On the other hand, the offline system is in charge of both the replication of the data and their full event reconstruction.

The **online system** [83] is composed of three different parts: the data acquisition (**DAQ**) takes the data from the front-end electronics to the permanent storage; the timing and fast control (**TFC**) is the part in charge of synchronising the data readout stages between the front-end and the EFF by a distribution of the beam-synchronous clock, the L0 trigger, the synchronous resets and the fast control commands and the experiment control system (**ECS**) is in charge of controlling the different sub-detectors as well as the monitoring of the good behaviour of the LHCb experiment during the operating state of the whole detector.

The **offline system** [84] is based on a computing model in which the data are distributed and stored in different locations (called Tiers). This scheme is divided in three different levels:

- **Tier-0:** Corresponds to CERN. Raw data from the detector is stored here before it is transferred to the Tier-1 centres.
- **Tier-1:** There are a total of seven Tier-1 centres. They are IN2P3 (in France), GRIDKA (in Germany), CNAF (in Italy), NIKHEF (in the Netherlands), PIC (in Spain), CERN (in Switzerland) and RAL (in the United Kingdom). The Tier-1 centres' task is to perform a full reconstruction and stripping of the data. Once this is done, the output is saved in a file accessible for physical analyses.
- **Tier-2:** There are more than one hundred Tier-2 centres around the different LHCb members. Their main task is to be in charge of the production of simulation data.

3.4.7 Detector performance

The detector performance can be classified according to the tasks it carries out, regardless which sub-detectors are involved. These tasks are tracking, vertexing (the ability to find a good-quality vertex) and particle identification.

The **tracking** reconstruction performance is affected by scattering effects and dE/dx energy loss. Once a track is reconstructed, it is refitted taking those effects into account. The relative resolution is dependent on the momentum, being of 0.4% for low momentum tracks ($p_{\mathrm{T}} \sim 5$ GeV) and of 0.6% for large momentum tracks ($p_{\mathrm{T}} \sim 100$ GeV).

Since the B and D mesons (those for which the LHCb experiment is optimized for) have long lifetimes, they have a large IP with respect to the primary vertex (PV). Hence, a good resolution in the position of the PV as well as in the IP are needed to distinguish between particles coming from the PV or the secondary vertex (SV). The **vertexing** resolution is related to the number of tracks coming out of it. Figure 3.26 shows the PV resolution as a function of the number of tracks reconstructed on the vertex for 2012 data [85]. The IP resolution dependance on the value of the momentum and also on the position (it is not symmetric) has been found to be (3.3):

$$\begin{aligned} \sigma_x &= (13.2 \pm 24.7/p_{\mathrm{T}})\ \mu\mathrm{m} \\ \sigma_y &= (12.2 \pm 24.4/p_{\mathrm{T}})\ \mu\mathrm{m} \end{aligned} \tag{3.3}$$

The **Particle identification** performance can be analysed from the point of view of

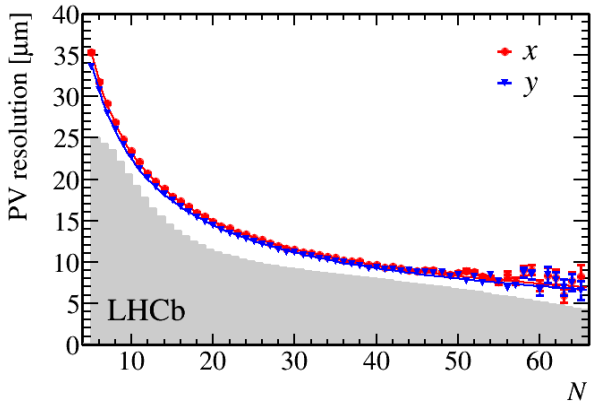

Figure 3.26: PV resolution in x (red) and y (blue) coordinates as a function of the track multiplicity. The histogram shows the distribution of number of tracks per reconstructed PV for all events that pass the high level trigger. This corresponds to 2012 data.

what particles are reconstructed.

- Regarding **hadron** identification, the average efficiency for kaon identification is of ∼95% for a momentum in the range 2–100 GeV. The corresponding pion as kaon misidentification is of ∼5%. Figure 3.27 shows this for different PID requirements for 2012 data when the magnet polarity was set on *down* [86].

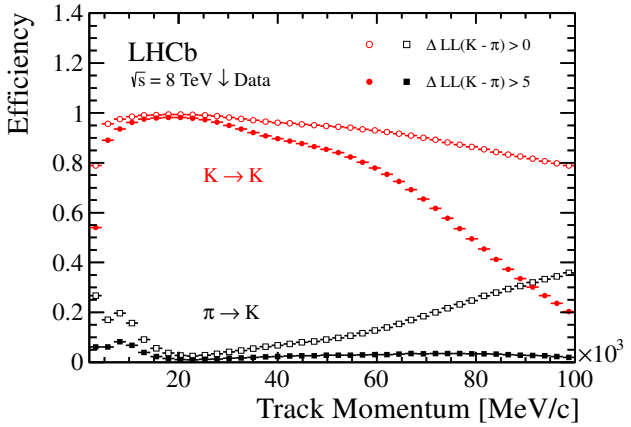

Figure 3.27: Kaon identification and pion misidentification performance for 2012 data, magnet *down*. Two sets of data are represented, each corresponding to a cut on the PID.

- **Electron** identification is performed mainly by assessing the distance of reconstructed tracks to the ECAL clusters. Other information, such as the energy

depositions in the HCAL and in the PS is also used as discriminant variable. All this is then combined with RICH and muon system information to build a likelihood. For the case of electrons, the average identification efficiency for a cut of $\Delta\log\mathcal{L}^{CALO}(e-h) > 2$ is measured to be $(91.9 \pm 1.3)\%$ with a misidentification rate of $(4.54 \pm 0.02)\%$ in $B^{\pm} \to J/\psi(\to e^+e^-)K^{\pm}$ decays [87]. Figure 3.28 shows the dependence of the electron identification (left) and misidentification (right) as hadrons with respect to the momentum for various cuts.

- Regarding **photon and π^0 identification**, ECAL clusters without associated track are considered as photons. In order to do that, the reconstructed tracks are extrapolated to the ECAL plane and a χ^2_γ estimator is built. A candidate is assigned to be a neutral particle when $\chi^2_\gamma > 4$. Photons converted after the magnet are identified requiring a SPD hit in the cell in front of the centre of the ECAL cluster [88]. Neutral pions are also reconstructed in the ECAL. These π^0's can be resolved (if the two photons it decays into are sufficiently separated so it is possible to detect them individually) or merged (if the two photons it decays into are not sufficiently separated and therefore leave a single cluster in the ECAL). Using data from $B^0 \to K^{*0}\gamma$ and merged π^0's from minimum bias samples and using an algorithm design for the γ/π^0 separation, the photon selection efficiency is of $\sim$90% with a π^0 rejection of $\sim$60%.

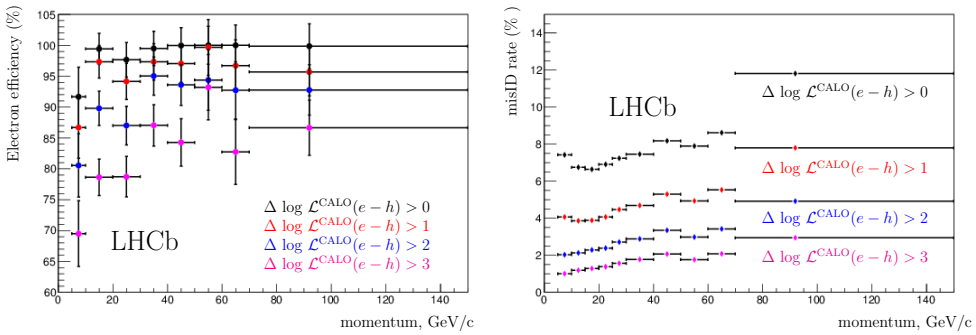

Figure 3.28: Electron identification performances for various Δ log $\mathcal{L}^{CALO}(e-h)$ cuts: electron efficiency (left) and misidentification rate (right) as functions of the track momentum.

- A minimum momentum of 3 GeV is necessary for a **muon** to traverse the calorimeters and reach the M2 and M3 stations, while those with an energy larger than 6 GeV are able to travel through the whole LHCb before leaving it [87]. The identification of a track as a muon is based on the association of hits around its extrapolated trajectory in the muon system [89]. The performance of the muon identification is obtained from data using muons from $J/\psi \to \mu\mu$ decays. Figure 3.29 shows the efficiency of the muon candidate selection as a function of the muon

candidate momentum for different ranges for the particle momentum. On average, the muon identification efficiency is measured to be of 98% with a corresponding pion misidentification $< 0.6\%$ [90].

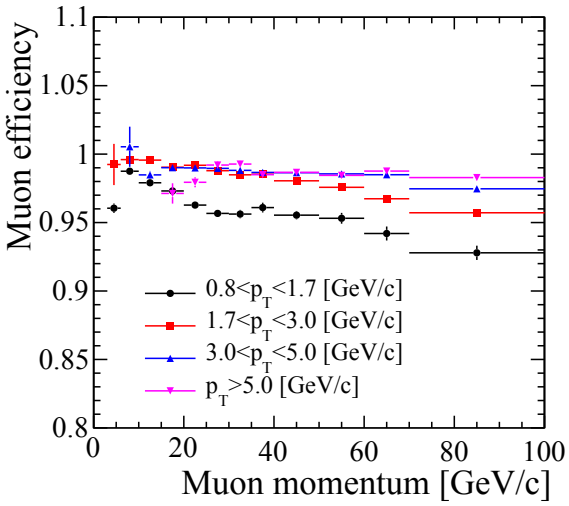

Figure 3.29: Muon identification performances as a function on the muon candidate momentum. The identification is dependent on the momentum. The figure shows different efficiencies for different momentum ranges.

3.4.8 Summary of Run 1

Although the work included in this thesis only used data from 2011 and 2012, the conditions for 2009 and 2010 are also included to try to make a detailed summary of the whole Run 1 period of the LHC [87].

At the end of **2009**, LHCb recorded its first pp collisions at the injection energy of the LHC ($\sqrt{s} = 0.9\,\text{TeV}$). These data were used to finalise the commissioning of the sub-detector systems and reconstruction software, as well as to perform a first alignment and calibration of the tracking, calorimeter and PID systems. The VELO was always kept at its *open* position.

During **2010**, the conditions changed due to the ramp-up of the LHC luminosity, where the beams had an energy of 3.5 TeV. Pile-up (μ_{vis}, average number of visible interactions per beam crossing [91]) increased to 2.5 for a luminosity of $10^{32}\ \text{cm}^{-2}\,\text{s}^{-1}$, although it was demonstrated that the physics output was not compromised [87]. Figure 3.30 shows, for the whole Run 1 period, the evolution of the pile-up with the instantaneous luminosity at the LHCb interaction point.

In the year **2011** the number of bunches increased from 368 to 1300, which corresponds to the largest possible value for a bunch spacing of 50 ns. This led to a reduction of the pile-up. By a luminosity levelling procedure, the instantaneous luminosity could be

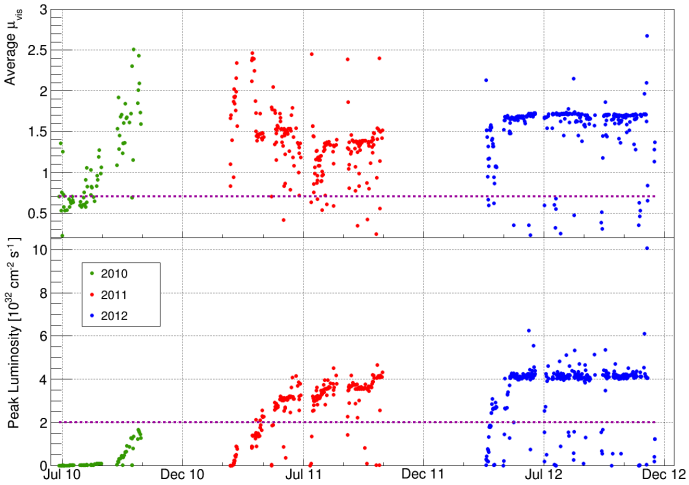

Figure 3.30: Average number of visible interactions per bunch crossing (pile-up) and instantaneous luminosity (top and bottom, respectively) at the LHCb interaction point for the 2010-2012 period. The purple horizontal lines show the design values.

kept stable during the fills, so the effects of luminosity decay would be minimised, which allowed to maintain the same trigger configuration during a fill and reduce systematic uncertainties due to changes in the detector occupancy.

In **2012** the beam energy was increased to 4 TeV. The processing power on the Event Filter Farm (EFF) increased by 20% with respect to 2011 and was better utilized by temporarily saving part of the HLT1-accepted events to disk, deferring the execution of the HLT2 to moments when the farm was idle.

The integrated luminosity recorded by LHCb was of 38 pb^{-1} in 2010, 1.11 fb^{-1} in 2011 and 2.08 fb^{-1} in 2012. The evolution of the integrated luminosity is shown in Fig. 3.31. Luminosity calibrations were carried out with the LHCb detector for the various centre-of-mass energy values at which data have been taken. Both the "van der Meer scan" and "beam-gas imaging" luminosity calibration methods were employed [92]. For proton-proton interactions at $\sqrt{s} = 8$ TeV a combined precision of 1.12% for the luminosity calibration was reached. Applying the calibration to the full Run 1 data set determines the luminosity with a precision of 1.16%. This represents the most precise luminosity measurement achieved so far at a bunched-beam hadron collider.

The average operational efficiency (ratio between recorded and delivered luminosity) was 93% [87]. The main inefficiency sources are the procedure used to keep the VELO safe and the non-conformities in the implementation of the read-out protocol for some sub-detectors.

During Run 1 the magnet polarity was inverted about twice a month [87]. This is done to reduce charged particles detection asymmetries that could appear if the magnet was always kept at the same polarity. This is necessary to reach the design sensitivity in *CP* violation measurements, which requires control on detection asymmetries to a

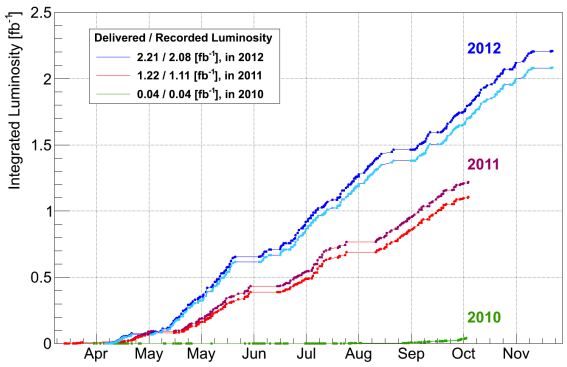

Figure 3.31: Integrated luminosity in LHCb during Run 1. Delivered (dark lines) are recorded (light lines) are displayed.

precision of at least 10^{-3}.

Proton-lead collisions took place in January and February 2013 with a centre-of-mass energy of 5 TeV and closed the Run 1 period. The integrated recorded luminosity was of 1.6 nb^{-1}. Although proton-lead and lead-lead collisions are not among the LHCb benchmarks, measurements from them are taken for calibration purposes and for physical measurements, in order to improve the current knowledge of the QCD structure [93, 94]. The LHCb program on ion collisions for Run 2 is ambitious and includes measurements on heavy flavour, soft QCD and electroweak physics [95].

4

Monitoring of SPD cells efficiency and detector ageing

In order to have good quality data, the correct calibration of the different sub-detectors of the LHCb experiment is mandatory. In the case of the Scintillator Pad Detector (SPD, introduced in 3.4.2) once the calibration is done, a periodic monitoring is needed to ensure a correct functioning. The SPD is in charge of the separation between photons and electrons at the L0 trigger level and provides a multiplicity counter at that stage. This chapter describes the monitoring of its performance along the LHC Run 1 and beginning of Run 2, when a drop in efficiency for some SPD cells was observed and diagnosed to be an effect of the ageing of the photomultipliers (PMTs), scintillator and fibers. The calibration of the SPD sub-detector is highly detailed elsewhere [80, 96].

The SPD is composed of a total of 6016 cells distributed in a total of 100 very front ends (VFE), each one connected to a 64-channel MAPMT. Figure 4.1 shows the disposition of these VFEs, with a clear separation of the sides of the detector (A-side on the right or C-side on the left) and the calorimeter areas (inner, middle and outer). All the SPD cells have a square shape and a depth of 1.5 cm. However, the other two dimensions depend on the part of the sub-detector, since a larger granularity is desired for larger occupancies, which correspond to cells closer to the beam pipe. The size for the different cells is: inner cells are 4×4 cm^2, middle cells are 6×6 cm^2 and outer cells are 12×12 cm^2.

In this chapter, a short introduction about how the SPD collects the signal and its response and output is given, as well as a short review of the calibration process. After that, a complete description of the calculation of efficiencies for its cells is presented, followed by the comparison of these efficiencies for different data taking periods. A discussion about the efficiency recovery of the SPD cells and the correction of the calibration factors closes the chapter.

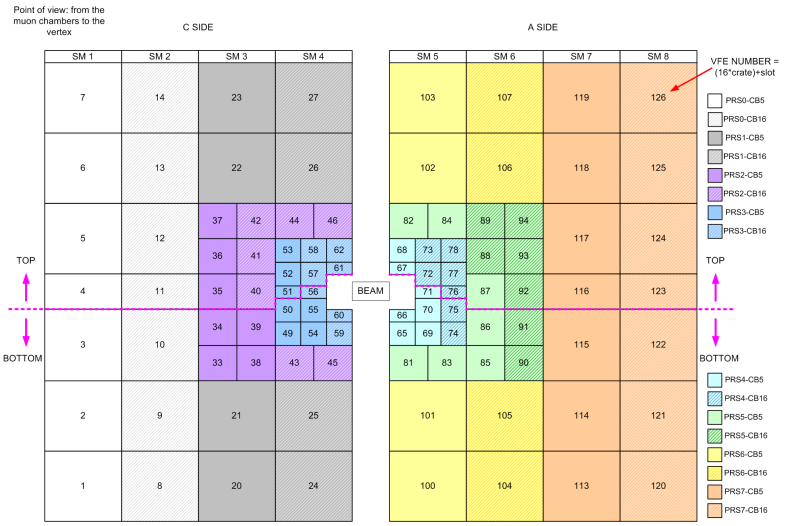

Figure 4.1: Disposition of the 100 SPD very front ends and their ID. The different sizes for the different parts of the sub-detector (inner, middle and outer) can be noted.

4.1 Energy deposition of minimum ionizing particles in the SPD

When charged particles traverse a thin material, they deposit a certain amount of energy, given by the Landau distribution. The mathematical expression of its probability density function, which is characterised by a narrow peak and a long tail towards positive values, is given by [97]

$$\psi(\lambda) = \frac{1}{2i\pi} \int_{c-i\infty}^{c+i\infty} e^{(s \log s + \lambda s)} \, \mathrm{d}\, s, \tag{4.1}$$

where c is any real positive number and λ is defined as

$$\lambda \equiv \frac{E - E_{MIP}}{\Delta}, \tag{4.2}$$

where E_{MIP} is the most probable energy loss by a Minimum Ionizing Particle (MIP) and Δ is an absorber-dependent parameter. In the case of the SPD cells, made of polystyrene, $\Delta = 0.13$ MeV.

The total amount of material traversed by a particle when it travels through a SPD cell depends on the incident angle. If the angle with respect to the normal direction of the cell plane is zero (and therefore the total traversed material corresponds to the depth of the cell, which is the minimum possible material traversed), the average energy left is 2.85 MeV [98], which is the quantity E_{MIP}. If an extrapolation from the interaction point to the SPD sub-detector is made, it can be seen that the maximum amount of traversed material allowed corresponds to a 107 % of the SPD cell depth.

The efficiency of a cell is computed as the integral of the probability density function between a given energy value and infinity.

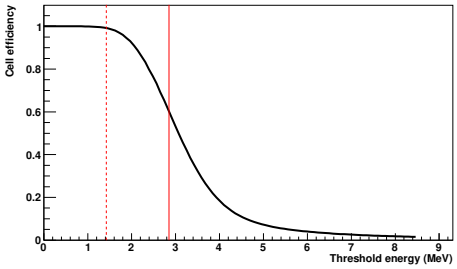

Figure 4.2: Expected efficiency of the SPD response to particles as a function of the threshold value. The solid vertical line indicates the position of E_{MIP} and the dashed vertical line indicates the position of the comparator threshold set at 0.5 E_{MIP}.

4.2 SPD response and output

Once a particle reaches the SPD plane, light produced in the scintillator material is collected by means of fibers and guided to a PMT that amplifies the photoelectrons into a current, which is then integrated in an ASIC that, added to the intrinsic offset to the electronics, constitutes the SPD output signal in a binary form (1 if it is above the threshold or 0 if it is not). To allow working at the nominal 40 MHz rate for the LHC, each SPD channel consists of two alternating sub-channels running at half-rate which implement their own integrator and comparator with respect to the threshold, set at 0.5 E_{MIP}.

For a threshold set at 0.5 E_{MIP}, the efficiency is expected to be around 95 % for the average 11.5 photoelectrons/MIP generated in the PMT photo-cathode. The relation between the cell efficiency and the threshold can be seen in Fig. 4.2.

4.3 SPD Calibration

The SPD response calibration consists on calculating the MIP position (in terms of cell efficiency as a function of the threshold). Before performing the calibration, a pre-calibration of the SPD was carried out in the laboratory (before the detector installation) [96]. The number of photoelectrons per MIP produced at each photo-cathode when a MIP traverses the detector cells was measured using vertical cosmic rays. The set-up consisted in eight scintillation counters with dimensions of $16 \times 100 \times 2$ cm ^{3}. The PMT gain per channel was measured at the laboratory by using a LED that illuminated directly the whole PMT surface and changing the bias voltage from 450 V to 800 V. The gain per channel was measured to be

$$G_{PMT}^{LED} \propto \frac{\mu_s^{LED}}{N_{phe}^{LED}}, \tag{4.3}$$

where μ_s is the mean of the distribution of the measured charge at the PMT anode and N_{phe} is the number of photo-electrons produced at the photo-cathode, which follows a

Poisson distribution. The dependence of the PMT gain on the HV can be parametrised by

$$G_{PMT} = G_0 V^{\alpha}. \tag{4.4}$$

For normal detector operation, the HV applied to the PMT is chosen so the channel with the highest PMT gain produces an integrated charge of 100 fC/MIP, which would prevent premature ageing of the PMTs. On average, that HV corresponds to 580 V. The uncertainties for G_0 and α are small, leading to a precision for G_{PMT} of around 3 %.

The SPD was calibrated before and at the beginning of Run 1 [80] through two different approaches: making use of cosmic rays and making use of tracks from collisions produced at a centre-of-mass energy of 7 GeV.

4.3.1 Calibration with cosmic data

The calibration with cosmic data [96], carried out before the presence of beams in the LHC, was performed using four different values for the threshold in order to study the efficiency distribution for the different cells for each of those thresholds. Tracks using information from ECAL and HCAL were reconstructed. The method used to obtain the correction factors (factors introduced to module the threshold) was to compare the efficiency measured with the threshold value at 1 E_{MIP}. After that, a set of requirements (summarized in Table 4.1) was applied to the cosmic rays data for the calibration.

Table 4.1: List of requirements for cosmic rays tracks considered for the SPD calibration. The PS hit had to be closer than 3 times the extrapolation uncertainty of the track to the PS plane.

	Cut Value	Units
Max. amount of material traversed	1.2× material thickness	
Arrival time	> 5 and < 10	ns
Number of SPD hits	1	
Number of PS hits	1	
Track uncertainty	< 150	mm
PS energy	> 1.14	MeV

Cosmic rays calibration allowed the calibration at VFE level due to the low rate of cosmic rays. Figure 4.3 shows the calibration factor introduced for each VFE to the pre-calibrated gains.

4.3.2 Calibration with data from 2010 collisions

Data from LHC collisions at seven different threshold values were used for calibration carried out in the first half of 2010. The first six points taken correspond to 0.3, 0.5, 0.8, 1.0, 1.4 and 1.8 $E^{pre.}_{MIP}$, the energy corresponding to a MIP at the pre-calibration level. The criterion used to choose them was to have enough points in the transition region (region with non-zero slope in Fig. 4.2) to maximise the sensitivity to E_{MIP} and also to

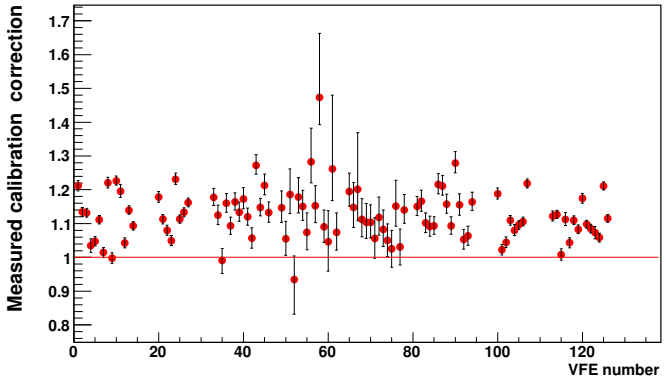

Figure 4.3: Calibration factor per VFE that needed to be applied to the pre-calibrated gains, calculated from cosmics data. The horizontal line would have corresponded to a perfect pre-calibration that had not needed any correction.

ensure that the maximum and minimum efficiency was reached in all the cells [96]. The tracks used for this calibration were all T-tracks selected by the minimum bias stripping stream. T-tracks were used since, in principle, any track with a relatively perpendicular incidence to the SPD is useful for calibration, so no requirements were set on the VELO or TT. Table 4.2 shows the selection required to the tracks to be considered for the calibration, which will be motivated in 4.4.1.

Table 4.2: List of requirements for tracks considered for the SPD calibration. The extrapolation of the tracks was required to be at least at 3σ away from the edge of the effective cell, where σ is the extrapolation uncertainty. Coincidence between SPD and PS cells was also required.

	Cut Value	Units
Track χ^2/ndf	< 2.5	
Extrapolated uncertainty	< 1.5	mm
Number of track hits	> 18	
Traversed material	< 18	mm
Cell side reduction for each end	8	mm
Min. Energy in PS cell	> 1.5	MeV
Max. Energy in PS cell	< 4	MeV

Fitting the curve from Fig. 4.2 to the measured cell efficiency-threshold curve, the correction factor to the thresholds can be extracted as well as the number of photoelectrons and the maximum efficiency reachable by each cell. Figure 4.4 shows the distribution of the correction factors in each region of the SPD. On average, the correction factor is about 0.8, which means that the pre-calibration had overestimated the detector and electronics response by a 20%.

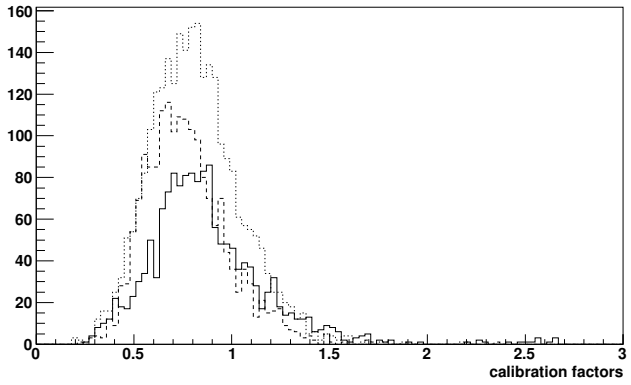

Figure 4.4: Distribution of calibration factors to be applied to the cells, obtained from 2010 collisions, for inner (solid line), middle (dashed lines) and outer (dotted line).

Once the correction factor for each of the cells was extracted, it was applied to the SPD electronics. At the beginning of the 2011 data taking the SPD efficiency was checked and it was found to be 95 % on average with an RMS of 3 %.

4.4 Monitoring of SPD cells efficiency using tracks

Different types of tracks can be used for the calculation of the SPD efficiency, although only two of them are considered: T-tracks and long tracks (see Fig. 3.16). The statistics available for T-tracks is larger than the one for long tracks and therefore they are the choice when one wants to look into a short period of time. If, however, the period to be studied is large enough, long tracks are preferred due to their better resolution and quality. The following results and studies presented are all performed making use of long tracks.

4.4.1 Track requirements

A certain set of conditions, detailed in Table 4.3, is required for a track to be considered for the calculation of the SPD efficiency. Slight modifications to the ones detailed in 4.2 are introduced due to changes in the data treatment (such as the reconstruction process).

The requirement on the track χ^2/ndf and the minimum number of hits are used to reduce the contamination from ghost tracks (see 4.4.2), while the requirements on the position uncertainty ensure a good extrapolation from the reconstructed track to the SPD plane. The cut on the amount of traversed material is motivated by the amount of energy the particle is to leave in the SPD cells due to a high incidental angle. The cuts on the distance to the cell edge are introduced to help mitigate the effect alignment problems. Regarding cuts related to the Preshower sub-detector (PS), two aspects are to be taken into account:

Table 4.3: List of requirements for a long track to be considered for the SPD efficiency calculation.

	Cut Value	Units
Preshower energy lower limit	1.5	MeV
Preshower energy upper limit	4.0	MeV
Maximum amount of material traversed	1.2× material thickness	
Maximum distance to the cell edge	8	mm
Maximum distance to the cell edge	3× position uncertainty	
Minimum number of hits	22	
Maximum track χ^2/ndf	2.15	
Maximum position uncertainty	1.5	mm

- Energy deposited in the PS: The requirements on Table 4.3 ensure that only single particles are accepted (a larger interval in the allowed energy range could imply the inclusion of more than one particle).
- Only events where the extrapolation in the PS plane is in the cell behind the SPD hit are kept.

4.4.2 Ghost probability

A requirement that deserves special attention is the ghost probability. Ghost tracks are reconstructed tracks that do not match true particles. They can have two different origins:

- Tracks that are entirely made up from noise hits.
- Tracks reconstructed with hits from different particles.

Ghosts tracks can bias the efficiency estimation to lower values. Despite the requirement on the number of hits needed for a track to be reconstructed, and due to the different running conditions in 2011 and 2012 (with a larger pile-up in the latter), the presence of ghost tracks could still affect the efficiency measurement. To deal with this issue, a tight cut on the ghost probability was introduced (ghost probability to be smaller than 0.1). This requirement was chosen to keep high efficiencies while removing large amounts of ghost tracks.

4.5 Efficiency evolution through Run 1

As it was stated before, a drop in the SPD efficiency was observed with during Run 1. Figure 4.5 shows the distribution of efficiencies of all the SPD cells in June, 2011 (when the total integrated luminosity was of about 0.6 fb^{-1}), where the efficiency tends to a

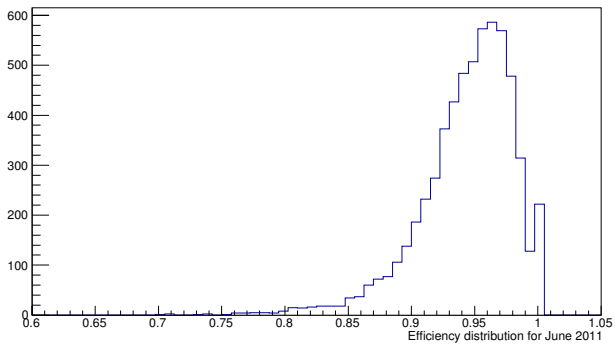

Figure 4.5: Efficiency distribution for all the SPD cells. The data correspond to June, 2011.

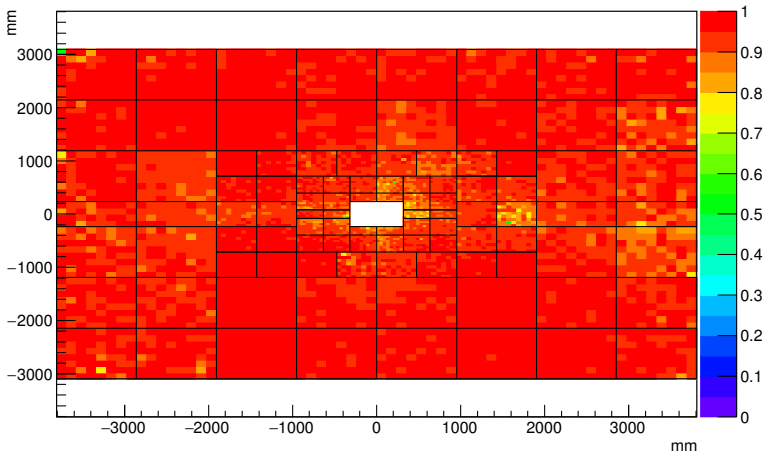

Figure 4.6: Efficiency distribution for all the SPD cells in the SPD plane. The data correspond to June, 2011.

value around 95 %. Figure 4.6 shows the same efficiencies, locating them in the SPD plane.

The SPD monitoring, which is performed periodically, led to the observation of a drop in the efficiencies for many of the SPD cells at the end of Run 1. This was expected due to the large amount of radiation at which the SPD was exposed during that period. The SPD cell efficiencies, in Fig. 4.7, corresponding to April 2012 and a total integrated luminosity of 1.1 fb^{-1}, clearly show an ageing effect. As the Run 1 went on, the amount of radiation increased and with it the ageing effect increased, as shown in Fig. 4.8, where the efficiency of the SPD is shown for data taken in November, 2012. The drop in efficiencies can be clearly observed in Fig. 4.9, where the difference of efficiencies between November, 2012, and June, 2011, is represented.

Table 4.4 summarizes the average efficiency for each of the areas of the SPD in

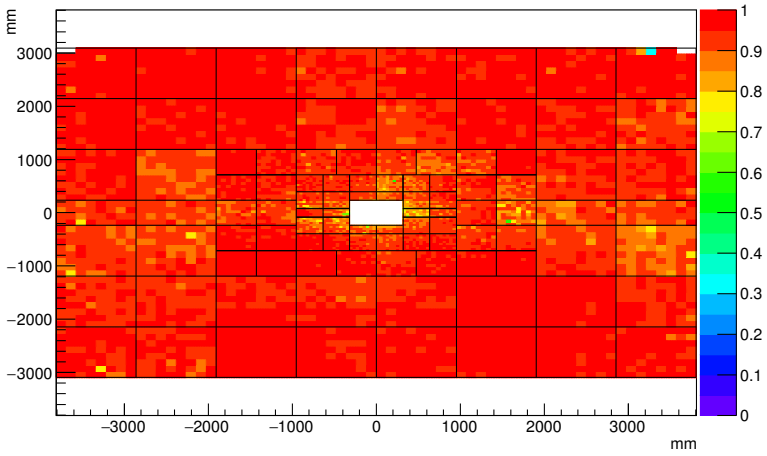

Figure 4.7: Efficiency distribution for all SPD cells in April, 2012.

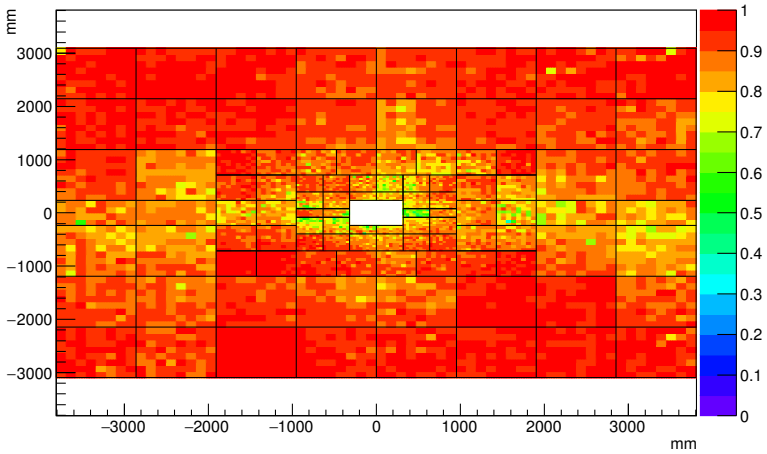

Figure 4.8: Efficiency distribution for all the SPD cells in the SPD plane. The data correspond to November, 2012.

different dates. The efficiency drop in all of them is clear and more pronounced for the inner part, which is expected since that it is the part with higher occupancies and therefore larger accumulated signal.

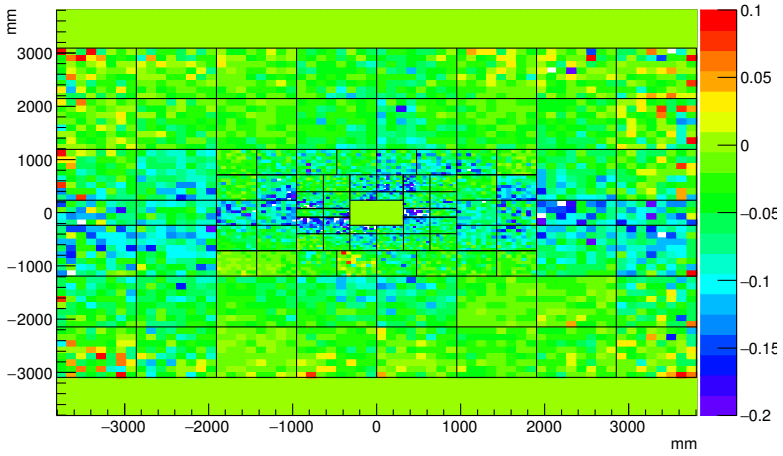

Figure 4.9: Efficiency difference distribution for all SPD cells November, 2012, and June, 2011. The efficiency drop is clear.

Table 4.4: Average efficiencies for the different parts of the SPD for three different time periods. The efficiency drop is clear for all three parts. The integrated luminosity at each moment is also included.

	Inner Part	Middle part	Outer part	Int. lumi.
June 2011	$(91.9 \pm 0.7)\%$	$(94.6 \pm 0.5)\%$	$(95.7 \pm 0.4)\%$	0.6 fb^{-1}
April 2012	$(91.5 \pm 0.7)\%$	$(94.3 \pm 0.6)\%$	$(94.9 \pm 0.4)\%$	1.1 fb^{-1}
November 2012	$(83.9 \pm 0.9)\%$	$(88.7 \pm 0.8)\%$	$(91.6 \pm 0.5)\%$	3.2 fb^{-1}

4.6 Efficiency drop analysis

The analysis of this drop in efficiencies and the reasons why it had taken place followed a series of steps:

- Confirmation of the reason for the efficiency drop.
- Use of cosmic ray data for monitoring the possible recovery/annealing (2012-2014).
- Use of collision data for the new calibration (2015).

The next subsections describe in detail these steps.

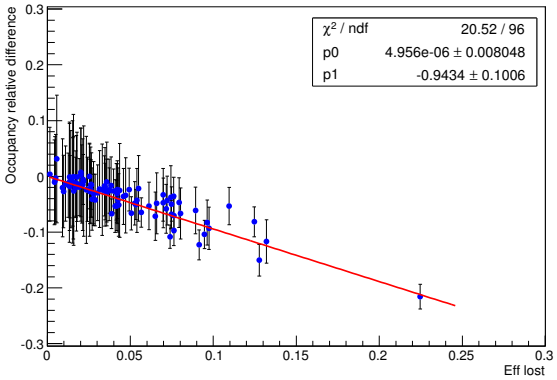

Figure 4.10: SPD occupancy variation as a function of the efficiency loss for the different VFEs between November, 2012, and October, 2011. The red line corresponds to a fit to the distribution of points and gives an idea of the clear correlation between efficiency loss and occupancy.

4.6.1 Identification of the reason for the efficiency drop

Two possible reasons for the efficiency drop were considered: the presence of ghosts in the reconstructed data and the effect of the ageing due to the accumulated collected charge [99, 100]. The ageing effect is the sum of two different processes: the ageing of the photocathode of the PMT, which implies the loss of quantum efficiency, and the ageing of the multiplication chain, which implies a gain reduction.

Since the sub-detector occupancy (number of SPD cells with a non-zero signal per event) is ghost-independent, a study of this observable would point to the presence of ageing of the cells of the SPD if a drop in the average occupancy was observed. Figure 4.10 shows the correlation between efficiency loss and occupancy for the SPD VFEs, which confirms the presence of ageing. This part of the analysis made clear that a tight requirement on the ghost probability would highlight the presence of ageing of the SPD cells. Some annealing[1], by which the response of the SPD cells would be partially recovered with time, was expected during the first LHC Long Shutdown (LS1) [102].

4.6.2 Cosmic Rays data

During the LS1, from December 2012, to February 2015, the evolution of the efficiency drop was assessed with cosmic rays runs taken at the beginning and at the end of the shutdown. There are two main reasons for the choice of cosmic ray data: cosmic rays are a *standard candle* with a constant rate with time (so no change between two time periods is expected) and cosmic rays data would help to avoid the need for a full calibration before Run 2 if there was a full efficiency recovery. A total number of 1.3×10^9 events were recorded. The cosmic rays rate, measured by the SPD, was much larger than expected (6600 Hz instead of the 400 Hz measured in 2009 [80]) due to the presence of radiation

[1] Diffusion of atoms within a solid material towards its equilibrium state [101].

in the LHCb cavern produced by the presence of beams during the Run 1, which was high enough to trigger as signal. Requiring a minimum amount of energy in the PS cell coincident with the triggered SPD cell helped to get rid of the events where the triggering was due to radiation (under the assumption that those particles would not have enough energy to give signal in the PS).

A series of changes in the SPD configuration was needed with respect to the one detailed in Table 4.3. These changes included:

- Since the cosmic rays do not travel through the whole detector, it was not possible to reconstruct tracks and therefore this requirement was removed. However, the requirement that the SPD and PS cells giving signal to be one in front of the other was kept.
- The requirement on the amount of traversed material was removed since the cosmic rays traverse the SPD cell from above, so the amount of material traversed tends to be the cell side size. The requirement for the coincidence between SPD and the PS helped to avoid the cosmic ray to leave an energy larger than the one corresponding to one MIP.

A large number of problems appeared when the cosmic rays data were analysed:

- Cosmic rays are not synchronized with the LHCb clock. However, and under the assumption that cosmic rays traverse more material than tracks do, the amount of energy left in the SPD cell in the running time of the LHCb clock would be in the range valid for a MIP particle (i.e., the desychronization between the cosmic ray and the LHCb clock would compensate the large amount of energy deposited in the cell) in such a way that the two effects would compensate each other.
- A few noisy cells had to be masked during the data taking due to the large rate they were giving, masking the real effect from cosmic rays[2].
- Three VFEs were vetoed due to mis-calibration of the PS coincident VFEs[3].
- One VFE was vetoed due its chaotic behaviour[4]. This VFE was observed to give much more occupancy than expected and was switched off during the data taking.
- The PS encoding system, which gathers measured energy values for a quicker processing but masks energy distributions, prevented the search for energy depositions around the E_{MIP} energy. This distribution would have been helpful to establish a parallelism to 2010 data [80].
- The configuration of the high voltages (HV) for the SPD did not allow a study of the data cell-by-cell. All the cells in the same VFE are connected to the same

[2]These noisy cells belonged all to the same VFE (VFE ID = 24), which would be replaced during the LS1.

[3]VFEs ID = 9, 27 and 116.

[4]VFE ID = 70. This VFE was replaced during the LS1.

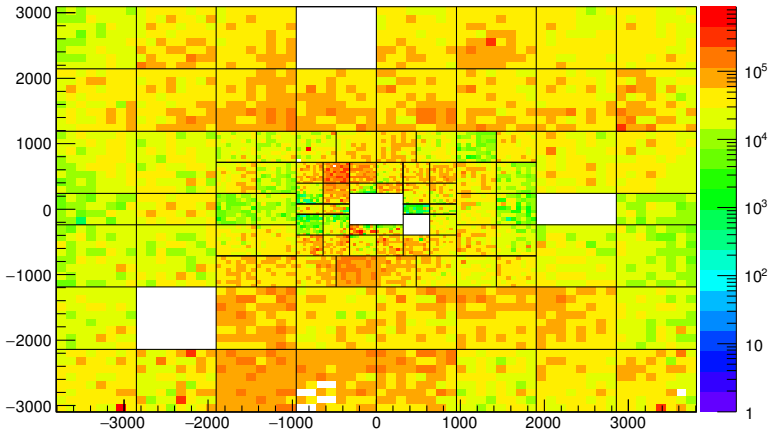

Figure 4.11: SPD occupancy for the cosmics campaign data. The pattern observed for the efficiency drop distribution can be spotted. The blank spaces correspond to vetoed VFEs or cells.

HV and therefore it was not possible to change it for one of them while keeping it unchanged for the others, so the behaviour of the occupancy with respect to HV could not be studied for cells in the same VFE.

At the end of the cosmics campaign the ageing effect was still present, since the SPD occupancy, taking into account all the previously mentioned aspects, showed the same pattern (Fig. 4.11) than the efficiency drop distribution, as shown in Fig. 4.8. Unfortunately, and due to the low statistics available after applying all the vetoes and the different considerations, no quantitative conclusions could be extracted. This meant that a study about the state of the SPD was needed at the beginning of Run 2, making use of tracks, to perform a correct calibration of the SPD cells.

4.6.3 Efficiency check with tracks in Run 2

Since cosmic data were not enough to complete a quantitative study of the recovery of the SPD efficiencies, collision data taken at the beginning of Run 2 were used to quantify its effect and determine if a new SPD calibration procedure was needed.

The tracks used for this study correspond to data taken between August and October, 2015, and were reconstructed with Reco15 reconstruction version and selected with Stripping23r1 version. The tracks were asked to fulfill the same requirements than in 2012 data (Table 4.3). Due to the incomplete configuration of the PS sub-detector, a small fraction of cells ($< 1\%$) could not be studied.

After performing the calculation of the efficiency for the SPD cells, the efficiency drop pattern could still be spotted (Fig. 4.12). However, and as it was expected, a certain level of recovery could also be seen (up to 10% in some cells), as shown in Fig. 4.13. Table 4.5 shows the average efficiencies for the different parts of the SPD for the data taken at the

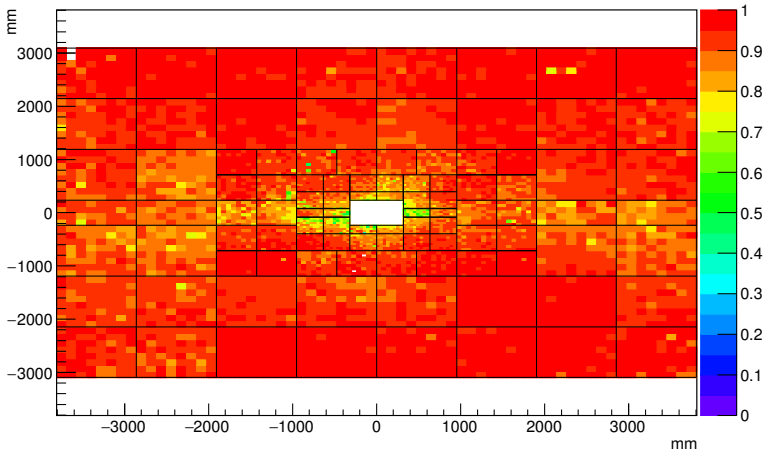

Figure 4.12: SPD cells efficiency for Run 2 collisions data collected from August, 2015 to October, 2015. The efficiency drop pattern can still be identified.

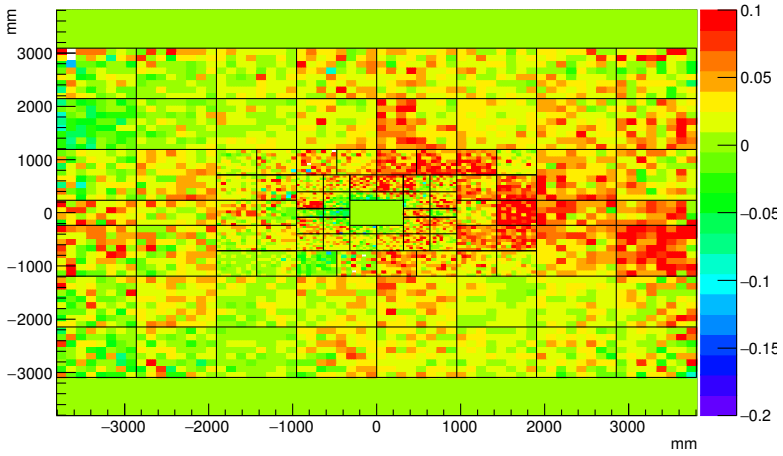

Figure 4.13: SPD cells efficiency difference between the beginning of Run 2 and the end of Run 1. A recovery in the measured efficiencies is observed.

end of Run 1 and at the beginning of Run 2 (before and after the corrections explained in Sec. 4.7), where it can be seen that a degree of recovery was reached as we compare those values with the ones from Table 4.4. On average, the recovery could be quantified as a 3%.

4.7 Correction to calibration factors at the beginning of Run 2

Using October 2015 efficiencies, corrections to the calibration coefficients for those cells with efficiencies below 90% (1716 cells) were extracted and applied in November, 2015 (the cells for which the efficiency was above 90% remained uncorrected since the efficiency was of the desired level). The corrections were estimated from the expected efficiency curve with respect to the energy threshold. During November, 2015, and after the corrections were applied, data were taken, allowing the study of the behaviour of the SPD with the new configuration scheme. These data were reconstructed using Reco15a reconstruction version and Stripping22b and were collected in 2.51 TeV collisions. Despite the low statistics available, the effect of these corrections was clear, as shown in Fig. 4.14. In Table 4.5 one can see the comparison of the latest calibration with the efficiencies from November, 2012 and October, 2015, for comparison. Figure 4.15 shows the efficiency for the different VFEs for both October, 2012 (end of Run 1) and November, 2015 (after the new configuration is applied). For these data, different values for the ghost probability cut were tested, with no major changes in the SPD efficiencies. The cut could be loosened up to 0.4, which is the cut present in the stripping used, with a gain in the number of tracks of 2.5%.

Table 4.5: Average efficiencies for the different parts of the SPD for the end of Run 1 (November, 2012) and beginning of Run 2, before (October, 2015) and after (November, 2015) the new configuration was applied.

	Inner Part	Middle part	Outer part
November 2012	$(83.9 \pm 0.9)\%$	$(88.7 \pm 0.7)\%$	$(91.6 \pm 0.5)\%$
October 2015	$(86.8 \pm 0.9)\%$	$(92.4 \pm 0.6)\%$	$(94.0 \pm 0.5)\%$
November 2015	$(94.0 \pm 0.6)\%$	$(93.4 \pm 0.6)\%$	$(94.2 \pm 0.5)\%$

With this new calibration, the SPD is calibrated to give a performance for the Run 2 similar to that at the beginning of Run 1, with an average cell efficiency of about 95%.

Due to the larger energy reached during the Run 2, the ageing effect on the SPD cells is expected to be more relevant. A constant monitoring of the SPD efficiencies would be of great use to observe this effect for possible corrections.

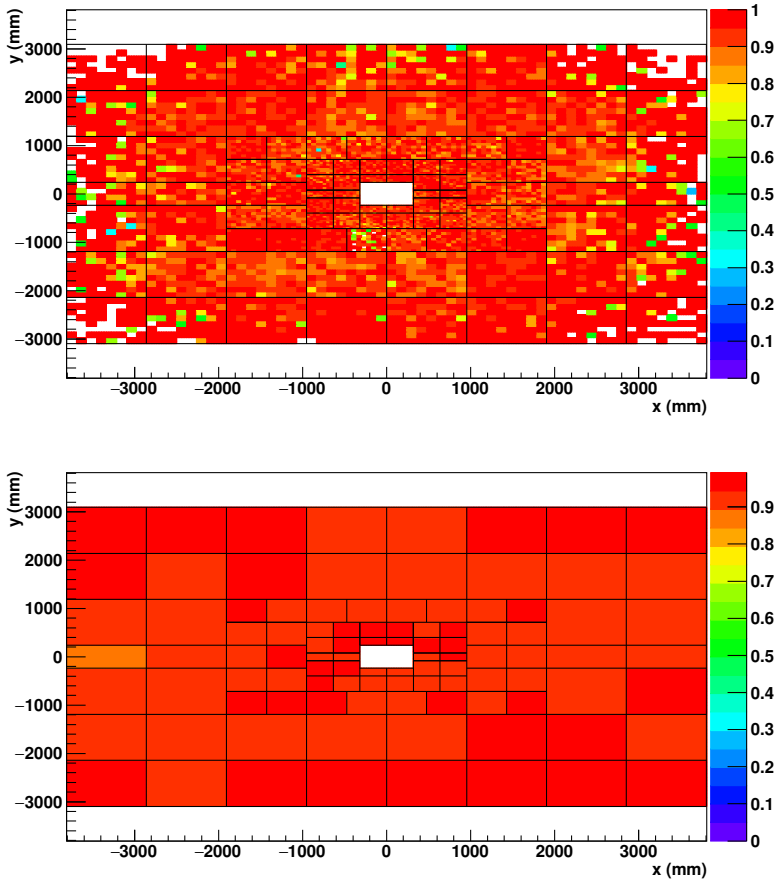

Figure 4.14: SPD cells (up) and VFE (down) efficiency for November, 2015, after the new configuration was applied.

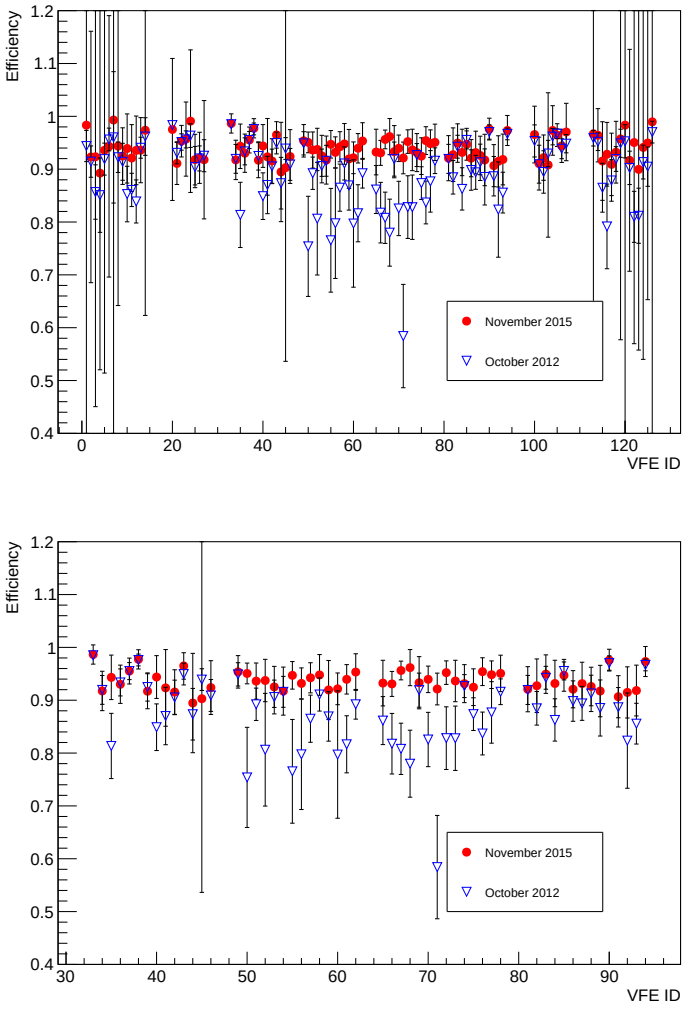

Figure 4.15: VFE efficiency comparison for October, 2012, and November, 2015. Efficiency recovery is clear for the different VFEs once the corrections are applied. The plot on the top shows all the VFEs while the plot on the bottom focuses on the VFEs placed in the inner and middle parts of the SPD.

5

Resampling tool for the γ/π^0 separation variable

Neutral pions mostly decay into two photons. A π^0 is referred to as *resolved* if the two photons the π^0 decays into are sufficiently separated in the ECAL and therefore are reconstructed as two different clusters. If the angle between the two photons is small and a single cluster is reconstructed the π^0 is called *merged*. Figure 5.1 illustrates the π^0 efficiency (defined as the number of π^0 identified over the number of π^0 in the detector acceptance with a $p_{\mathrm{T}} > 200$ MeV) dependence with the π^0 transverse momentum [88].

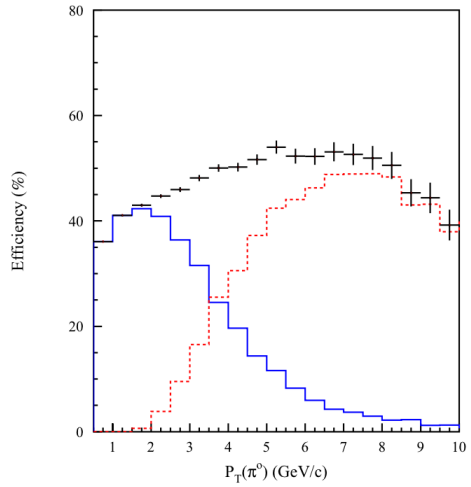

Figure 5.1: π^0 efficiency as a function of the transverse momentum. The proportion between merged (red) and resolved (blue) π^0 is shown, as well as the sum of them.

In 70% of the cases, a merged π^0 is misidentified with a single photon. In addition to this, around 88% of the photons detected by the calorimeter are originated in a π^0 decay. Therefore, a correct particle identification for ECAL clusters is an important requisite for the analysis of radiative decays, where one of the main sources of physical

backgrounds is that where the final state is the same than for the signal decay except that a π^0 substitutes the photon [77].

A multivariate tool for the identification of photons and merged neutral pions has been developed [103], making use of the properties of the cluster. Since the output of the tool is not reproduced accurately by the LHCb simulation software, two additional tools (calibration and resampling tools), that will be described in this chapter, have been developed to cope with the differences between data and simulation for the case of photons and neutral pions. Both tools are framed in the URANIA [104] project and seek the correct calculation of the efficiencies through different approaches: the calibration tool provides efficiency tables in bins of topological and kinematical variables, similarly to what the PIDCalib package [105] does for the charged particle identification and the resampling tool produces a new variable for the γ/π^0 separation variable based on the topological and kinematical variables of the photon.

5.1 γ/π^0 separation tool

Previous studies proved the usefulness of ECAL cluster shape variables for the γ/π^0 separation [106]. The method for γ/π^0 separation is based on the broader shape of the calorimeter cluster for a merged π^0 with respect to that for a single photon.

For a given cluster of N cells, being (x_i, y_i) the position and e_i the energy of the i-th cell, the position spread matrix elements is defined as:

$$S_{XX} = \frac{\sum_{i=1}^{N} e_i (x_i - x_c)^2}{\sum_{i=1}^{N} e_i}, \quad S_{YY} = \frac{\sum_{i=1}^{N} e_i (y_i - y_c)^2}{\sum_{i=1}^{N} e_i}, \tag{5.1}$$

$$S_{XY} = S_{YX} = \frac{\sum_{i=1}^{N} e_i (x_i - x_c)(y_i - y_c)}{\sum_{i=1}^{N} e_i}, \tag{5.2}$$

where (x_c, y_c) is the baricentre of the cluster, computed as $x_c = \frac{\sum_i e_i x_i}{\sum_i e_i}$ and $y_c = \frac{\sum_i e_i y_i}{\sum_i e_i}$.

From this, four shape variables are defined:

- The shower shape ($r2$) is related to the size of the cluster:

$$r2 = < r^2 > = S_{XX} + S_{YY} = \frac{\sum_{i=1}^{N} e_i ((x_i - x_c)^2 + (y_i - y_c)^2)}{\sum_{i=1}^{N} e_i}. \tag{5.3}$$

- The $r2r4$ variable informs about the importance of the tails:

$$r2r4 = 1 - \frac{< r^2 >^2}{< r^4 >}. \tag{5.4}$$

- The κ variable is related to the ratio of the eigenvalues of the matrix S, which is $(1+\kappa)/(1-\kappa)$. Thus, it corresponds to the relation between the major and minor semiaxes of an ellipse.

$$\kappa = \sqrt{1 - 4\frac{S_{XX}S_{YY} - S_{XY}^2}{(S_{XX} + S_{YY})^2}} = \sqrt{1 - 4\frac{\det S}{\mathrm{Tr}^2 S}}. \tag{5.5}$$

- The asymmetry (*asym*) provides information about the orientation of the ellipse or correlation between X and Y coordinates.

$$\text{asym} = \frac{S_{XY}}{\sqrt{S_{XX}S_{YY}}}. \tag{5.6}$$

The energy of the cluster (E_{cl}) is excluded as discriminant variable in order to avoid biases due to different spectra of the signal and background samples used for training of the multivariate tool. The energy of the seed cell, E_{seed}, and of the second most energetic cell of the cluster, E_{2nd}, are, however, used through the ratios

$$\frac{E_{\text{seed}}}{E_{\text{cl}}} \quad \text{and} \quad \frac{(E_{\text{seed}} + E_{2nd})}{E_{\text{cl}}}.$$

Other variables are constructed from PS information: a first set of variables contains the multiplicity of hits in the 3×3 PS cells matrix in front of the seed of the electromagnetic cluster, with different requirements on the minimum energy deposited in the cells. Four multiplicities are used: *multi*, *multi*15, *multi*30 and *multi*45, where the number refers to the minimum energy required per cell (in MeV) and *multi* is just pedestal subtracted signal.

Other shape variables are defined similarly to the ones already presented for ECAL from the signal deposited in the 3×3 PS cells: $E^{PS}_{\text{max}}/E^{PS}_{\text{sum}}$, $E^{PS}_{2nd}/E^{PS}_{\text{sum}}$, $r2PS$ and *asymPS*, where E^{PS}_{sum} is the total energy deposited in the 3×3 cells, E^{PS}_{max} the energy in most energetic cell and E^{PS}_{2nd} the second highest energy deposited. Other variables, such as $E^{PS}_{5}/E^{PS}_{\text{sum}}$ (where E^{PS}_{5} refers to the energy in the central cell), κPS and $r2r4PS$ were considered, but were discarded since no improvement in the separation power was reached when using them.

5.1.1 Implementation of the tool

The variables introduced in the previous section are taken as input for the TMVA [107] tool. A Fisher discriminant, a Boosted Decision Tree (BDT) and a Multi Layer Perceptron (MLP) are compared. For the training of the tool, MC10 samples are used, which reproduce the conditions of data taken in 2010, at $\sqrt{s} = 7$ TeV and $\nu = 2.5$.

True photons from 10^6 $B^0 \to K^{*0}\gamma$ events are taken as signal sample. A loose preselection (listed in Table 5.1) is used to select the photons from the B^0 candidates. These reconstructed photons are required to have only one cluster associated and a minimum E_{T} of 2 GeV (minimum E_{T} for a π^0 to be reconstructed as merged). With these criteria, a sample of 250k photons is kept.

The background is obtained from the list of simulated samples detailed in Table 5.2 by requiring the π^0 from the B decay to be reconstructed and selected as a photon following the same criteria as Table 5.1 (except the PID requirement). From these, a total of $\sim$ 44k merged π^0 reconstructed as photons are selected.

Both signal and background samples are divided in training and testing subsamples for the tool. The three regions of the calorimeter are studied separately because of the

Table 5.1: List of cuts used for $B^0 \to K^{*0}\gamma$ preselection.

Track $\chi^2_{\rm IP}$	> 25
Track $p_{\rm T}$	> 500 MeV/c
Kaon PID$_K$−PID$_\pi$	> -10
Kaon PID$_K$−PID$_p$	> -10
Pion PID$_K$−PID$_\pi$	< 10
K^{*0} vertex χ^2/ndf	< 9
γ $E_{\rm T}$	> 2 GeV
B^0 $p_{\rm T}$	> 2 GeV/c
B^0 $\chi^2_{\rm IP}$	< 9
B^0 DIRA	> 0.9998
B^0 $\Delta M_{\rm PDG}$	< 1 GeV/c^2

Table 5.2: List of MC samples, with their corresponding size, used as π^0 background for the training of the tool. The number of events finally kept after the $B^0 \to K^{*0}\gamma$ preselection are shown in the last column.

MC sample decay	Events generated	Events offline selected
$B^0 \to K^+K^-\pi^0$	1.8M	24k
$B^0_s \to K^+K^-\pi^0$	2.0M	34k
$B^+ \to K^{*+}(\to K^+\pi^0)\pi^-\pi^+$	2.0M	5k
$B^0 \to D^0(\to K\pi\pi^0)K^{*0}$	2.5M	4k
$B^+ \to D^0(\to K\pi\pi^0)\pi^+$	105k	0.1k
$B^0 \to D^{*+}\pi^+\pi^-\pi^+\pi^0$	1.0M	0.4k
$B^+ \to K^{*+}(\to K^+\pi^0)K^+K^-$	100k	0.1k
$B^+ \to J/\psi\,(\to \rho\pi^0)K^+$	100k	0.7k

different size of the cells. Distributions of the input variables for the inner, middle and outer region are shown in Figs. A.1– A.9, that can be found in Appendix A.

From the methods tested, the MLP provides the best discrimination, with around 5-15% less background retention for the same signal efficiency compared to the BDT and Fisher discriminants. The variable ranking is detailed in Table 5.3 for the 10 most discriminant variables in each calorimeter region.

5.1.2 Performance

Using the trained MLP in the test subsample, the distribution of the output obtained is shown in Fig. 5.2 for both signal and background in the three calorimeter regions. Background rejection as function of the signal efficiency (ROC curve) is shown in Fig. A.10 for those simulated events in Appendix A. Efficiencies as a function of the MLP output

Table 5.3: Variable ranking given by the MLP for the different calorimeter regions, showing only the 10 most discriminant variables.

Ranking	Inner	Middle	Outer
#1	$r2$	$r2$	$r2r4$
#2	$r2r4$	$r2r4$	$r2$
#3	$r2PS$	$r2PS$	$\|asym\|$
#4	$\|asym\|$	$(E_{\text{seed}} + E_{2nd})/E_{\text{cl}}$	$r2PS$
#5	$(E_{\text{seed}} + E_{2nd})/E_{\text{cl}}$	$\|asym\|$	$(E_{\text{seed}} + E_{2nd})/E_{\text{cl}}$
#6	$multi45$	$multi30$	$multi45$
#7	$multi30$	$multi15$	$multi$
#8	$multi15$	$multi45$	PS $E_{\text{max}}/E_{\text{sum}}$
#9	PS $E_{\text{max}}/E_{\text{sum}}$	$multi$	$multi15$
#10	κ	PS $E_{\text{max}}/E_{\text{sum}}$	$multi30$

are shown in Fig. A.11.

Table 5.4 shows the signal and background efficiencies when cutting at 0.6 (which corresponds to the usual requirement for radiative decays) on the TMVA output. A high signal efficiency around 98% is obtained with a rejection around 45% of the merged π^0 (reconstructed as photons) background. The use of the PS variables in addition to the ECAL ones helps to decrease the background efficiency for high signal efficiencies by around 5%.

The tool gives a better performance on simulated merged π^0 reconstructed as π^0, since their cluster shapes are slightly different to the ones for those reconstructed as photons.

The effect of applying a cut in this γ/π^0 discriminating variable on $B^0 \to K^{*0}\gamma$ data (selected with a soft preselection) is shown in Fig. 5.3, where a significant rejection of background events can be observed, while keeping roughly the same amount of signal candidates (peak around the nominal B^0 mass).

Table 5.4: Efficiency for signal (photons) and background (π^0) requiring MLP output>0.6.

	ϵ_{sig}	ϵ_{bkg}
Inner (%)	97	52
Middle (%)	98	55
Outer (%)	98	57

5.1.3 Data versus Monte-Carlo comparison

A comparison between background-subtracted data samples and simulation samples is performed in order to check the behaviour of the variables. The samples used for this comparison are $B^0 \to K^{*0}\gamma$ and $D^0 \to K\pi\pi^0$ for photons and neutral pions, respectively.

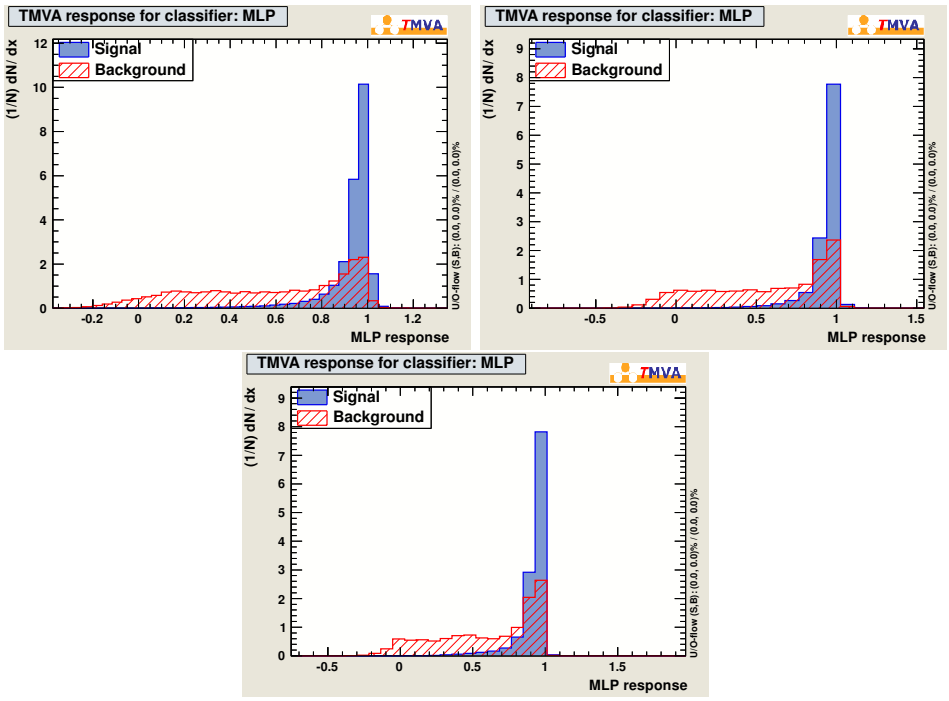

Figure 5.2: Output of the MLP for signal and background MC samples for inner (top left), middle (top right) and outer (bottom) calorimeter regions.

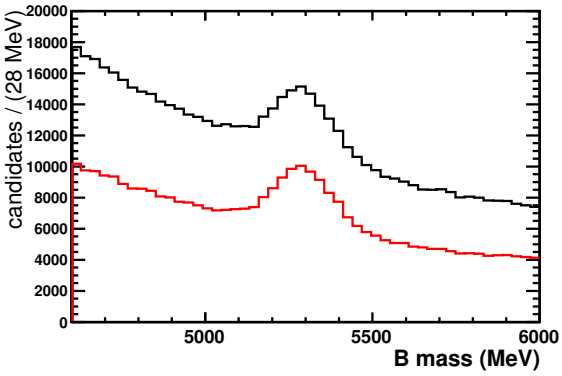

Figure 5.3: B mass distribution of $B^0 \to K^{*0}\gamma$ stripping candidates (black) and candidates with MLP output>0.6 (red).

The selection used for these samples will be presented in the next sections. Figures 5.4 and 5.5 compare MC and data for discriminant variables from ECAL and PS, respectively, for the inner region of the calorimeter (the corresponding ones for the middle and outer parts can be found in Appendix A). Due to the low number of candidates for the merged π^0 calibration sample in MC, π^0's from the $B \to K\pi\pi^0$ decay have been used instead (around 27k candidates), applying a reweighing on π^0 momentum to take into account

the differences with respect to π^0 from $D^0 \to K\pi\pi^0$ data. The disagreement on the γ/π^0 separation variable, which will be discussed in the following sections, is clear.

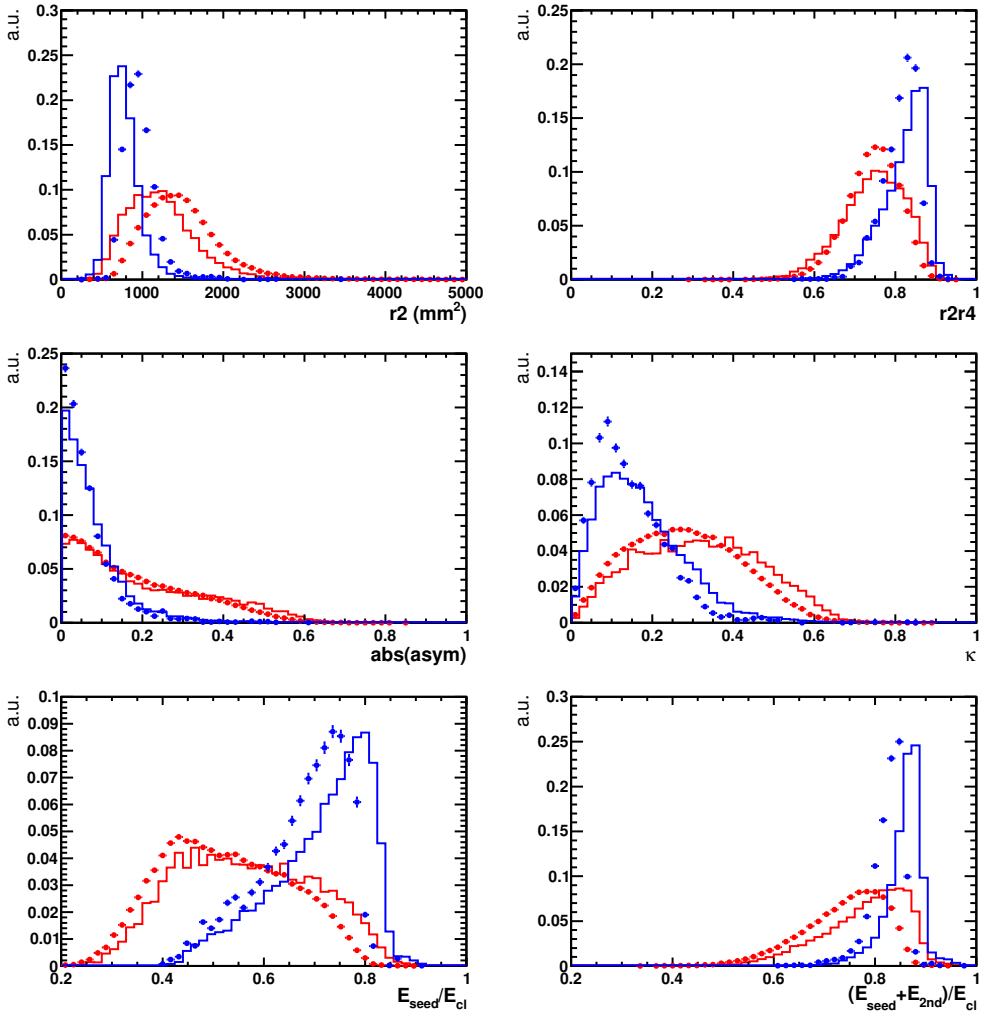

Figure 5.4: Comparison between MC (full line histograms) and data (points) for discriminant variables from ECAL of photons from $B^0 \to K^{*0}\gamma$ (in blue) and merged π^0 from $K\pi\pi^0$ decays (in red) for the inner region.

5.1.4 Calibration with real data

Currently, the γ/π^0 separation discriminant is part of the B radiative decay selections, where the default requirement ($\gamma/\pi^0 > 0.6$), as shown in Table 5.4, provides a good rejection power of the π^0 background with virtually no loss of photon efficiency. However, the efficiency at the requirement of the γ/π^0 separation variable needs to be quantified in a precise way for real data as the performance on real data might differ from what is

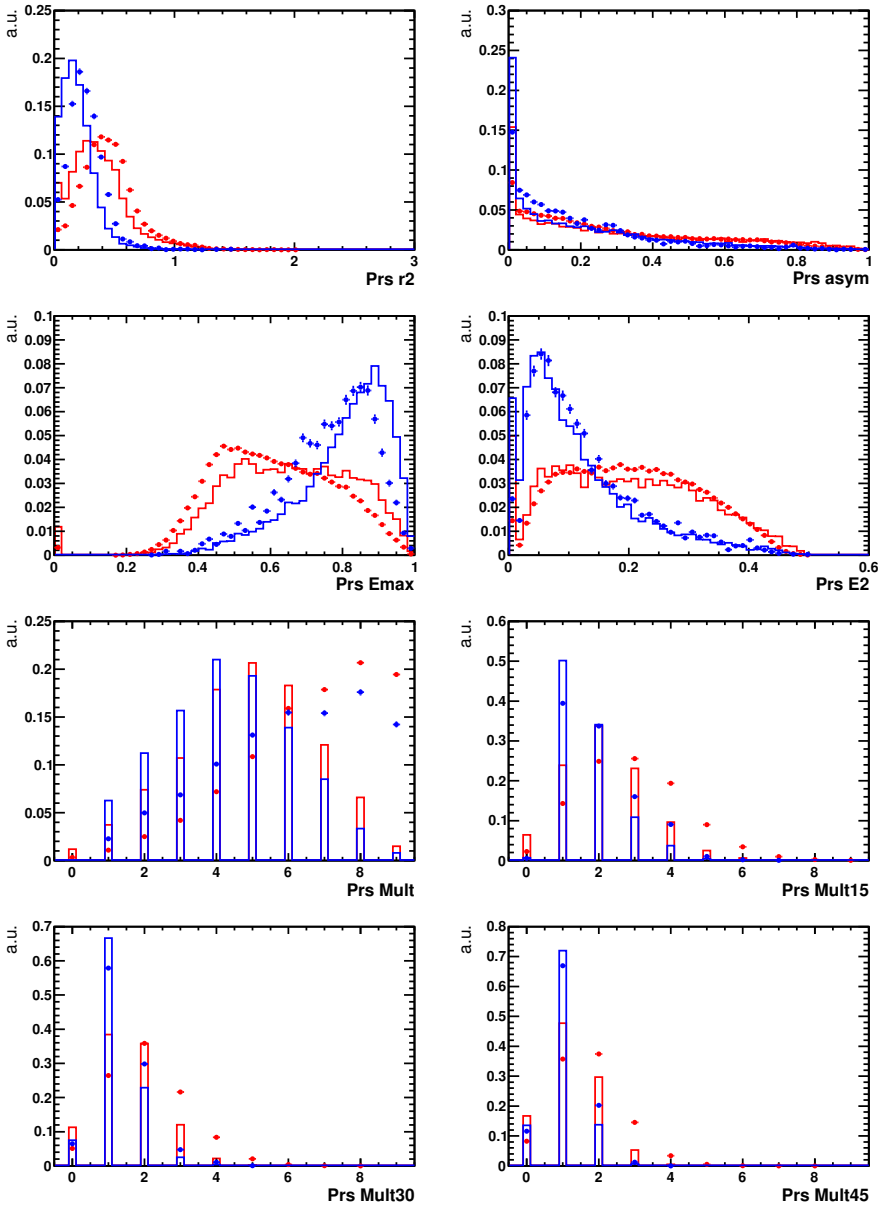

Figure 5.5: Comparison between MC (full line histograms) and data (points) for discriminant variables from PS of photons from $B^0 \to K^{*0}\gamma$ (in blue) and merged π^0 from $K\pi\pi^0$ decays (in red) for the inner region.

estimated using simulation.

In order to get a true estimate of the selection efficiency for a given cut on the γ/π^0 separation variable, calibration samples from real data are provided: $B^0 \to K^{*0}\gamma$ for photons and $D^0 \to K\pi\pi^0$ (selected from $D^{*+} \to D^0\pi^+$) for merged π^0. The $B^0 \to K^{*0}\gamma$ sample includes the full dataset collected by the LHCb detector over the 2011–2012 run

period, corresponding to $3\,\text{fb}^{-1}$ of integrated luminosity. The offline selection applied to select signal events is taken from Ref. [3] and summarized in Table 5.5. In order to get a background-subtracted $B^0 \to K^{*0}\gamma$ sample to use for the calibration, the B^0 invariant mass distribution is modeled following the same reference and the sPlot technique [108] is then used to extract weights for the signal component. With the mentioned selection, we have 19370 sWeighted signal candidates in real data for 45150 candidates in MC. The $D^0 \to K\pi\pi^0$ sample is obtained only using 2011 data and is selected from $D^{*+} \to D^0\pi^+$ with a very tight mass cut on $|M_{D^{*+}} - M_{D^0}|$, hence resulting in a very clean $D^0 \to K\pi\pi^0$ sample. The offline selection, summarized in Table 5.6, and the invariant mass fit are explained elsewhere [109]. The sPlot technique is also used to extract a background-subtracted $D^0 \to K\pi\pi^0$ sample. The total number of selected events is of 409826 for real data and 1884 for MC. An example of the B^0 mass and $D^0 \to K\pi\pi^0$ mass fit for 2011 data is shown in Fig. 5.6.

Table 5.5: List of cuts used for $B^0 \to K^{*0}\gamma$ offline selection.

Track χ^2_{IP}	> 25
Track p_{T}	> 500 MeV/c
Largest track p_{T}	> 1200 MeV/c
Kaon $\text{PID}_K - \text{PID}_\pi$	> 5
Kaon $\text{PID}_K - \text{PID}_p$	> 2
Pion $\text{PID}_K - \text{PID}_\pi$	< 0
K^{*0} vertex χ^2/ndf	< 9
K^{*0} ΔM_{PDG}	< 50 MeV/c^2
γ E_{T}	> 2600 MeV
B^0 p_{T}	> 3 GeV/c
B^0 χ^2_{IP}	< 9
B^0 pointing angle	> 20 mrad
B^0 $\lvert\cos\theta_{\text{helicity}}$	< 0.8
B^0 isolation $\Delta\chi^2$	> 2
B^0 FD χ^2	> 100
B^0 ΔM_{PDG}	< 1 GeV/c^2

Figure 5.7 shows the γ/π^0 separation cut efficiency for both $B^0 \to K^{*0}\gamma$ and $D^0 \to K\pi\pi^0$ as a function of the requirement value and for a fixed requirement on the photon identification variable $\gamma_{CL} > 0.25$. For real data, the number of events is extracted from fits to the B^0 and D^0 mass distributions, as shown previously. The difference between MC and data is clear. The cut on $\gamma_{CL} > 0.25$, along with the typical cut on $\gamma/\pi^0 > 0.6$, gives a 95% efficiency for $B^0 \to K^{*0}\gamma$ and 50% for $D^0 \to K\pi\pi^0$ for data. The photon efficiency as a function of the π^0 rejection is shown in Fig. 5.8 for both real data and MC.

To overcome the discrepancies between data and simulation, two data-driven MC

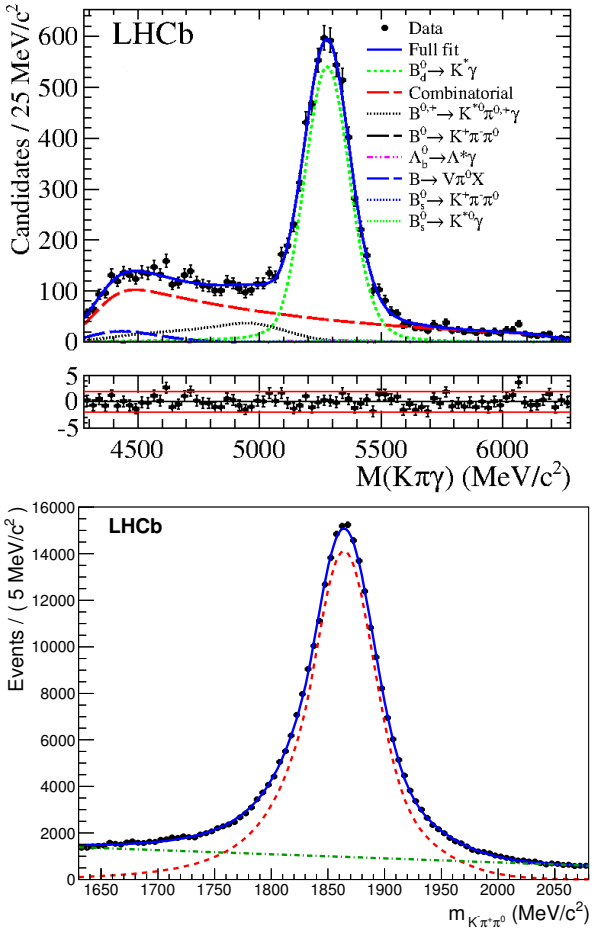

Figure 5.6: Mass distribution of reconstructed $B^0 \to K^{*0}\gamma$ (up) and $D^0 \to K\pi\pi^0$ (down) candidates obtained in the 2011 data sample. For both cases the blue curve corresponds to the mass shape fit. The $B^0 \to K^{*0}\gamma$ signal is represented by a green dotted line while the $D^0 \to K\pi\pi^0$ signal is represented by a red dashed line. The various background contaminations presents in the fits are noted.

performance calibration tools have been developed: one to extract cut efficiencies from real data and other for the resampling of the γ/π^0 separation variable in MC, useful to reproduce in MC the distribution of the γ/π^0 separation variable of real data. Both tools are implemented in the `GammaPi0SeparationCalib` package in URANIA, the documentation of which can be found in [110].

5.2 Efficiency table tool

The efficiency table tool reproduces for neutral pions and photons what already exists for charged particles [105] by also assuming that efficiencies for a given PID cut are

Table 5.6: List of cuts used for $D^0 \to K\pi\pi^0$ offline selection.

Track χ^2_{IP}	> 16
Track ghost probability	< 0.2
Track p_{T}	> 300 MeV/c
Kaon $\text{PID}_K - \text{PID}_\pi$	> 0
Pion $\text{PID}_K - \text{PID}_\pi$	< 5
π^0 E_{T}	> 2000 MeV
D^0 p_{T}	> 4 GeV/c
D^0 χ^2_{IP}	< 9
D^0 DIRA	> 0.9999
D^0 FD χ^2	> 64
D^0 M	$[1.6, 2.1]$ GeV/c^2
Slow pion χ^2_{IP}	< 16
D^{*+} p_{T}	> 4 GeV/c
D^{*+} χ^2_{IP}	< 16
D^{*+} FD χ^2	< 16
$\lvert M_{D^{*+}} - M_{D^0} - 145.421 \rvert$	< 2 MeV/c^2

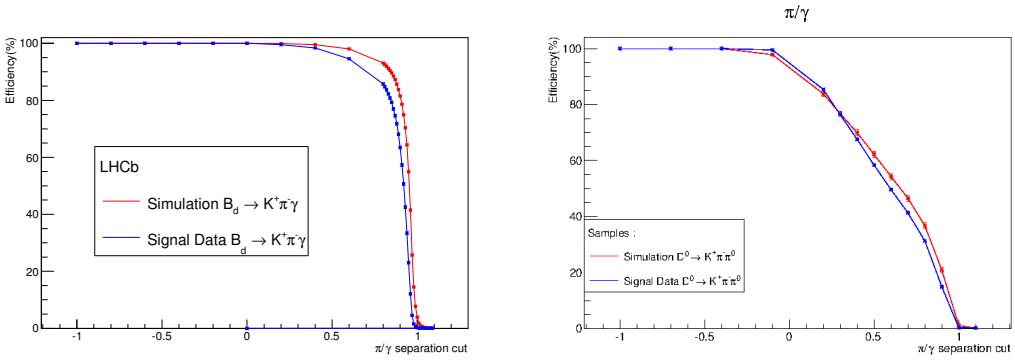

Figure 5.7: γ/π^0 separation efficiency as a function of the cut value. The distribution of signal data (MC) $B^0 \to K^{*0}\gamma$ (left) and $D^0 \to K\pi\pi^0$ (right) is shown in blue (red).

approximately constant within a given bin of the variables the PID depends on. The binned efficiency can be then used with the simulation to extract efficiencies or as weight for the MC sample, so the weighted distribution would match the data distribution.

In this case, the γ/π^0 separation variable is binned as a function of the photon (π^0) E_{T} and the pseudo-rapidity (which is related to the region of the ECAL, for which the separation variable has different performances). Figures 5.9 and 5.10 show that binning in pseudorapidity and transverse momentum is necessary since the γ/π^0 distribution is

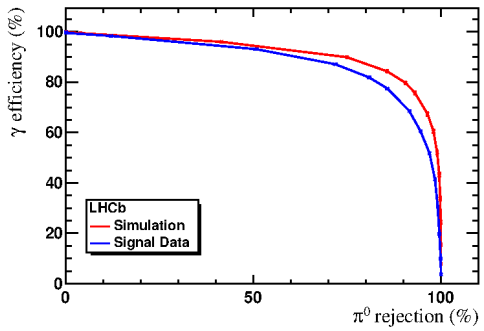

Figure 5.8: Photon efficiency as a function of π^0 rejection efficiency for the γ/π^0 separation tool for MC (red) and data (blue) for the $B^0 \to K^{*0}\gamma$ decay.

different when looking at different bins for these variables.

A possible dependence on the event multiplicity, as it appears in the case of charged particles, has also been studied. Two event multiplicity related variables were considered: the number of primary vertices and the number of hits in the SPD sub-detector. For each of them a binning was selected in such a way that the calibration samples had a similar number of sWeighted events in each of the bins. The γ/π^0 separation variable distribution for photons, shown in Figs. A.16– A.19, is compared for each of these bins and compatible distributions (within the statistical limits of the calibration samples) were found. As a consequence, no dependency on the event multiplicity is included. Due to the size of the calibration samples, it is not possible to have a large number of bins for the calibration variables but different binning schemes were tested, all of them being compatible. A default binning scheme is provided, but the tool allows the user to choose their own.

5.3 MC resampling tool

In addition to the possibility of using the calibration tool to extract the efficiency of a given cut in the γ/π^0 separation variable, another tool has been developed to allow the use of a data-like γ/π^0 separation variable in MC samples. This tool is based on the idea of *resampling*, which is the random regeneration of the γ/π^0 separation variable in MC samples to match the distribution in data, opening the possibility of including the γ/π^0 separation variable in multivariate discriminants, similarly to what is done in the case of charged particles (*e.g.* in the case of the $B^0 \to K^{*0}\mu^+\mu^-$ [111]).

This tool allows the resampling of the γ/π^0 separation variable for photons and for neutral pions. As for the efficiency table tool, the resampling tool uses the particle E_{T} and its pseudorapidity as calibration variables in order to obtain a set of histograms with the shape of the γ/π^0 separation variable (for each bin). These histograms can then be used to generate a random value of the variable to attach to a given MC sample.

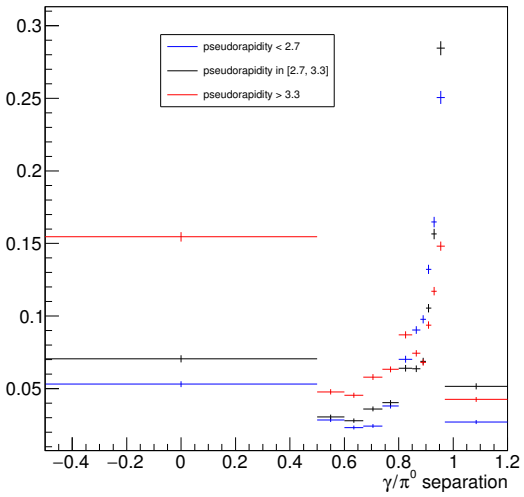

Figure 5.9: Comparison of the γ/π^0 variable distribution for different pseudo-rapidity bins. The fact that the distributions differ points out that binning in this variable is necessary. The data here corresponds to real $B^0 \to K^{*0}\gamma$ decays from the calibration samples.

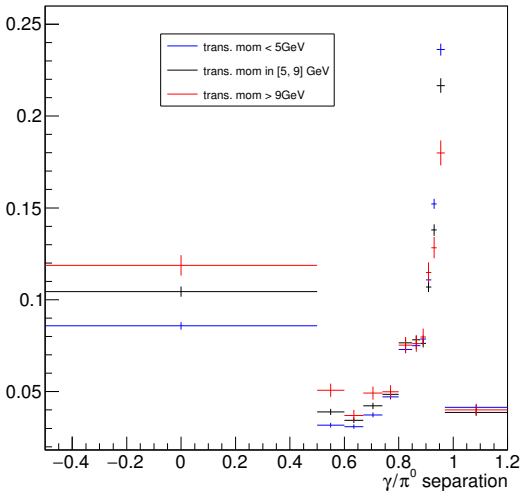

Figure 5.10: Comparison of the γ/π^0 variable distribution for different photon transverse energy bins. The fact that the distributions differ points out that binning in this variable is necessary. The data here corresponds to real $B^0 \to K^{*0}\gamma$ decays from the calibration samples.

With sufficiently large statistics, the distribution of the new, randomly-generated, γ/π^0 separation variable would match that of real data. The usage of this tool implies the loss of correlation to other variables than the particle E_{T} and the pseudo-rapidity, so its use has to be carefully cross-checked case by case.

5.3.1 Validation of the method for photons

As a first test of the validity of the method, the resampling of the calibration data sample is performed. Figure 5.11 shows the comparison between the original and resampled γ/π^0 separation distributions (for real data), with a high degree of compatibility. As a second test, the resampling of a $B^0 \to K^{*0}\gamma$ MC sample is performed using the histograms extracted from the calibration sample. Figure 5.12 shows the original MC variable, the resampled MC distribution and the the background-subtracted data distribution. The distribution of the resampled MC is similar to the data distribution, while the original MC distribution is not.

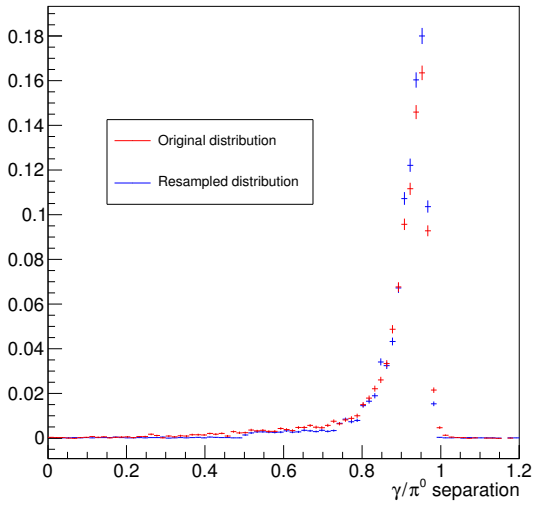

Figure 5.11: Comparison between the original (red line) and resampled (blue line) γ/π^0 separation variable for $B^0 \to K^{*0}\gamma$ data. The slight disagreement around 0.95 is related to the binning scheme, related to the low statistics from the calibration samples. The histograms are normalised to unity.

The resampling tool has been checked to be working also in other radiative channels by applying it to a background-subtracted data $B_s^0 \to \phi\gamma$ sample. The background-subtraction was performed by applying the sPlot method using the B_s^0 mass as discriminant. Figure 5.13 shows a comparison between the original γ/π^0 separation data distribution and the resampled one. The agreement is clear, which means that the tool could be used for different radiative channels.

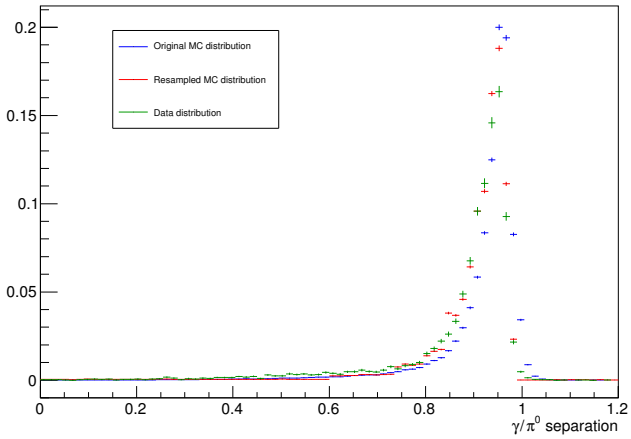

Figure 5.12: Comparison between the original MC γ/π^0 separation distribution (blue line), the resampled one (red line) and the data one (green line) for the case of the $B^0 \to K^{*0}\gamma$ decay. The differences between MC and data are attenuated when the resampling tool is applied.

Once checked that the method works successfully on a real data sample different than the calibration sample, the final test consists in the resampling of a MC $B_s^0 \to \phi\gamma$ sample. Figure 5.14 shows the original and the resampled MC distributions as well as the data distribution, so differences can be spotted. A satisfactory agreement between the resampled MC distribution and the data distribution can be seen. The good performance of the tool for both the $B^0 \to K^{*0}\gamma$ and the $B_s^0 \to \phi\gamma$ channels motivates the use of this tool for other radiative channels.

5.3.2 Validation of the method for neutral pions

The same steps as for the validation of the method for photons are followed. In this case, the alternative sample corresponds to a sWeighted $D^0 \to \pi\pi\pi^0$ sample from 2012 data.

Figure 5.15 shows the resampling of the calibration sample ($D^0 \to K\pi\pi^0$), where the resampled distribution matches the original one. Figure 5.15 shows the original and resampled distributions of the γ/π^0 variable for the alternative sample. The agreement between the two distributions is good and therefore confirms that the resampling tool works for neutral pions.

Figure 5.16 illustrates the mentioned disagreement between sWeighted selected data and MC samples for the $D^0 \to K\pi\pi^0$ and $D^0 \to \pi\pi\pi^0$ channels regarding the γ/π^0 variable, showing the need of the resampling of the MC variable to get a more accurate distribution. Due to the small size of the π^0 MC samples, no resampling for these MC samples is performed here.

As for the case of the efficiency table tool, different binning schemes for the calibration variables were tested, giving compatible results. The tool allows the user to select their own

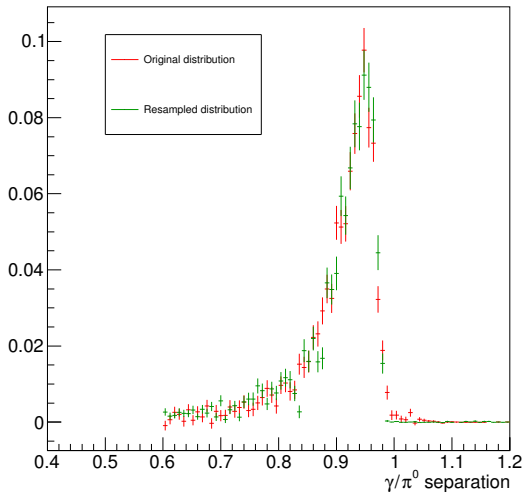

Figure 5.13: Comparison between an original data γ/π^0 separation distribution (red line) and a resampled one (green line) for a background-subtracted $B_s^0 \to \phi\gamma$ data sample distribution.

binning scheme, although a default one is available. Figure 5.17 shows the resampling of the real data γ/π^0 separation variable for different binning schemes, detailed in Table 5.7.

Table 5.7: Binning schemes shown in Fig. 5.17. The first option is the chosen as default one.

Binning Option	Transv. Mom. Bins	Pseudo-rapidity bins
Opt. 1	$[2600, 3700, 4320, 5180, 6300, 8607, 34751]$	$[1.5, 2.3, 2.8, 3.25, 4.7]$
Opt. 2	$[2600, 3700, 4320, 5180, 6300, 8607, 34751]$	$[1.5, 2.6, 2.9, 3.2, 4.7]$
Opt. 3	$[2600, 3700, 4320, 5180, 6300, 8607, 34751]$	$[1.5, 2.6, 3.0, 4.7]$
Opt. 4	$[2600, 3700, 4320, 5180, 6300, 8607, 34751]$	$[1.5, 2.2, 2.8, 3.3, 4.7]$
Opt. 5	$[2600, 3700, 4600, 5480, 6300, 8900, 34751]$	$[1.5, 2.3, 2.8, 3.25, 4.7]$

5.3.3 Limitations to the resampling tool

The resampling tool, as it has been shown throughout this section, has a good performance at describing the γ/π^0 separation variable for simulation samples, reaching a good agreement with data distributions making use of kinematic variables.

However, there exist limitations to the resampling tool. These limitations are related to the loss of correlation information between the calibration variables and the rest of variables and to the worse performance of the tool for small simulation samples, where

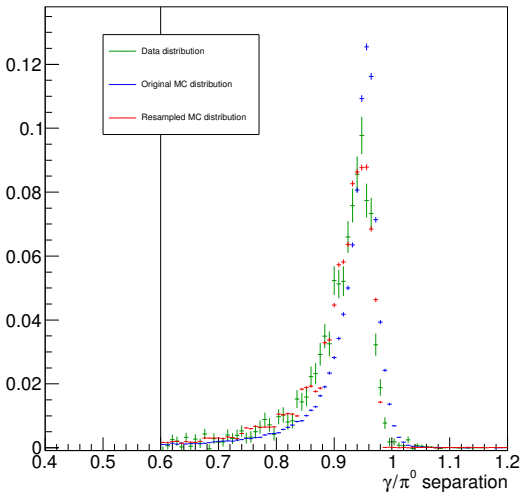

Figure 5.14: Comparison between an original γ/π^0 separation distribution (blue line), a resampled one (red line) and a background-subtracted $B_s^0 \to \phi\gamma$ data sample distribution (green line). There is a clear agreement between the data distribution and the resampled MC one. The vertical line at γ/π^0 separation $= 0.6$ corresponds to cut at offline level that cannot be avoided at data level. The MC has been cut accordingly.

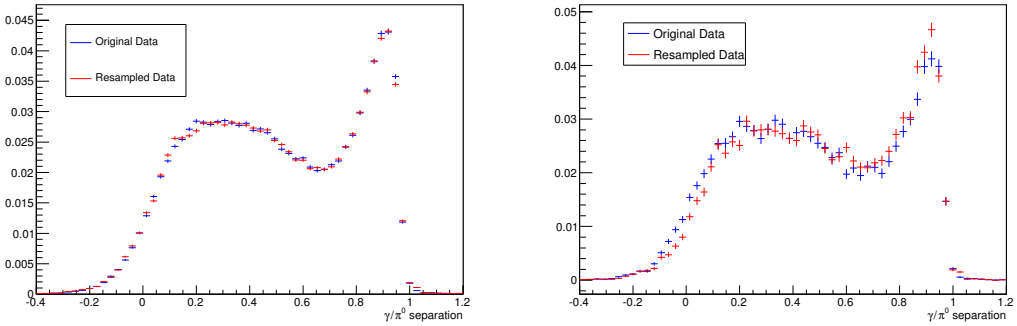

Figure 5.15: Comparison between an original γ/π^0 separation distribution (blue line) and the resampled one (red line) for the case of $D^0 \to K\pi\pi^0$ (left) and $D^0 \to \pi\pi\pi^0$ (right), where $D^0 \to \pi\pi\pi^0$ corresponds to the calibration sample.

the resampled γ/π^0 separation variable distribution may differ from the data one. Other limitations to take into account are the ones related to the possible differences in terms of the kinematics among the different decays and also the fact that using the sPlot technique implies the presence of peaking backgrounds events inside the signal region that could be treated as signal events.

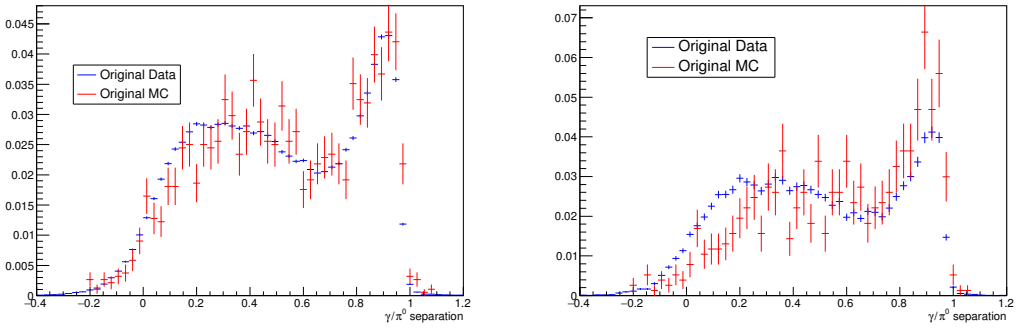

Figure 5.16: Comparison between the γ/π^0 separation distribution for a sWeighted selected data sample (blue line) and a MC sample (red line) for the case of the $D^0 \rightarrow K\pi\pi^0$ sample (left) and $D^0 \rightarrow \pi\pi\pi^0$ (right).

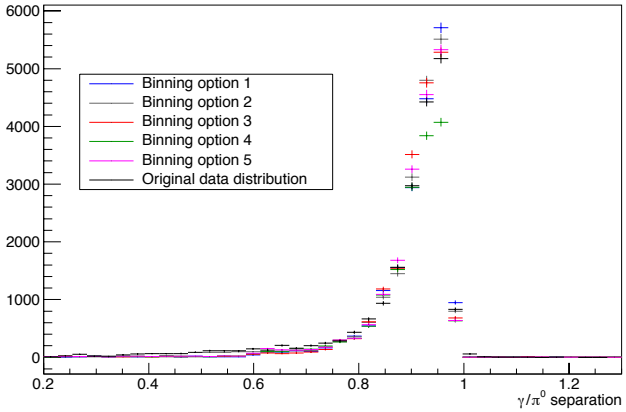

Figure 5.17: Distribution of the γ/π^0 separation variable (for photons) for different binning schemes tested for the two calibration variables using $B^0 \rightarrow K^{*0}\gamma$ data. The different colours correspond to the different schemes, that are fully explained in Table 5.7. The distribution related to the data calibration sample corresponds to the black points. The proposed scheme as default one corresponds to the blue points.

5.4 Conclusions

A tool for the γ/π^0 separation that makes use of the ECAL cluster shapes and information from the PS sub-detector has been introduced. Two different approaches are available for its calibration: the efficiency table tool, which provides an assignment of efficiencies as function of kinematic variables for MC events extracted from a sWeighted offline selected data sample and the resampling tool, which produces a new set of values for the γ/π^0 variable constructed from pure γ/π^0 samples obtained from Run 1 data variables.

6

Study of $b \to hh\gamma$ decays in Run 1

This chapter presents the study of the radiative decays $B^0 \to K^{*0}\gamma$, $B_s^0 \to \phi\gamma$ and $\Lambda_b^0 \to \Lambda^{*0}\gamma$ from data collected during the first run of the LHC. Its main goals are threefold: the measurement of the branching fraction of the $B_s^0 \to \phi\gamma$ decay through its ratio with $B^0 \to K^{*0}\gamma$, the first observation of the baryonic decay $\Lambda_b^0 \to \Lambda^{*0}\gamma$ and the measurement of its branching fraction normalized to $B^0 \to K^{*0}\gamma$, and the measurement of the *CP* asymmetry of the $B^0 \to K^{*0}\gamma$ and $\Lambda_b^0 \to \Lambda^{*0}\gamma$ modes.

The main concern of this analysis lies in the extraction of the signal yield for each of the three different decay modes. To do this, the line shape of the distributions of the selected B^0, B_s^0 and Λ_b^0 candidates has to be determined, including a complete description of the possible backgrounds that contaminate our samples.

The B^0, B_s^0 and Λ_b^0 candidates are reconstructed by the combination of an intermediate resonance, (K^*, ϕ or Λ^{*0}, respectively) and a photon. The resonance candidates are built from pairs of oppositely charged tracks: a kaon and a pion for the K^*, two kaons for ϕ and a kaon and a proton in the case of the Λ^{*0}. This resonance is then combined with a photon to build the b-candidate.

In the case of the K^* and ϕ resonances, a requirement on the invariant mass of the two tracks is applied around their corresponding measured mass, detailed in Table 6.1 (where the natural widths are also displayed).

Table 6.1: Mass and natural width of the K^* and ϕ resonances [4].

	Mass (MeV)	Natural width (MeV)
K^*	895.81 ± 0.19	47.4 ± 0.6
ϕ	1019.461 ± 0.019	4.266 ± 0.031

In the case of the Λ_b^0 decay, no requirement in the mass of the intermediate state is required so all the possible states are allowed to contribute. These states have different masses, spins and natural widths, and are expected to interfere with each other, making it impossible to precisely disentangle each single distribution without a dedicated amplitude analysis. Figure 6.1 shows the theoretically reconstructed Λ^{*0} resonances in terms of

the proton-kaon invariant mass, where the overlap between them can be observed [112]. Table 6.2 details the different observed Λ^{*0} decays into a proton-kaon pair.

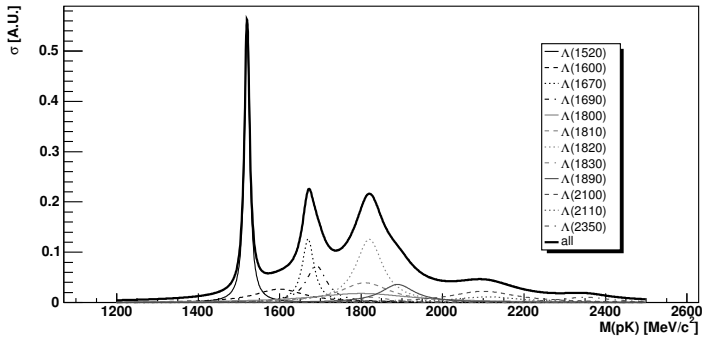

Figure 6.1: Approximate pK mass spectrum for $\Lambda_b^0 \to pK\gamma$ decays. Non-resonant contributions are neglected, as well as interference effects. The overlap between the many possible resonances is clear.

Table 6.2: List of observed Λ^{*0} decays into a proton-kaon pair. The Λ^{*0} spin is also included. Many of the observables have not been measured precisely and a range is reported.

	Mass (MeV)	Natural width (MeV)	Spin
$\Lambda^{*0}(1520)$ [113]	1519.5 ± 1.0	15.6 ± 1.0	3/2
$\Lambda^{*0}(1600)$ [113]	1560–1700	50–250	1/2
$\Lambda^{*0}(1670)$ [113]	1660–1680	25–50	1/2
$\Lambda^{*0}(1690)$ [113]	1685–1695	50–70	3/2
$\Lambda^{*0}(1710)$ [113]	1713 ± 13	180 ± 40	1/2
$\Lambda^{*0}(1800)$ [113]	1720–1850	200–400	1/2
$\Lambda^{*0}(1810)$ [113]	1750–1850	50–250	1/2
$\Lambda^{*0}(1820)$ [113]	1815–1825	70–90	5/2
$\Lambda^{*0}(1830)$ [113]	1810–1830	60–110	5/2
$\Lambda^{*0}(1890)$ [113]	1850–1910	60–200	3/2
$\Lambda^{*0}(2000)$ [113]	≈ 2000	-	1/2
$\Lambda^{*0}(2020)$ [113]	≈ 2020	-	7/2
$\Lambda^{*0}(2050)$ [113]	2056 ± 22	493 ± 60	3/2
$\Lambda^{*0}(2100)$ [113]	2090–2110	100–250	7/2
$\Lambda^{*0}(2110)$ [113]	2090–2140	150–250	5/2
$\Lambda^{*0}(2325)$ [114]	≈ 2325	-	3/2
$\Lambda^{*0}(2350)$ [113]	2340–2370	100-250	9/2

In order to cancel as many systematics as possible, especially those regarding the photon, the selections will be kept as close as possible. For a total cancellation of

the systematic effects, all the channels should have the same kinematics and the same topology. Unfortunately, and due to the different nature of the final state particles, this is not true in this case. The main differences to be spotted between the decays selections are:

- Different particle identification requirements since the final state particles are different for each channel.
- Different mass window requirements for the resonances due to the different natural widths for K^* and ϕ and the inclusion of all the possible Λ^{*0} cases.
- Different vertex reconstruction efficiency since the difference between the resonances masses and that for the final state particles is different for each channel and so will be the angle between the tracks.

The transverse energy (E_{T}) spectrum of the photon (as shown in Fig. 6.2) is very similar for the three channels and therefore the associated systematic uncertainty cancels out in the ratios for the same selection and reconstruction criteria for all the channels. For the case of the $\Lambda_b^0 \to \Lambda^{*0}\gamma$ only the $\Lambda^{*0}(1520)$ resonance is included.

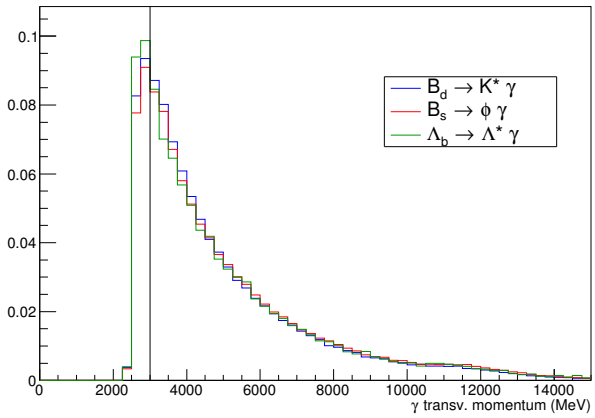

Figure 6.2: Transverse energy of the reconstructed MC photons for the signal decays. For the case of the $\Lambda_b^0 \to \Lambda^{*0}\gamma$ decay, only the $\Lambda^{*0}(1520)$ intermediate resonance is included. No differences above the 3 GeV, the critical region for the analysis, are observed.

6.1 Current theoretical and experimental status

Theoretical uncertainties are larger for exclusive radiative decays then for inclusive ones due to the need to include form factors. However, exclusive decays are easier to access in an experiment such as LHCb, and it is possible to find certain observables where the dependence on non-perturbative calculations is minimized. This is not true in the case of branching fractions, as shown in Table 6.3, where the current status of theoretical and

experimental results is detailed. No prediction for $\Lambda_b^0 \to \Lambda^{*0}\gamma$ exists and this decay has not yet been measured, nor any radiative decays of b-baryons, although studies on how to extract the photon polarisation from these decays have been carried out in the context of LHCb [112].

Table 6.3: Current theoretical prediction for the branching fractions for $B^0 \to K^{*0}\gamma$ and $B_s^0 \to \phi\gamma$ by Ali, Pecjak and Greub [1] and experimental results by the CLEO [115], BaBar [116], Belle [117, 118] and LHCb [3] collaborations.

	$B^0 \to K^{*0}\gamma$ ($\times 10^{-5}$)	$B_s^0 \to \phi\gamma$ ($\times 10^{-5}$)
Theory	4.3 ± 1.4	4.3 ± 1.4
CLEO	$4.55^{+0.72}_{-0.68} \pm 0.34$	-
BaBar	$4.47 \pm 0.10 \pm 0.16$	-
Belle	$4.01 \pm 0.21 \pm 0.17$	$5.7^{+1.8+1.2}_{-1.5-1.1}$
LHCb	-	3.5 ± 0.4

Regarding the direct $\mathcal{A}^{CP}$, it is expected to be small within the SM since these processes are double Cabibbo suppressed. No prediction is available for the $\Lambda_b^0 \to \Lambda^{*0}\gamma$, while the one for $B^0 \to K^{*0}\gamma$ [2] involves large uncertainties. Table 6.4 compares the theoretical prediction and experimental measurements.

Table 6.4: Current theoretical prediction for the $\mathcal{A}^{CP}$ for $B^0 \to K^{*0}\gamma$ by Matsumori, Sanda, and Keum [2] and experimental results by the CLEO [115], BaBar [116], Belle [117] and LHCb [3] collaborations.

	$\mathcal{A}^{CP}$ $(B^0 \to K^{*0}\gamma)$
Theory	$-(0.61 \pm 0.46)\%$
CLEO	$(8 \pm 13 \pm 3)\%$
BaBar	$(-1.6 \pm 2.2 \pm 0.7)\%$
Belle	$(-1.5 \pm 4.4 \pm 1.2)\%$
LHCb	$(0.8 \pm 1.7 \pm 0.9)\%$

6.2 Data samples and software versions

6.2.1 Data

The analysis is performed over data collected by the LHCb experiment during the whole Run 1, which covers the running period between March, 2011 to December, 2012. The total available integrated luminosity is of 3 fb^{-1}, of which 1 fb^{-1} were collected at a centre-of-mass energy of 7 TeV in 2011 and 2 fb^{-1} at 8 TeV in 2012 [87].

Collected data have been reprocessed using Reco14 version of the reconstruction configuration and the Stripping20 configuration of the stripping selection. Reconstruction

has been performed with BRUNEL and stripping with DAVINCI.

6.2.2 Monte Carlo simulation

Signal and background studies have been performed using simulated samples, corresponding to the MC2011 and MC2012 simulation campaigns, in both cases with a requirement on the photon transverse momentum to be greater than 1.5 GeV. In order to mimic as much as possible the running conditions of the bulk of data from 2011 and 2012, the mean number of visible interactions per crossing is set to $\nu = 2.0$ in the MC2011 series and to $\nu = 2.5$ in the MC2012 series, the centre-of-mass energy is set to 7 TeV and 8 TeV for 2011 and 2012, respectively. Moreover, different TCKs are used for each case (0x00790038 for $B^0 \to K^{*0}\gamma$ and $B_s^0 \to \phi\gamma$, 0x00760037 for $\Lambda_b^0 \to \Lambda^{*0}\gamma$ for MC2011 and 0x009f0045 for $B^0 \to K^{*0}\gamma$ and $B_s^0 \to \phi\gamma$ and 0x009f0045 for $\Lambda_b^0 \to \Lambda^{*0}\gamma$ for MC2012, respectively). Table 6.5 summarises the statistics of the simulated samples used in the analysis. The total number of events generated for the signal modes are 12,576,038, 12,554,506 and 17,141,849 for $B^0 \to K^{*0}\gamma$, $B_s^0 \to \phi\gamma$ and $\Lambda_b^0 \to \Lambda^{*0}\gamma$, respectively. For the different studies involving the simulation samples and whenever it corresponds, the proportion between MC2012 and MC2011 is the same as the one for the data collected in 2012 and 2011.

6.3 Event selection

The event selection of the signal decays is done in a series of steps, namely

- Trigger selection: data taken by the LHCb are filtered by the L0 and HLT trigger stages. Only the events that are selected by the trigger are stored.
- Stripping selection: data passing the trigger are reconstructed and selected to produce data samples for physics analyses. For this analysis, the radiative stripping stream is used.
- Offline loose selection: a set of loose requirements in topological and kinematical variables is applied to the data in order to reduce the background contamination while keeping as much signal as possible.
- Offline tight selection: a new set of requirements, much tighter this time, is applied to the data in order to achieve the largest possible signal significance. The events passing these requirements are the ones used for the analysis.

6.3.1 Trigger

The LHCb trigger, as explained before, is divided in different stages: L0, HLT1 and HLT2. The same requirements at L0 and HLT1 stages are demanded for the three signal channels, while the requirement on HLT2 is different for each of them.

Table 6.5: Statistics of the MC samples used in this study. Each of the samples is split in two halves of approximately the same size, corresponding to the two possible polarities of the magnet. The first section accounts for the signal decay channels while the second one accounts for the background channels. For all the cases Sim08 was used except for the $B^0 \to K^* \eta'$ decay, where Sim06 was used. The event type for each of the decays is also included.

	Number of events ($\times 10^6$)	Event Type
$B^0 \to K^{*0}\gamma$	12.6	11102202
$B_s^0 \to \phi\gamma$	12.6	13102202
$\Lambda_b^0 \to \Lambda^{*0}(1520)\gamma$	2.9	15102203
$\Lambda_b^0 \to \Lambda^{*0}(1670)\gamma$	5.1	15102228
$\Lambda_b^0 \to \Lambda^{*0}(1820)\gamma$	5.1	15102230
$\Lambda_b^0 \to \Lambda^{*0}(1830)\gamma$	5.1	15102240
$B^0 \to J/\psi\, K^{*0}$	2.0	11154001
$B^0 \to K_1^0\gamma$	1.5	11202602
$B^0 \to \rho^0\gamma$	2.9	11102222
$B^0 \to K\pi\pi^0$	1.5	11102432
$B_s^0 \to J/\psi\,\phi$	0.6	13144032
$B^+ \to D^{*0}\pi^+\pi^-\pi^0$	1.9	12265403
$B^+ \to \eta' K^+$	1.0	12203410
$B^+ \to K_1^+\gamma$	1.5	12203225
$B^+ \to K^*{}_2\gamma$	1.3	12203212
$B^+ \to K^{*+}\phi$	1.5	12103412
$B^+ \to \phi K^+\gamma$	3.1	12103202
$B^+ \to D^0\rho^+$	1.5	12165511
$B^+ \to K_1(1270)\eta$	3.1	12203410
$B^+ \to K^+K^-\pi^+\pi^0$	1.3	12103441
$B^+ \to K^+\pi^-\pi^+\pi^0$	1.5	12203203
$B^+ \to K^*\pi^+\gamma$	1.5	12203203
$B^+ \to \rho^+\rho^0$	1.2	12103401
$B^0 \to D^0(\to K^+K^-)\pi^0$	1.9	11162410
$B^0 \to D^0(\to K^+\pi^-)\pi^0$	1.9	11162400
$B^0 \to K^*\eta'$	0.9	11102441

Events are required to have a high transverse momentum photon. Therefore the L0Electron and L0Photon channels, which select events with an electromagnetic deposition in the ECAL with large transverse energy, are required (the L0Electron line is used since photons converted after the magnet are also used). The specific requirements for each of the L0 channels are included in Table 6.6 for 2011 and 2012. The additional L0PhotonHi and L0ElectronHi, with harder requirements on the photon, are also considered.

The decay products of the signal decays are the result of a b-decay and therefore are expected to have a high transverse momentum as well as a high impact parameter.

For this reason, the chosen HLT1 lines are Hlt1TrackAllL0 and Hlt1TrackPhoton single track lines: the former selects photons (L0Electron or L0Photon) with a hard cut on the required track while the latter is looser on the p_{T} of the track but requires a tighter cut on the E_{T} of the photon (L0ElectronHi or L0PhotonHi). This can be seen in Table 6.6.

Table 6.6: Transverse energy required on the ECAL deposition for the different L0 and HLT1 channels for 2011 and 2012. Values in parenthesis indicate that no explicit threshold is applied, but is a consequence of a previous cut.

	Photon E_{T} for 2011 (MeV)	Photon E_{T} for 2012 (MeV)	Track p_{T} (MeV)
L0Electron	2500	2600	-
L0Photon	2500	2600	-
L0ElectronH	4200	4200	-
L0PhotonH	4200	4200	-
Hlt1TrackAllL0	(2500)	(2600)	1700
Hlt1TrackPhoton	(4200)	(4200)	1200

The approach in HLT2 is different for the three signal channels. While there exist exclusive lines for the $B^0 \to K^{*0}\gamma$ and $B_s^0 \to \phi\gamma$ decays, there is none for the $\Lambda_b^0 \to \Lambda^{*0}\gamma$ one so the inclusive radiative topological lines are used (Table 6.8). However, the latter lines were not active for the whole Run 1 period, and therefore the integrated luminosity associated to this decay does not correspond to the previously mentioned 3 fb^{-1}. In this case, the integrated luminosity is 2.8 fb^{-1}. Table 6.7 details the luminosities for each year and magnet polarisation available for each of the decays. This implies an uncertainty in the branching fractions ratios, that will be discussed in the corresponding sections. All the HLT2 lines selected for the analysis are listed in Table 6.8.

Table 6.7: Available luminosity (in pb^{-1}) available for each of the signal decays due to the presence or absence of the HLT2 lines.

	2011		2012	
	MagUp	MagDown	MagUp	MagDown
$B^0 \to K^{*0}\gamma$	496 ± 22	610 ± 25	1015 ± 32	1053 ± 32
$B_s^0 \to \phi\gamma$	496 ± 22	610 ± 25	1015 ± 32	1053 ± 32
$\Lambda_b^0 \to \Lambda^{*0}\gamma$	310 ± 18	408 ± 20	1015 ± 32	1053 ± 32

The HLT2 trigger lines used for the $\Lambda_b^0 \to \Lambda^{*0}\gamma$ are actually two lines, since Hlt2RadiativeTopoPhotonL0 became Hlt2RadiativeTopoPhoton and Hlt2RadiativeTopoTrackTOS became Hlt2RadiativeTopoTrack in 2012. Both lines are designed for the selection of two oppositely charged tracks and a photon. However, Hlt2RadiativeTopoPhoton selects candidates with a hard photon and softer tracks,

Table 6.8: Chosen HLT2 lines for the three different signal channels. While there is an exclusive line for $B^0 \to K^{*0}\gamma$ and $B_s^0 \to \phi\gamma$, there is none for $\Lambda_b^0 \to \Lambda^{*0}\gamma$, which justifies the choice of four radiative topological lines for this channel.

Decay	HLT2 lines
$B^0 \to K^{*0}\gamma$	Hlt2Bd2KstGamma
$B_s^0 \to \phi\gamma$	Hlt2Bs2PhiGamma
$\Lambda_b^0 \to \Lambda^{*0}\gamma$	Hlt2RadiativeTopoTrack or Hlt2RadiativeTopoPhoton or Hlt2RadiativeTopoTrackTOS or Hlt2RadiativeTopoPhotonL0 or

whereas Hlt2RadiativeTopoTrack does the opposite. More details about these lines can be found elsewhere [119].

A triggered event is said to be TOS (Trigger On Signal) if the signal is the responsible for the triggerization of a given line. If, however, the reason for the event to have triggered is independent of the signal, that is, if the signal were to be removed the trigger line would fire anyway, the event is said to be TIS (Trigger Independent of Signal) in that line. These two possibilities are not exclusive, and an event can be both TIS and TOS if both the signal and the rest of the event could be responsible for the triggerization of the event. Similarly, an event can be TOB (Trigger On Both) if both the signal and the rest of the event are necessary for the triggerization. This characterization is used to better control the efficiencies by requiring that either the photon or the tracks candidates are explicitly involved in the event of the triggering at the L0, HLT1 and HLT2 stages by fulfilling the TOS requirement in each of the trigger stages.

6.3.2 Stripping

After the trigger stage, events are reconstructed and stripped centrally in order to keep the analyses computing time under control as well as the storage requirements. The Radiative stream is designed as a sum of lines, each performing an exclusive selection of a radiative b-decay. For this analysis, Stripping20r0 and Stripping20r1 have been used for 2012 and 2011 data, respectively. The specific lines used for this analysis are B2KstarGamma_B2VG, Bs2PhiGamma_B2VG and Lb2PKGammaLb2PKGamma for $B^0 \to K^{*0}\gamma$, $B_s^0 \to \phi\gamma$ and $\Lambda_b^0 \to \Lambda^{*0}\gamma$, respectively, with selection summarized in Tables 6.9 and 6.10

6.3.3 Loose preselection

A set of loose cuts is applied to the stripped sample in order to reduce the background while keeping as much signal as possible. The cut values are decided by comparison of the MC samples and the data sidebands, defined as the mass region separated from

Table 6.9: Stripping 20r0 and 20r1 selections for $B^0 \to K^{*0}\gamma$ and $B_s^0 \to \phi\gamma$. On the top, common cuts grouped by track cuts, photon cuts, vector resonance cuts with specific cuts for ϕ and K^* and B candidate cuts.

		S20r0 (2012)	S20r1 (2011)
Track χ^2		< 3	
Track χ^2_{IP}		> 16	
Track p_{T}	(MeV)	> 500	
Track p	(MeV)	> 5000	
Track Ghost Probability		< 0.5	< 0.4
At least 1 track with:			
Track χ^2		< 2.5	
Track IP	(mm)	> 0.1	
Track p_{T}	(MeV)	> 1000	
Photon E_{T}	(MeV)	> 2500	
Photon CL		> 0.25	
V meson p_{T}	(MeV)	> 500	
V meson p	(MeV)	> 3000	
V meson daughters DOCA	(mm)	< 0.5	
V meson daughters $\sum p_{\text{T}}$	(MeV)	> 1500	
V meson χ^2_{vtx}		< 9	
K^* ΔM_{PDG}	(MeV)	< 150	
ϕ ΔM_{PDG}	(MeV)	< 15	
B daughters $\sum p$	(MeV)	> 5000	
B daughters combined mass	(MeV)	$[4000, 7000]$	
B χ^2_{vtx}		< 9	
B χ^2_{IP}		< 9	
B DIRA	(mrad)	< 20	
B χ^2 $_{FD}$		> 81	

the b candidate nominal mass by more than 300 MeV for each of the channels. All these requirements are applied after the resampling of the γ/π^0 separation variable for the simulation samples using the resampling tool from Chapter 5. From now on, all distributions involving this variable will show the resampled value.

The following requirements are applied:

- Decay kinematics: Tracks impact parameter χ^2 (χ^2_{IP}), the photon energy, the b candidate flight direction, its flight distance χ^2, the isolation of the reconstructed vertex and the b candidate transverse momentum.

Table 6.10: Stripping 20r0p1 and 20r1 selections for $\Lambda_b^0 \to \Lambda^{*0}\gamma$ grouped by track cuts, photon cuts, resonance cuts, Λ_b^0 candidate cuts and PID cuts. As it can be seen, cuts for both Stripping versions are very similar.

		S20r0p1 (2012)	S20r1 (2011)
Track χ^2/ndf		< 3	
Track χ^2_{IP}		> 16	
K p_{T}	(MeV)	> 500	
K p	(MeV)	> 1000	> 3000
Track Ghost Probability		< 0.4	
p p_{T}	(MeV)	> 1200	
p p	(MeV)	> 10000	
Photon E_{T}	(MeV)	> 2500	
Photon CL		> 0.25	
Λ^{*0} mass window	(MeV)	< 2500	
Λ^{*0} vertex χ^2/ndf		< 9	
Λ^{*0} daughters $\sum p_{\text{T}}$	(MeV)	> 1500	
B daughters $\sum p_{\text{T}}$	(MeV)	> 5000	
B vertex χ^2/ndf		< 9	
B χ^2_{IP}		< 9	
cos(B candidate DIRA)		> 0.9998	
B mass	(MeV)	$[4000, 7000]$	
B χ^2 $_{FD}$		> 0.81	
K DLL$_{K\pi}$		> 5	
K DLL$_{K\pi}$- DLL$_{p\pi}$		> 0	
p DLL$_{p\pi}$		> 10	
p DLL$_{p\pi}$- DLL$_{K\pi}$		> 0	
Number of tracks		< 500	

- Neutral and charged electromagnetic clusters in the ECAL are separated based on their compatibility with extrapolated tracks [88]. The difference in likelihoods for the photon and other particles hypothesis are transformed into a confidence-level variable (CL) distributed in the range $[0, 1]$, defined as:

$$CL_\gamma = \frac{\tanh(\Delta \ln \mathcal{L}) + 1}{2}. \tag{6.1}$$

- Helicity angle of the decay, defined as the angle between the momentum of any of the daughters of the K^* (ϕ) and the momentum of the b-meson in the rest frame of the K^* (ϕ). This requirement is only used for the selection of the $B^0 \to K^{*0}\gamma$ and $B_s^0 \to \phi\gamma$ decays (since any angular momentum contribution from Λ^{*0} is allowed)

and its function is the discrimination of decays where a neutral pion is found in the final state instead of the photon. For the signal decay, the helicity angle is expected to follow a $\sin^2(\theta_H)$ function, while backgrounds where the γ is substituted by a π^0 would follow a $\cos^2(\theta_H)$ function.

- Fiducial cuts: They ensure the events to be completely contained within the LHCb geometry and include requirement on the tracks pseudorapidity, the PV position and the tracks momenta. An additional cut, key for the study of the $\mathcal{A}^{CP}$, is added in order to remove effects of the different polarities of the magnet at the data-taking period. The parameters for the requirement on the bending-plane momentum were optimized and used in previous LHCb analyses [120, 121] and the effect can be observed in Fig. 6.3 for kaons and in Fig. 6.4 for the pions in the $B^0 \to K^{*0}\gamma$ decay. The corresponding distributions for the $\Lambda_b^0 \to \Lambda^{*0}\gamma$ decay can be found in Fig. B.1 for kaons and in Fig. B.2 for protons. The effect is less clear in the case of protons due to the cut on momentum at stripping level.

Table 6.11 shows the specific values for the requirements, which are the same for all the channels, except for the cut on the helicity angle, which is not included in the $\Lambda_b^0 \to \Lambda^{*0}\gamma$.

Table 6.11: Pre-selection cuts grouped by track cuts, photon cuts, vector resonance cuts, B candidate cuts and fiducial cuts. These cuts are applied after the resampling of the MC sample γ/π^0 separation variable using the resampling tool.

		Preselection
Track χ^2_{IP}		> 20
Photon E_{T}	(MeV)	> 3000
Photon CL		> 0.25 and $\neq 0.5$
Photon/π^0 separation		> 0.4
V meson abs(cos(helicity))		< 0.9
B candidate p_{T}	(MeV)	> 1000
B candidate χ^2_{IP}		< 8
B isolation		< 0 or > 2
B flight distance χ^2		> 0
Fiducial cut on $\lvert p_x \rvert$	(MeV)	$\leq 0.317(p_z - 2400)$
Track η		[2, 4.5]
Track momentum	(GeV)	< 100
PV z	(mm)	[-100, 100]
B χ^2_{IP} *nextbest* (if PV > 1)		> 50

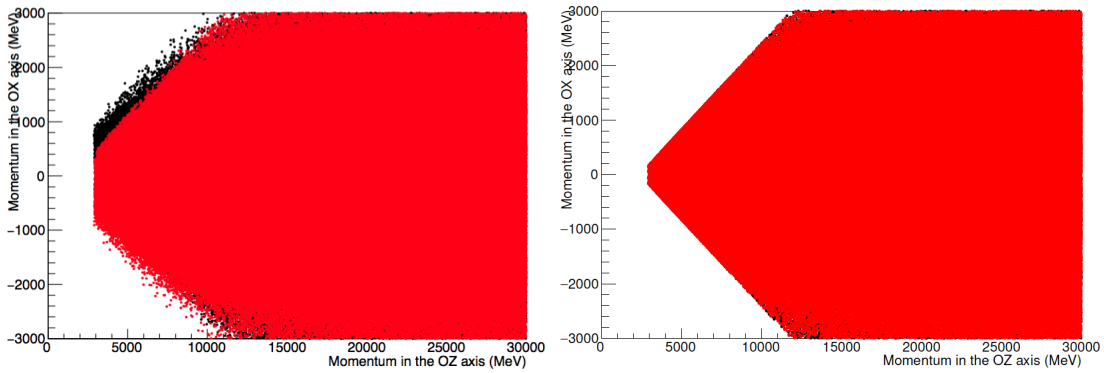

(a) Magnet Up.

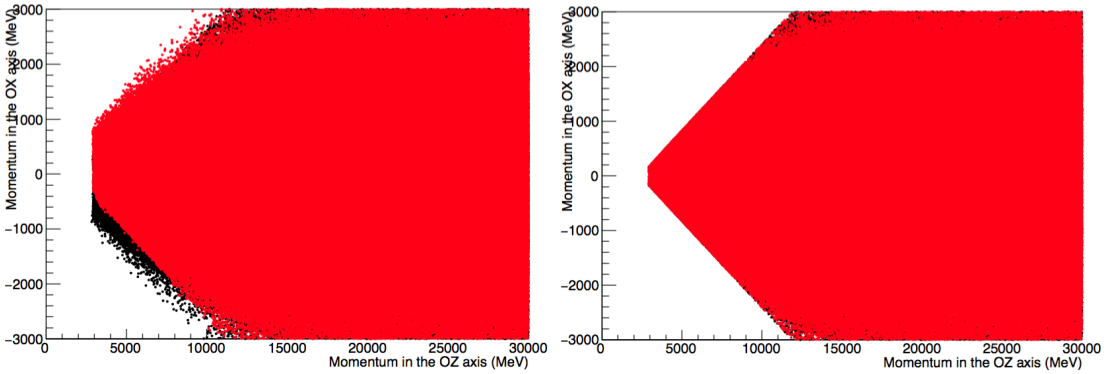

(b) Magnet Down.

Figure 6.3: p_z versus p_x distributions for the kaon candidate within the $B^0 \to K^{*0}\gamma$ decay before (left) and after (right) the fiducial cut included in the preselection. The artificial asymmetry, consequence of the different polarities for the LHCb magnet, can be seen. Black points correspond to events associated to a B^0 and red points correspond to those associated to a $\overline{B}^0$.

6.3.4 Tight offline selection

The tight offline selection involves the optimization of three different variables. These variables are the ones related to the particle identification (PID), to the isolation of the reconstructed vertex and to a multivariate discriminator built to reject combinatorial background. The PID and the variable used for combinatorial background rejection cut values are optimized simultaneously, while the isolation one is performed later, on its own.

Multivariate analysis

After the preselection, a multivariate analysis (MVA) method is used to separate signal and combinatorial background events. For the training, MC events are used as signal while data upper side-band events (defined as the region above 300 MeV from the nominal B mass) are used as background. To avoid biases, the samples are split into two by

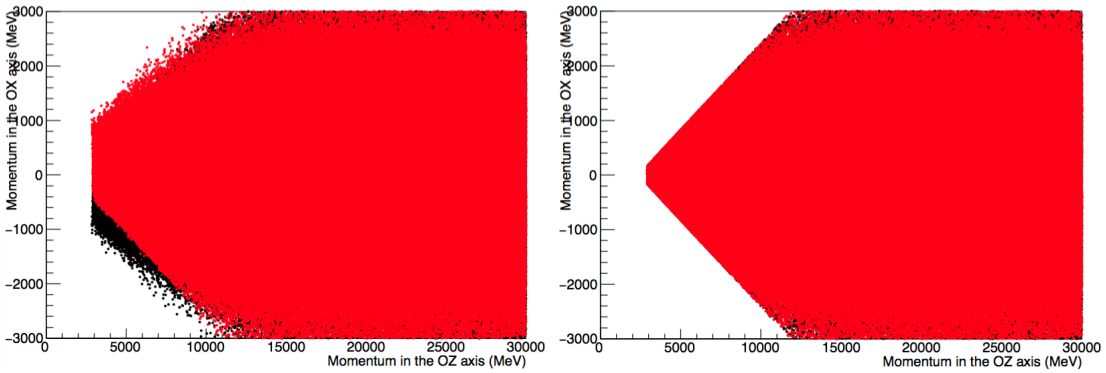

(a) Magnet Up.

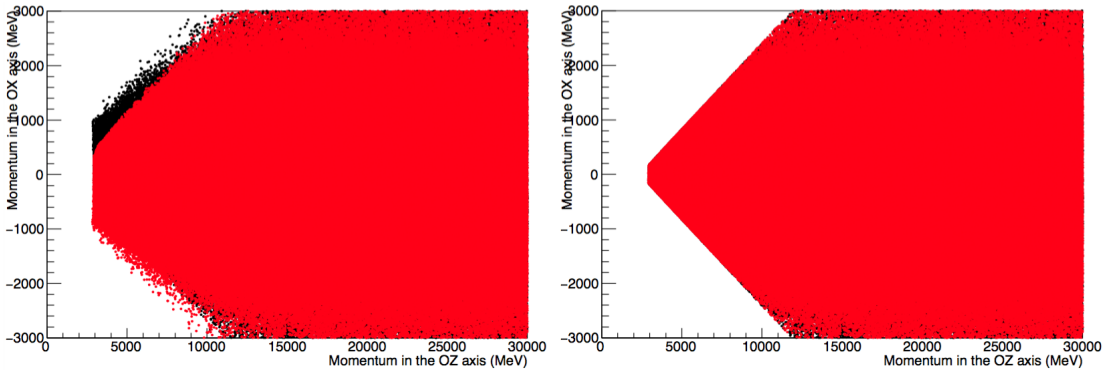

(b) Magnet Down.

Figure 6.4: p_z versus p_x distributions for the pion candidate within the $B^0 \to K^{*0}\gamma$ decay before (left) and after (right) the fiducial cut included in the preselection. The artificial asymmetry, consequence of the different polarities for the LHCb magnet, can be seen. Black points correspond to events associated to a B^0 and red points correspond to those associated to a $\overline{B}^0$.

means of a random number. One of the samples is used for training an MVA which is applied to the other half and vice versa. Different possibilities for the multivariate method were tested. The Boosted Decision Tree (BDT) is found to be the one giving highest signal efficiency for the same background rejection, as it can be seen in Fig. 6.5. Figure 6.6 shows the output of the BDT, where it is possible to see the discrimination between signal (blue) and background (red).

The use of a MVA method is restricted to the $B^0 \to K^{*0}\gamma$ and $B_s^0 \to \phi\gamma$ modes due to two different reasons. Firstly, the number of events in the upper side-band for the Λ_b^0 reconstructed invariant mass is too low to perform a good training of the BDT and, secondly, the contribution for the different intermediate resonances is unknown, which complicates the training process since the proportion of each of the simulation samples for each of the resonances is not known.

Choice of variables: As a first step, all variables related to kinematic and topological properties are used for the training of the BDT. This gives a total of twenty initial variables

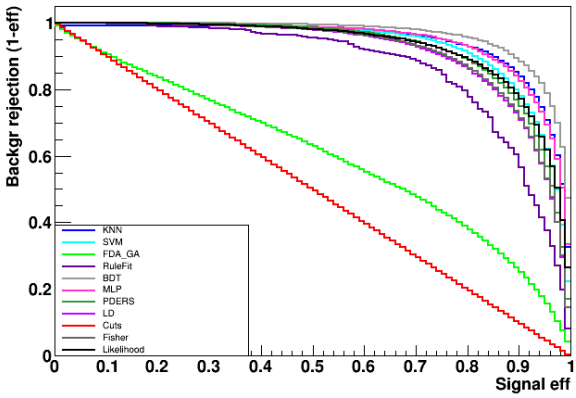

Figure 6.5: ROC curve for the different multivariate analysis methods considered. The Boosted Decision Tree is seen to give the best performance in terms of the signal efficiency vs. background rejection.

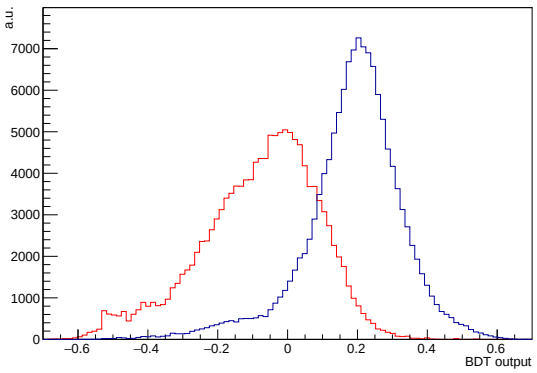

Figure 6.6: BDT output in the case of the $B_s^0 \to \phi\gamma$ mode, with clear discrimination for signal (blue) and background (red). The corresponding one for $B^0 \to K^{*0}\gamma$ is equivalent.

including the momentum (p) and transverse momentum (p_{T}) of the two tracks, the vector resonance and the b-hadron, the χ^2 of the impact parameter (IP) of the tracks, the vector resonance and the B mother with respect to the primary vertex, the track reconstruction χ^2, the χ^2 of the secondary vertex (SV) fit, the direction angle (DIRA, defined as the angle between the direction of the momentum of the reconstructed b-hadron and the direction defined by the primary and secondary vertices), the helicity angle of the vector resonance, the flight distance (FD) of the b-hadron before decaying and the isolation of the decay.

In order to simplify the BDT, a reduction of the number of the variables used in the training is performed. The variables are removed one by one in an iterative fashion: the one with the smallest contribution (given by the BDT algorithm itself) to the BDT

performance is removed and the BDT is re-trained. This process is done iteratively until the BDT shows a significant worsening of the ROC curve. The final variables for each channel are shown in Table 6.12. The only different variables from those used for the loose preselection are the track χ^2, which is related to the goodness of the track reconstruction, the intermediate state $\chi^2_{\rm IP}$ to ensure it is incompatible with primary vertices and the tracks and intermediate states $p_{\rm T}$, which are expected to be large for signal tracks.

Table 6.12: Variables used for the BDT training for each channel ordered according to their discriminating power.

$B^0 \to K^{*0}\gamma$	$B^0_s \to \phi\gamma$
K^* $\chi^2_{\rm IP}$	min($\chi^2_{\rm IP}$)
B $p_{\rm T}$	B $p_{\rm T}$
K^* $p_{\rm T}$	min(track $p_{\rm T}$)
log(B FD χ^2)	B p
K^* p	log(B FD χ^2)
B p	min(track χ^2)
min(track $\chi^2_{\rm IP}$)	min(track p)
max(track χ^2)	
min(track χ^2)	
K^* helicity	

Particle Identification (PID)

The three channels studied in this analysis have a very similar topology: in all of the three final states there are two oppositely charged tracks and a photon.

Therefore, the ability to correctly tell what particles the tracks correspond to acquires great importance. This analysis makes use of PID variables based on information collected by different sub-detectors and combined through a neutral net (NN). These variables, called ProbNNX, give a probability that the corresponding track is of the type X.

These variables can be combined in multiple ways to create new variables in order to give a better performance in terms of signal efficiency and background rejection. Within the Radiative Decays sub-WG, a detailed study about which variable to use for each of the particles has been developed, making use of the PID signal efficiency tables provided by the PIDCalib package. The study [122] consisted on testing the different ProbNN and DLL PID variable combinations on offline selected simulated samples by applying the PIDCalib PID efficiency tables and computing the signal efficiency and background rejection for each variable combination for many different requirement values. All the calculated performances are compared in a graph (like 6.7) and the combination of variables giving the best performance (in terms of signal efficiency vs. background rejection) is the selected one for the PID selection.

Figure 6.7 shows how the different combinations perform in terms of signal efficiency and background rejection in the case in which the best variable for kaon selection is sought (the plots corresponding to the pion and proton selection can be found in B.3 and B.4, respectively. Table B.1 details the correspondence between the variables and the markers in the plots.). The samples used for these studies correspond to offline selected (from Table 6.13) MC-true samples to which weights extracted from the PIDCalib package have been applied. The optimal combination of variables is chosen by selecting that with the largest signal efficiency and with largest background rejection. As shown in Fig. 6.7, the variable combinations are studied separately for each type of possible mis-identification (in this case, pions and protons). Due to the large production of pions at LHCb, these particles will be the main source of background for the selection of kaons and protons, while kaons will constitute the main source of background for the pion selection. This means that if more than one variable gives a good performance, the one rejecting the larger amount of pions should be the one to choose.

The conclusion of these performance studies is that the variables to use are: ProbNNk variable for kaon selection, ProbNNpi*(1-ProbNNk)*(1-ProbNNp) for pions and ProbNNp*(1-ProbNNk)*(1-ProbNNpi) for protons.

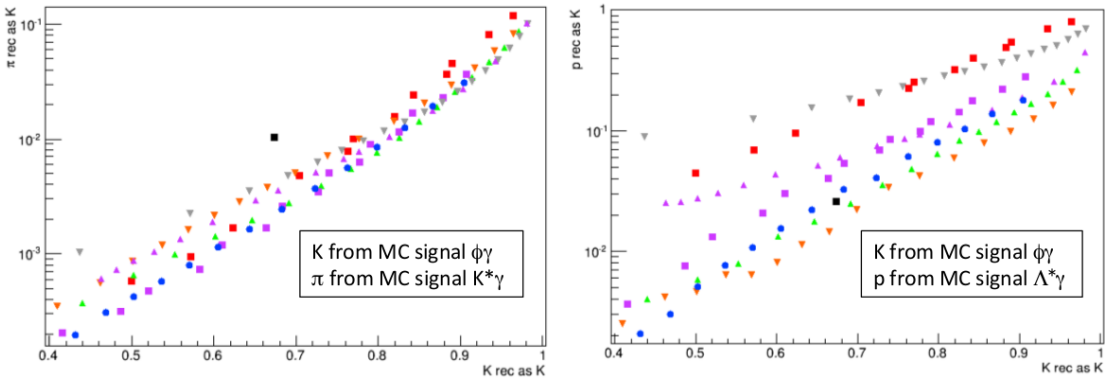

Figure 6.7: Different combinations of PID variables and their performance in terms of signal efficiency and background rejection, in the case of kaon selection (π rejection for the plot on the left and proton rejection for the plot on the right). It can be seen that the best variable for this case is the one represented by green triangles, which corresponds to the variable *ProbNNk*.

Tight offline selection optimization

The optimization of the tight offline selection consists of finding the requirement value for which the figure of merit (FOM) [123]:

$$FOM = S/\sqrt{S+B} \tag{6.2}$$

is maximised, where S (B) is the number of signal (background) events that pass the cuts. This maximisation of the FOM is performed over the events that fall within $\pm$300 MeV of the b-hadron nominal mass (which is defined as *signal region*).

Table 6.13: Offline selection used for the PID studies.

Track χ^2_{IP}		> 25
Max track p_{T}	(MeV)	> 1200
Min track p_{T}	(MeV)	> 500
V meson isolation		< 0 or > 2
V meson χ^2_{vtx}		< 9
Photon E_{T}	(MeV)	> 3000
Photon CL		> 0.25 and $\neq 0.5$
Photon/π^0 separation		> 0.6
B candidate p_{T}	(MeV)	> 3000
B candidate χ^2_{IP}		< 9
B candidate DIRA	(mrad)	< 20
B candidate FD χ^2		> 100

The way the optimization works is the following: cuts on each of the tracks PID variables and on the BDT variable are applied at the same time and a fit to the b-hadron reconstructed invariant mass is performed. This fit includes contributions from the other channels involved in the analysis and from generic missing-pion and missing-kaon contributions, as well as a component to model the combinatorial background. For each of these sets of cuts, the correspondent fit gives as output a value for the signal and background yields in the signal region. From them, the value of the FOM can be computed and the set of cuts giving the highest value of the FOM is the one chosen.

For the case of the Λ_b^0 decay, since there is no BDT applied, the process is simpler. The set of variable in this case consists only of the cut on the PID variable. Apart from that, the whole procedure is the same: different cuts on the PID variable are applied, the FOM is computed and the PID cut that corresponds to the largest value of the FOM is the value that is kept for the selection. Figure 6.8 shows the fitted invariant mass distribution for the signal channels for the BDT and PID values that maximise the FOM.

To avoid possible biases due to statistical fluctuations, the samples are divided in a random fashion in two sub-samples before the optimization. The same set of cuts for each of the sub-samples is found to be the optimal for each of the channels.

Isolation

The isolation variable describes how other particles in the event are compatible with the signal vertex by looking at the change of the χ^2_{vtx} when adding an extra track. For a good isolation, the minimal variation of the χ^2_{vtx} must be large. This variable is very useful for the rejection of partially reconstructed backgrounds.

The way the isolation variable is optimized is the same than for the previous scenario:

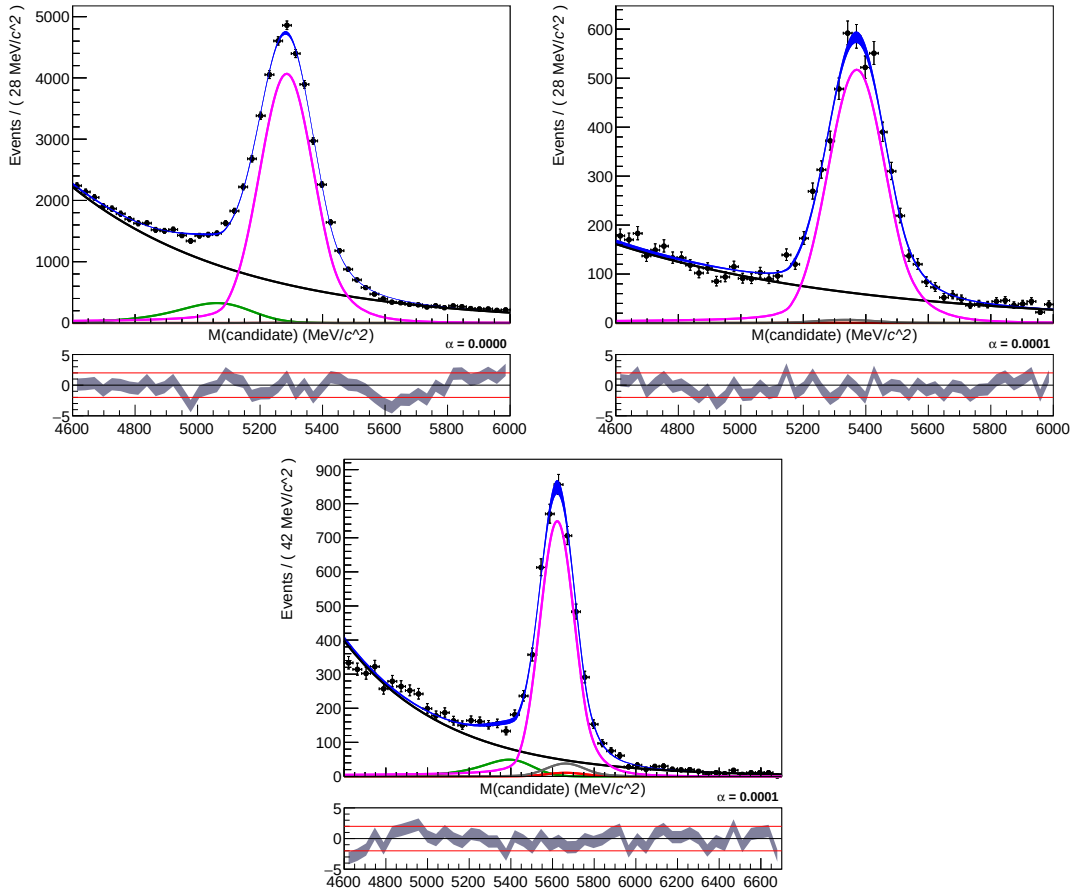

Figure 6.8: Fit to the invariant mass distribution for the $B^0 \to K^{*0}\gamma$ (top left), $B_s^0 \to \phi\gamma$ (top right) and $\Lambda_b^0 \to \Lambda^{*0}\gamma$ (bottom) for the BDT and PID values that maximise the FOM. The blue curve describes the total fit, the pink curve describes the signal contribution, modeled by a double crystal ball; the red and gray curves describe the cross-feed background, also modeled with double crystal balls; the black curve describes the combinatorial background, modeled by an exponential function and the green curve describes a generic contribution for a partially reconstructed background where a pion has been lost, modeled by the convolution of an ARGUS function and a Gaussian function.

different values for the isolation variable are tried, computing the value of the FOM for each of them, with the data sample split it two. The isolation variable cut value giving the largest value for the FOM is the one kept for the final selection. Again, the maximisation of the FOM is performed over the events that fall within ± 300 MeV of the b-hadron nominal mass.

Multiple Candidates

The presence of multiple candidates in the data samples at this point of the analysis is found to be very different among each of the signals:

- For the B^0 decay, there is a total of 0.91% multiple candidates,
- For the B_s^0 decay, there is a total of 0 multiple candidates in the available sample,
- For the Λ_b^0 decay, there is a total of 0.02% multiple candidates,

where the multiplicity is always two. It was checked that the candidates multiplicity corresponds to $\sim 90\%$ of cases to *reflection*, where the two tracks are mis-identified with each other. Because this is the main source of multiple candidates, it is the only one taken into account when dealing with them.

Due to the very low amount of multiple candidates in the B_s^0 and Λ_b^0 samples, only the ones in the B^0 sample are dealt with. Many different approaches were tried, including selecting a random candidate and leave the other one out, selecting the candidate giving the best agreement for the b-hadron direction and the segment linking the primary and the secondary vertex and using different possibilities making use of the tracks PID. Finally, it was decided to make use of the PID to get rid of the multiple candidates: the candidate to keep is the one where the product of the selected particles PID value is larger than the product of the mis-identification of the tracks.

6.3.5 Final selection

The different selection steps detailed previously conform the final offline selection for the three signal channels, that can be summarized in Table 6.14. Fiducial cuts, to ensure the events to be contained within the LHCb acceptance, are implemented.

6.4 Signal shape

Using MC2012 samples, the shape of the mass peaks for B^0, B_s^0 and Λ_b^0 has been studied. In the three cases, a double-tail Crystal Ball PDF [124] is used with one tail at each side

Table 6.14: Final offline selections for the $B^0 \to K^{*0}\gamma$, $B_s^0 \to \phi\gamma$ and $\Lambda_b^0 \to \Lambda^{*0}\gamma$ decays. The trigger cuts are not included. For the B^0 decay, the cut on PID that helps to get rid off the multiple candidates is not included either.

		$B^0 \to K^{*0}\gamma$	$B_s^0 \to \phi\gamma$	$\Lambda_b^0 \to \Lambda^{*0}\gamma$
Tracks cuts				
$\chi^2_{\rm IP}$		> 20	> 20	> 20
Photon cuts				
$p_{\rm T}$	(MeV)	> 3000	> 3000	> 3000
CL			> 0.25 and $\neq 0.5$	
γ/π^0 separation		> 0.4	> 0.4	> 0.4
Intermediate resonance				
Absolute value for Helicity		< 0.9	< 0.9	-
***b*-hadron cuts**				
$p_{\rm T}$	(MeV)	> 1000	> 1000	> 1000
$\chi^2_{\rm IP}$		< 8	< 8	< 8
Flight distance χ^2		> 0	> 0	> 0
$\Delta\ \chi^2_{\rm VS}$ (isolation)		> 2	> 2	> 4
PID cuts				
Kaon PID		> 0.1	> 0.1	> 0.05
Pion PID		> 0.05	-	-
Proton PID		-	-	> 0.25
BDT cut				
BDT		> -0.025	> 0.025	-
Fiducial cuts				
Tracks pseudo-rapidity		$[2, 4.5]$	$[2, 4.5]$	$[2, 4.5]$
Max track p	(GeV)	< 100	< 100	< 100
PV z	(mm)	$[-100, 100]$	$[-100, 100]$	$[-100, 100]$
B $\chi^2_{IP,nextbest}$ (if nPVs > 1)		> 50	> 50	> 50

of the Gaussian core[1]:

$$\mathrm{CB}(m;\mu,\sigma,\alpha_L,n_L,\alpha_R,n_R) = \begin{cases} A_L\left(B_L - \dfrac{m-\mu}{\sigma}\right)^{-n_L} & \text{for } \dfrac{m-\mu}{\sigma} \leq -\alpha_L, \\ \exp\left\{-\dfrac{(m-\mu)^2}{2\sigma^2}\right\} & \text{for } -\alpha_L < \dfrac{m-\mu}{\sigma} < \alpha_R, \\ A_R\left(B_R + \dfrac{m-\mu}{\sigma}\right)^{-n_R} & \text{for } \dfrac{m-\mu}{\sigma} \geq \alpha_R, \end{cases} \tag{6.3}$$

[1]In the low mass region, possible losses in the photon energy due to the fiducial volume of the calorimeter are accounted for by one of the Crystal Balls. The tail at high masses can be partially explained by the spread in the error of the reconstructed b-candidate, as it has been observed by other LHCb analyses [125, 126] and the pile-up present. Another contribution to the high mass tail is the observed correlation between events in the high invariant mass and events with large error on the B mass.

where $\alpha_{L(R)} > 0$ and

$$A_i = \left(\frac{n_i}{|\alpha_i|}\right)^{n_i} \exp\left\{-\frac{|\alpha_i|^2}{2}\right\}, \qquad B_i = \frac{n_i}{|\alpha_i|} - |\alpha_i|, \tag{6.4}$$

The parameters $n_{L(R)}$ and $\alpha_{L(R)}$ are extracted from a fit to MC samples and then fixed for the fit to data, while the μ and σ are allowed to float. Table 6.15 summarizes the parameters as extracted from the fits to the $B^0 \to K^{*0}\gamma$, $B_s^0 \to \phi\gamma$ and $\Lambda_b^0 \to \Lambda^{*0}\gamma$ MC2011 and MC2012 samples so it is possible to compare the fitted values (the μ and σ values are not required to be compatible since they will be fitted in the fit to the data). The values for MC2012 are taken for the fit to the data due to the larger amount of data events in the 2012 data sample than in the 2011 one. Figures 6.9, 6.10, 6.11, correspond to the fits to the MC2012 samples for $B^0 \to K^{*0}\gamma$, $B_s^0 \to \phi\gamma$ and $\Lambda_b^0 \to \Lambda^{*0}\gamma$, respectively.

Table 6.15: Fit results for $B^0 \to K^{*0}\gamma$, $B_s^0 \to \phi\gamma$ and $\Lambda_b^0 \to \Lambda^{*0}\gamma$ (using the $\Lambda^{*0}(1520)$ resonance since it is the one expected to give the largest yield) for MC2011 (top) and MC2012 (bottom) samples.

	$B^0 \to K^{*0}\gamma$	$B_s^0 \to \phi\gamma$	$\Lambda_b^0 \to \Lambda^{*0}\gamma$
μ (MeV)	5291.69 ± 0.61	5379.86 ± 0.61	5630.81 ± 1.20
σ (MeV)	96.23 ± 0.58	98.85 ± 0.57	98.29 ± 1.15
α_L	2.391 ± 0.046	2.35 ± 0.04	2.36 ± 0.07
α_R	-1.5245 ± 0.047	-1.75 ± 0.06	-1.63 ± 0.10
n_L	0.871 ± 0.098	0.79 ± 0.08	0.90 ± 0.12
n_R	7.8 ± 1.1	4.2 ± 0.6	7.6 ± 2.0
μ (MeV)	5275.04 ± 0.47	5364.67 ± 0.54	5619.0 ± 1.8
σ (MeV)	85.74 ± 0.43	86.18 ± 0.51	87.3 ± 1.7
α_L	2.459 ± 0.035	2.363 ± 0.035	2.31 ± 0.11
α_R	-1.4824 ± 0.032	-1.5223 ± 0.041	-1.509 ± 0.13
n_L	0.661 ± 0.059	0.643 ± 0.053	0.88 ± 0.17
n_R	5.42 ± 0.42	5.38 ± 0.53	8.3 ± 1.8

6.5 Background description

The invariant mass distributions, even after the whole offline selection contain a non-negligible amount of background contamination. These backgrounds can be divided in different groups:

- Peaking backgrounds: Candidates from b-hadron decays with a very similar topology as the signal up to some mis-identification. Cross-feed backgrounds are a special

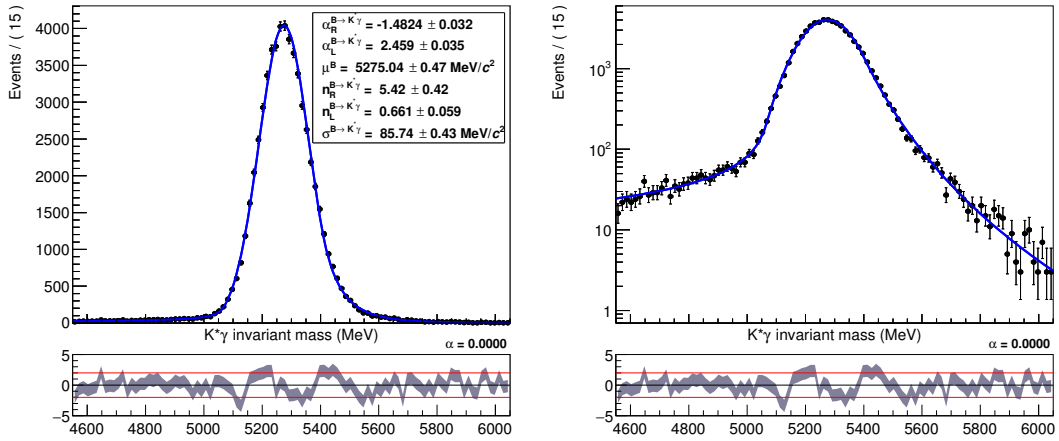

Figure 6.9: The $B^0 \to K^{*0}\gamma$ signal in the full sample fitted with a double Crystal Ball PDF.

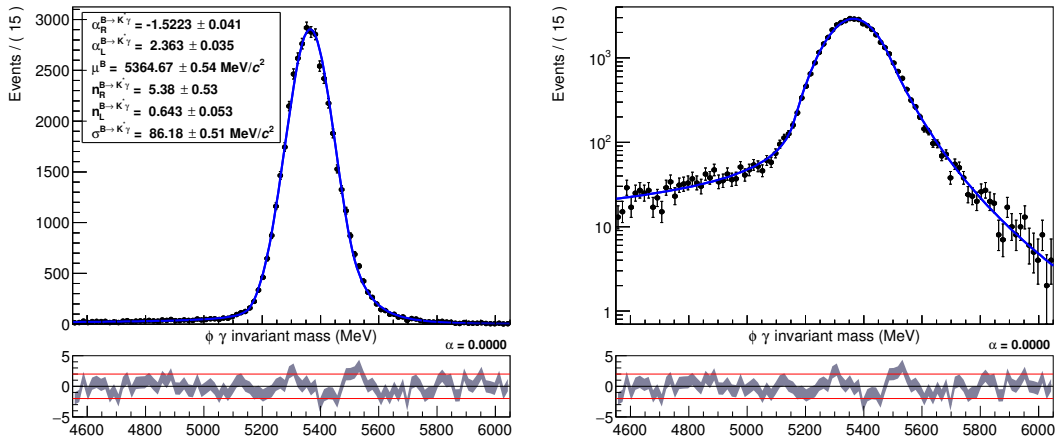

Figure 6.10: The $B_s^0 \to \phi\gamma$ signal in the full sample fitted with a double Crystal Ball PDF.

case of peaking backgrounds, where events from one signal channel are mis-identified as background of the other signal channels.

- Combinatorial background: This type of background is related to those cases in which the three final state particles (*i.e.*, the two tracks and the photon) are not actually the result of a b-hadron decay but in which the topological requirements are still satisfied.

- Partially reconstructed background: This type of background contains those decays ob b-hadrons for which tone of more final state particles have not been reconstructed, mimicking the signal topology.

Simulated samples for different background decays are studied (see Table 6.16). The

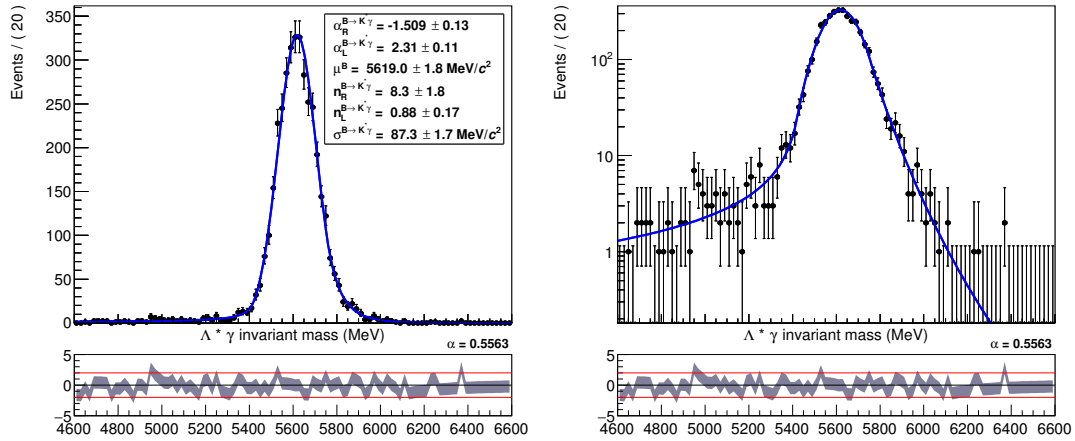

Figure 6.11: The $\Lambda_b^0 \to \Lambda^{*0}\gamma$ signal in the full sample fitted with a double Crystal Ball PDF.

relative contamination from each of these background decays is computed as the ratio between the expected number of events for these decays and the expected number of events for the signal decays:

$$C_{\text{bkg}} \equiv \frac{N_{\text{bkg}}}{N_{\text{sig}}} = \frac{f_{\text{bkg}}}{f_{\text{sig}}} \frac{\mathcal{B}_{\text{bkg}}}{\mathcal{B}_{\text{sig}}} \frac{\epsilon_{\text{bkg}}}{\epsilon_{\text{sig}}}, \tag{6.5}$$

where $\mathcal{B}$ $(B \to X)$ is the total branching fraction for the whole decay chain, f_X is the fragmentation factor (f_d for the B^0 decay, f_s for the B_s^0 decay and f_Λ for the Λ_b^0 decay) and ϵ corresponds to the total selection efficiency. The different fragmentation factors are used via their ratios, and their values [127], detailed in Eq. 6.6, are considered to be constant, due to the low number of events present at large momentum.

Background channels will be considered negligible if the expected contamination is under 0.1%. Table 6.16 shows the studied background channels and whether they can be considered as relevant or negligible.

$$\begin{aligned} f_s/f_d &= 0.267^{+0.021}_{-0.020} \\ f_s/(f_u + f_d) &= 0.134 \pm 0.004^{+0.011}_{-0.010} \\ f_{\Lambda_b^0}/(f_u + f_d) &= (0.404 \pm 0.017 \pm 0.027 \pm 0.105(Br^2)) \\ &\quad \times [1 - 0.031 \pm 0.004 \pm 0.003 \times p_{\text{T}}(\text{ GeV})] \end{aligned} \tag{6.6}$$

The offline selection largely reduces the number of relevant backgrounds. In addition, in the case of the Λ_b^0 decay, most of the studied channels are negligible due to the mass difference between any of the final state particles involved in those channels and the

[2]Br reflects an absolute scale uncertainty due to the the poor knowledge of the $\Lambda_c^+ \to pK\pi$ decay branching fraction.

Table 6.16: List of decay channels studied for the background description. It is also listed if they are to be considered negligible (N) or relevant (in this case the value for the contamination is included) for each of the different signal channels. As the table points out, some of the simulated samples were not available (marked by -).

Decay Channel	$B^0 \to K^{*0}\gamma$	$B_s^0 \to \phi\gamma$	$\Lambda_b^0 \to \Lambda^{*0}\gamma$
$B^0 \to J/\psi\, K^{*0}$	N	N	N
$B^0 \to K_1^0\gamma$	$(8.15 \pm 0.15)\%$	$(2.23 \pm 0.21)\%$	$(0.36 \pm 0.07)\%$
$B^0 \to \rho^0\gamma$	$(1.40 \pm 0.06)\%$	N	N
$B^0 \to K\pi\pi^0$	$(0.25 \pm 0.03)\%$	$(0.18 \pm 0.06)\%$	-
$B_s^0 \to J/\psi\,\phi$	N	N	N
$B^+ \to D^{*0}\pi^+\pi^-\pi^0$	N	N	N
$B^+ \to \eta' K^+$	N	N	N
$B^+ \to K_1^+\gamma$	$(12.98 \pm 0.26)\%$	$(1.27 \pm 0.16)\%$	-
$B^+ \to K_2^*\gamma$	$(1.54 \pm 0.07)\%$	N	N
$B^+ \to K^{*+}\phi$	N	N	-
$B^+ \to \phi K^+\gamma$	N	$(0.83 \pm 0.13)\%$	$(0.19 \pm 0.01)\%$
$B^+ \to D^0\rho^+$	$(4.87 \pm 0.12)\%$	$(7.37 \pm 0.37)\%$	-
$B^+ \to K_1(1270)\eta$	N	N	-
$B^+ \to K^+K^-\pi^+\pi^0$	N	N	-
$B^+ \to K^+\pi^-\pi^+\pi^0$	N	N	-
$B^+ \to K^*\pi^+\gamma$	N	N	-
$B^+ \to \rho^+\rho^0$	$(1.63 \pm 0.07)\%$	N	-
$B^0 \to D^0(\to K^+K^-)\pi^0$	-	-	N
$B^0 \to D^0(\to K^+\pi^-)\pi^0$	-	-	N
$B^0 \to K^*\eta'$	$(2.04 \pm 0.03)\%$	N	-
$B_s^0 \to \phi\pi^0$	-	(see text)	-

proton mass (present in the final state of the Λ_b^0 decay) making the reconstructed invariant mass for the decay to be far away from the signal region.

Cross-feed backgrounds are modeled with double tailed Crystal Ball functions, with shape parameters extracted from fits to simulation. Figures 6.12, 6.13, 6.14 show the fit to the cross-feed backgrounds to $B^0 \to K^{*0}\gamma$, $B_s^0 \to \phi\gamma$ and $\Lambda_b^0 \to \Lambda^{*0}\gamma$, respectively, with the obtained shape parameters detailed in Table 6.17.

The combinatorial background is described by different functions for the meson and the baryon channels since the use of the multivariate tool reduces their presence to a level in which the usage of an exponential to describe them is very unstable. In the case of the Λ_b^0 decay, no multivariate tool is used so the combinatorial background is expected to be larger than for other channels. In this case, an exponential function is used. The polynomial function used for the meson channels and the exponential function for the

Table 6.17: Fitted parameters for the cross-feed contamination for the signal channels.

		$B^0 \to K^{*0}\gamma$	$B_s^0 \to \phi\gamma$	$\Lambda_b^0 \to \Lambda^{*0}\gamma$
$B^0 \to K^{*0}\gamma$	μ (MeV)	-	5371.7 ± 6.6	5667 ± 20
	σ scale	-	1.155 ± 0.078	1.47 ± 0.28
	α_H	-	-0.8355 ± 0.092	0.80 ± 0.23
	α_L	-	1.86 ± 0.20	1.29 ± 0.39
	n_H	-	48 ± 29	48 ± 25
	n_L	-	1.00 ± 0.40	12 ± 12
$B_s^0 \to \phi\gamma$	μ (MeV)	5295.2 ± 2.2	-	5600 ± 11
	σ scale	1.095 ± 0.028	-	1.31 ± 0.11
	α_H	-1.439 ± 0.14	-	-0.6767 ± 0.091
	α_L	1.78 ± 0.10	-	2.04 ± 0.26
	n_H	6.4 ± 2.6	-	48 ± 29
	n_L	1.52 ± 0.29	-	1.26 ± 0.90
$\Lambda_b^0 \to \Lambda^{*0}\gamma$	μ (MeV)	5355.1 ± 9.5	5343 ± 18	-
	σ scale	1.483 ± 0.091	1.69 ± 0.16	-
	α_H	-1.896 ± 0.26	-2.530 ± 0.90	-
	α_L	0.63 ± 0.11	0.76 ± 0.14	-
	n_H	4.9 ± 3.8	2.9 ± 8.6	-
	n_L	11.0 ± 8.6	15 ± 13	-

baryon channel are described by the form:

$$\begin{aligned} \text{Comb}(m; p_0) &= 1 + p_0 m, \\ \text{Exp}(m; \tau) &= e^{-m*\tau}, \end{aligned} \tag{6.7}$$

where m makes reference to the invariant mass and p_0 and τ are the floating parameters in the fit. For all the cases, the yield is left free in the fit.

6.5.1 Backgrounds to $B^0 \to K^{*0}\gamma$

The amount of b-hadron decays that could potentially contaminate the $B^0 \to K^{*0}\gamma$ data sample is large. However, the analysis selection reduces these contaminations to just a few of them, as shown in Table 6.16. These are described in this section.

Partially reconstructed backgrounds

For the case of the $B^0 \to K^{*0}\gamma$ decay, partially reconstructed backgrounds can be of different nature: cases where only one pion (neutral or charged) is not reconstructed, cases where a kaon is missing with an additional mis-identification, cases where two pions are mis-identified (as a kaon and as a photon) and cases where another photon related

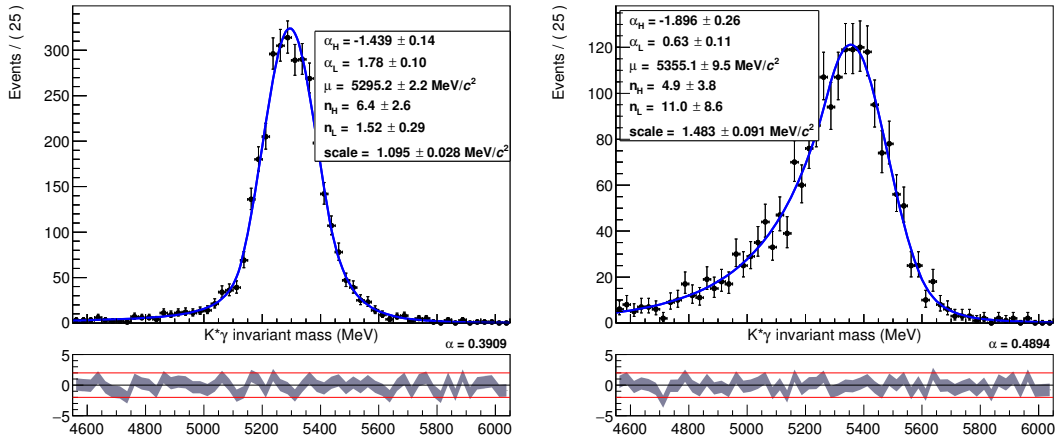

Figure 6.12: Cross-feed contaminations for $B^0 \to K^{*0}\gamma$. In both cases ($B_s^0 \to \phi\gamma$ on the left and $\Lambda_b^0 \to \Lambda^{*0}\gamma$ on the right) the simulation samples are fitted with double-tail Crystal Balls. The parameters extracted from these fits are fixed in the fit to data.

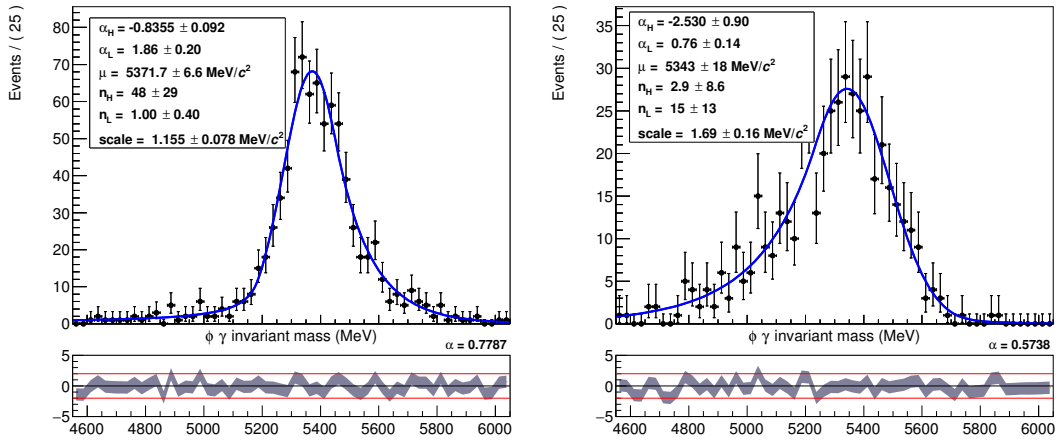

Figure 6.13: Cross-feed contaminations for $B_s^0 \to \phi\gamma$. In both cases ($B^0 \to K^{*0}\gamma$ on the left and $\Lambda_b^0 \to \Lambda^{*0}\gamma$ on the right) the simulation samples are fitted with double-tail Crystal Balls. The parameters extracted from these fits will be fixed in the fit to data.

to the decay is not reconstructed. These cases must be considered separately because, due to the signal mass resolution, they affect very differently the signal region. The contribution for all these decays into the reconstructed B^0 invariant mass distribution is described by the convolution of an ARGUS [128] and a Gaussian function. The shape parameters for the PDF are extracted from a fit to a simulated sample of the decay reconstructed as the signal but the yield is left free in the final fit.

In the case of the $B^0 \to K_1^0\gamma$, $B^+ \to K_1^+\gamma$ and $B^+ \to K_2^+\gamma$ decays, the final state

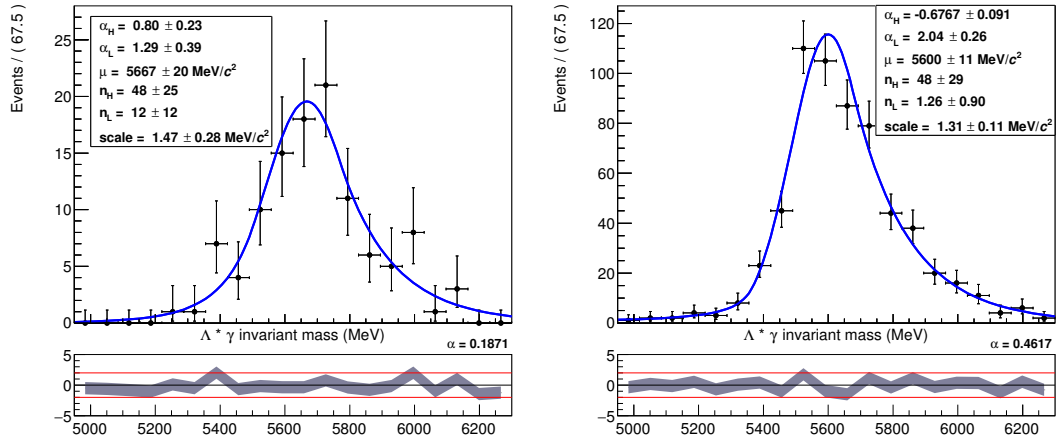

Figure 6.14: Cross-feed contaminations for $\Lambda_b^0 \to \Lambda^{*0}\gamma$. In both cases ($B^0 \to K^{*0}\gamma$ on the left and $B_s^0 \to \phi\gamma$ on the right) the simulation sample is fitted with a bifurcated Crystal Ball. The parameters extracted from these fits will be fixed in the fit to data.

is composed of a kaon, two pions and a photon. However, one of the pions is not reconstructed (a neutral one for the first case and a charged one for the others) mimicking the signal channel decay. Figures 6.15 to 6.17 show the fit to simulated samples of these decays. Since these decays have the same final state, all the different contributions are put together in the invariant mass fit. The parameters chosen for this contribution are the ones corresponding to $B^+ \to K_1^+\gamma$ since the simulation sample from which these parameters are extracted is the largest one among the background channels and therefore have the lowest parameter uncertainties. This contribution will include all the possible contributions from missing pion decays not considered in this analysis.

In the case of the $B^0 \to K^*\eta'$ decay, a photon from the $\eta \to \gamma\gamma$ decay is not reconstructed and therefore the reconstructed event mimics the signal. Due to the unavailability of simulated samples for this decay for this analysis, the shape parameters and contamination are extracted from elsewhere [129]. The distribution is described by an exponentially modified Gaussian (EMG) function where the parameters values, which will be fixed in the fit, are shown in Table 6.18.

There are other partially reconstructed backgrounds that contribute to the invariant mass distribution. In the reconstruction of these backgrounds, more than one particle is not reconstructed and, in addition, mis-identification of at least one of the particles takes place. In the case of the $B^+ \to D^0\rho^+$ decay, a total of three different decay channels are to take into account: those in which the D^0 decays into $K_S^0\pi\pi$, into $K\pi\pi^0$ and into $K\pi\pi\pi$. Of these decays, only the last two contribute to our signal decay after the whole selection is applied. A function result of the convolution of an ARGUS and a Gaussian functions can be used to describe both of them together. Due to the low statistics available in the simulated tuples once the selection is applied, the parameters are taken from elsewhere [129], $c = 0.0 \pm 35$, scale $= 1.97 \pm 0.74$ and $p = 1.31 \pm 0.46$ while the

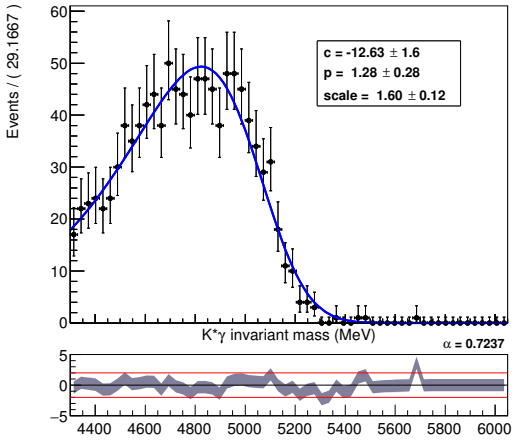

Figure 6.15: $B^0 \to K_1^0\gamma$ simulation sample reconstructed as $B^0 \to K^{*0}\gamma$. The *scale* parameter refers to the scale to the width of the signal Crystal Ball function. The mass offset is fixed to the π^0 mass.

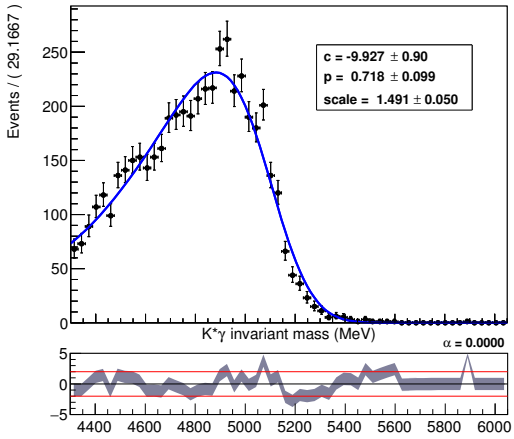

Figure 6.16: $B^+ \to K_1^+\gamma$ simulation sample reconstructed as $B^0 \to K^{*0}\gamma$. The *scale* parameter refers to the scale to the width of the signal Crystal Ball function. The mass offset is fixed to the π^+ mass.

mass offset is fixed to the π mass. Regarding $B^+ \to \rho^+\rho^0$, a total of four pions form the final state: three charged ones and a neutral one. This results in an mass offset with respect to the signal channel of about 220 MeV. Figure 6.18 shows the distribution for this background.

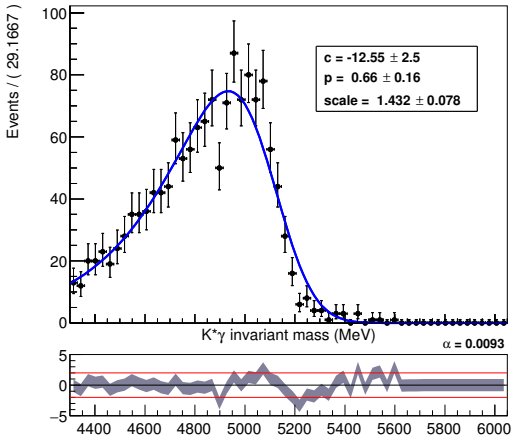

Figure 6.17: $B^+ \to K_2^+\gamma$ simulation sample reconstructed as $B^0 \to K^{*0}\gamma$. The *scale* parameter refers to the scale to the width of the signal Crystal Ball function. The mass offset is fixed to the π^+ mass.

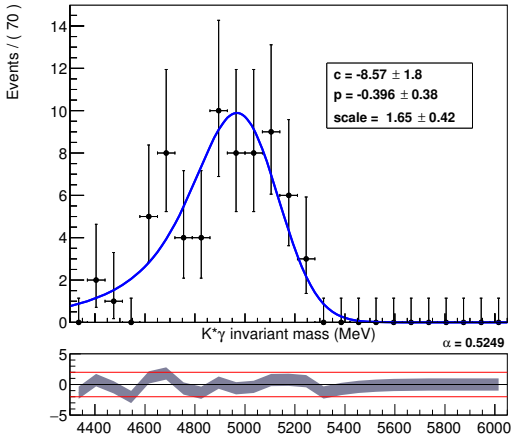

Figure 6.18: $B^+ \to \rho^+\rho^0$ simulation sample reconstructed as $B^0 \to K^{*0}\gamma$. The *scale* parameter refers to the scale to the width of the signal Crystal Ball function. The mass offset is fixed to the difference between the mis-identified kaon mass and the two missing pions.

Peaking backgrounds

These completely reconstructed physical decays are characterized by the fact that their topology is the same as the signal decay but with different particles in the final state. In the case of the $B^0 \to K^{*0}\gamma$, two peaking backgrounds are found to be non-negligible, and correspond to the $B^0 \to \rho^0\gamma$ and the $B^0 \to K\pi\pi^0$ decays. In the first case, the intermediate resonance is a ρ^0, which decays into two oppositely-charged pions and one of them is mis-identified as a kaon, mimicking the signal channel. In the second case,

the mis-identification occurs at a different level: the final state tracks are the same than for the signal channel, but instead of a photon, the decay product related to the ECAL cluster is a π^0. Also, in this second case, the K and the π are produced as both the result of the decay of a K^* and from a non-resonant state. Since these decays are fully reconstructed b-hadron decays and are very similar to radiative decays, the chosen PDF is, as in the case of the signal channels, a double-tailed Crystal Ball distribution. Figure 6.19 shows the fit to these peaking backgrounds. Contrary to the case of partially reconstructed backgrounds, the contamination of these backgrounds is fixed in the data fit since the contribution is expected to be at the same place than the signal mode and the fit would be unable to tell the difference if the yield was left free.

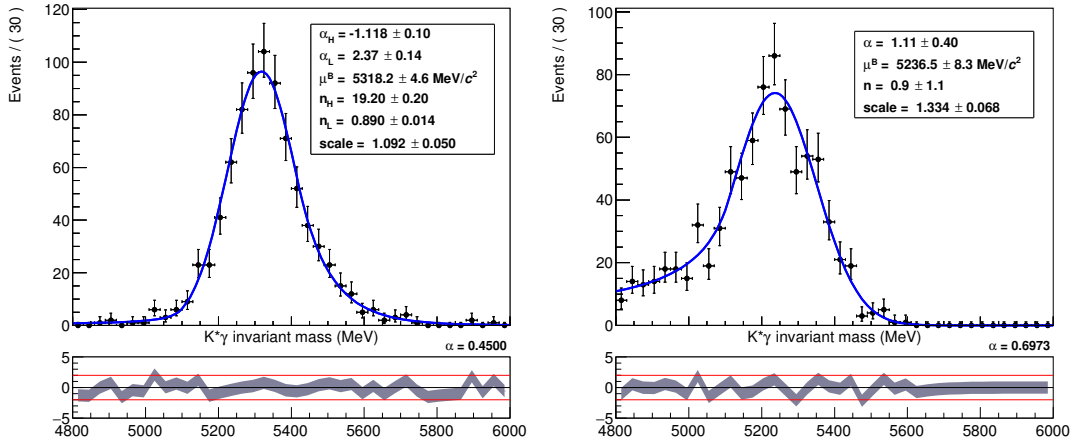

Figure 6.19: $B^0 \to \rho^0\gamma$ (left) and $B^0 \to K\pi\pi^0$ (right) simulation samples reconstructed as $B^0 \to K^{*0}\gamma$. The *scale* parameter refers to the scale to the width of the signal Crystal Ball function.

Tables 6.18–6.20 summarize the value for the fitted parameters for the backgrounds to $B^0 \to K^{*0}\gamma$ for the considered backgrounds.

6.5.2 Backgrounds to $B_s^0 \to \phi\gamma$

The amount of decays considered as possible contaminations for the $B_s^0 \to \phi\gamma$ decay is large. However, due to the tight selection and the narrow ϕ mass window these contaminations are reduced to just a few. This section will describe the non-negligible ones from Table 6.16.

Partially reconstructed backgrounds

In the case of the $B_s^0 \to \phi\gamma$ decay, the non-negligible partially reconstructed backgrounds are related to decays where one of the tracks has not been reconstructed. These backgrounds are $B^+ \to \phi K\gamma$ and $B^0 \to K_1^*\gamma$, where the missing particle is a K and a π, respectively. In the second case, in addition, a pion is mis-identified as a kaon. As in

Table 6.18: Fitted parameters for the partially reconstructed backgrounds when reconstructed as $B^0 \to K^{*0}\gamma$. In all the cases, the PDF that describes the contribution is an ARGUS function convoluted with a Gaussian function.

$B^0 \to K_1^0\gamma$	c	-12.63 ± 1.6
	σ scale	1.60 ± 0.12
	p	1.3 ± 0.3
$B^+ \to K_1^+\gamma$	c	-9.9 ± 0.9
	σ scale	1.49 ± 0.05
	p	0.72 ± 0.10
$B^+ \to K_2^+\gamma$	c	-13 ± 2
	σ scale	1.43 ± 0.08
	p	0.66 ± 0.16
$B^+ \to D^0\rho^+$	c	0 ± 35
	σ scale	2.0 ± 0.7
	p	1.3 ± 0.5

the case of the partially reconstructed backgrounds for $B^0 \to K^{*0}\gamma$, the PDF used for the distribution description is the convolution of an ARGUS and a Gaussian function. Figure 6.20 shows the distribution for the first of these contaminations. For $B^0 \to K_1^*\gamma$, the number of events in the simulation sample after the offline selection is too low to perform any study of the shape, so the same shape parameters than in the case of the $B^0 \to K^{*0}\gamma$ are assumed to be valid here. The yield for the two different distributions is left free in the data fit.

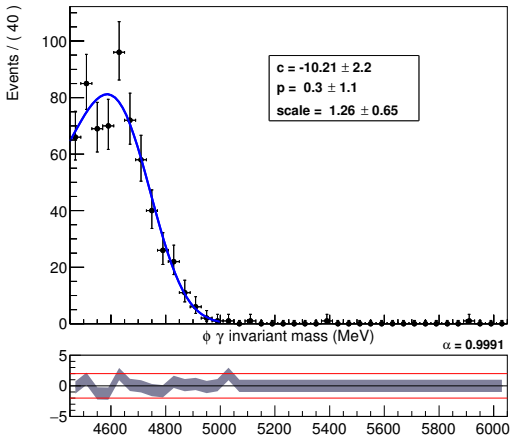

Figure 6.20: $B^+ \to \phi K\gamma$ reconstructed as $B_s^0 \to \phi\gamma$. The *scale* parameter refers to the scale to the width of the signal Crystal Ball function.

Table 6.19: Fitted parameters for the peaking backgrounds when reconstructed as $B^0 \to K^{*0}\gamma$. In all the cases, the PDF that describes the contribution is a double crystal ball.

$B^0 \to \rho^0\gamma$	α_H		-1.12 ± 0.10
	α_L		2.37 ± 0.14
	μ	(MeV)	5318 ± 5
	n_H		19.2 ± 0.2
	n_L		0.890 ± 0.014
	σ scale		1.09 ± 0.05
	Contamination		$(0.204 \pm 0.011)\%$
$B^0 \to K\pi\pi^0$	α		1.1 ± 0.4
	n		0.9 ± 1.1
	μ	(MeV)	5237 ± 8
	σ scale		1.33 ± 0.07
	Contamination		$(0.274 \pm 0.004)\%$
$B_s^0 \to \phi\gamma$	α_H		-1.44 ± 0.14
	α_L		1.78 ± 0.10
	μ	(MeV)	5295 ± 2
	n_H		6 ± 3
	n_L		1.5 ± 0.3
	σ scale		1.10 ± 0.03
	Contamination		$(5.4 \pm 1.3)\%$
$\Lambda_b^0 \to \Lambda^{*0}\gamma$	α_H		-1.9 ± 0.3
	α_L		0.63 ± 0.11
	μ	(MeV)	5356 ± 10
	n_H		5 ± 4
	n_L		11 ± 9
	σ scale		1.48 ± 0.09
	Contamination		$(4.1 \pm 0.8)\%$

Peaking backgrounds

Since no simulated sample for $B_s^0 \to \phi\pi^0$ is available, it is assumed that the ratio of selection efficiencies of the photon and the π^0 channel are the same for the B^0 and B_s^0 modes. This is a good assumption since the photon and the π^0 have essentially the same kinematics in the two channels. This implies the same efficiency for the γ/π^0 separation requirement and rejection for $B_s^0 \to \phi\gamma$ and $B_s^0 \to \phi\pi^0$, respectively, as it does for $B^0 \to K^{*0}\gamma$ and $B^0 \to K^*\pi^0$. Since the γ/π^0 separation variable is not well reproduced by the simulation, the variable in $B^0 \to K^*\pi^0$ samples is weighed to reproduce the performance in data with the γ/π^0 separation tool [103]. In addition to the ratio of efficiencies, the ratio of branching fractions is also needed in order to predict the

Table 6.20: Fitted parameters for backgrounds with missing particles and misidentification when reconstructed as $B^0 \to K^{*0}\gamma$. The PDF that describes each contribution is detailed.

$B^0 \to K^*\eta'$ (EMG)	Mass offset (MeV)	57.51
	σ scale	1.24
	λ	0.0019
	Contamination	$(2.04 \pm 0.14)\%$
$B^+ \to \rho^+\rho^0$ (ARGUS $\otimes$ Gaus)	Mass offset(MeV)	220.00
	c	-8.6 ± 1.8
	p	-0.4 ± 0.4
	σ scale	1.7 ± 0.4
	Contamination	$(3.38 \pm 3.77)\%$

contaminations. The $B_s^0 \to \phi\pi^0$ has not yet been observed, but it is predicted to be 1.6×10^{-7} [130], which corresponds to less than 0.5 % of the $B_s^0 \to \phi\gamma$ rate. On the other hand, the $B^0 \to K^*\pi^0$ branching fraction has measured to be $(3.3 \pm 0.6) \times 10^{-6}$, which corresponds to about 7.6 % of the $B^0 \to K^{*0}\gamma$ rate. For this analysis, the ratios of the branching fractions between the photon and the neutral pions are assumed to be the same for both channels. This implies that the contamination for $B_s^0 \to \phi\pi^0$ is the same as for $B^0 \to K^*\pi^0$. However, since the B_s^0 decay is symmetric in the helicity angle while the B^0 is not, efficiency differences are expected. The contamination is, consequently, computed from the contamination of the $B^0 \to K^*\pi^0$ channel without the helicity angle requirement. This contamination is then multiplied by the ratio of efficiency of the angle cut between $B_s^0 \to \phi\gamma$ and $B_s^0 \to \phi\pi^0$. This contamination is fixed in the fit. This background is modeled with a single Crystal Ball PDF and its shape parameters, introduced in the fit, are summarised in Table 6.21.

Table 6.21 summarizes the value for the fitted parameters for the backgrounds to $B_s^0 \to \phi\gamma$ for each of the considered backgrounds.

6.5.3 Backgrounds to $\Lambda_b^0 \to \Lambda^{*0}\gamma$

All the peaking backgrounds considered for the $\Lambda_b^0 \to \Lambda^{*0}\gamma$ decay are found to be negligible after the whole selection is applied, so, apart from the already considered combinatorial and cross-feed backgrounds, only partially reconstructed backgrounds are to be taken into account. Contamination from mis-identification backgrounds contribute far from the signal region due to the large different in terms of the tracks masses.

Partially reconstructed backgrounds

For the case of the $\Lambda_b^0 \to \Lambda^{*0}\gamma$ decay, the only partially reconstructed decays with a non-negligible contribution into the signal are the same ones than for $B_s^0 \to \phi\gamma$, *i.e.*, $B^+ \to \phi K\gamma$ and $B^0 \to K_1^*\gamma$. Due to the low number of events present in the simulation

Table 6.21: Fitted parameters for the different backgrounds when reconstructed as $B_s^0 \to \phi\gamma$. The contaminations related to the cross-feed backgrounds are calculated with simulation samples where the whole selection is applied.

$B^+ \to \phi K^+\gamma$ (ARGUS $\oplus$ Gaus)	c		-10 ± 2
	σ scale		1.3 ± 0.7
	p		0.3 ± 1.1
$B^0 \to K_1^*\gamma$ (ARGUS $\oplus$ Gaus)	c		-12.63 ± 1.6
	σ scale		1.60 ± 0.12
	p		1.3 ± 0.3
$B^0 \to K^{*0}\gamma$ (Double Crystal Ball)	α_H		-0.84 ± 0.09
	α_L		1.9 ± 0.2
	μ	(MeV)	5372 ± 7
	n_H		50 ± 30
	n_L		1.0 ± 0.4
	σ scale		1.16 ± 0.08
	Contamination		0.0000783 ± 0.0000007
$\Lambda_b^0 \to \Lambda^{*0}\gamma$ (Double Crystal Ball)	α_H		-2.5 ± 0.9
	α_L		0.76 ± 0.14
	μ	(MeV)	5343 ± 18
	n_H		3 ± 9
	n_L		15 ± 13
	σ scale		1.69 ± 0.16
	Contamination		0.0051 ± 0.0004
$B_s^0 \to \phi\pi^0$ (Crystal Ball)	Mass offset (MeV)		50
	σ scale		1.2
	a		0.58
	n		3.1
	Contamination		$(0.21 \pm 0.09)\%$

samples, the shape parameters could not be extracted and therefore the shape parameters from the $B_s^0 \to \phi\gamma$ case are used, with their yields left free in the real data fit.

Table 6.22 summarizes the value for the fitted parameters for the backgrounds to $\Lambda_b^0 \to \Lambda^{*0}\gamma$ for each of the considered backgrounds.

Given the fit result concerning this channel, additional contributions at low Λ_b^0 mass have been studied. Backgrounds where two or three particles (either kaons, pions or mixtures of both) have been included in the fit. In these studies, the shape of the contributions, as well as the yield, was left free to vary (for a fixed PDF, considered to be a convolution of an ARGUS PDF and a Gaussian PDF, since these contributions correspond all to partially reconstructed backgrounds). For all the different possibilities,

the fitted contribution for these backgrounds was found to be negligible, so no additional partially reconstructed backgrounds were added to the final fit.

Table 6.22: Fitted parameters for the different backgrounds when reconstructed as $\Lambda_b^0 \to \Lambda^{*0}\gamma$. The contaminations related to the cross-feed backgrounds are calculated with simulation samples where the whole selection is applied.

$B^+ \to \phi K^+\gamma$ (ARGUS $\oplus$ Gaus)	c		-10 ± 2
	σ scale		1.3 ± 0.7
	p		0.3 ± 1.1
$B^0 \to K_1^*\gamma$ (ARGUS $\oplus$ Gaus)	c		-12.63 ± 1.6
	σ scale		1.60 ± 0.12
	p		1.3 ± 0.3
$B^0 \to K^{*0}\gamma$ (Double Crystal Ball)	α_H		0.8 ± 0.2
	α_L		1.3 ± 0.4
	μ	(MeV)	5670 ± 20
	n_H		50 ± 30
	n_L		12 ± 12
	σ scale		1.5 ± 0.3
	Contamination		$(0.0182 \pm 0.0002)\%$
$B_s^0 \to \phi\gamma$ (Double Crystal Ball)	α_H		-0.68 ± 0.09
	α_L		2.0 ± 0.3
	μ	(MeV)	5600 ± 11
	n_H		50 ± 30
	n_L		1.3 ± 0.9
	σ scale		1.31 ± 0.11
	Contamination		$(3.1 \pm 0.05)\%$

6.5.4 Compatibility between 2011 and 2012 samples

Despite differences in the data and simulation samples between 2011 and 2012, mainly due to the different centre-of-mass energies at which they were collected/simulated, this analysis performs a single fit to the whole Run 1 dataset. This is possible since the differences are small, as shown in Fig. 6.21 in the case of $B^0 \to K^{*0}\gamma$ (top left), $B_s^0 \to \phi\gamma$ (top right) and $\Lambda_b^0 \to \Lambda^{*0}\gamma$ (bottom).

6.6 Fit to the invariant mass distributions

The yields for the $B^0 \to K^{*0}\gamma$, $B_s^0 \to \phi\gamma$ and $\Lambda_b^0 \to \Lambda^{*0}\gamma$ decays and the measurement of the raw *CP* violation (A_{raw}^{CP}) for $B^0 \to K^{*0}\gamma$ and $\Lambda_b^0 \to \Lambda^{*0}\gamma$ are extracted by performing a simultaneous fit to a total of five invariant mass distributions (one for $B_s^0 \to \phi\gamma$ and

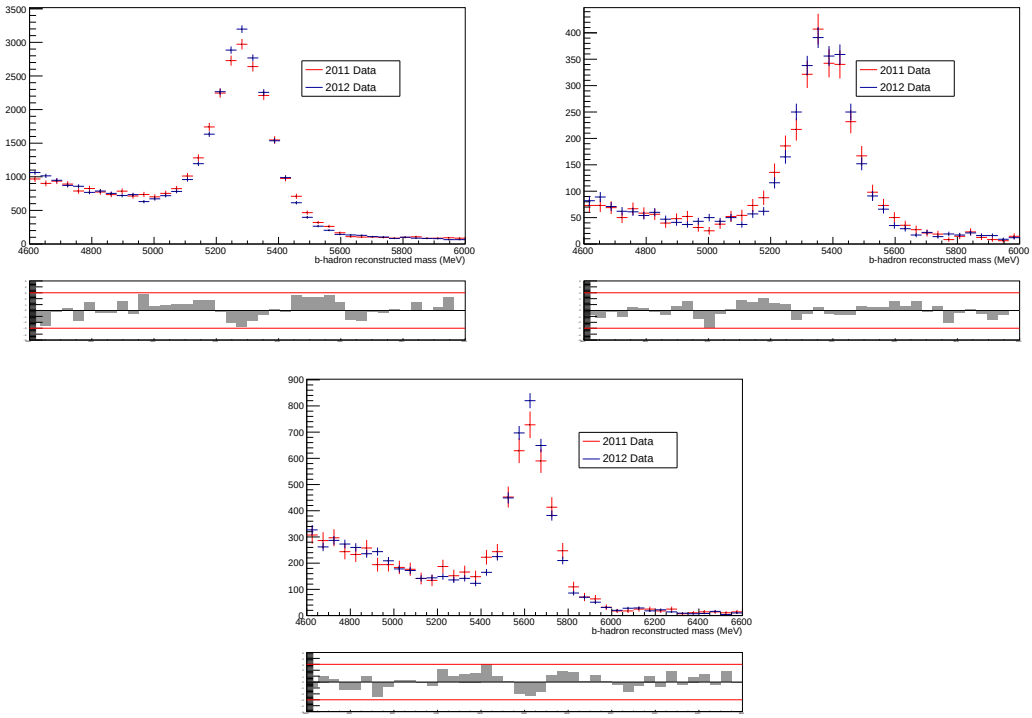

Figure 6.21: Reconstructed B^0 (top left), B_s^0 (top right) and Λ_b^0 (bottom) mass after the whole offline selection for 2011 and 2012. The compatibility of the two distributions motivates the use of a single fit for the whole Run 1.

one per *CP*-flavour for $B^0 \to K^{*0}\gamma$ and $\Lambda_b^0 \to \Lambda^{*0}\gamma$) with the RooFit toolkit [131], which makes use of the MINUIT minimization routines [132]. The yields for $B_s^0 \to \phi\gamma$ and $\Lambda_b^0 \to \Lambda^{*0}\gamma$ are extracted as the ratio with respect to the $B^0 \to K^{*0}\gamma$ yield. For the two fits related to each of the *CP*-flavours for $B^0 \to K^{*0}\gamma$ and $\Lambda_b^0 \to \Lambda^{*0}\gamma$, the shape of the signal is forced to be same.

The fit results are shown in Table 6.23. A total of 27602 ± 262 $B^0 \to K^{*0}\gamma$, 3993 ± 93 $B_s^0 \to \phi\gamma$ and 4029 ± 96 $\Lambda_b^0 \to \Lambda^{*0}\gamma$ events are found. This constitutes a very clear first observation of a radiative decay of a b-baryon.

For the three signal channels the yields of the peaking backgrounds are fixed from simulation, as well as the ratio of yields for the cross-feed backgrounds. On the other hand, the yields related to the partially reconstructed backgrounds and the combinatorial background are left free. Tables 6.18, 6.21 and 6.22 summarize the parameters included in the fit for $B^0 \to K^{*0}\gamma$, $B_s^0 \to \phi\gamma$ and $\Lambda_b^0 \to \Lambda^{*0}\gamma$, respectively, and the parameters extracted from the fits are summarized in Table 6.24, 6.25 and 6.26.

Table 6.23: Summary of the fitted parameters for the signal channels for the whole Run 1 dataset. The statistical uncertainty is included.

	$B^0 \to K^{*0}\gamma$	$B_s^0 \to \phi\gamma$	$\Lambda_b^0 \to \Lambda^{*0}\gamma$
Yield	27615 ± 249	-	-
Yield/Yield($B^0 \to K^{*0}\gamma$)	-	0.133 ± 0.003	0.149 ± 0.003
μ (MeV)	5285.7 ± 0.8	5366.2 ± 1.9	5622.0 ± 1.8
σ (MeV)	89.6 ± 0.8	90.2 ± 1.9	85.0 ± 1.7
A_{raw}^{CP}	$(1.4 \pm 0.8)\%$	-	$(6.1 \pm 1.8)\%$

Table 6.24: Summary of the fitted background parameters for $B^0 \to K^{*0}\gamma$ for the two possible *CP*-states.

	$B^0 \to K^{*0}\gamma$	$\overline{B}^0 \to \overline{K}^{*}\gamma$
Combinatorial Background		
p_0 (MeV^{-1})	-0.25 ± 0.15	0.04 ± 0.25
Contamination	0.21 ± 0.03	0.15 ± 0.03
$B^+ \to D^0\rho^+$		
Contamination	0.184 ± 0.009	0.189 ± 0.014
Missing pion decays		
Contamination	0.40 ± 0.02	0.37 ± 0.02
$B^+ \to \rho^+\rho^0$		
Contamination	0.00 ± 0.05	0.03 ± 0.04

Validation of the fit

In order to assess the quality of the fit, its stability has been studied by performing a large number of simulated pseudo-experiments, generating samples following the shape

Table 6.25: Summary of the fitted background parameters for $B_s^0 \to \phi\gamma$.

	$B_s^0 \to \phi\gamma$
Combinatorial Background	
p_0 (MeV^{-1})	-0.66 ± 0.05
Contamination	0.40 ± 0.03
$B^+ \to \phi K^+\gamma$	
Contamination	0.082 ± 0.014

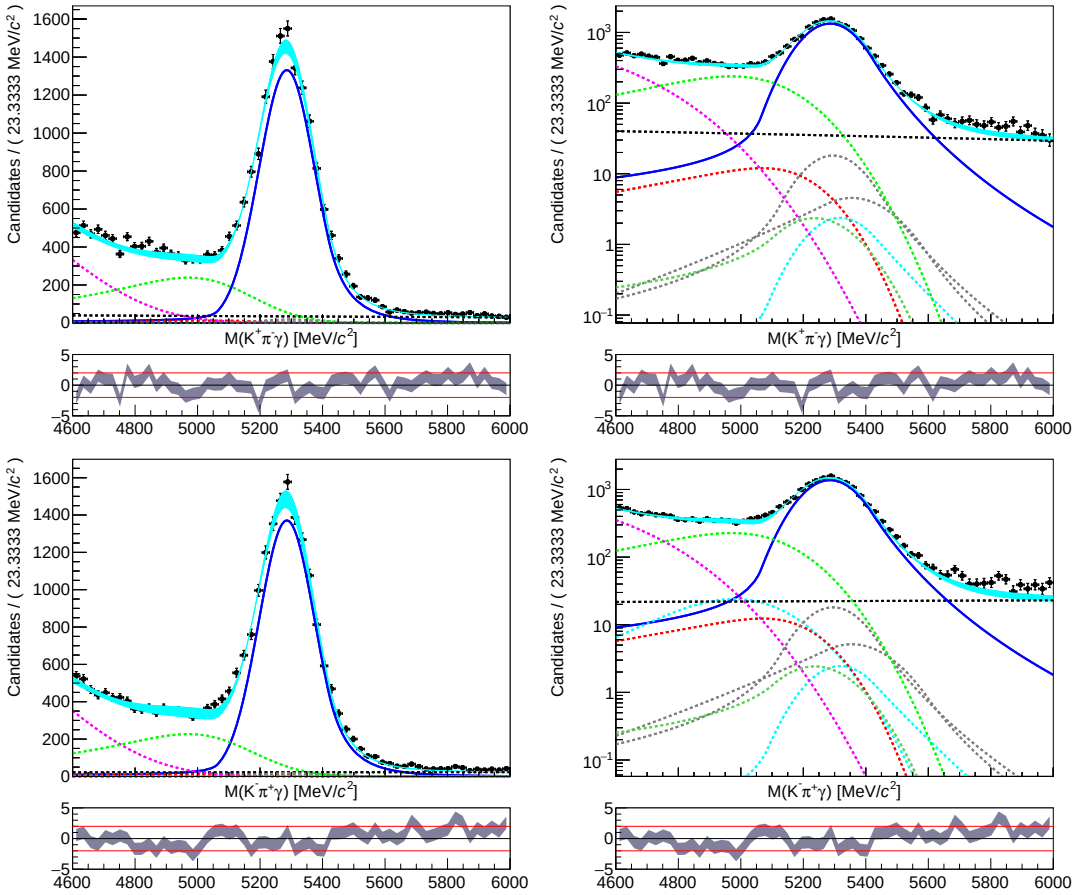

Figure 6.22: Fit to $B^0 \to K^{*0}\gamma$ candidates in the total 3.2 fb^{-1} dataset in the linear (left) and logarithmic (right) scales in the case of B^0 (top) and $\overline{B}^0$ (bottom) *CP*-states. The black points represent the data and the fit result is represented as a solid light blue line. The solid dark blue line corresponds to the signal contribution, the combinatorial background is represented by a dashed black line while the cross-feed contaminations are shown as dashed grey lines. The partially reconstructed decays where a pion is missing are represented by a dashed light green line and the partially reconstructed background $B^+ \to D^0\rho^+$ is represented by a dashed pink line. The light blue line under the B^0 peak corresponds to the peaking background $B^0 \to \rho^0\gamma$ while $B^0 \to K\pi\pi^0$ is described by the dashed dark green line. The partially reconstructed background $B^0 \to K^*\eta'$ is represented by a dashed red line and the $B^+ \to \rho^+\rho^0$ is represented by a dashed light blue line.

of the fitted PDF. The pull distribution for a given parameter x ($\mathcal{P}_x$) is given by:

$$\mathcal{P}_x = \frac{x_{Fit} - x_{data}}{\sigma_x}, \tag{6.8}$$

extracted from a set of Monte Carlos experiment, is used to test the stability of a fit. If the fit behaves well, $\mathcal{P}_x$ follows a Gaussian distribution centered at zero with a standard

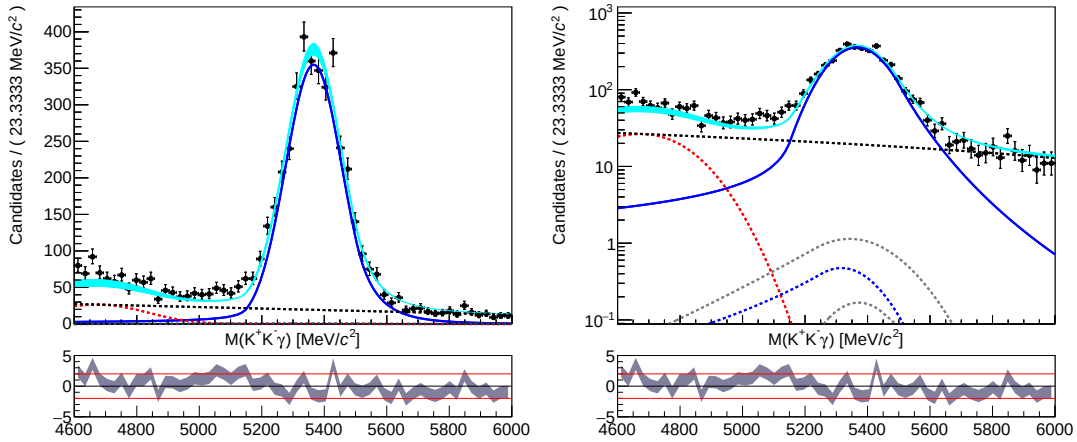

Figure 6.23: Fit to $B_s^0 \to \phi\gamma$ candidates in the total 3.2 fb^{-1} dataset in the linear (left) and logarithmic (right) scales. The black points represent the data and the fit result is represented as a solid light blue line. The signal is represented by a solid dark blue line. The combinatorial background is described by the dashed black line. The cross-feed contaminations are given by dashed grey lines. The partially reconstructed background $B^+ \to \phi K^+\gamma$ is represented by the dashed red line while the peaking background $B_s^0 \to KK\pi^0$ is represented by the dashed dark blue line.

Table 6.26: Summary of the fitted parameters for $\Lambda_b^0 \to \Lambda^{*0}\gamma$ for the two possible CP-states.

	$\Lambda_b^0 \to \Lambda^{*0}\gamma$	$\overline{\Lambda}_b^0 \to \overline{\Lambda}^*\gamma$
Combinatorial Background		
τ (MeV^{-1})	-0.00185 ± 0.00007	-0.00184 ± 0.00008
Contamination	1.06 ± 0.08	0.98 ± 0.08
$B^0 \to K_1\gamma$		
Contamination	0.14 ± 0.04	0.21 ± 0.04
$B^+ \to \phi K^+\gamma$		
Contamination	-0.009 ± 0.049	0.06 ± 0.05

deviation of one. Deviation from those values indicates the presence of biases (for the μ value) or errors in the uncertainties estimations (for the σ value).

A total of 10,675 pseudo-experiments samples have been generated following the model PDF with the parameters set at the values extracted from the fit. Figure 6.25 shows the pull distributions for the $B^0 \to K^{*0}\gamma$ and $\Lambda_b^0 \to \Lambda^{*0}\gamma$ A_{raw}^{CP} parameters, fitted with a Gaussian function, while Fig. 6.26 shows the pull distributions for the three signal channel yields (number of $B^0 \to K^{*0}\gamma$ events and the relative number of events for $B_s^0 \to \phi\gamma$ and $\Lambda_b^0 \to \Lambda^{*0}\gamma$ with respect to the former). The pull distributions for the rest of fitted parameters can be found in Fig. B.5–Fig.B.11. It can be concluded that all

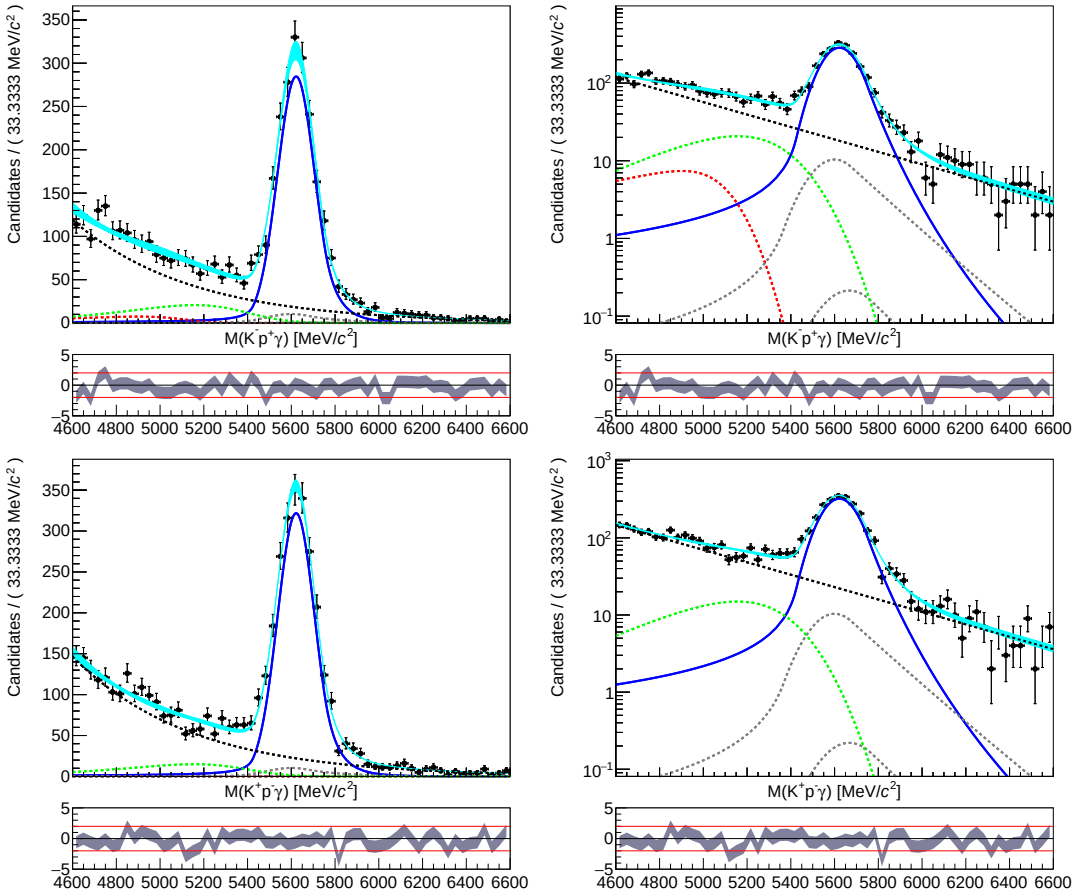

Figure 6.24: Fit to $\Lambda_b^0 \to \Lambda^{*0}\gamma$ candidates in the total 2.8 fb^{-1} dataset in the linear (left) and logarithmic (right) scales in the case of $\overline{\Lambda}_b^0$ (top) and Λ_b^0 (bottom) *CP*-states. The black points represent the data and the fit result is represented as a solid light blue line. The signal is represented by the solid dark blue line, while the dashed black line representes the combinatorial background. The cross-feed contaminations are given by the dashed grey lines. The partially reconstructed background $B^+ \to \phi K^+\gamma$ is represented by the dashed red line while the partially reconstructed background $B^0 \to K_1\gamma$ contribution is described by the dashed green line.

the parameters and their errors have been correctly estimated and therefore the fit is stable under variations of the input data as well as that the signal parameters and their uncertainties have been correctly extracted within the model.

6.7 Extraction of ratios of branching fractions

For a given B decay, the expected yield is given by

$$N = 2 \times \sigma_{b\bar{b}} \times \mathcal{L} \times f \times \mathcal{B}(B \to X) \times \epsilon, \tag{6.9}$$

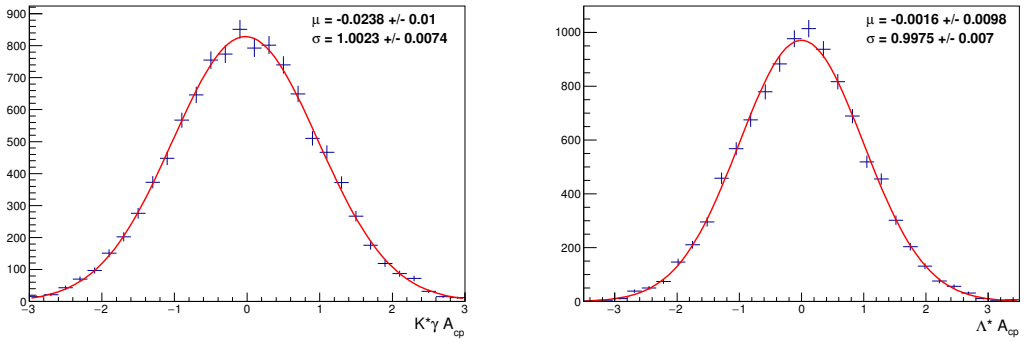

Figure 6.25: Pull distributions for the $\mathcal{A}^{CP}$ for $B^0 \to K^{*0}\gamma$ (left) and $\Lambda_b^0 \to \Lambda^{*0}\gamma$ (right). The fit of the pull distributions to a Gaussian function is shown in a red line, with its parameters on the top right corner of each plot.

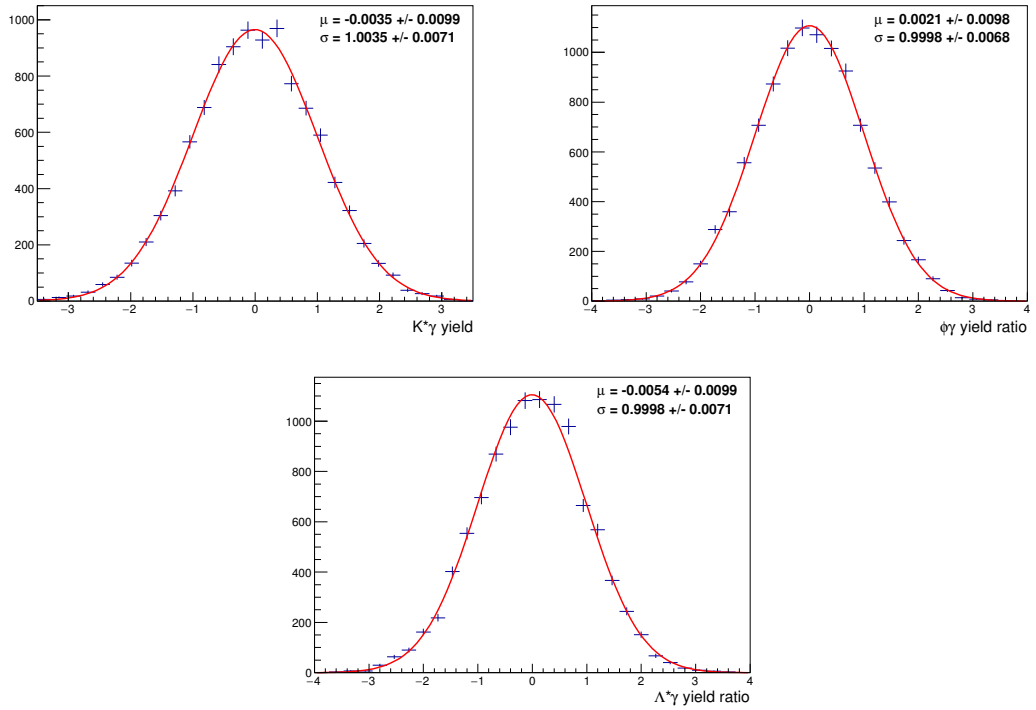

Figure 6.26: Pull distributions for the yields for $B^0 \to K^{*0}\gamma$ (top left), $B_s^0 \to \phi\gamma$ (top right) and $\Lambda_b^0 \to \Lambda^{*0}\gamma$ (bottom). The fit of the pull distributions to a Gaussian function is shown in a red line, with its parameters on the top right corner of each plot.

where $\mathcal{L}$ is the integrated luminosity, $\sigma_{b\bar{b}}$ is the production cross-section, f is the b-hadron hadronization fraction, $\mathcal{B}$ is the branching fraction of the decay and ϵ is the total efficiency of the whole selection process.

The ratio of branching fractions of $B^0 \to K^{*0}\gamma$ with respect to $B_s^0 \to \phi\gamma$ and $\Lambda_b^0 \to \Lambda^{*0}\gamma$ would then be written as

$$\begin{aligned}
\frac{\mathcal{B}(B^0 \to K^{*0}\gamma)}{\mathcal{B}(B_s^0 \to \phi\gamma)} &= \frac{N_{B^0\to K^{*0}\gamma}}{N_{B_s^0\to\phi\gamma}} \frac{\mathcal{B}(\phi \to KK)}{\mathcal{B}(K^{*0} \to K\pi)} \frac{f_s}{f_d} \frac{\epsilon_{B_s^0\to\phi\gamma}}{\epsilon_{B^0\to K^{*0}\gamma}}, \\
\frac{\mathcal{B}(B^0 \to K^{*0}\gamma)}{\mathcal{B}(\Lambda_b^0 \to \Lambda^{*0}\gamma)} &= \frac{N_{B^0\to K^{*0}\gamma}}{N_{\Lambda_b^0\to\Lambda^{*0}\gamma}} \frac{\mathcal{B}(\Lambda^{*0} \to pK)}{\mathcal{B}(K^{*0} \to K\pi)} \frac{f_{\Lambda_b}}{f_d} \frac{\epsilon_{\Lambda_b^0\to\Lambda^{*0}\gamma}}{\epsilon_{B^0\to K^{*0}\gamma}} \frac{\mathcal{L}_{\Lambda_b^0\to\Lambda^{*0}\gamma}}{\mathcal{L}_{B^0\to K^{*0}\gamma}},
\end{aligned} \tag{6.10}$$

where the ratio of the signal yields is the inverse value of the one extracted from the fit and the ratio of luminosities for the $B_s^0 \to \phi\gamma$ case cancels out.

The efficiency for each channel is split into trigger, reconstruction and selection without PID requirements, and PID selection. The reason for separating the calculation of the selection efficiency from the PID efficiency is that the PID distributions are not accurately described by the simulation, and therefore cannot be extracted directly from MC. With this splitting in mind, the ratio of efficiencies between the two channels can be written as

$$r_\epsilon^{\phi\gamma} \equiv \frac{\epsilon_{B_s^0\to\phi\gamma}}{\epsilon_{B^0\to K^{*0}\gamma}} = \frac{\epsilon^{RecoSelNoPID}_{B_s^0\to\phi\gamma}}{\epsilon^{RecoSelNoPID}_{B^0\to K^{*0}\gamma}} \frac{\epsilon^{Trigger}_{B_s^0\to\phi\gamma}}{\epsilon^{Trigger}_{B^0\to K^{*0}\gamma}} \frac{\epsilon^{PID}_{B_s^0\to\phi\gamma}}{\epsilon^{PID}_{B^0\to K^{*0}\gamma}}, \tag{6.11}$$

and similarly for $\Lambda_b^0 \to \Lambda^{*0}\gamma$. All the efficiencies ratios except from the PID one have been extracted from simulation with a correction applied to the track reconstruction efficiency due to disagreements between data and simulation. The ratio of efficiencies of PID cuts has been extracted making use of a data-driven reweighing method on the Monte Carlo simulation [105]. The value of the efficiencies is calculated for the 2011 simulation and 2012 simulation separately and averaged proportionally to the amount of collected data each year.

6.7.1 Ratio of luminosities

Since the integrated luminosity for the two meson channels is the same, the ratio of this factor cancels out. This is not the case for the $\Lambda_b^0 \to \Lambda^{*0}\gamma$ decay, since the HLT2 lines used were not active for a the first part of the Run 1 (see Table 6.7). Therefore, the ratio of integrated luminosities is:

$$r_{\mathcal{L}}^{\Lambda_b^0\to\Lambda^{*0}\gamma} = \frac{(2.79 \pm 0.05)\ \text{fb}^{-1}}{(3.17 \pm 0.06)\ \text{fb}^{-1}} = 0.878 \pm 0.006. \tag{6.12}$$

6.7.2 Ratio of signal yields

The signal yields ratios are directly extracted from the simultaneous fit (see Table 6.23). The magnitudes involved in the branching fraction ratio calculation are the inverse to

the fitted values for the signal yields and are 7.52 ± 0.17 for $B_s^0 \to \phi\gamma$ and 6.71 ± 0.14 for $\Lambda_b^0 \to \Lambda^{*0}\gamma$.

The first set of systematic uncertainties in the determination of these ratios is related to the fact that several components of the fit used to obtain them (both shape parameters and contaminations) have been fixed from simulation. These have been studied in three groups: signal shapes, partially reconstructed background shapes and peaking background shapes and contamination. The systematic effect of each of these has been evaluated by repeating the fit on data a large number of times, each time fixing the shape and contamination — when fixed — to a random variation, under their uncertainties, of each of the relevant parameters. The spread of the distribution of the relevant yield ratio is then reported as the systematic uncertainty, and is found to be 0.013, 0.017 and 0.018 for the signal, partially reconstructed background and peaking background of $B_s^0 \to \phi\gamma$, respectively, and 0.016, 0.045 and 0.036 for $\Lambda_b^0 \to \Lambda^{*0}\gamma$.

Additionally, a systematic is assigned to account for the specific choice of PDF of the combinatorial background. Data are refitted using an alternative PDF and the difference with the nominal result is taken as a systematic error. In particular an exponential (linear polynomial) is used as an alternative to the combinatorial background model for the B^0 and B_s^0 (Λ_b^0) modes. This alternative combinatorial description produces an effect of 0.0011 and 0.002 for the $B_s^0 \to \phi\gamma$ and the $\Lambda_b^0 \to \Lambda^{*0}\gamma$ ratios, respectively.

The $\mathcal{A}^{CP}$ for the peaking backgrounds has been neglected due to the low contamination and taking into account the measured $\mathcal{A}^{CP}$.

Combining the systematic errors of the background model and the signal model in quadrature, the signal yields ratios are:

$$\begin{aligned} r_N^{B^0\to K^{*0}\gamma/B_s^0\to\phi\gamma} &\equiv r_N^{\phi\gamma} = 7.52 \pm 0.17\,(\text{stat}) \pm 0.03\,(\text{syst}) \\ r_N^{B^0\to K^{*0}\gamma/\Lambda_b^0\to\Lambda^{*0}\gamma} &\equiv r_N^{\Lambda^{*0}\gamma} = 6.71 \pm 0.14\,(\text{stat}) \pm 0.06\,(\text{syst}). \end{aligned} \tag{6.13}$$

6.7.3 Ratio of the intermediate states decays branching fractions

Not all possible decays for the intermediate resonances are contemplated in the analysis and therefore the corresponding branching fractions for the ones used need to be added. In particular, for the meson modes, the ones used are $K^{*0} \to K^{\pm}\pi^{\mp}$ and $\phi \to K^{\pm}K^{\mp}$. For the case of the baryon mode, the measurement corresponds to $\Lambda_b^0 \to pK\gamma$, since all the different possibilities for the intermediate state are considered. This implies that, by definition, $\mathcal{B}(\Lambda^{*0} \to pK) = 1$.

The branching fractions of the decay of the intermediate states to the studies final states can be found in [4]:

$$\begin{aligned} \mathcal{B}(K^{*0} \to K^{\pm}\pi^{\mp}) &= (66.507 \pm 0.014)\%, \\ \mathcal{B}(\phi \to K^{+}K^{-}) &= (48.9 \pm 0.5)\%, \end{aligned} \tag{6.14}$$

and therefore the ratio of intermediate states decays branching fractions are:

$$\begin{aligned} r_{\mathcal{B}}^{\phi\gamma} &\equiv \frac{\mathcal{B}(\phi \to K^{\pm}K^{\mp})}{\mathcal{B}(K^{*0} \to K^{\pm}\pi^{\mp})} = 0.735 \pm 0.008 \\ r_{\mathcal{B}}^{\Lambda^{*0}\gamma} &\equiv \frac{\mathcal{B}(\Lambda^{*0} \to pK)}{\mathcal{B}(K^{*0} \to K^{\pm}\pi^{\mp})} = 1.5036 \pm 0.0003. \end{aligned} \tag{6.15}$$

The errors of these quantities will be considered as systematic uncertainties.

6.7.4 Ratio of hadronization factors

The LHCb experiment has performed the measurement of the ratio of hadronization factors making use of b-hadron decays into charm states, in particular $B_s^0 \to D_s^- \pi^+$ and $B^0 \to D^- K^+$ for the f_s/f_d ratio [133] and $\Lambda_b^0 \to \Lambda_c^+ \pi^-$ for the f_{Λ_b}/f_d ratio [134]. In both cases, a dependence on the p_{T} of the b-candidate is observed, although in the case of f_s/f_d, it is neglected. For the case of the baryon decay, the ratio can be written as

$$f_{\Lambda_b}/f_d = a + \exp(b + c \times p_{\mathrm{T}}(\,\mathrm{GeV})), \tag{6.16}$$

where $a = 0.151 \pm 0.016^{+0.024}_{-0.025}$, $b = -0.573 \pm 0.040^{+0.101}_{-0.097}$ and $c = -0.095 \pm 0.007 \pm 0.014$ ($\,\mathrm{GeV}^{-1}$) [134]. Making use of the offline selected and background subtracted Λ_b^0 candidates p_{T}, the ratios of hadronization factors are:

$$\begin{aligned} r_{hadron.factors}^{\phi\gamma} &\equiv f_s/f_d = 0.256 \pm 0.020, \\ r_{hadron.factors}^{\Lambda^{*0}\gamma} &\equiv f_{\Lambda_b^0}/f_d = 0.38 \pm 0.05. \end{aligned} \tag{6.17}$$

The errors of these quantities will be considered as systematic uncertainties.

6.7.5 Ratio of efficiencies

The calculation of the ratio of efficiencies is performed differently for $B_s^0 \to \phi\gamma$ and $\Lambda_b^0 \to \Lambda^{*0}\gamma$, due to the samples used for each of the calculations.

For the case of $B_s^0 \to \phi\gamma$, the efficiency is calculated from simulation samples and is the result of a series of the efficiencies related to each of the steps involved in the selection. A value for the efficiency for each of the steps is computed and the total efficiency is the product of all of them.

In the case of $\Lambda_b^0 \to \Lambda^{*0}\gamma$, a 2-dimensional efficiency is determined in bins of the B-mass constrained pK mass and the *proton angle* (angle between the Λ^{*0} direction in the Λ_b^0 rest-frame and the proton direction in the Λ^{*0} rest frame, as shown in Fig. 6.27, [112]), since we do not have any knowledge of the resonance content in the proton-kaon system. The efficiency for each of the bins is calculated and assigned as the average from simulation samples for the different resonances, which have been tested to be compatible bin-by-bin. Once the binning is established and the efficiency for each of the bins is computed, the global efficiency is calculated from the background-subtracted data sample, propagating the uncertainties coming from the efficiency calculation and the sPlot as a systematic

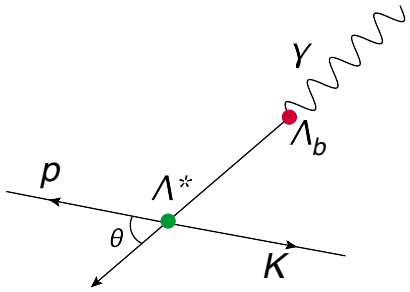

Figure 6.27: Definition of the proton angle (θ), which is the angle between the proton momentum in the Λ^{*0} rest-frame and the Λ^{*0} momentum in the Λ_b^0 rest-frame.

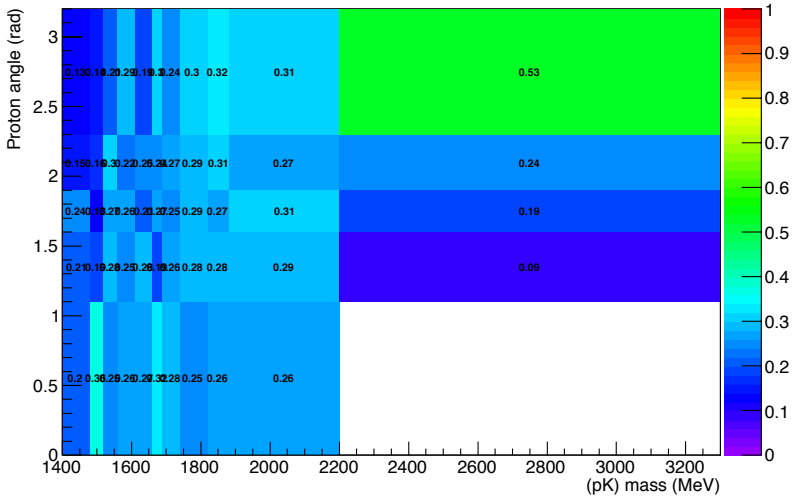

Figure 6.28: $\Lambda_b^0 \to \Lambda^{*0}\gamma$ 2-dimensional efficiency map for the full selection. The binning for the intermediate resonance and the proton angle cosine has been optimised for smooth transition of the efficiencies from one bin to the next.

uncertainty. Figure 6.28 shows the 2-dimensional efficiency bins for the full selection. The blank bin indicates zero efficiency.

As guidance lines, the step efficiency for each of the used simulated samples (corresponding to the intermediate states $\Lambda^{*0}(1520)$, $\Lambda^{*0}(1670)$, $\Lambda^{*0}(1820)$ and $\Lambda^{*0}(1830)$), will be detailed in the following subsections but the binning method has only been applied to the global selection. The PID efficiencies as well as corrections to the track efficiency are not included in the method and therefore will be applied in the final calculation.

Ratio of reconstruction and selection efficiencies

The reconstruction and selection efficiency is the combination of the whole offline selection process excluding the PID and the trigger selections. Therefore, this efficiency includes the acceptance efficiency, the reconstruction efficiency, the preselection efficiency, the BDT efficiency, the γ/π^0 separation efficiency and the isolation efficiency. The efficiency for each of the steps is calculated on simulation samples by dividing the number of offline-selected events between the size of the samples and then the ratio is computed, excepting the acceptance efficiency, which is given by the MC generation tables.

The systematic uncertainties are divided in two types: one associated to the limited size of the simulated samples and one associated with the remaining data/MC differences. The former is calculated directly through the ratio explained before and the latter is calculated applying the selection on weighed MC samples. This weighing is obtained by calculating an event-by-event weight for the MC samples that makes the variable distributions between data and MC be equivalent. This weighing is calculated making use of a multivariate tool [135] which uses sPlotted data and simulation as inputs and determines event-by-event weights to correct for the differences between simulation and data. The variables (the distributions of which for simulation and data are shown in the Appendix C) used for the weighing are related to the event multiplicity (number of tracks), helicity angle distribution and topology (tracks χ^2/ndf, tracks $\chi^2_{\rm IP}$, b-hadron momentum and transverse momentum, b-hadron flight distance χ^2, resonance momentum and transverse momentum and resonance $\chi^2_{\rm IP}$). Once the weighing is performed, the efficiency is calculated in the same way it has been done previously. The difference between the two values of the ratio of efficiencies is assigned as the systematic uncertainty. Table 6.27 summarizes the efficiency for the $B^0 \to K^{*0}\gamma$ and $B^0_s \to \phi\gamma$ modes for the simulated samples and the reweighed ones. Table 6.28 shows the ratio of efficiencies for each of the steps for the simulation samples and the reweighed simulation samples.

Table 6.27: Efficiency of each of the reconstruction and offline selection steps from simulated $B^0 \to K^{*0}\gamma$, and $B^0_s \to \phi\gamma$ samples, for simulated and reweighed simulation samples. The reweighed efficiencies corresponding to the acceptance and stripping and reconstruction selection steps are assumed to be the same than in the non-reweighed samples, since, due to the unavailability of simulated samples, the calculation could not be performed. The global efficiency is also included.

	$B^0 \to K^{*0}\gamma$	Reweighed $B^0 \to K^{*0}\gamma$	$B^0_s \to \phi\gamma$	Reweighed $B^0_s \to \phi\gamma$
Acceptance (%)	24.33 ± 0.03	24.33 ± 0.03	26.45 ± 0.03	26.45 ± 0.03
Strip. and Reco. (%)	3.471 ± 0.005	3.471 ± 0.005	2.811 ± 0.005	2.811 ± 0.005
Preselection (%)	64.18 ± 0.07	63.37 ± 0.22	67.58 ± 0.08	67.21 ± 0.64
BDT (%)	81.93 ± 0.07	80.49 ± 0.18	88.95 ± 0.06	88.90 ± 0.47
Isolation (%)	93.71 ± 0.05	93.81 ± 0.11	90.37 ± 0.07	90.41 ± 0.40
γ/π^0 separation (%)	95.94 ± 0.04	95.98 ± 0.09	95.74 ± 0.05	96.02 ± 0.27
Global selection(%)	0.3992 ± 0.0010	0.3878 ± 0.0019	0.3867 ± 0.0010	0.385 ± 0.005

Even if the different steps are very similar from one channel to another, different efficiencies are expected due to the different kinematics for each of the channels. Since

Table 6.28: Ratio of efficiencies for $B_s^0 \to \phi\gamma$ with respect to $B^0 \to K^{*0}\gamma$ for each of the selection steps for the simulation and for the reweighed simulation samples. The global ratio is also included.

	Ratio	Reweighed Ratio
Acceptance	1.0871 ± 0.0018	1.0871 ± 0.0018
Strip. and Reco.	0.8099 ± 0.0019	0.8099 ± 0.0019
Preselection	1.0530 ± 0.0017	1.061 ± 0.011
BDT	1.0857 ± 0.0012	1.104 ± 0.006
Isolation	0.9644 ± 0.0009	0.964 ± 0.004
γ/π^0 separation	0.9979 ± 0.0007	1.000 ± 0.003
Global selection	0.969 ± 0.003	0.991 ± 0.013

Table 6.29: Correction factors to the tracking efficiencies for all the tracks involved in the decays final states. The opposite charge for the different tracks is implied.

	$B^0 \to K^{*0}\gamma$	$B_s^0 \to \phi\gamma$	$\Lambda_b^0 \to \Lambda^{*0}\gamma$
K	1.013 ± 0.006	1.011 ± 0.006	1.012 ± 0.007
π	1.013 ± 0.008	-	-
p	-	-	1.012 ± 0.006

the efficiencies are calculated making use of simulated events, it is important that the different variables are well-described in the simulation. Since this is not the case for the tracking variables, a correction to the tracking efficiency is needed. This correction is applied making use of a tool [136, 137] that utilises the $J/\psi \to \mu^+\mu^-$ decay as calibration channel and considers that the ratio of efficiencies between simulation and real data is the same for sufficiently small 2D bins of momentum and pseudorapidity for the calibration channel and any other decay. The tool then extracts a correction that is to be applied to the tracking efficiency from ratios of efficiencies for tracks within real data and simulation samples. In this work, the correction to the tracking efficiency is found to be of the order of 1%, as shown in Table 6.29 (the uncertainty in this correction will also be added as a systematic).

The global ratio of selection efficiencies for $B_s^0 \to \phi\gamma$ with respect to $B^0 \to K^{*0}\gamma$, adding the systematic uncertainties in quadrature, is then:

$$r^{B_s^0 \to \phi\gamma / B^0 \to K^{*0}\gamma}_{RecoSelNoPID} \equiv \frac{\epsilon^{RecoSelNoPID}_{B_s^0 \to \phi\gamma}}{\epsilon^{RecoSelNoPID}_{B^0 \to K^{*0}\gamma}} = 0.965 \pm 0.026. \tag{6.18}$$

Concerning the $\Lambda_b^0 \to \Lambda^{*0}\gamma$ mode, Table 6.30 shows the efficiencies for the different Λ^{*0} simulation samples. The ratio of selection efficiencies for $\Lambda_b^0 \to \Lambda^{*0}\gamma$ with respect to $B^0 \to K^{*0}\gamma$ is calculated as explained previously. No efficiency for intermediate steps is calculated since it would be necessary to perform a new fit for each step to extract

Table 6.30: Efficiency of each of the reconstruction and offline selection steps from simulated $\Lambda_b^0 \to \Lambda^{*0}\gamma$ samples with different intermediate states. The global efficiency is also included.

	$\Lambda_b^0 \to \Lambda^{*0}(1520)\gamma$	$\Lambda_b^0 \to \Lambda^{*0}(1670)\gamma$	$\Lambda_b^0 \to \Lambda^{*0}(1820)\gamma$	$\Lambda_b^0 \to \Lambda^{*0}(1830)\gamma$
Acceptance (%)	26.15 ± 0.06	25.28 ± 0.04	40.04 ± 0.07	39.90 ± 0.08
Strip. and Reco. (%)	2.261 ± 0.011	1.7243 ± 0.00007	0.96667 ± 0.00005	0.96213 ± 0.00005
Preselection (%)	61.21 ± 0.25	61.04 ± 0.19	60.62 ± 0.23	60.90 ± 0.22
Isolation (%)	82.13 ± 0.25	87.35 ± 0.17	88.86 ± 0.19	88.79 ± 0.19
γ/π^0 separation (%)	95.82 ± 0.15	95.95 ± 0.10	96.02 ± 0.12	96.11 ± 0.12
Global selection (%)	0.2848 ± 0.0021	0.2230 ± 0.0009	0.2002 ± 0.0014	0.1995 ± 0.0010

the proper background-subtracted distributions from data, and this is not possible in all steps. There are three sources of systematics: one related to the use of the sPlots, another to the size of the simulation sample and, finally, one related to data/MC differences. The first two, as discussed before, have been taken into account together in the calculation of the efficiency, while the third is obtained by comparing the nominal result with the reweighed simulation. The global selection efficiency for the $\Lambda_b^0 \to \Lambda^{*0}\gamma$ decay is found to be $(0.247 \pm 0.013)\%$ (it is computed to be $(0.252 \pm 0.003)\%$ for the reweighed MC), which leads to a value for the ratio of selection efficiencies of $\Lambda_b^0 \to \Lambda^{*0}\gamma$ with respect to $B^0 \to K^{*0}\gamma$ of:

$$r^{\Lambda_b^0 \to \Lambda^{*0}\gamma / B^0 \to K^{*0}\gamma}_{RecoSelNoPID} \equiv \frac{\epsilon^{RecoSelNoPID}_{\Lambda_b^0 \to \Lambda^{*0}\gamma}}{\epsilon^{RecoSelNoPID}_{B^0 \to K^{*0}\gamma}} = 0.604 \pm 0.036. \tag{6.19}$$

Ratio of trigger efficiencies

The ratios of trigger efficiencies have been evaluated from offline selected simulation events. Depending on the decay channel, the trigger efficiencies calculation is different.

Both the $B^0 \to K^{*0}\gamma$ and $B_s^0 \to \phi\gamma$ simulation samples were produced following the reference TCKs [119] for 2011 and 2012, 0x00790038 and 0x009f0045, respectively. The calculation of the efficiency of the TOS selection is then performed by calculating the ratio of the events after and before the application of the TOS trigger requirement.

Table 6.31 details the trigger efficiencies for $B^0 \to K^{*0}\gamma$ and $B_s^0 \to \phi\gamma$ for the different trigger stages for the MC and the reweighed MC sample, from where the systematic uncertainty will be extracted. The ratio between the two channels is shown in Table 6.32.

The overall trigger efficiency ratio, taking into account the systematic uncertainty, is:

$$r^{B_s^0 \to \phi\gamma / B^0 \to K^{*0}\gamma}_{Trigger} \equiv \frac{\epsilon^{Trigger}_{B_s^0 \to \phi\gamma}}{\epsilon^{Trigger}_{B^0 \to K^{*0}\gamma}} = 1.003 \pm 0.005. \tag{6.20}$$

The TISTOS method [138] is used to cross-check the efficiency values. The TISTOS method consists on selecting, for a simulation sample, a sub-sample that is independent of signal and calculating the TOS efficiency. As the TIS sub-sample is expected to be unbiased, the TOS efficiency over the TIS sub-sample is equivalent to the trigger TOS

Table 6.31: Trigger efficiency for $B^0 \to K^{*0}\gamma$ and $B_s^0 \to \phi\gamma$ at the different trigger levels and the global one for the simulation and the reweighed simulation samples. The MC-statistical uncertainty is included.

	$B^0 \to K^{*0}\gamma$	Reweighed $B^0 \to K^{*0}\gamma$	$B_s^0 \to \phi\gamma$	Reweighed $B_s^0 \to \phi\gamma$
L0 Trigger (%)	77.60 ± 0.09	77.56 ± 0.19	77.58 ± 0.10	77.32 ± 0.57
HLT1 Trigger (%)	76.21 ± 0.11	75.82 ± 0.19	72.12 ± 0.12	72.27 ± 0.62
HLT2 Trigger (%)	85.69 ± 0.10	85.53 ± 0.16	90.86 ± 0.09	90.69 ± 0.40
Global Trigger (%)	50.68 ± 0.11	50.30 ± 0.20	50.84 ± 0.12	49.27 ± 0.61

Table 6.32: Trigger efficiency for $B^0 \to K^{*0}\gamma$ and $B_s^0 \to \phi\gamma$ at the different trigger levels and the global one for the simulation and the reweighed simulation samples. The MC-statistical uncertainty is included.

	Ratio	Reweighed Ratio
L0 Trigger	0.9997 ± 0.0017	0.997 ± 0.008
HLT1 Trigger	0.946 ± 0.002	0.953 ± 0.009
HLT2 Trigger	1.0603 ± 0.0016	1.060 ± 0.005
Global Trigger	1.003 ± 0.003	1.007 ± 0.013

efficiency for data, which can not be directly calculated due to the unavailability of the data samples prior the trigger stage. The efficiencies calculated with this method are given in Table 6.33, where it can be seen that due to the small size of the signal samples, the uncertainties are pretty large. The TISTOS efficiency ratio is 1.00 ± 0.23, which is compatible with the simulation efficiency shown in Eq. 6.20, even if we do not take into account the uncertainty in the TISTOS efficiency.

Table 6.33: TISTOS efficiencies for the $B^0 \to K^{*0}\gamma$ and $B_s^0 \to \phi\gamma$ channels. The global efficiency is included.

	$B^0 \to K^{*0}\gamma$	$B_s^0 \to \phi\gamma$
L0 Trigger (%)	89.11 ± 1.97	85.25 ± 5.70
HLT1 Trigger (%)	78.28 ± 2.33	70.49 ± 7.65
HLT2 Trigger (%)	75.88 ± 5.12	88.07 ± 14.99
Global Trigger (%)	52.93 ± 4.08	52.92 ± 11.25

Table 6.34 shows the trigger efficiencies for the simulated $\Lambda_b^0 \to \Lambda^{*0}\gamma$ decays. These samples were generated with the 0x00760037 and 0x009f0045 TCKs for 2011 and 2012, respectively [119].

As mentioned before, the efficiencies associated to the $\Lambda_b^0 \to \Lambda^{*0}\gamma$ decay have been calculated making use of background subtracted data samples, using the 2-dimensional binning explained above. The global trigger efficiency for the $\Lambda_b^0 \to \Lambda^{*0}\gamma$ is found to be

Table 6.34: Trigger efficiency for the different simulated $\Lambda_b^0 \to \Lambda^{*0}\gamma$ samples with at the different trigger stages. The global trigger efficiency is included.

	$\Lambda_b^0 \to \Lambda^{*0}(1520)\gamma$	$\Lambda_b^0 \to \Lambda^{*0}(1670)\gamma$	$\Lambda_b^0 \to \Lambda^{*0}(1820)\gamma$	$\Lambda_b^0 \to \Lambda^{*0}(1830)\gamma$
L0 Trigger (%)	76.24 ± 0.32	76.29 ± 0.24	76.47 ± 0.27	76.68 ± 0.27
HLT1 Trigger (%)	84.00 ± 0.31	87.31 ± 0.21	87.57 ± 0.24	87.80 ± 0.24
HLT2 Trigger (%)	75.64 ± 0.40	81.64 ± 0.26	83.83 ± 0.28	83.47 ± 0.28
Global Trigger (%)	48.44 ± 0.37	54.38 ± 0.28	56.14 ± 0.31	56.20 ± 0.31

$(54.4 \pm 2.4)\%$ and therefore the trigger efficiency ratio for the $\Lambda_b^0 \to \Lambda^{*0}\gamma$ with respect to $B^0 \to K^{*0}\gamma$ is calculated to be

$$r_{Trigger}^{\Lambda_b^0 \to \Lambda^{*0}\gamma / B^0 \to K^{*0}\gamma} \equiv \frac{\epsilon_{\Lambda_b^0 \to \Lambda^{*0}\gamma}^{Trigger}}{\epsilon_{B^0 \to K^{*0}\gamma}^{Trigger}} = 1.073 \pm 0.048. \tag{6.21}$$

Despite the possible mis-simulation of the L0, which would not be corrected by the reweighing, no extra systematic uncertainty is added in any of the trigger efficiency ratios due to the fact that the photon E_{T} spectrum is very similar among the decays, this cancelling any large effects.

Ratio of PID efficiencies

The PID selection refers only to requirements applied on the tracks identification variables. The PID efficiencies are to be understood as an average of the individual efficiencies that can be assigned to each event.

As pointed out in 6.3.4, the variables used for the PID selection correspond to the combination of variables built through a multivariate tool. The method used to determine the efficiency has been developed by the LHCb Particle IDentification group [105]. Calibration samples of well-known decays (such as $D^{*+} \to D^0(\to K^-\pi^+)\pi_s$) are reconstructed without the aid of PID variables, a method is used to subtract the background to the samples, now pure. The key idea of the data-driven method used for the efficiency calculation is that, for a bin built from PID-independent variables, all tracks of a given type would have the same efficiency for a certain bin. The variables used to bin are those in which the PID algorithms are more dependent, and are the track momentum, the track transverse momentum, the track pseudorapidity (η) and the number of tracks in the event (which is related to the multiplicity of the event). However, not all these variables are independent and therefore the p, η and the number of tracks in the event are used in this case. Once the binning and the PID requirements are decided, the method builds a series of efficiency tables, which the PID software package uses to perform the efficiency calculation.

The PID efficiency for a given event is the product of the efficiencies of the tracks and therefore it is not correct to consider the p and η distributions of the tracks independently and sum over the efficiency of each bin. Instead, the PID efficiency is to be considered as

a weight per event and, from that value, the integrated efficiency can be calculated. The PID efficiencies are different for the 2011 and 2012 simulation samples, but compatible within uncertainties and therefore the average is taken.

The systematic uncertainty associated to the PID efficiency is related to the use of the PIDCalib tool and is calculated from the PIDCalib calibration samples ($D^{*\pm} \to D^0(\to K^+\pi^-)\pi^\pm$ for $B^0 \to K^{*0}\gamma$ and $B^0_s \to \phi\gamma$ and $\Lambda \to pK$ for $\Lambda^0_b \to \Lambda^{*0}\gamma$) as the difference between the efficiency calculated from the application of the PIDCalib method on the calibration samples and the efficiency obtained by directly applying the PID cut on the calibration sample.

Table 6.35 details the PID efficiency for each case taking into account the MC-statistical and systematic uncertainties.

Table 6.35: PID efficiencies, split by magnet polarity, including MC-statistical and systematic uncertainties, respectively. The PID efficiency for each of the resonances is calculated by making the product of the efficiencies for the tracks.

		Magnet Up	Magnet Down	Average
$B^0 \to K^{*0}\gamma$	ϵ_K (%)	$97.54 \pm 0.28 \pm 0.26$	$97.84 \pm 0.28 \pm 0.32$	$97.69 \pm 0.20 \pm 0.21$
	ϵ_π (%)	$99.53 \pm 0.31 \pm 0.67$	$99.18 \pm 0.31 \pm 0.03$	$99.35 \pm 0.22 \pm 0.34$
	ϵ_{K^*} (%)	$97.08 \pm 0.41 \pm 0.70$	$97.04 \pm 0.41 \pm 0.32$	$97.06 \pm 0.29 \pm 0.39$
$B^0_s \to \phi\gamma$	ϵ_{K^+} (%)	$97.64 \pm 0.32 \pm 0.31$	$98.02 \pm 0.32 \pm 0.32$	$97.83 \pm 0.23 \pm 0.22$
	ϵ_{K^-} (%)	$97.64 \pm 0.32 \pm 0.31$	$98.02 \pm 0.32 \pm 0.32$	$97.83 \pm 0.23 \pm 0.22$
	ϵ_ϕ (%)	$95.34 \pm 0.62 \pm 0.43$	$96.08 \pm 0.63 \pm 0.32$	$95.71 \pm 0.45 \pm 0.43$
$\Lambda^0_b \to \Lambda^{*0}\gamma$	ϵ_K (%)	$83.38 \pm 0.63 \pm 0.11$	$83.54 \pm 0.64 \pm 0.46$	$83.46 \pm 0.45 \pm 0.24$
	ϵ_p (%)	$65.43 \pm 0.49 \pm 0.62$	$70.31 \pm 0.51 \pm 0.10$	$67.87 \pm 0.36 \pm 0.31$
	$\epsilon_{\Lambda^{*0}}$ (%)	$54.56 \pm 0.58 \pm 0.62$	$58.74 \pm 0.62 \pm 0.35$	$56.64 \pm 0.42 \pm 0.35$

Thus, the ratio of PID efficiencies is, combining the two systematic uncertainties:

$$\begin{aligned} r_{PID}^{B^0_s\to\phi\gamma/B^0\to K^{*0}\gamma} &\equiv \frac{\epsilon_{B^0_s\to\phi\gamma}}{\epsilon_{B^0\to K^{*0}\gamma}} = 0.986 \pm 0.008 \\ r_{PID}^{\Lambda^0_b\to\Lambda^{*0}\gamma/B^0\to K^{*0}\gamma} &\equiv \frac{\epsilon_{\Lambda^0_b\to\Lambda^{*0}\gamma}}{\epsilon_{B^0\to K^{*0}\gamma}} = 0.584 \pm 0.005. \end{aligned} \tag{6.22}$$

Total efficiency ratio calculation

As stated before, the total efficiency for the offline selection is calculated as the product of the different efficiencies for each of the selection steps and the correction to the tracking reconstruction efficiency. The efficiency ratios for $B^0_s \to \phi\gamma$ and $\Lambda^0_b \to \Lambda^{*0}\gamma$ with respect to $B^0 \to K^{*0}\gamma$ are therefore calculated to be:

$$\begin{aligned} r_\epsilon^{B^0_s\to\phi\gamma} &= 0.954 \pm 0.027 \\ r_\epsilon^{\Lambda^0_b\to\Lambda^{*0}\gamma} &= 0.378 \pm 0.017, \end{aligned} \tag{6.23}$$

6.7.6 Results

Table 6.36 summarizes the systematic uncertainties calculated in the previous sections, while a summary of the different factors entering in the calculation of the ratio of branching fractions is included in Table 6.37.

Table 6.36: Summary of the systematic uncertainties entering in the branching fraction ratios calculation.

	$\mathcal{B}(B^0 \to K^{*0}\gamma / B_s^0 \to \phi\gamma)$	$\mathcal{B}(B^0 \to K^{*0}\gamma / \Lambda_b^0 \to \Lambda^{*0}\gamma)$
Luminosities ratio	-	± 0.006
Signal yields ratio	± 0.03	± 0.06
Resonances branching fractions	± 0.008	± 0.0003
Hadronization factors ratio	± 0.020	± 0.05
Efficiencies ratio	± 0.027	± 0.017

Table 6.37: Summary of the various contributions to the ratio of branching fractions. The two uncertainties quoted in r_N correspond, respectively, to the statistical and systematic errors.

	$\mathcal{B}\ (B^0 \to K^{*0}\gamma / B_s^0 \to \phi\gamma)$	$\mathcal{B}\ (B^0 \to K^{*0}\gamma / \Lambda_b^0 \to \Lambda^{*0}\gamma)$
$r_{\mathcal{L}}$	-	0.878 ± 0.006
r_N	$7.52 \pm 0.17 \pm 0.03$	$6.71 \pm 0.14 \pm 0.06$
$r_{\mathcal{B}}$	0.735 ± 0.008	1.5036 ± 0.0003
$r_{hadron.factors}$	0.256 ± 0.020	0.382 ± 0.051
r_ϵ	0.954 ± 0.027	0.378 ± 0.017

Combining the information from Table 6.37, the ratios of branching fractions are:

$$\begin{aligned} \frac{\mathcal{B}(B^0 \to K^{*0}\gamma)}{\mathcal{B}(B_s^0 \to \phi\gamma)} &= 1.350 \pm 0.031\,(\text{stat}) \pm 0.041\,(\text{syst}) \pm 0.107(f_s/f_d) \\ \frac{\mathcal{B}(B^0 \to K^{*0}\gamma)}{\mathcal{B}(\Lambda_b^0 \to \Lambda^{*0}\gamma)} &= 1.279 \pm 0.027\,(\text{stat}) \pm 0.059\,(\text{syst}) \pm 0.171(f_\Lambda/f_d). \end{aligned} \tag{6.24}$$

Using the measured value of $\mathcal{B}(B^0 \to K^{*0}\gamma)$ [4], it is possible to extract the value for the branching fraction of the $B_s^0 \to \phi\gamma$ and $\Lambda_b^0 \to \Lambda^{*0}\gamma$ decays:

$$\begin{aligned} \mathcal{B}(B_s^0 \to \phi\gamma) &= (3.21 \pm 0.28) \times 10^{-5} \\ \mathcal{B}(\Lambda_b^0 \to \Lambda^{*0}\gamma) &= (3.39 \pm 0.48) \times 10^{-5}. \end{aligned} \tag{6.25}$$

which, in the case of the $B_s^0 \to \phi\gamma$, is the world's most precise measurement and is in agreement with the theoretical prediction (see Table 6.3) and, for $\Lambda_b^0 \to \Lambda^{*0}\gamma$, constitutes the first measurement of its branching fraction.

Figure 6.29 shows the non-efficiency corrected proton-kaon invariant mass distribution for the background-subtracted data sample. This can be compared to Fig. 6.1, which

corresponds to an approximation of the proton-kaon mass spectrum for $\Lambda_b^0 \to \Lambda^{*0}\gamma$ decays.

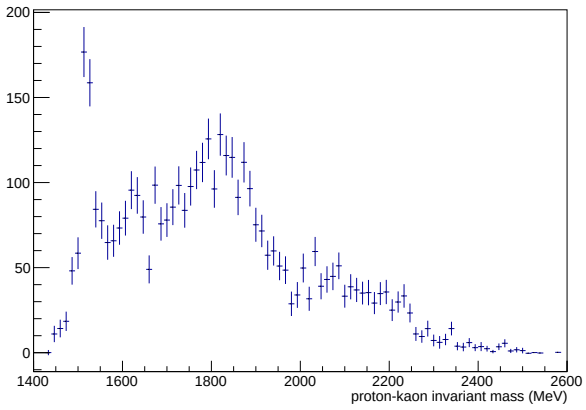

Figure 6.29: Proton-kaon pair Λ_b^0-mass constrained pK mass for the $\Lambda_b^0 \to \Lambda^{*0}\gamma$ background-subtracted data sample.

6.8 Measurement of direct $\mathcal{A}^{CP}$

As stated before, the direct $\mathcal{A}^{CP}$ for a given decay $B \to f$ is

$$\mathcal{A}^{CP} = \frac{\Gamma(b \to \bar{f}) - \Gamma(\bar{b} \to f)}{\Gamma(b \to \bar{f}) + \Gamma(\bar{b} \to f)}, \tag{6.26}$$

which can be written, in terms of the yields for one or another flavour for the B meson and the Λ_b^0 baryon, as

$$\begin{aligned} \mathcal{A}^{CP} &= \frac{N(\overline{B}^0) - N(B^0)}{N(\overline{B}^0) + N(B^0)} \\ \mathcal{A}^{CP} &= \frac{N(\Lambda_b^0) - N(\overline{\Lambda}_b^0)}{N(\Lambda_b^0) + N(\overline{\Lambda}_b^0)}. \end{aligned} \tag{6.27}$$

The fit described in 6.6, by construction, gives the *raw* value of the $\mathcal{A}^{CP}$, which is found to be $(1.42 \pm 0.81)\%$ for $B^0 \to K^{*0}\gamma$ and $(6.1 \pm 1.8)\%$ for $\Lambda_b^0 \to \Lambda^{*0}\gamma$. The fit stability and error estimation have also been checked to be correct, as shown in Fig. 6.25. To obtain the physical value for this observable, the A_{raw}^{CP} needs to be corrected for the asymmetry of production of b hadrons in pp collisions and for the difference in the detection of matter and antimatter.

The physical $\mathcal{A}^{CP}$ can therefore be written as

$$\begin{aligned} \mathcal{A}^{CP}(B^0 \to K^{*0}\gamma) &= A_{raw}^{CP}(B^0 \to K^{*0}\gamma) - A_D(K\pi) - \kappa A_P(B^0) \\ \mathcal{A}^{CP}(\Lambda_b^0 \to \Lambda^{*0}\gamma) &= A_{raw}^{CP}(\Lambda_b^0 \to \Lambda^{*0}\gamma) - A_D(Kp) - A_P(\Lambda_b^0), \end{aligned} \tag{6.28}$$

where A_D and A_P represent the detection and production asymmetries, respectively. The κ_{B^0} factor is a dilution factor due to the initial state particle oscillation. There is no dilution factor in the case of the Λ_b^0 since these particles do not oscillate.

6.8.1 A_{raw}^{CP} systematic uncertainties

The systematic uncertainties on A_{raw}^{CP} concern mainly the extraction of the signal yields, and therefore are calculated in the same way as those corresponding to the ratio of yields in the branching fraction measurement. The spread of A_{raw}^{CP} found due to the signal parameters is 0.17% and 0.19% for $B^0 \to K^{*0}\gamma$ and $\Lambda_b^0 \to \Lambda^{*0}\gamma$, respectively. The equivalent numbers for partially reconstructed and peaking backgrounds are 0.043% and 0.02%, and 0.17% and 0.53%, respectively. The variations of the combinatorial PDF give rise to systematics of 0.02% and 0.10% for $B^0 \to K^{*0}\gamma$ and $\Lambda_b^0 \to \Lambda^{*0}\gamma$. It is worth noting the large reduction of the systematic uncertainty thanks to the inclusion of the $\Lambda_b^0 \to \Lambda^{*0}\gamma$ decay in the fit, when compared to previous measurements at LHCb [3]. The global uncertainty for $B^0 \to K^{*0}\gamma$ and $\Lambda_b^0 \to \Lambda^{*0}\gamma$, calculated from the quadrature of the variations, is 0.05% and 0.57%, respectively.

The $\mathcal{A}^{CP}$ for the peaking backgrounds have been considered to be zero.

6.8.2 Detection asymmetries

The detector material responds differently to the presence of matter and antimatter when interacting and is different for each particle. For a given final state, the total detection asymmetry is the sum of the detection asymmetry of each of the final state particles.

The detection asymmetry for pions has previously been measured by the LHCb experiment [139] to be $A_D^{\pi} = (0.00 \pm 0.25)\%$, while the detection asymmetry for kaons and protons is calculated for this case, making use of previous LHCb analysis in which the asymmetry has been measured in terms of the transverse momentum and rapidity (for kaons) and momentum (for protons) [140]. The found detection asymmetry for protons and kaons is $(1.395 \pm 0.012)\%$ and $(-1.2159 \pm 0.0015)\%$, respectively, and they correspond, in each case, to the detection efficiency for positively-charged particles with respect to negatively-charged particles.

With this, the detection asymmetry for $B^0 \to K^{*0}\gamma$ and $\Lambda_b^0 \to \Lambda^{*0}\gamma$ is $(1.22 \pm 0.25)\%$ and $(2.611 \pm 0.012)\%$, respectively.

Another correction that needs to be introduced is related to the bias induced by the magnetic field, that spreads the particles with different charge to different regions of the detector. If the instrumental performance presented any non-uniformity, a bias in the asymmetry could be introduced. To reduce this possible bias, the magnetic field polarity is flipped regularly during the data taking. The values of the A_{raw}^{CP} at different polarities are compatible within statistical uncertainty and with the luminosity-weighed average, which is, at the same time, compatible with the raw asymmetry when measured to the full data samples, as shown in Table 6.43.

As the luminosity is slightly unbalanced between the two polarities, a residual bias

Table 6.38: *CP* asymmetry measured for each magnet polarity. The last column gives the luminosity-weighed average. Note that the integrated luminosity for the $\Lambda_b^0 \to \Lambda^{*0}\gamma$ decay is not 3 fb^{-1} due to the HLT2 lines not being active for the whole Run 1.

	Magnet Up	Magnet Down	Luminosity-weighed average
$B^0 \to K^{*0}\gamma$			
$\int \mathcal{L}dt$ (pb^{-1})	1511 ± 39	1663 ± 41	3227 ± 57
A_{raw}	$(0.86 \pm 1.45)\%$	$(2.1 \pm 1.2)\%$	$(1.51 \pm 0.93)\%$
Signal candidates	14855 ± 190	12798 ± 171	27653 ± 256
$\Lambda_b^0 \to \Lambda^{*0}\gamma$			
$\int \mathcal{L}dt$ (pb^{-1})	1325 ± 39	1461 ± 41	2786 ± 53
A_{raw}	$(8.13 \pm 1.23)\%$	$(3.77 \pm 2.69)\%$	$(5.84 \pm 1.53)\%$
Signal candidates	2228 ± 41	1893 ± 65	4121 ± 77

could remain. It can be extracted as

$$\Delta A_M = \frac{\mathcal{L}^{up} - \mathcal{L}^{down}}{\mathcal{L}^{up} + \mathcal{L}^{down}} \times \frac{A_{raw}^{down} - A_{raw}^{up}}{2}, \tag{6.29}$$

where $\mathcal{L}^{up(down)}$ is the amount of luminosity collected in the up (down) polarity magnet configuration. For the $B^0 \to K^{*0}\gamma$ and $\Lambda_b^0 \to \Lambda^{*0}\gamma$ cases, it is found

$$\begin{aligned} \Delta A_M(B^0 \to K^{*0}\gamma) &= (0.03 \pm 0.05)\% \\ \Delta A_M(\Lambda_b^0 \to \Lambda^{*0}\gamma) &= (0.11 \pm 0.08)\%, \end{aligned} \tag{6.30}$$

where the uncertainty is related to the finite size of the sample.

6.8.3 Production asymmetries

Due to the quark content of the protons, b- and $\bar{b}$-hadrons are not produced at the same rate at the LHC. The production asymmetry (A_P) can be written in terms of the different production rates as

$$\begin{aligned} A_P(B^0) &= \frac{R(\overline{B}^0) - R(B^0)}{R(\overline{B}^0) + R(B^0)} \\ A_P(\Lambda_b^0) &= \frac{R(\Lambda_b^0) - R(\overline{\Lambda}_b^0)}{R(\Lambda_b^0) + R(\overline{\Lambda}_b^0)}. \end{aligned} \tag{6.31}$$

The LHCb experiment has performed measurements of the production asymmetries for the b-hadrons for the whole Run 1 [141], finding a dependency on the b-hadron transverse momentum and its rapidity. The production asymmetries, averaging over the

whole kinematical and pseudorapidity spectra, are found to be

$$\begin{aligned} A_P(B^0)(\sqrt{s} = 7\,\text{TeV}) &= (-0.4 \pm 0.6)\% \\ A_P(B^0)(\sqrt{s} = 8\,\text{TeV}) &= (-0.95 \pm 0.42)\% \\ A_P(\Lambda_b^0)(\sqrt{s} = 7\,\text{TeV}) &= (1.8 \pm 1.9)\% \\ A_P(\Lambda_b^0)(\sqrt{s} = 8\,\text{TeV}) &= (4.1 \pm 1.3)\%, \end{aligned} \tag{6.32}$$

where the uncertainty accounts for both the statistic and systematic effects. Making use of the integrated luminosity collected each year as a weight, the production asymmetries are

$$\begin{aligned} A_P(B^0) &= (-0.75 \pm 0.34)\% \\ A_P(\Lambda_b^0) &= (3.49 \pm 1.08)\%, \end{aligned} \tag{6.33}$$

where the uncertainty will be added as a systematic in the $\mathcal{A}^{CP}$ measurement.

As pointed out before, the dilution factor is only relevant for the $B^0 \to K^{*0}\gamma$ case since the Λ_b^0 particle does not oscillate. This dilution factor is defined as

$$\kappa = \frac{\int \cos(\Delta m_d t)\, \mathrm{e}^{-\Gamma_d t}\, \epsilon(t) dt}{\int \cosh(\frac{\Delta\Gamma_d}{2} t)\, \mathrm{e}^{-\Gamma_d t}\, \epsilon(t) dt} \tag{6.34}$$

where Δm_d and $\Delta\Gamma_d$ are the mass and decay width differences between the mass eigenstates of the B^0 and $\overline{B}^0$ system, Γ_d is the average of their decay widths and $\epsilon(t)$ is the decay-time acceptance function of the signal selection. The value for Δm_d, $\Delta\Gamma_d$ and Γ_d are taken from previous LHCb measurements [142, 143] and the HFAG averages [144]. The decay-time acceptance function has been extracted from data by means of a fit to background-subtracted data using the following PDF:

$$\epsilon(t) = \frac{[a(t - t_0)]^n}{1 + [a(t - t_0)]^n}, \tag{6.35}$$

where a, t_0 and n are free parameters governing the decay-time acceptance of the selection and reconstruction. The a parameter is kept inside the brackets in order to reduce the correlation between the a and the n parameters. Figure 6.30 shows the decay-time acceptance fitted distribution. Table 6.39 gives the fitted values for the free parameters in the fit as well as the calculated value for κ. A different parametrisation of the acceptance, including an upper decay-time acceptance parameter, has been tried, but the same value of κ has been obtained. As a consequence, no additional systematic uncertainty is assigned to κ.

6.8.4 Results

Adding the calculated (summarized in Table 6.41) corrections to the measured A_{raw}^{CP}, the direct *CP* asymmetry for $B^0 \to K^{*0}\gamma$ and $\Lambda_b^0 \to \Lambda^{*0}\gamma$ using the full Run 1 LHCb data

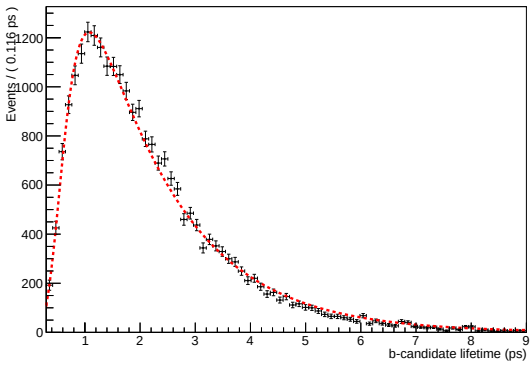

Figure 6.30: Fit of the decay time acceptance function of signal events, extracted with sPlot technique.

Table 6.39: Fitted values for the free parameters of the decay time acceptance function for reconstructed $B^0 \to K^{*0}\gamma$ decays and calculated κ factor.

Parameter	Value
a (ps^{-1})	1.41 ± 0.15
n	3.3 ± 0.4
t_0 (ps)	0.02 ± 0.07
κ	0.41 ± 0.06

sample is measured to be

$$\begin{aligned} \mathcal{A}^{CP}(B^0 \to K^{*0}\gamma) &= (0.54 \pm 0.81\,(\text{stat}) \pm 0.30\,(\text{syst}))\% \\ \mathcal{A}^{CP}(\Lambda_b^0 \to \Lambda^{*0}\gamma) &= (0.11 \pm 1.80\,(\text{stat}) \pm 1.22\,(\text{syst}))\%. \end{aligned} \tag{6.36}$$

where the detailed budget of systematic uncertainties is contained in Table 6.40.

6.8.5 Cross-checks

A series of cross-checks was performed in order to validate the measured value for the raw $\mathcal{A}^{CP}$. These cross-checks were performed over the data corresponding to 2011 and 2012 separately and over the data corresponding to the two possible polarities for the LHCb magnet. Tables 6.42 shows these results, making it clear the compatibility among them.

These values confirm the value obtained when the Run 1 dataset is studied as a whole. However, the central value for the $\mathcal{A}^{CP}$ for the $B^0 \to K^{*0}\gamma$ decay differs slightly from the previously measured by the LHCb [3]. The reason for this remains unclear. A possible explanation would be that the difference is the result of a series of different features of the analysis, such as the inclusion of fiducial cuts in the event selection process.

Table 6.40: Summary of the systematic uncertainties entering in the $\mathcal{A}^{CP}$ calculation.

	$\mathcal{A}^{CP}$ $(B^0 \to K^{*0}\gamma)$	$\mathcal{A}^{CP}$ $(\Lambda_b^0 \to \Lambda^{*0}\gamma)$
Background and signal modeling	$\pm 0.05\%$	$\pm 0.57\%$
Detection asymmetry	$\pm 0.25\%$	$\pm 0.012\%$
Magnetic field asymmetry	$\pm 0.05\%$	$\pm 0.08\%$
Production asymmetry	$\pm 0.15\%$	$\pm 1.08\%$

Table 6.41: Summary of the contributions entering in the $\mathcal{A}^{CP}$ calculation.

	$\mathcal{A}^{CP}$ $(B^0 \to K^{*0}\gamma)$		$\mathcal{A}^{CP}$ $(\Lambda_b^0 \to \Lambda^{*0}\gamma)$	
	Correction (%)	Uncertainty (%)	Correction (%)	Uncertainty(%)
Modeling (ΔA_{model})	0.0	0.05	0.0	0.57
Detect. asym. (A_D)	1.22	0.25	2.611	0.012
Mag. field asym. (ΔA_M)	0.03	0.05	0.11	0.08
Prod. asym. (A_P)	-0.31	0.15	3.49	1.08

Table 6.42: Summary of the measured raw $\mathcal{A}^{CP}$ for different years and polarities.

	$\mathcal{A}^{CP}$ $(B^0 \to K^{*0}\gamma)$	$\mathcal{A}^{CP}$ $(\Lambda_b^0 \to \Lambda^{*0}\gamma)$
Complete Run 1 sample	$(1.42 \pm 0.81)\%$	$(6.1 \pm 1.8)\%$
2011	$(1.39 \pm 1.36)\%$	$(8.3 \pm 4.1)\%$
2012	$(1.45 \pm 0.97)\%$	$(5.5 \pm 2.0)\%$
Magnet Up	$(0.94 \pm 1.11)\%$	$(8.5 \pm 2.5)\%$
Magnet Down	$(2.0 \pm 1.2)\%$	$(3.5 \pm 3.0)\%$

7

Conclusions

This thesis has presented the study of radiative $b \to hh\gamma$ decays at LHCb, performing the world's best measurement of the $B_s^0 \to \phi\gamma$ branching fractions and observing for the first time a radiative decay of a b-baryon, $\Lambda_b^0 \to \Lambda^{*0}\gamma$. Since the measurement of radiative b decays in LHCb requires a very good knowledge of the photon, my contributions to that topic, that is, the calibration of the SPD sub-detector after its ageing in Run 1 and the creation of a tool for the calibration of photons and π^0 efficiencies, have also been presented.

The periodic monitorization throughout the Run 1 of the SPD sub-detector, used to separate charged from neutral clusters in the ECAL, showed an increasing mis-calibration of the SPD cells in terms of their efficiencies. Before and right after the beginning of the Run 1, the SPD cells were calibrated to have an average efficiency of about 95%. The collisions that took place during the Run 1 period implied the presence of radiation inside the LHCb cavern and some of the SPD cells efficiencies decreased; the effect being more visible in those cells close to the beam pipe. While a recovery of the SPD cells efficiency was observed as a consequence of the process of annealing, a new calibration of the SPD cells was needed in order to recover high efficiencies. As a first step, cosmic rays were used to assess the state of recovery of the cells, and afterwards data from the first collisions from Run 2 was used to produce a new calibration to correct the remaining inefficiencies. The new hardware configuration was introduced and the SPD cells were observed to behave as expected, similarly to the beginning of Run 1.

One of the most dangerous backgrounds when studying decays involving photons at LHCb is π^0 that have been reconstructed as a single cluster in the ECAL. A tool has been developed to distinguish this background based on the idea that the clusters that these particles form in the ECAL are slightly different: through variables related to the energy and the shape of the cluster, a multivariate discriminator was built to distinguish between those particles. Two complementary tools were developed in order to facilitate the calculation of the efficiencies of the discriminant, since its behaviour is not well modelled in simulation: the calibration table tool and the resampling tool. The idea is very similar for the two of them and is based on the idea that given a sufficiently small bin of pseudo-rapidity and transverse momentum, the efficiency for a certain cut is the

same for all the decays that involve a photon or a π^0. The calibration table tool, following the same procedure used for charged particle identification, allows to obtain a table of efficiencies in bins of the photon transverse energy and pseudo-rapidity from pure samples of photons and π^0. These tables can be used, along with the kinematics from simulation, to calculate the efficiency of the requirements on the discriminant. The resampling tool, on the other hand, allows to randomly generate values of the discriminator in bins of the same variables as before using the distribution of the same reference samples. This is very useful if one wants to include the discriminator in the training of multivariate classifiers but comes with the cost of the loss of correlations to other variables of the decay.

The analysis discussed in Chapter 6 presents the first observation of a radiative decay of the Λ_b^0 baryon and the world's best measurements of the branching fractions and direct *CP* asymmetries of the involved decay modes. A total of four measurements have been performed using the whole LHCb Run 1 dataset: the branching fractions of $B_s^0 \to \phi\gamma$ and $\Lambda_b^0 \to \Lambda^{*0}\gamma$ have been measured with respect to $B^0 \to K^{*0}\gamma$ and the value for the direct $\mathcal{A}^{CP}$ for $B^0 \to K^{*0}\gamma$ and $\Lambda_b^0 \to \Lambda^{*0}\gamma$ have been obtained.

The ratio of branching fractions have been measured to be

$$\begin{aligned} \frac{\mathcal{B}(B^0 \to K^{*0}\gamma)}{\mathcal{B}(B_s^0 \to \phi\gamma)} &= 1.350 \pm 0.031\,(\text{stat}) \pm 0.041\,(\text{syst}) \pm 0.107(f_s/f_d) \\ \frac{\mathcal{B}(B^0 \to K^{*0}\gamma)}{\mathcal{B}(\Lambda_b^0 \to \Lambda^{*0}\gamma)} &= 1.279 \pm 0.027\,(\text{stat}) \pm 0.059\,(\text{syst}) \pm 0.171(f_\Lambda/f_d). \end{aligned} \tag{7.1}$$

from which it is possible to compute the branching fractions of $B_s^0 \to \phi\gamma$ and $\Lambda_b^0 \to \Lambda^{*0}\gamma$:

$$\begin{aligned} \mathcal{B}(B_s^0 \to \phi\gamma) &= (3.21 \pm 0.28) \times 10^{-5} \\ \mathcal{B}(\Lambda_b^0 \to \Lambda^{*0}\gamma) &= (3.39 \pm 0.48) \times 10^{-5}, \end{aligned} \tag{7.2}$$

These improve the previous measurements in terms of both the statistical and systematic uncertainties. It is worth noting, however, that the measurement of the branching fraction of $\Lambda_b^0 \to \Lambda^{*0}\gamma$ is dominated (apart from the ratio of hadronization fractions) by a large systematic caused by the lack of knowledge of the resonance contents of the pK system. This could probably be improved, in a future work, by the study of a double ratio of branching fractions involving J/ψ channels, which could be used to control the systematic uncertainties of the pK system.

The direct *CP* asymmetries of $B_s^0 \to \phi\gamma$ and $\Lambda_b^0 \to \Lambda^{*0}\gamma$ have been measured to be

$$\begin{aligned} \mathcal{A}^{CP}(B^0 \to K^{*0}\gamma) &= (0.54 \pm 0.81\,(\text{stat}) \pm 0.30\,(\text{syst}))\% \\ \mathcal{A}^{CP}(\Lambda_b^0 \to \Lambda^{*0}\gamma) &= (0.11 \pm 1.8\,(\text{stat}) \pm 1.22\,(\text{syst}))\%. \end{aligned} \tag{7.3}$$

In this case, the improvement in the systematic uncertainties of $\mathcal{A}^{CP}$ of $B^0 \to K^{*0}\gamma$ with respect to the previous LHCb measurement — crucial to avoid falling into the systematics-dominated regime — is remarkable, and it is driven by the inclusion of the $\Lambda_b^0 \to \Lambda^{*0}\gamma$ mode in the fit, the $\mathcal{A}^{CP}$ of which has been measured for the first time here.

During the recently started LHC Run 2, a large amount of data is expected, which will help to reduce the uncertainties associated to the measurements presented here. In addition, a larger amount of data will also allow the measurement of new observables via the use of radiative decays, such as a the photon polarization in $B \to K\pi\pi\gamma$ decays and isospin asymmetry of $B^0 \to K^{*0}\gamma$, among others.

Bibliography

[1] A. Ali, B. D. Pecjak, and C. Greub, *Towards $B \to V\gamma$ decays at NNLO in SCET*, The European Physical Journal C **55** (2008), no. 4 577.

[2] M. Matsumori, A. I. Sanda, and Y.-Y. Keum, *CP asymmetry, branching ratios and isospin breaking effects of $B^0 \to K^{*0}\gamma$ with perturbative QCD approach*, Phys. Rev. D **72** (2005) 014013.

[3] R. Aaij *et al.*, *Measurement of the ratio of branching fractions $\mathcal{B}(B^0 \to K^{*0}\gamma)/\mathcal{B}(B_s^0 \to \phi\gamma)$ and the direct CP asymmetry in $B^0 \to K^{*0}\gamma$*, Nucl. Phys. **B867** (2013) 1.

[4] Particle Data Group, K. A. Olive *et al.*, *Review of Particle Physics*, Chin. Phys. **C38** (2014) 090001.

[5] ATLAS collaboration, G. Aad *et al.*, *Observation of a new particle in the search for the Standard Model Higgs boson with the ATLAS detector at the LHC*, Phys. Lett. **B716** (2012) 1, `arXiv:1207.7214`.

[6] CMS collaboration, S. Chatrchyan *et al.*, *Observation of a new boson at a mass of 125 GeV with the CMS experiment at the LHC*, Phys. Lett. **B716** (2012) 30, `arXiv:1207.7235`.

[7] A. D. Sakharov, *Violation of CP invariance, C asymmetry, and baryon asymmetry of the universe*, Soviet Physics Uspekhi **34** (1991), no. 5 392.

[8] M. Kobayashi and T. Maskawa, *CP Violation in the Renormalizable Theory of Weak Interaction*, Prog. Theor. Phys. **49** (1973) 652.

[9] M. E. Shaposhnikov, *Possible Appearance of the Baryon Asymmetry of the Universe in an Electroweak Theory*, JETP Lett. **44** (1986) 465, Pisma Zh. Eksp. Teor. Fiz.44,364(1986).

[10] J. H. Christenson, J. W. Cronin, V. L. Fitch, and R. Turlay, *Evidence for the 2π Decay of the K_2^0 Meson*, Phys. Rev. Lett. **13** (1964) 138.

[11] Belle collaboration, K. Abe *et al.*, *Observation of Large CP Violation in the Neutral B Meson System*, Phys. Rev. Lett. **87** (2001) 091802.

[12] BaBar collaboration, B. Aubert *et al.*, *Measurement of the $B^0 - \overline{B}^0$ Oscillation Frequency with Inclusive Dilepton Events*, Phys. Rev. Lett. **88** (2002) 221803.

[13] M. Y. Han and Y. Nambu, *Three-Triplet Model with Double* SU(3) *Symmetry*, Phys. Rev. **139** (1965) B1006.

[14] S. L. Glashow, *Partial Symmetries of Weak Interactions*, Nucl. Phys. **22** (1961) 579.

[15] S. Weinberg, *A Model of Leptons*, Phys. Rev. Lett. **19** (1967) 1264.

[16] A. Salam, *Weak and Electromagnetic Interactions*, Conf. Proc. **C680519** (1968) 367.

[17] A. Pomarol. *Lectures on the Frontiers of the SM (2011).*

[18] I. Antoniadis and D. Ghilencea, *Supersymmetry after the Higgs discovery*, Eur. Phys. J. C **74** (2014), no. 5 2841.

[19] P. Fayet, *The supersymmetric standard model*, Eur. Phys. J. C **74** (2014), no. 5 2837.

[20] I. Melzer-Pellmann and P. Pralavorio, *Lessons for SUSY from the LHC after the first run*, Eur. Phys. J. C **74** (2014), no. 5 2801.

[21] B. Bellazzini, C. Cski, and J. Serra, *Composite Higgses*, Eur. Phys. J. C **74** (2014), no. 5 2766.

[22] J. Ellis, *Supersymmetric fits after the Higgs discovery and implications for model building*, Eur. Phys. J. C **74** (2014), no. 5 2732.

[23] H. P. Nilles, *The strings connection: MSSM-like models from strings*, Eur. Phys. J. C **74** (2014), no. 5 2712.

[24] A. Djouadi, *Implications of the Higgs discovery for the MSSM*, Eur. Phys. J. C **74** (2014), no. 5 2704.

[25] R. Catena and L. Covi, *SUSY dark matter(s)*, Eur. Phys. J. C **74** (2014), no. 5 2703.

[26] G. G. Ross, *SUSY: Quo Vadis?*, Eur. Phys. J. C **74** (2014), no. 5 2699.

[27] P. Ramond, *SUSY: the early years (1966 to 1976)*, Eur. Phys. J. C **74** (2014), no. 5 2698.

[28] C. N. Yang and R. L. Mills, *Conservation of Isotopic Spin and Isotopic Gauge Invariance*, Phys. Rev. **96** (1954) 191.

[29] F. Englert and R. Brout, *Broken Symmetry and the Mass of Gauge Vector Mesons*, Phys. Rev. Lett. **13** (1964) 321.

[30] P. W. Higgs, *Broken symmetries, massless particles and gauge fields*, Phys. Lett. **12** (1964) 132.

[31] P. W. Higgs, *Broken Symmetries and the Masses of Gauge Bosons*, Phys. Rev. Lett. **13** (1964) 508.

[32] G. S. Guralnik, C. R. Hagen, and T. W. B. Kibble, *Global Conservation Laws and Massless Particles*, Phys. Rev. Lett. **13** (1964) 585.

[33] P. W. Higgs, *Spontaneous Symmetry Breakdown without Massless Bosons*, Phys. Rev. **145** (1966) 1156.

[34] T. W. B. Kibble, *Symmetry breaking in Non-Abelian gauge theories*, Phys. Rev. **155** (1967) 1554.

[35] R. Fleischer, *CP violation and the role of electroweak penguins in nonleptonic B decays*, Int. J. Mod. Phys. **A12** (1997) 2459, arXiv:hep-ph/9612446.

[36] A. Pich, *Effective field theory: Course*, in *Probing the standard model of particle interactions. Proceedings, Summer School in Theoretical Physics, NATO Advanced Study Institute, 68th session, Les Houches, France, July 28-September 5, 1997. Pt. 1, 2*, pp. 949–1049, 1998. arXiv:hep-ph/9806303.

[37] K. G. Wilson, *Nonlagrangian models of current algebra*, Phys. Rev. **179** (1969) 1499.

[38] G. Buchalla, A. J. Buras, and M. E. Lautenbacher, *Weak decays beyond leading logarithms*, Rev. Mod. Phys. **68** (1996) 1125.

[39] N. Cabibbo, *Unitary Symmetry and Leptonic Decays*, Phys. Rev. Lett. **10** (1963) 531.

[40] A. J. Buras and R. Fleischer, *Quark mixing, CP violation and rare decays after the top quark discovery*, Adv. Ser. Direct. High Energy Phys. **15** (1998) 65, arXiv:hep-ph/9704376.

[41] C. Dib, I. Dunietz, F. J. Gilman, and Y. Nir, *Standard Model Predictions for CP Violation in B^0 Meson Decay*, Phys. Rev. **D41** (1990) 1522.

[42] *CKM Fitter Group*, https://ckmfitter.in2p3.fr/.

[43] I. I. Y. Bigi and A. I. Sanda, *CP violation*, Camb. Monogr. Part. Phys. Nucl. Phys. Cosmol. **9** (2000) 1.

[44] S. L. Glashow, J. Iliopoulos, and L. Maiani, *Weak interactions with lepton-hadron symmetry*, Phys. Rev. **D2** (1970) 1285.

[45] *CERN in figures*, https://cds.cern.ch/record/1710513, 2014.

[46] L. Evans and P. Bryant, *LHC Machine*, Journal of Instrumentation **3** (2008), no. 08 S08001.

[47] C. Rubbia, *The Discovery of the W and Z bosons*, Phys. Rept. **239** (1994) 241.

[48] ALICE collaboration, K. Aamodt *et al.*, *The ALICE experiment at the CERN LHC*, JINST **3** (2008) S08002.

[49] ATLAS collaboration, G. Aad *et al.*, *The ATLAS Experiment at the CERN Large Hadron Collider*, JINST **3** (2008) S08003.

[50] CMS collaboration, S. Chatrchyan *et al.*, *The CMS experiment at the CERN LHC*, JINST **3** (2008) S08004.

[51] LHCf collaboration, O. Adriani *et al.*, *The LHCf detector at the CERN Large Hadron Collider*, JINST **3** (2008) S08006.

[52] MoEDAL collaboration, J. Pinfold *et al.*, *Technical Design Report of the MoEDAL Experiment*, CERN-LHCC-2009-006. MoEDAL-TDR-001.

[53] TOTEM collaboration, G. Anelli *et al.*, *The TOTEM experiment at the CERN Large Hadron Collider*, JINST **3** (2008) S08007.

[54] LHCb collaboration, A. A. Alves, Jr. *et al.*, *The LHCb Detector at the LHC*, JINST **3** (2008) S08005.

[55] LHCb collaboration, A. A. Alves, Jr. *et al.*, *LHCb reoptimized detector design and performance: Technical Design Report*, Technical Design Report LHCb, CERN, Geneva, 2003.

[56] LHCb collaboration, A. A. Alves, Jr. *et al.*, *LHCb: Technical Proposal*, Tech. Proposal, CERN, Geneva, 1998.

[57] LHCb collaboration, P. R. Barbosa-Marinho *et al.*, *LHCb VELO (VErtex LOcator): Technical Design Report*, Technical Design Report LHCb, CERN, Geneva, 2001.

[58] LHCb Collaboration, A. A. Alves, Jr. *et al.*, *LHCb reoptimized detector design and performance: Technical Design Report*, Technical Design Report LHCb, CERN, Geneva, 2003.

[59] J. Gassner, M. Needham, and O. Steinkamp, *Layout and Expected Performance of the LHCb TT Station*, LHCb-2003-140.

[60] LHCb collaboration, S. Amato *et al.*, *LHCb magnet: Technical Design Report*, Technical Design Report LHCb, CERN, Geneva, 2000.

[61] J. Andre *et al.*, *Status of the LHCb magnet system*, Applied Superconductivity, IEEE Transactions on **12** (2002) 366.

[62] J. Andre *et al.*, *Status of the LHCb dipole magnet*, Applied Superconductivity, IEEE Transactions on **14** (2004) 509.

[63] LHCb collaboration, P. R. Barbosa-Marinho *et al.*, *LHCb inner tracker: Technical Design Report*, Technical Design Report LHCb, CERN, Geneva, 2002.

[64] LHCb collaboration, P. R. Barbosa-Marinho *et al.*, *LHCb outer tracker: Technical Design Report*, Technical Design Report LHCb, CERN, Geneva, 2001.

[65] LHCb collaboration, S. Amato *et al.*, *LHCb calorimeters: Technical Design Report*, Technical Design Report LHCb, CERN, Geneva, 2000.

[66] A. Arefev *et al.*, *Beam Test Results of the LHCb Electromagnetic Calorimeter*, LHCb-2007-149.

[67] World Scientific, , (Singapore), World Scientific, 2006.

[68] Y. Guz and the LHCb collaboration, *The LHCb Hadron Calorimeter*, Journal of Physics: Conference Series **160** (2009), no. 1 012054.

[69] LHCb collaboration, P. R. Barbosa-Marinho *et al.*, *LHCb muon system: Technical Design Report*, Technical Design Report LHCb, CERN, Geneva, 2001.

[70] LHCb Collaboration, *LHCb muon system: addendum to the Technical Design Report*, Technical Design Report LHCb, CERN, Geneva, 2003.

[71] LHCb Collaboration, *LHCb muon system: second addendum to the Technical Design Report*, Technical Design Report LHCb, CERN, Geneva, 2005. Submitted on 9 Apr 2005.

[72] M. Adinolfi *et al.*, *Performance of the LHCb RICH detector at the LHC*, Eur. Phys. J. **C73** (2013) 2431, `arXiv:1211.6759`.

[73] N. H. Brook *et al.*, *LHCb RICH 1 engineering design review report*, CERN-LHCB-2004-121.

[74] LHCb collaboration, S. Amato *et al.*, *LHCb RICH: Technical Design Report*, Technical Design Report LHCb, CERN, Geneva, 2000.

[75] M. Adinolfi *et al.*, *LHCb RICH 2 engineering design review report*, LHCb-2002-009.

[76] LHCb collaboration, R. Antunes-Nobrega *et al.*, *LHCb trigger system: Technical Design Report*, Technical Design Report LHCb, CERN, Geneva, 2003.

[77] A. Puig Navarro and R. Graciani Diaz, *First measurements of radiative B decays in LHCb*, PhD thesis, Barcelona U., 2012, Presented 09 Mar 2012.

[78] R. Aaij *et al.*, *The LHCb Trigger and its Performance in 2011*, JINST **8** (2013) P04022, `arXiv:1211.3055`.

[79] LHCb HLT project, J. Albrecht, V. V. Gligorov, G. Raven, and S. Tolk, *Performance of the LHCb High Level Trigger in 2012*, J. Phys. Conf. Ser. **513** (2014) 012001, arXiv:1310.8544.

[80] R. Vázquez, *Measurement of the direct CP asymmetry in $B^0 \to K^{*0}\gamma$ decays with the LHCb detector*, PhD thesis, Barcelona U., Oct, 2012, Presented 12 Dec 2012.

[81] V. V. Gligorov, *A single track HLT1 trigger*, LHCb-PUB-2011-003.

[82] R. Aaij and J. Albrecht, *Muon triggers in the High Level Trigger of LHCb*, LHCb-PUB-2011-017.

[83] LHCb collaboration, P. R. Barbosa-Marinho *et al.*, *LHCb online system, data acquisition and experiment control: Technical Design Report*, Technical Design Report LHCb, CERN, Geneva, 2001.

[84] LHCb collaboration, R. Antunes-Nobrega *et al.*, *LHCb computing: Technical Design Report*, Technical Design Report LHCb, CERN, Geneva, 2005.

[85] *Vertex Resolution Conference Plots*, https://lbtwiki.cern.ch/bin/view/VELO/VELOConfPlots_VertexResols.

[86] *RICH PID Performance Plots*, https://lbtwiki.cern.ch/bin/view/RICH/RichPIDPerformancePlots.

[87] LHCb collaboration, R. Aaij *et al.*, *LHCb detector performance*, Int. J. Mod. Phys. **A30** (2015) 1530022, arXiv:1412.6352.

[88] O. Deschamps *et al.*, *Photon and neutral pion reconstruction*, LHCb-2003-091.

[89] F. Archilli *et al.*, *Performance of the muon identification at LHCb*, JINST **8** (2013) P10020, arXiv:1306.0249.

[90] E. Polycarpo Macedo *et al.*, *Performance of the Muon Identification in LHCb with 2011 data*, LHCb-INT-2012-016.

[91] LHCb collaboration, R. Aaij *et al.*, *Absolute luminosity measurements with the LHCb detector at the LHC*, JINST **7** (2012) P01010, arXiv:1110.2866.

[92] LHCb, R. Aaij *et al.*, *Precision luminosity measurements at LHCb*, JINST **9** (2014), no. 12 P12005, arXiv:1410.0149.

[93] LHCb collaboration, R. Aaij *et al.*, *Measurement of two-particle correlations in proton-ion collisions at $\sqrt{s_{NN}} = 5$ TeV*, arXiv:1512.0043.

[94] LHCb collaboration, R. Aaij *et al.*, *Observation of Z production in proton-lead collisions at LHCb*, JHEP **09** (2014) 030, arXiv:1406.2885.

[95] B. Schmidt, *Results from pPb collisions and prospects for heavy-ion interactions with LHCb*, LHCb-PROC-2015-028.

[96] R. Vazquez Gomez *et al.*, *Calibration and alignment of the SPD detector with cosmic rays and first LHC collisions*, LHCb-PUB-2011-024.

[97] L. Landau, *On the energy loss of fast particles by ionization*, J. Phys. (USSR) **8** (1944) 201.

[98] M. Calvo, *Backsplash Effects on SPD and Flavour Tagging in LHCb*, PhD thesis, Barcelona U., Barcelona, 2006, Presented on 09 Jan 2006.

[99] E. Aguiló *et al.*, *Mean current in Ps/Spd multiAnode PhotoMultipliers Tubes*, LHCb-2003-003.

[100] M. Calvi *et al.*, *Aging and time resolution measurements for the Hamamatsu R7600 multi-anode photomultiplier tube*, in *Nuclear Science Symposium and Medical Imaging Conference (NSS/MIC), 2011 IEEE*, pp. 1638–1641, Oct, 2011. doi: 10.1109/NSSMIC.2011.6154651.

[101] L. H. Van Vlack, *Elements of Materials Science and Engineering*, Pearson, 1989.

[102] A. T. Mamadalimov, B. L. Oksengendler, and N. N. Turaeva, *Electronic theory of irradiation-induced disordering and annealing in semiconductors*, Russian Physics Journal **49** (2006), no. 4 420.

[103] M. Calvo Gomez *et al.*, *A tool for γ/π^0 separation at high energies*, LHCb-PUB-2015-016.

[104] *LHCb Urania Project*, `http://lhcb-release-area.web.cern.ch/LHCb-release-area/DOC/urania/`.

[105] *LHCb Urania PIDCalib package*, `https://twiki.cern.ch/twiki/bin/view/LHCb/PIDCalibPackage`.

[106] S. Barsuk, *γ/π^0 separation at very high E_{T}*, Presentation at Calo Software Meeting on May 20, 2003.

[107] A. Hoecker *et al.*, *TMVA: Toolkit for Multivariate Data Analysis*, PoS **ACAT** (2007) 040, `arXiv:physics/0703039`.

[108] M. Pivk and F. R. Le Diberder, *sPlot: a statistical tool to unfold data distributions*, Nucl. Instrum. Meth. **A555** (2005) 356, `arXiv:physics/0402083`.

[109] D. A. Roa Romero, *Study of charmless $B^0_{d,s} \to h^+h'^-\pi^0$ decays in LHCb*, PhD thesis, Clermont-Ferrand U., May, 2013, Presented 24 May 2013.

[110] M. C. *et al.* , *Separation and Resampling Tool for the γ/π^0 separation variable*, `https://twiki.cern.ch/twiki/bin/view/LHCbPhysics/GammaPi0SeparationResamplingTool`.

[111] P. Group, *MC resampling tool for $B^0 \to K^{*0}\mu^+\mu^-$*, `https://twiki.cern.ch/twiki/bin/view/LHCb/GlobalParticleID#MC_resampling_tool`.

[112] F. Legger and T. Schietinger, *Photon helicity in Λ_b decays*, Phys. Lett. **B645** (2007) 204.

[113] H. Zhang, J. Tulpan, M. Shrestha, and D. M. Manley, *Multichannel parametrization of $\bar{K}N$ scattering amplitudes and extraction of resonance parameters*, Phys. Rev. **C88** (2013), no. 3 035205, `arXiv:1305.4575`.

[114] A. de Bellefon *et al.*, *New Data on the Reactions K- p –¿ anti-K0 n and K- p –¿ K- p Between 1.934-GeV/c and 2.516-GeV/c, Partial Wave Analysis of These Channels and SU(3) Classification of the New Y* States Observed*, Nuovo Cim. **A42** (1977) 403.

[115] CLEO Collaboration, T. E. Coan *et al.*, *Study of Exclusive Radiative B Meson Decays*, Phys. Rev. Lett. **84** (2000) 5283.

[116] BaBar collaboration, B. Aubert *et al.*, *Measurement of Branching Fractions and CP and Isospin Asymmetries in $B \to K^*(892)\gamma$ Decays*, Phys. Rev. Lett. **103** (2009) 211802, `arXiv:0906.2177`.

[117] Belle collaboration, M. Nakao *et al.*, *Measurement of the $B \to K^*\gamma$ branching fractions and asymmetries*, Phys. Rev. D **69** (2004) 112001.

[118] Belle collaboration, J. Wicht *et al.*, *Observation of $B_s^0 \to \varphi\gamma$ and Search for $B_s^0 \to \gamma\gamma$ Decays at Belle*, Phys. Rev. Lett. **100** (2008) 121801.

[119] A. Puig, *The LHCb trigger in 2011 and 2012*, LHCb-PUB-2014-046.

[120] LHCb, R. Aaij *et al.*, *Measurement of the difference of time-integrated CP asymmetries in $D^0 \to K^-K^+$ and $D^0 \to \pi^-\pi^+$ decays*, Phys. Rev. Lett. **116** (2016) 191601, `arXiv:1602.0316`.

[121] LHCb, R. Aaij *et al.*, *Observation of photon polarization in the $b \to s\gamma$ transition*, Phys. Rev. Lett. **112** (2014), no. 16 161801, `arXiv:1402.6852`.

[122] *PID studies and particle selection*, `https://indico.cern.ch/event/292215/contributions/666877/attachments/546224/752909/16Jan14_Radiatives.pdf`.

[123] L. Shchutska, A. Golutvin, and I. Belyaev, *Study of radiative penguin decays $B^0 \to K^{*0}\gamma$ and $B_s^0 \to \phi\gamma$ at LHCb*, LHCb-2007-030.

[124] T. Skwarnicki, *A study of the radiative CASCADE transitions between the Upsilon-Prime and Upsilon resonances*, PhD thesis, Cracow, INP, 1986.

[125] LHCb collaboration, R. Aaij *et al.*, *Measurement of the relative yields of the decay modes $B^0 \to D^-\pi^+$, $B^0 \to D^-K^+$, $B^0_s \to D^-_s\pi^+$, and determination of f_s/f_d for 7 TeV pp collisions*, LHCb-CONF-2011-013.

[126] K. Bruyn and P. Koppenburg, *Understanding the high mass tail of the reconstructed B mass distribution*, Talk at PPMTS on September 12, 2011.

[127] LHCb collaboration, R. Aaij *et al.*, *Measurement of b hadron production fractions in 7 TeV pp collisions*, Phys. Rev. **D85** (2012) 032008.

[128] H. Albrecht *et al.*, *Search for hadronic b→u decays*, Physics Letters B **241** (1990), no. 2 278.

[129] M. Calvo *et al.*, *Photon polarization in $B^0_s \to \phi\gamma$*, LHCb-ANA-2014-102.

[130] A. Ali *et al.*, *Charmless non-leptonic B_s decays to PP, PV and VV final states in the pQCD approach*, Phys. Rev. **D76** (2007) 074018, arXiv:hep-ph/0703162.

[131] W. Verkerke and D. Kirkby, *The RooFit toolkit for data modeling*, eConf **C0303241** (2003) MOLT007, arXiv:physics/0306116.

[132] F. James and M. Roos, *Minuit: A System for Function Minimization and Analysis of the Parameter Errors and Correlations*, Comput. Phys. Commun. **10** (1975) 343.

[133] LHCb collaboration, R. Aaij *et al.*, *Measurement of the fragmentation fraction ratio f_s/f_d and its dependence on B meson kinematics*, JHEP **04** (2013) 001, arXiv:1301.5286.

[134] LHCb collaboration, R. Aaij *et al.*, *Study of the kinematic dependences of Λ_b production in pp collisions and a measurement of the Lambda$_b \to \Lambda^+_c\pi^-$ branching fraction*, JHEP **08** (2014) 143, arXiv:1405.6842.

[135] A. Rogozhnikov, *Machine learning algorithms for high energy physics*, https://arogozhnikov.github.io/hep_ml/.

[136] M. De Cian, U. Straumann, O. Steinkamp, and N. Serra, *Track Reconstruction Efficiency and Analysis of $B^0 \to K^{*0}\mu^+\mu^-$ at the LHCb Experiment*, PhD thesis, Zurich U., Sep, 2013, Presented 14 Mar 2013.

[137] M. K. *et al.* , *LHCb tracking efficiencies*, https://twiki.cern.ch/twiki/bin/view/LHCb/LHCbTrackingEfficiencies.

[138] S. Tolk, J. Albrecht, F. Dettori, and A. Pellegrino, *Data-driven measurement of trigger efficiencies with the TisTos method*, LHCb-INT-2013-038.

[139] R. Aaij *et al.*, *Measurement of the production asymmetry in 7 TeV pp collisions* , Physics Letters B **713** (2012), no. 3 186 .

[140] LHCb Collaboration, R. Aaij *et al.*, *Observation of $J/\psi p$ Resonances Consistent with Pentaquark States in $\Lambda_b^0 \to J/\psi K^- p$ Decays*, Phys. Rev. Lett. **115** (2015) 072001.

[141] A. Carbone, F. Ferrari, S. Perazzini, and V. Vagnoni, *Measurement of B^0, B_s^0, B^+ and Λ_b^0 production asymmetries in 7 TeV and 8 TeV pp collisions* , LHCb-ANA-2016-037.

[142] LHCb, R. Aaij *et al.*, *A precise measurement of the B^0 meson oscillation frequency*, `arXiv:1604.0347`.

[143] LHCb, R. Aaij *et al.*, *Effective lifetime measurements in the $B_s^0 \to K^+K^-$, $B^0 \to K^+\pi^-$ and $B_s^0 \to \pi^+K^-$ decays*, Phys. Lett. **B736** (2014) 446, `arXiv:1406.7204`.

[144] Heavy Flavor Averaging Group, Y. Amhis *et al.*, *Averages of b-hadron, c-hadron, and τ-lepton properties as of summer 2014*, `arXiv:1412.7515`.

Appendices

Appendix A

Resampling tool for the γ/π^0 separation variable additional plots

TMVA input variables distributions for the inner, middle and outer parts

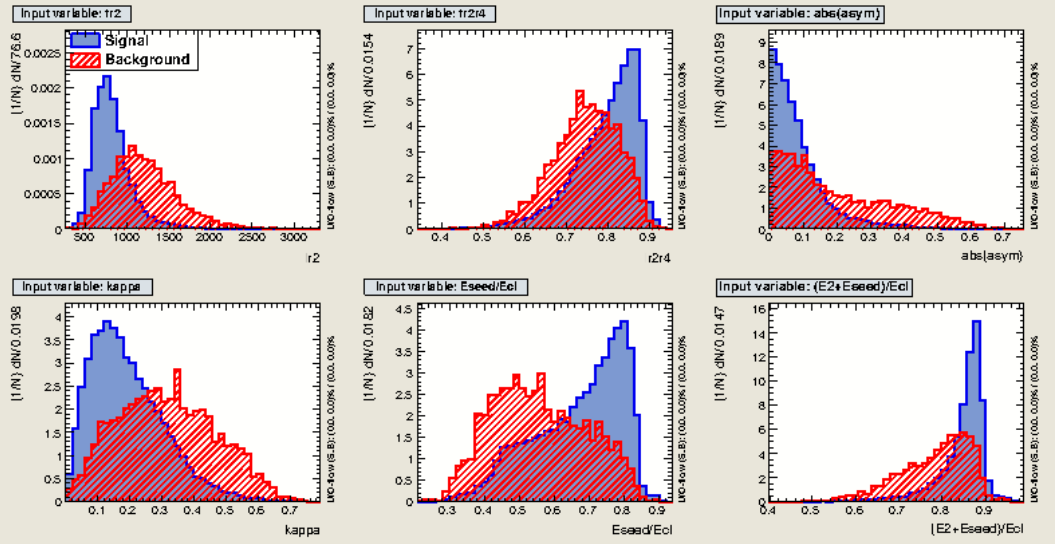

Figure A.1: Distributions of ECAL cluster shape variables $r2$, $r2r4$, $|asym|$, κ, $E_{\text{seed}}/E_{\text{cl}}$ and $(E_{\text{seed}} + E_{2nd})/E_{\text{cl}}$ for true MC photons (blue solid histogram) and true MC merged π^0 selected as photons (red dashed histogram) in the inner region. Histograms are normalized to unity.

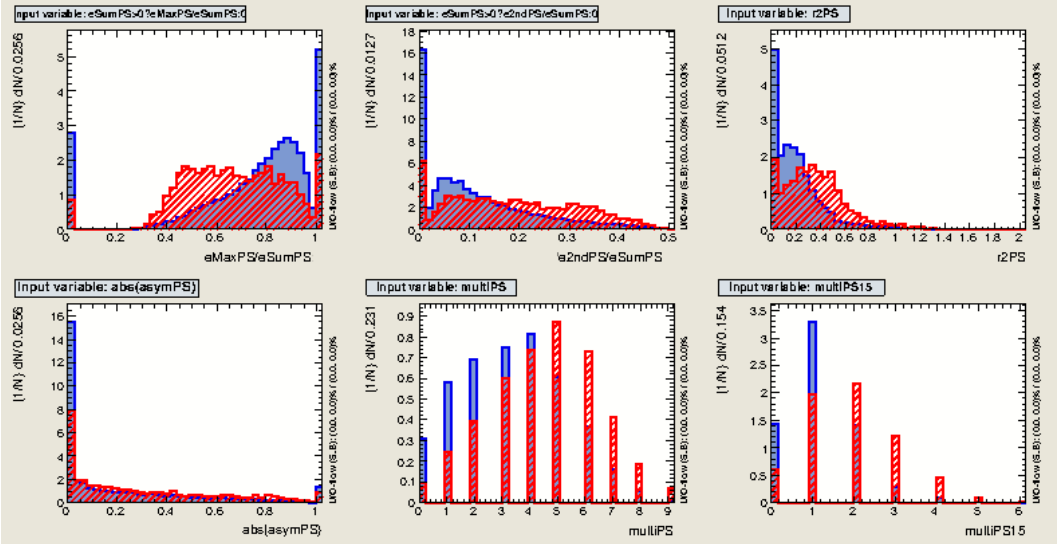

Figure A.2: Distributions of PS variables $E_{\max}/E_{\text{sum}}$, E_{2nd}/E_{sum}, $r2$, $|asym|$, $multi$ and $multi15$ for true MC photons (blue solid histogram) and true MC merged π^0 selected as photons (red dashed histogram) in the inner region. Histograms are normalized to unity.

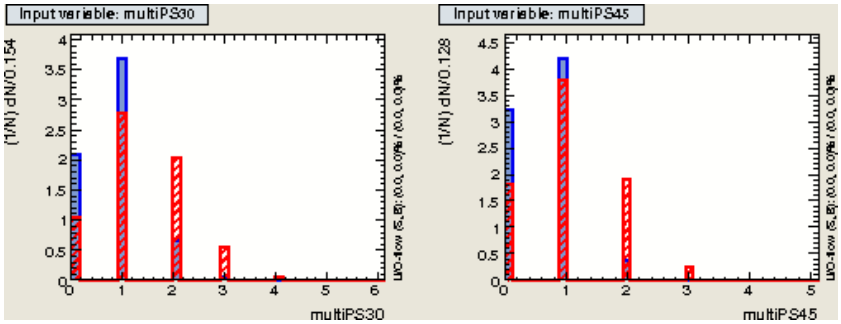

Figure A.3: Distributions of PS $multi30$ and $multi45$ for true MC photons (blue solid histogram) and true MC merged π^0 selected as photons (red dashed histogram) in the inner region. Histograms are normalized to unity.

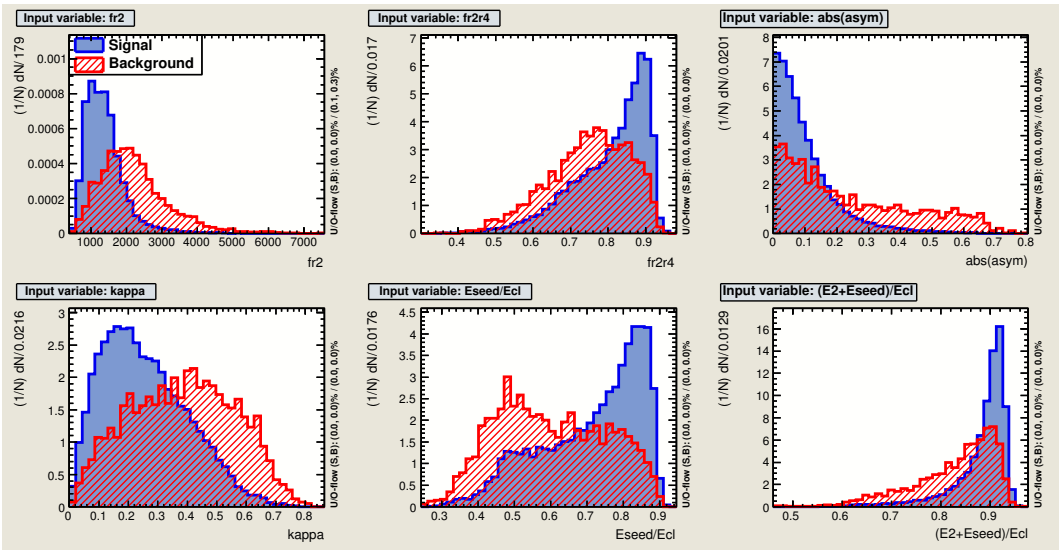

Figure A.4: Distributions of ECAL cluster shape variables $r2$, $r2r4$, $|asym|$, κ, $E_{\text{seed}}/E_{\text{cl}}$ and $(E_{\text{seed}} + E_{2nd})/E_{\text{cl}}$ for true MC photons (blue solid histogram) and true MC merged π^0 selected as photons (red dashed histogram) in the middle region. Histograms are normalized to unity.

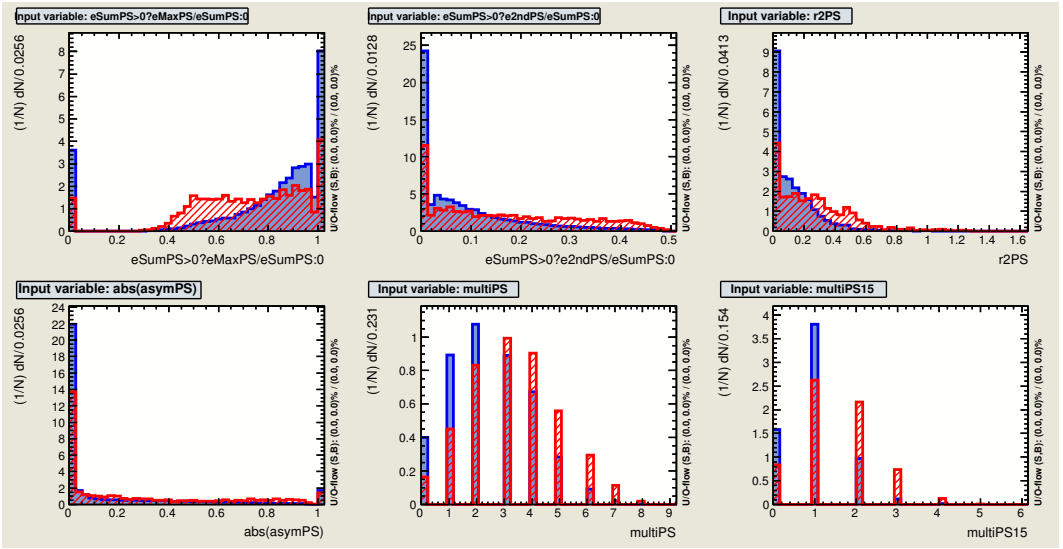

Figure A.5: Distributions of PS variables $E_{\text{max}}/E_{\text{sum}}$, E_{2nd}/E_{sum}, $r2$, $|asym|$, $multi$ and $multi15$ for true MC photons (blue solid histogram) and true MC merged π^0 selected as photons (red dashed histogram) in the middle region. Histograms are normalized to unity.

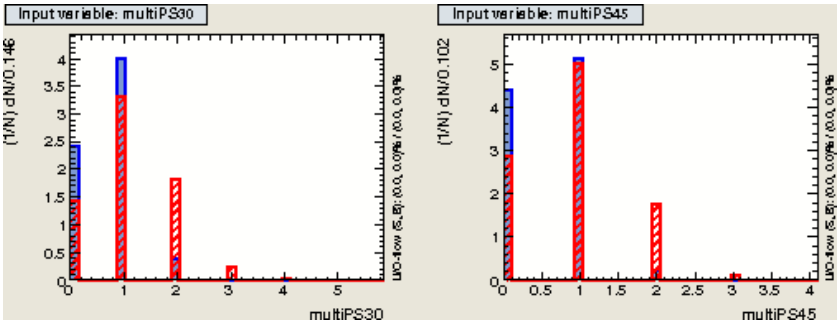

Figure A.6: Distributions of PS *multi*30 and *multi*45 for true MC photons (blue solid histogram) and true MC merged π^0 selected as photons (red dashed histogram) in the MIDDLE region. Histograms are normalized to unity.

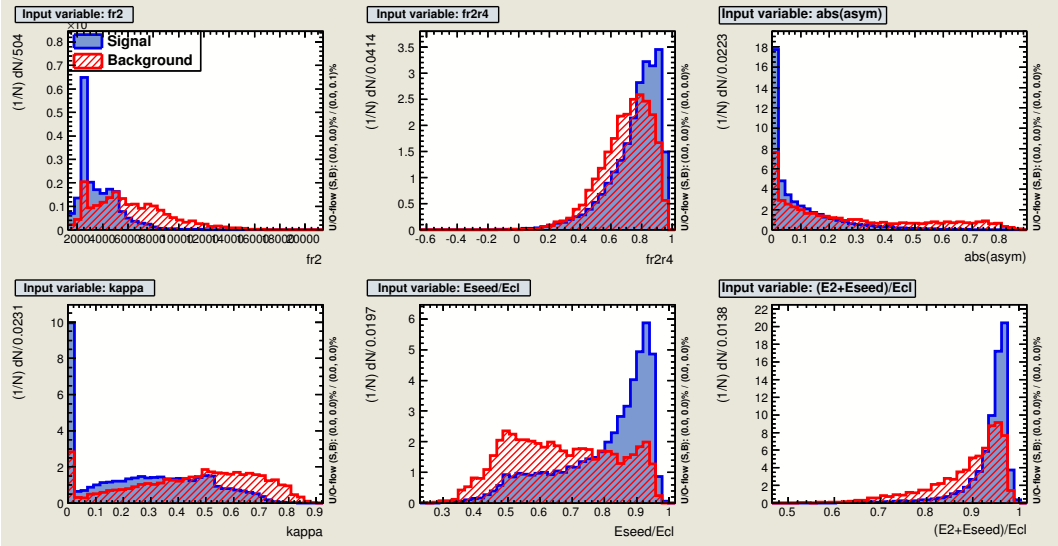

Figure A.7: Distributions of ECAL cluster shape variables $r2$, $r2r4$, $|asym|$, κ, $E_{\mathrm{seed}}/E_{\mathrm{cl}}$ and $(E_{\mathrm{seed}} + E_{2nd})/E_{\mathrm{cl}}$ for true MC photons (blue solid histogram) and true MC merged π^0 selected as photons (red dashed histogram) in the outer region. Histograms are normalized to unity.

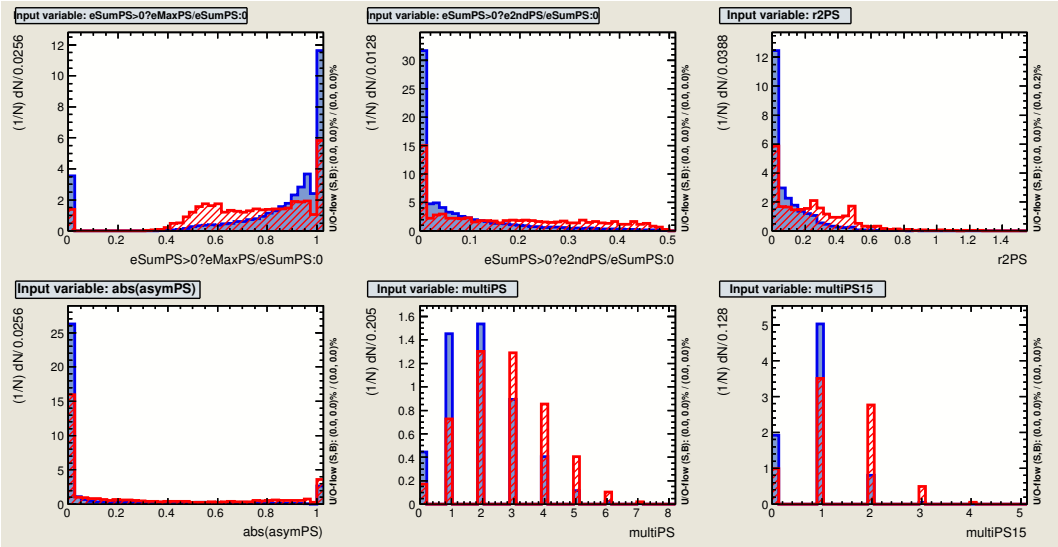

Figure A.8: Distributions of PS variables $E_{\max}/E_{\text{sum}}$, E_{2nd}/E_{sum}, $r2$, $|asym|$, *multi* and *multi*15 for true MC photons (blue solid histogram) and true MC merged π^0 selected as photons (red dashed histogram) in the outer region. Histograms are normalized to unity.

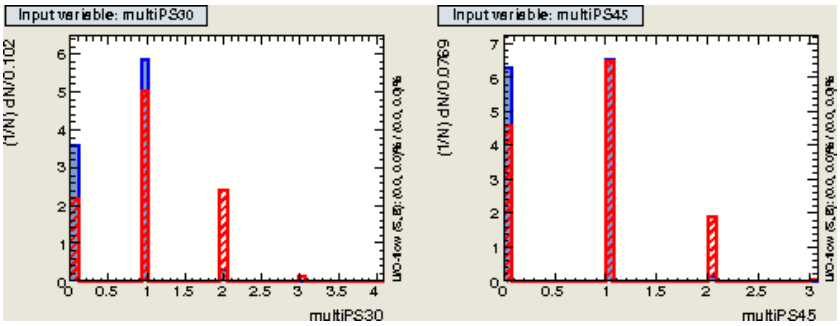

Figure A.9: Distributions of PS *multi*30 and *multi*45 for true MC photons (blue solid histogram) and true MC merged π^0 selected as photons (red dashed histogram) in the OUTER region. Histograms are normalized to unity.

Photon efficiency and rejection distribution and ROC curves

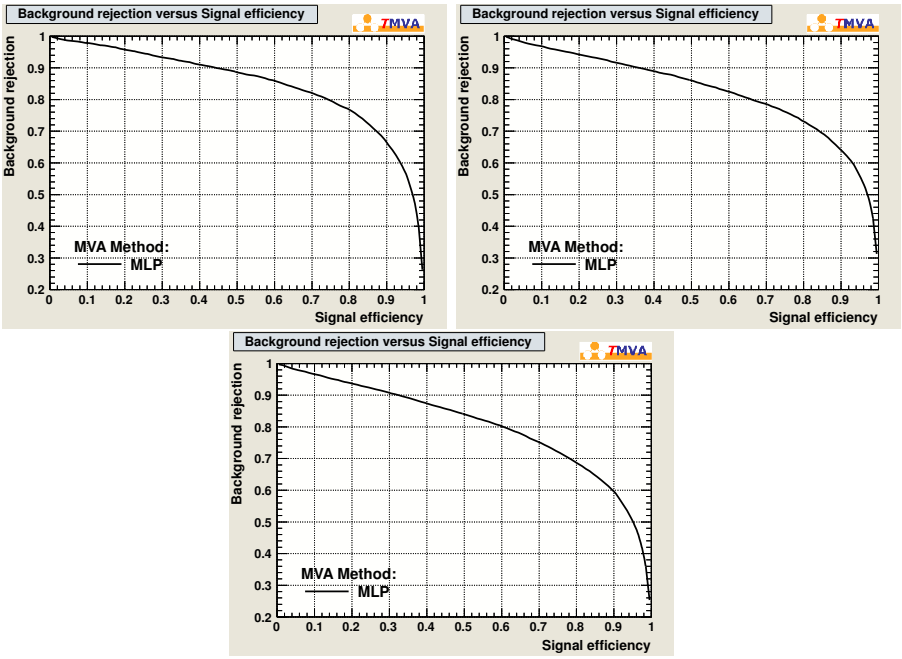

Figure A.10: Performance of the MLP tool on the test sample, different than the training one. The plots show the π^0 rejection vs photon efficiency for inner (top left), middle (top right) and outer (bottom) regions.

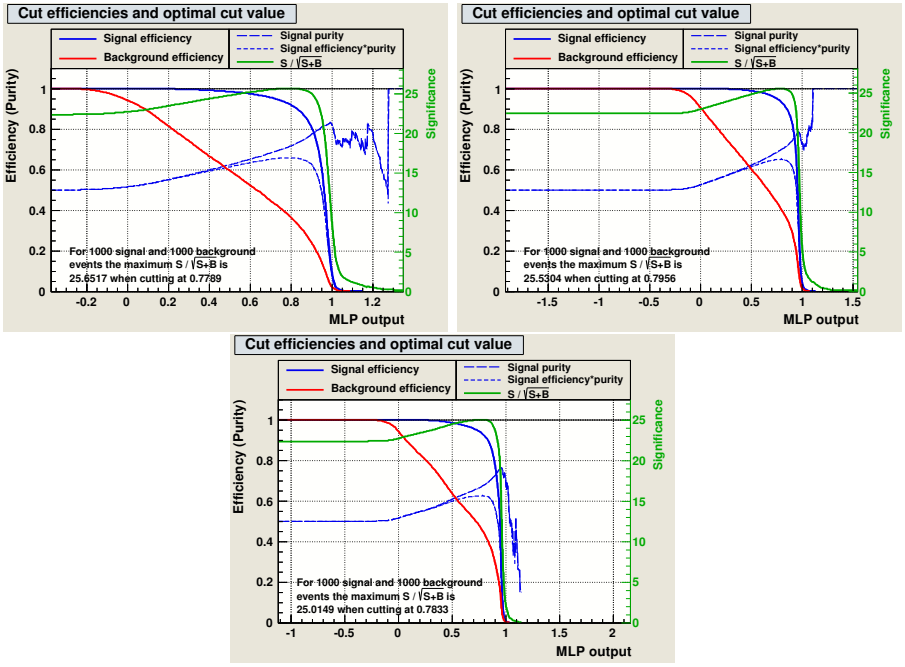

Figure A.11: Efficiencies for signal and background as a function of the MLP output cut value for inner (top left), middle (top right) and outer (bottom) calorimeter regions.

Data vs Monte-Carlo comparison for middle and outer

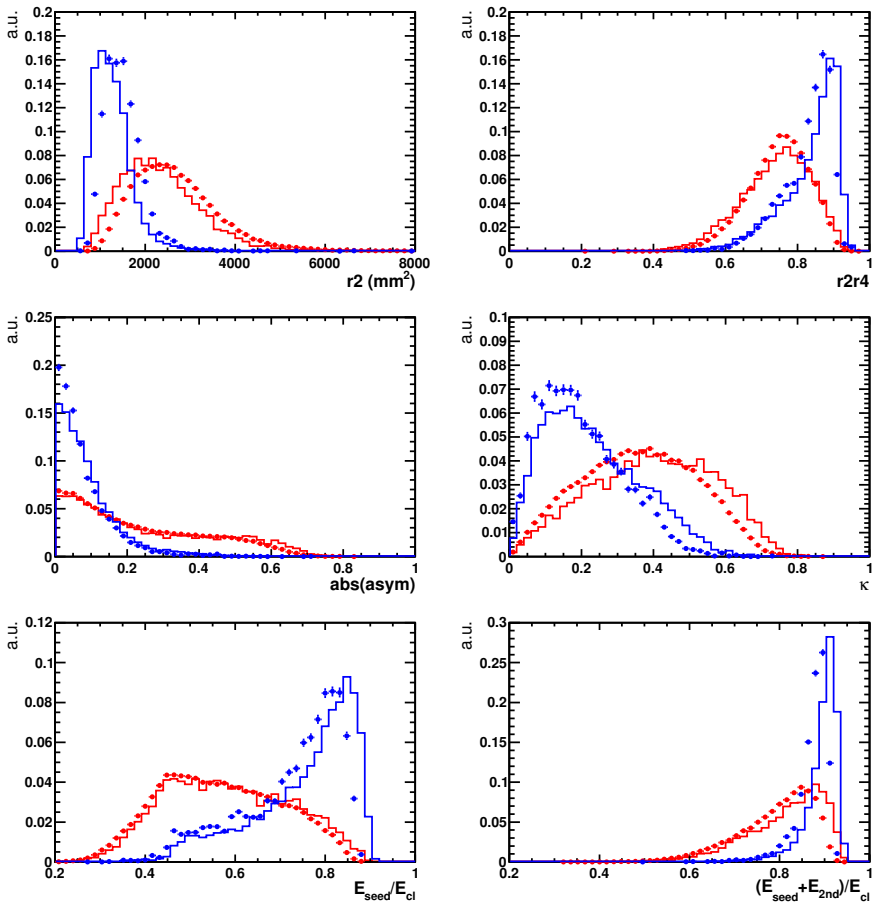

Figure A.12: Comparison between MC (full line histograms) and data (points) for discriminant variables from ECAL of photons from $B^0 \to K^{*0}\gamma$ (in blue) and merged π^0 from $K\pi\pi^0$ decays (in red). Middle region. Histograms are normalized to unity.

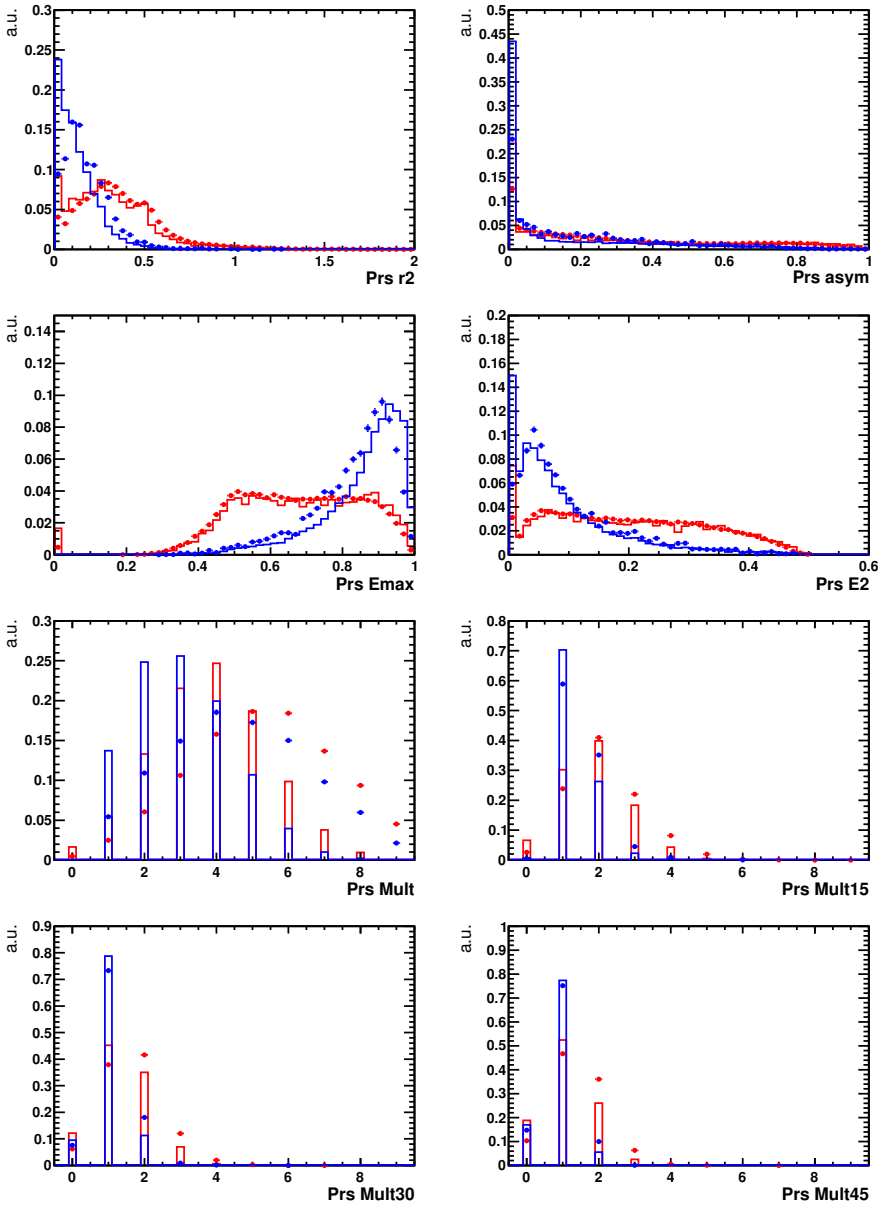

Figure A.13: Comparison between MC (full line histograms) and data (points) for discriminant variables from PS of photons from $B^0 \to K^{*0}\gamma$ (in blue) and merged π^0 from $K\pi\pi^0$ decays (in red). Middle region. Histograms are normalized to unity.

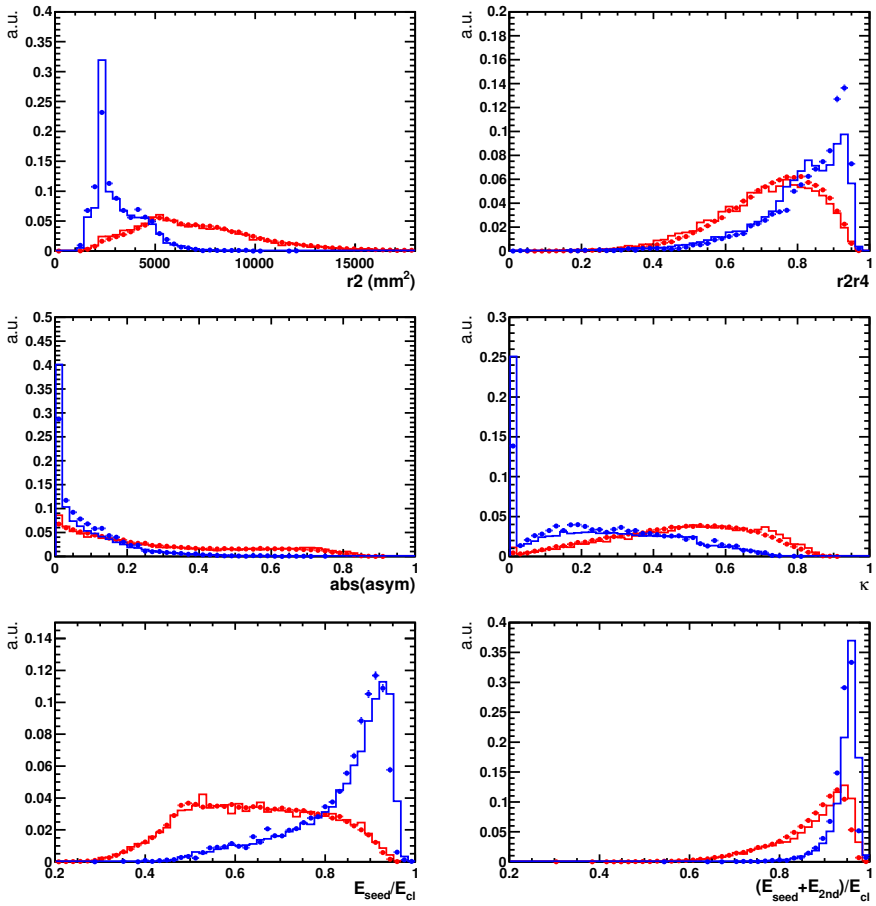

Figure A.14: Comparison between MC (full line histograms) and data (points) for discriminant variables from ECAL of photons from $B^0 \to K^{*0}\gamma$ (in blue) and merged π^0 from $K\pi\pi^0$ decays (in red). Outer region. Histograms are normalized to unity.

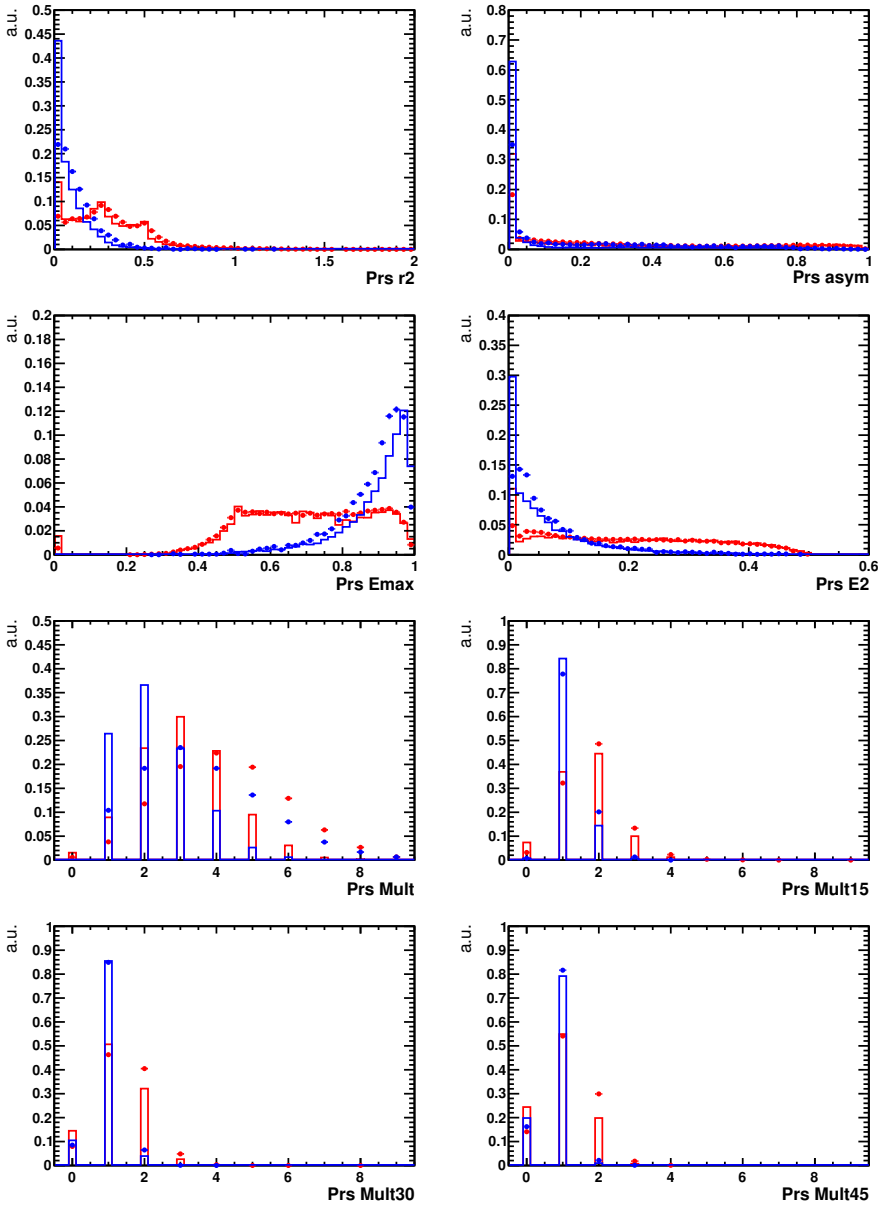

Figure A.15: Comparison between MC (full line histograms) and data (points) for discriminant variables from PS of photons from $B^0 \to K^{*0}\gamma$ (in blue) and merged π^0 from $K\pi\pi^0$ decays (in red). Outer region. Histograms are normalized to unity.

γ/π^0 efficiency table and resampling tools

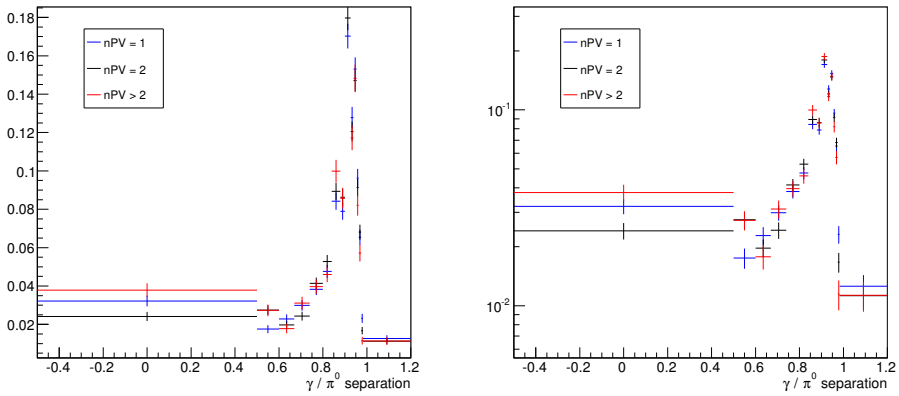

Figure A.16: Real data distributions (for the linear and logarithmic case in the left and right, respectively) of the γ/π^0 separation variable for the different bins chosen for the study of the effect of the multiplicity variables in the γ/π^0 separation for the case of the number of primary vertices observed in the event for the case of the $B^0 \to K^{*0}\gamma$ decay. The blue points correspond to the case in which only one primary vertex is observed, and the black and red ones correspond to two and more than two primary vertices respectively.

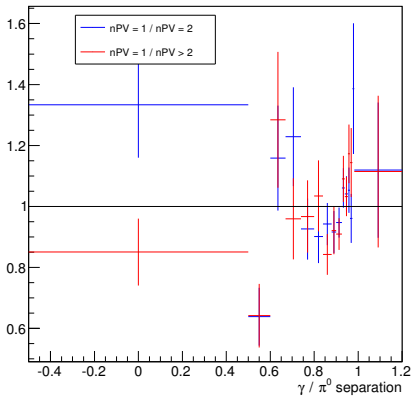

Figure A.17: Ratio of the γ/π^0 separation variable distributions for $nPV = 1$ and $nPV = 2$ in blue (for $nPV = 1$ and $nPV > 2$ in red) per event for real data $B^0 \to K^{*0}\gamma$. The line at one represents full compatibility.

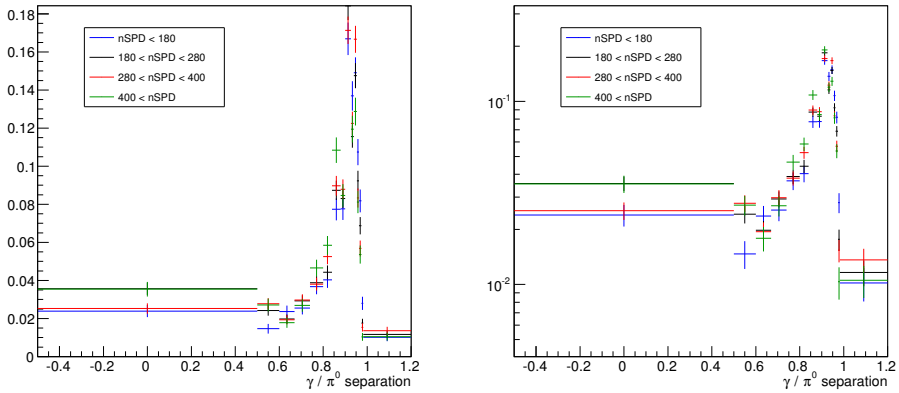

Figure A.18: Real data distributions (linear and logarithmic y-axis for left and right, respectively) of the γ/π^0 separation variable for the different bins chosen for the study of the effect of the multiplicity variables in the γ/π^0 separation for the case of the number of hits in the SPD per event for the case of the $B^0 \to K^{*0}\gamma$ decay. Blue points correspond to the case where less than 180 hits are collected by the SPD, black points to the interval between 180 and 280 hits, red points to the interval between 280 and 400 hits and the green points correspond to the cases in which there are more than 400 hits in the SPD.

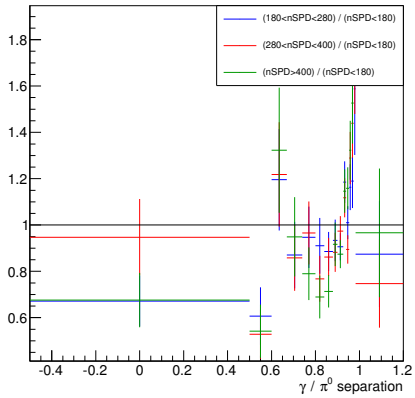

Figure A.19: Ratio of the γ/π^0 separation variable distributions for SPD hits between 180 and 280 and SPD hits < 180 hits (blue points), for SPD hits between 280 and 400 and SPD hits < 180 (red points) and for SPD hits > 400 and SPD < 180 (green points).

Appendix B

Branching Fraction and $\mathcal{A}^{CP}$ measurements. Additional plots

Fiducial cuts on the beam axis direction momentum for $\Lambda_b^0 \to \Lambda^{*0}\gamma$

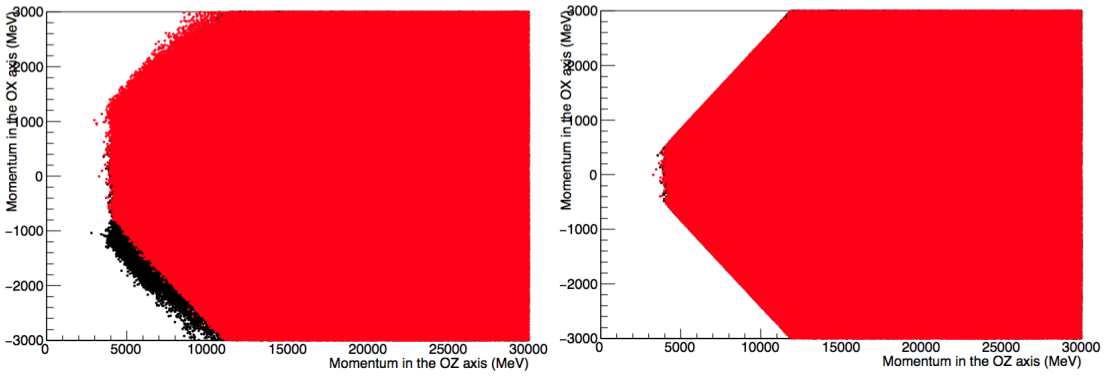

(a) Magnet Up.

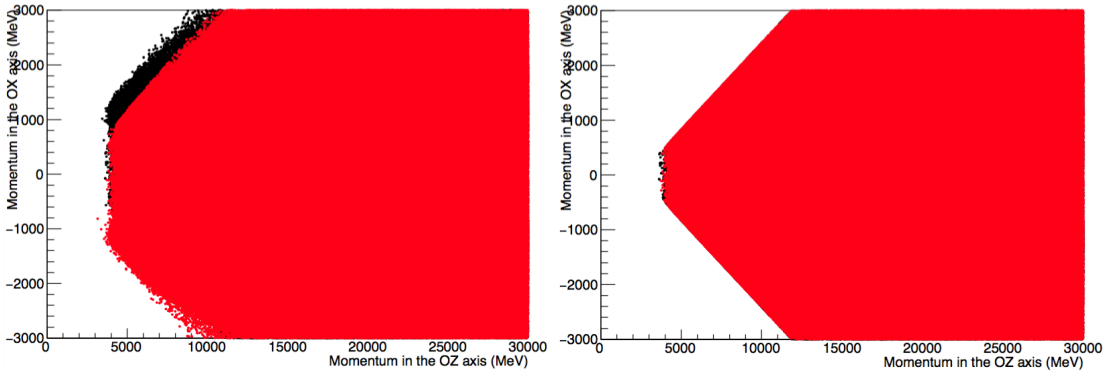

(b) Magnet Down.

Figure B.1: p_z versus p_x distributions for the kaon candidate within the $\Lambda_b^0 \to \Lambda^{*0}\gamma$ decay before (left) and after (right) the fiducial cut included in the preselection. The artificial asymmetry, consequence of the different polarities for the LHCb magnet, can be seen. Black points correspond to events associated to a Λ_b^0 and red points correspond to those associated to a $\overline{\Lambda}_b^0$.

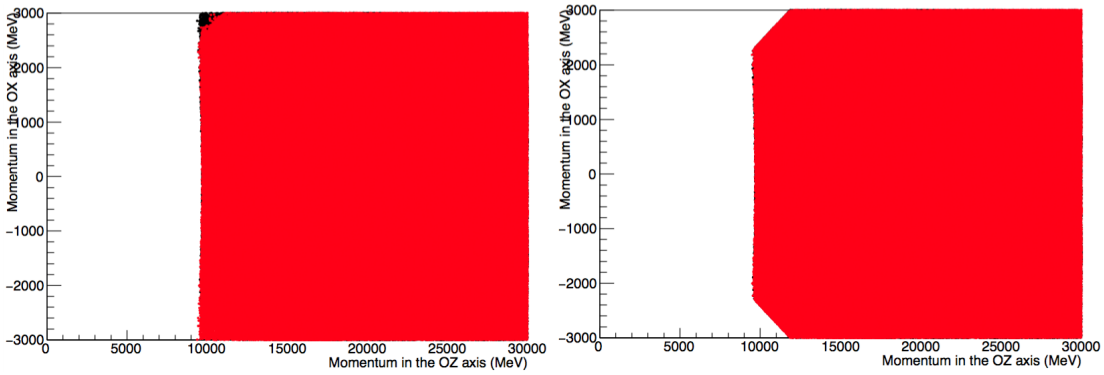

(a) Magnet Up.

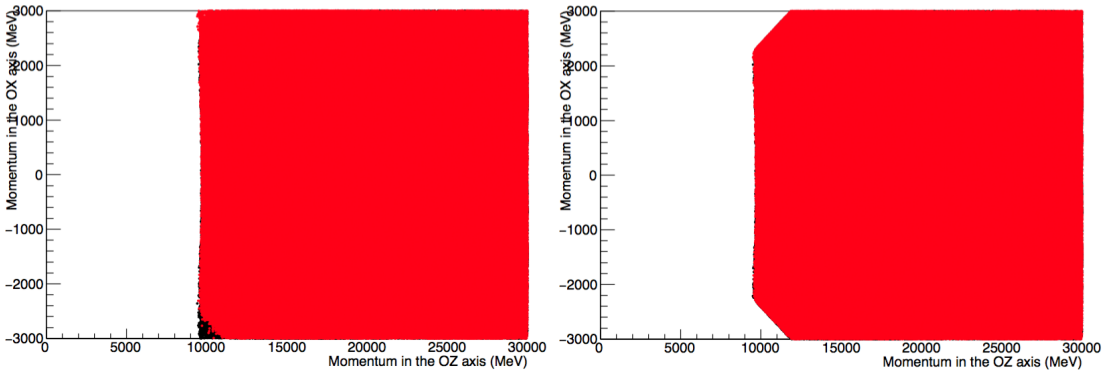

(b) Magnet Down.

Figure B.2: p_z versus p_x distributions for the proton candidate within the $\Lambda_b^0 \to \Lambda^{*0}\gamma$ decay before (left) and after (right) the fiducial cut included in the preselection. The artificial asymmetry, consequence of the different polarities for the LHCb magnet, can be seen. Black points correspond to events associated to a Λ_b^0 and red points correspond to those associated to a $\overline{\Lambda}_b^0$.

Particle Identification variables performance

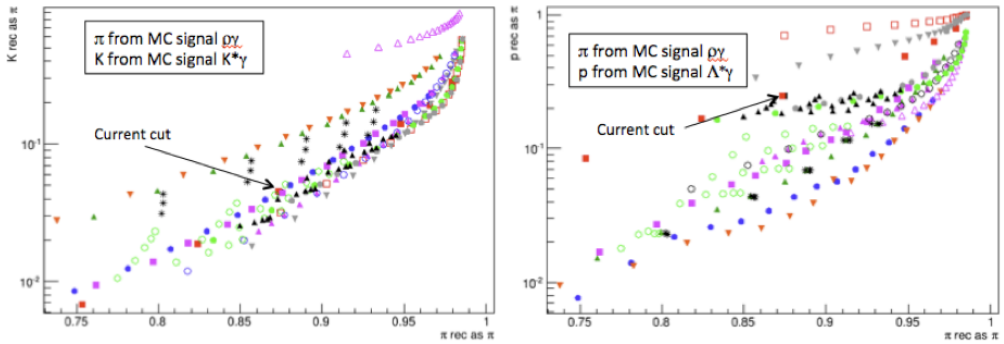

Figure B.3: Different combination of PID variables and their performance in terms of signal efficiency and background rejection, in the case of π selection (Kaon rejection for the plot on the left and proton rejection for the plot on the right). Each point corresponds to a cut value for the corresponding PID variable. It can be seen that the best variable for this case is the one represented by blue dots, which corresponds to the variable *ProbNNpi*(1-ProbNNk)*(1-ProbNNp)*.

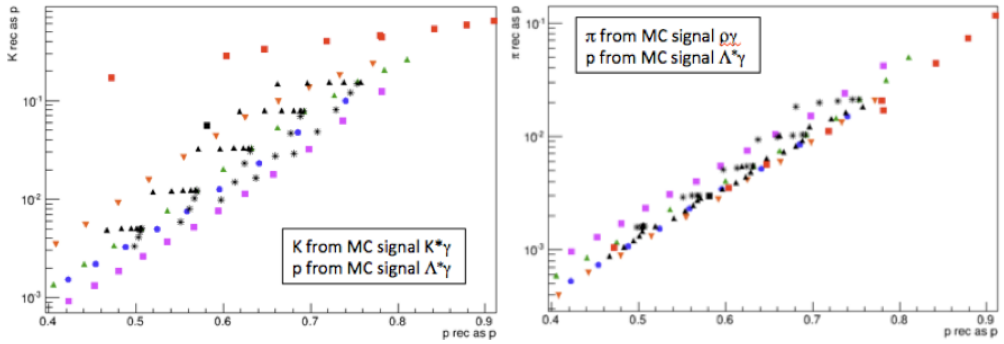

Figure B.4: Different combination of PID variables and their performance in terms of signal efficiency and background rejection, in the case of proton selection (Kaon rejection for the plot on the left and π rejection for the plot on the right). It can be seen that the best variable for this case is the one represented by blue dots, which corresponds to the variable *ProbNNp*(1-ProbNNk)*(1-ProbNNpi)*.

Table B.1: Correspondence between colours and variables for Figures B.3, B.4 and 6.7. The black square corresponds to the PID cuts used in other radiative decays [3].

Variable	Shape	Colour
ProbNNK	Triangle	Green
ProbNNp	Circle	Red
1 - ProbNNK	Void square	Red
ProbNNK * (1 - ProbNNpi) * (1 - ProbNNp)	Circle	Blue
ProbNNK * (1 - ProbNNp)	Inverse triangle	Orange
ProbNNK * (1 - ProbNNpi)	Inverse triangle	Gray
ProbNNp * (1 - ProbNNK)	Square	Violet
ProbNNpi * (1 - ProbNNp)	Circle	Green
ProbNNp * (1 - ProbNNK) * (1 - ProbNNpi)	Triangle	Blue
ProbNNp * (1 - ProbNNpi)	Void square	Gray
ProbNNpi * (1 - ProbNNK) * (1 - ProbNNp)	Triangle	Red
ProbNNpi * (1 - ProbNNK)	Cross	Green
ProbNNpi	Square	Blue
DLLK >	Inverse void triangle	Blue
DLLK <	Inverse void triangle	Pink
DLLp	Inverse void triangle	Green

Pull distributions for fitted parameters

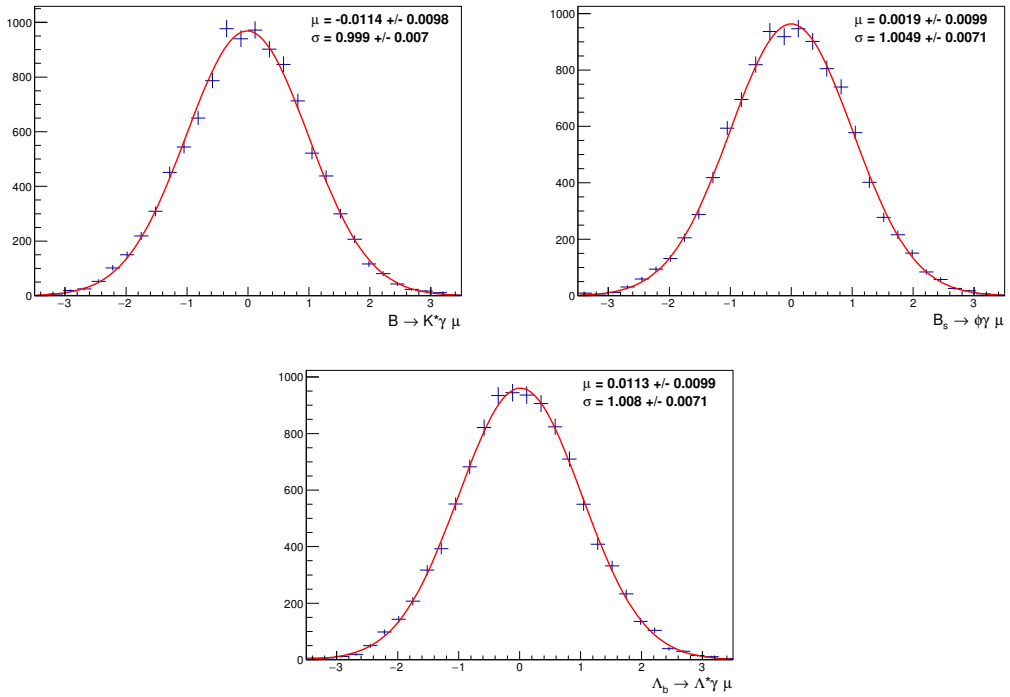

Figure B.5: Pull distributions for μ_{B^0} (top left), $\mu_{B_s^0}$ (top right) and $\mu_{\Lambda_b^0}$ (bottom). The fit of the pull distributions to a Gaussian function is shown in a red line, with its parameters on the top right corner of each plot.

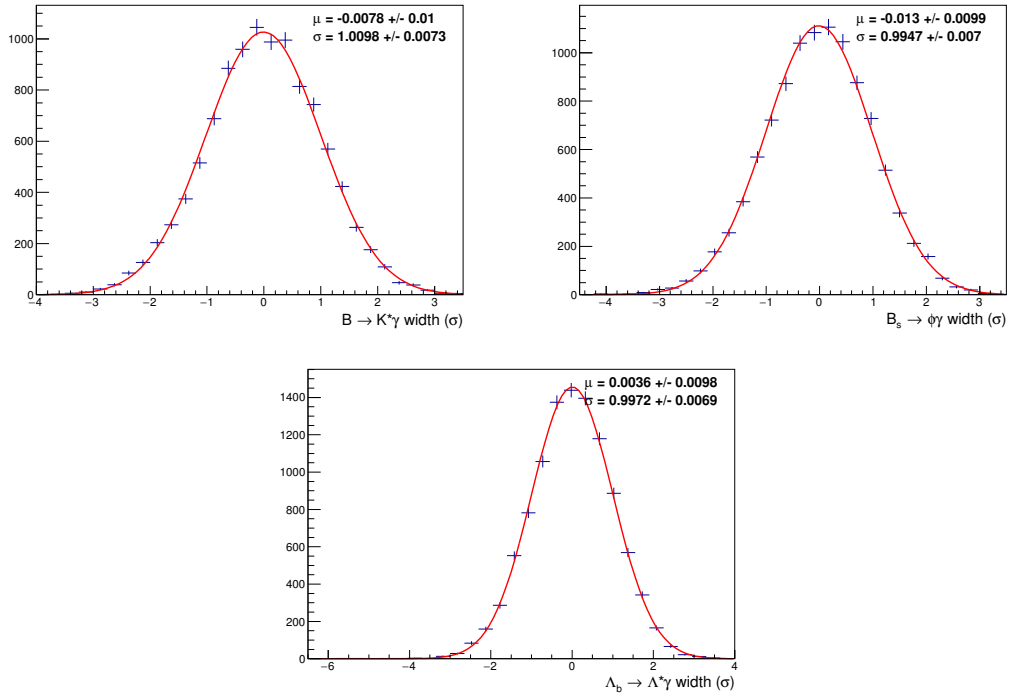

Figure B.6: Pull distributions for σ_{B^0} (top left), $\sigma_{B_s^0}$ (top right) and $\sigma_{\Lambda_b^0}$ (bottom). The fit of the pull distributions to a Gaussian function is shown in a red line, with its parameters on the top right corner of each plot.

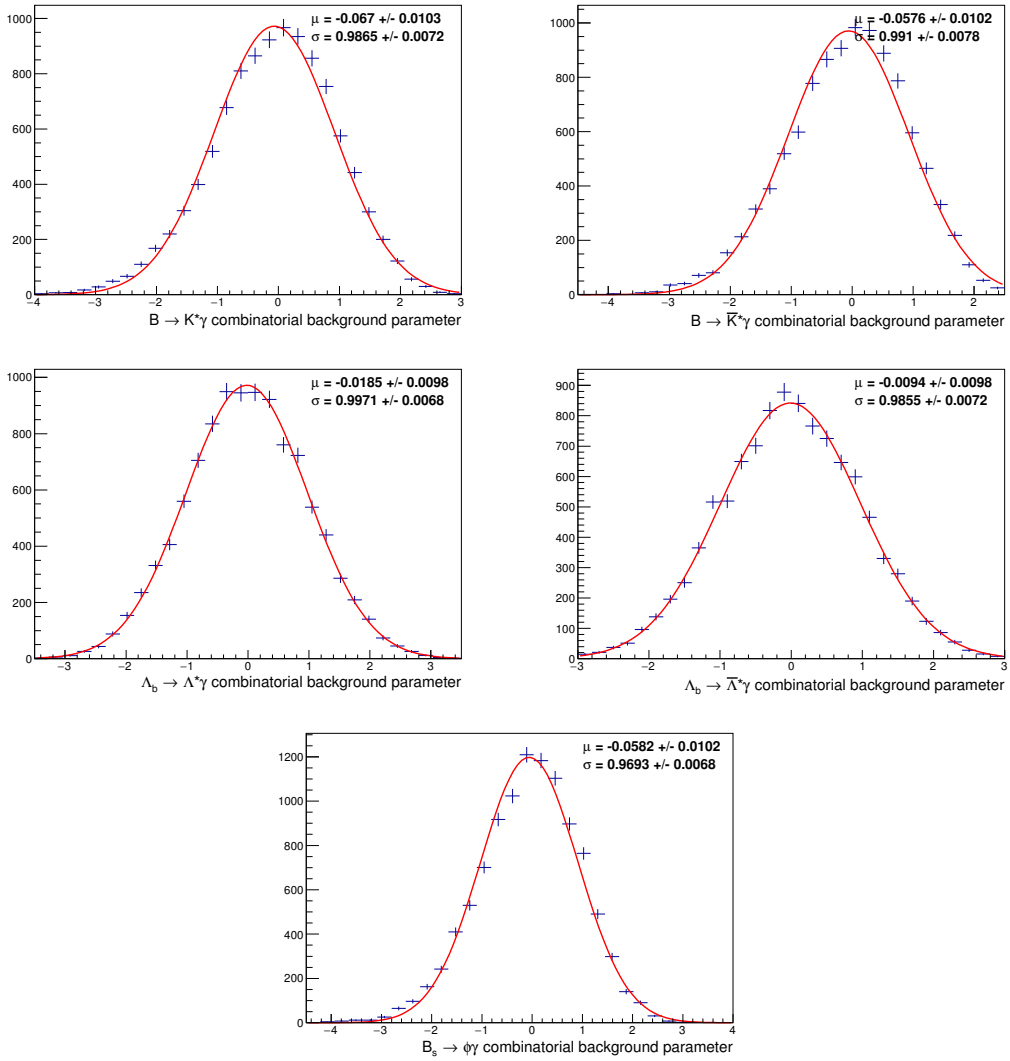

Figure B.7: Pull distributions for the combinatorial background parameter for $B^0 \to K^{*0}\gamma$ (top), $\Lambda_b^0 \to \Lambda^{*0}\gamma$ (middle) and $B_s^0 \to \phi\gamma$ (bottom). For the $B^0 \to K^{*0}\gamma$ and $\Lambda_b^0 \to \Lambda^{*0}\gamma$, the distributions on the left correspond to contamination in the B^0 (Λ_b^0) flavour while the distributions on the right correspond to contamination in the $\overline{B}^0$ ($\overline{\Lambda}_b^0$) flavour. The fit of the pull distributions to a Gaussian function is shown in a red line, with its parameters on the top right corner of each plot.

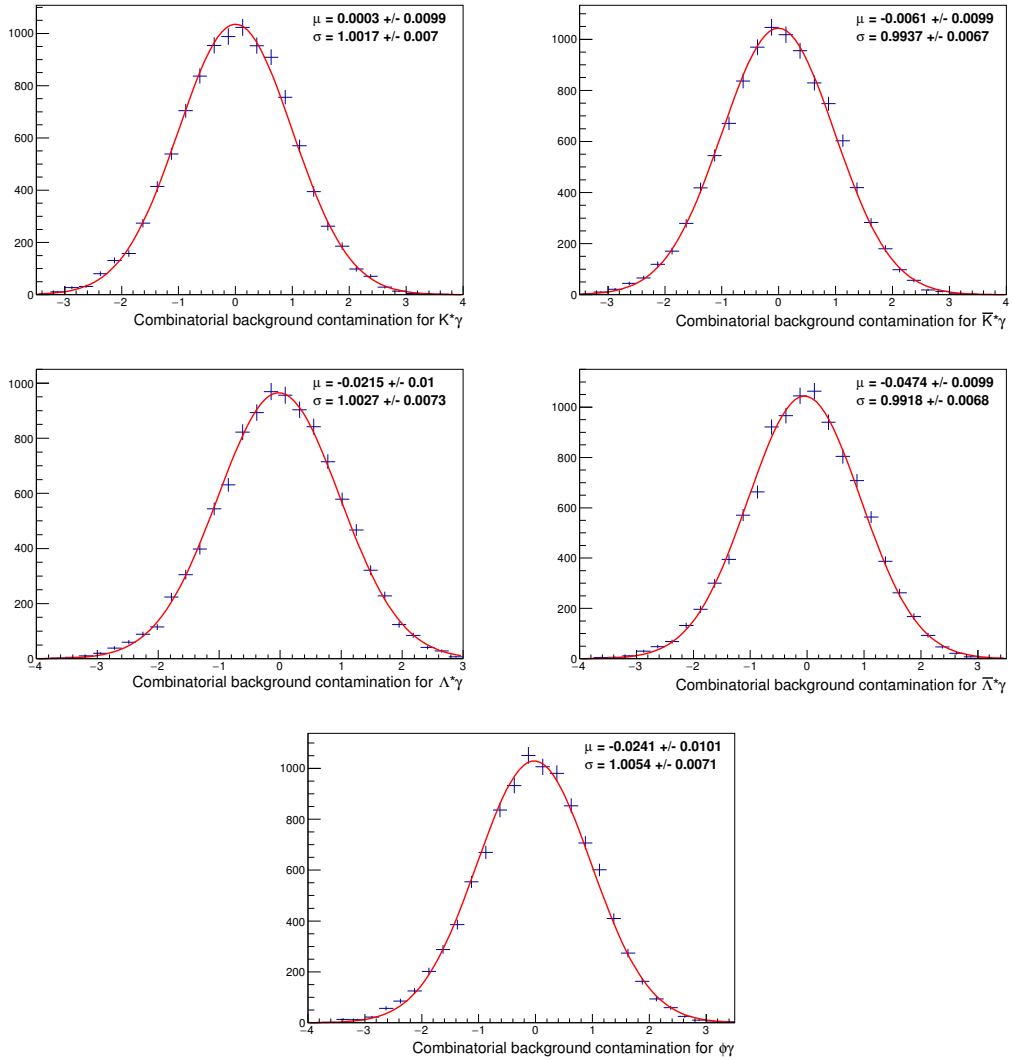

Figure B.8: Pull distributions for the combinatorial background contamination for $B^0 \to K^{*0}\gamma$ (top), $\Lambda_b^0 \to \Lambda^{*0}\gamma$ (middle) and $B_s^0 \to \phi\gamma$ (bottom). For the $B^0 \to K^{*0}\gamma$ and $\Lambda_b^0 \to \Lambda^{*0}\gamma$, the distributions on the left correspond to contamination in the B^0 (Λ_b^0) flavour while the distributions on the right correspond to contamination in the $\overline{B}^0$ ($\overline{\Lambda}_b^0$) flavour. The fit of the pull distributions to a Gaussian function is shown in a red line, with its parameters on the top right corner of each plot.

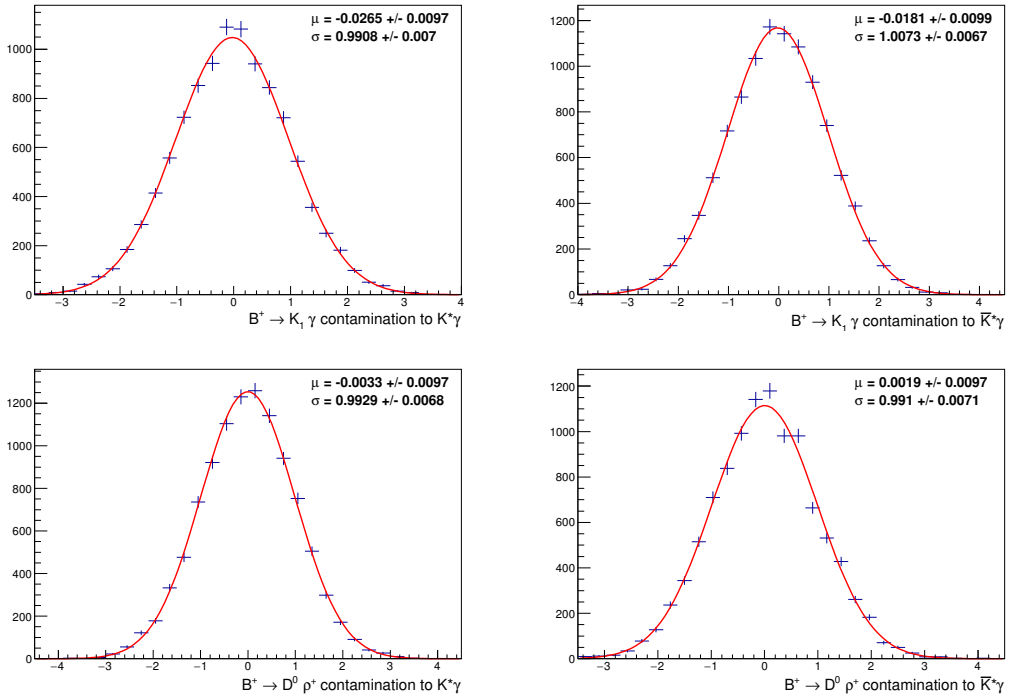

Figure B.9: Pull distributions for the partially reconstructed contamination for $B^0 \to K^{*0}\gamma$, for $B^+ \to K^{\cdot}1\gamma$ (top) and $B^+ \to D^0\rho^+$ (bottom). The distributions on the left correspond to contamination in the B^0 flavour while the distributions on the right correspond to contamination in the $\overline{B}^0$ flavour. The fit of the pull distributions to a Gaussian function is shown in a red line, with its parameters on the top right corner of each plot.

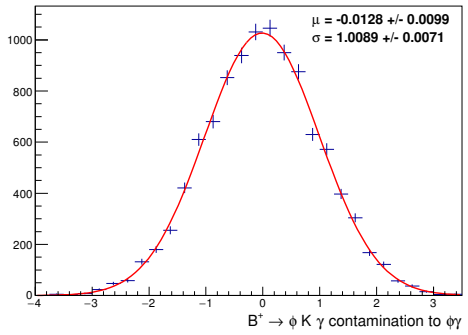

Figure B.10: Pull distributions for the partially reconstructed contamination for $B_s^0 \to \phi\gamma$, for $B^+ \to \phi K\gamma$. The fit of the pull distributions to a Gaussian function is shown in a red line, with its parameters on the top right corner of each plot.

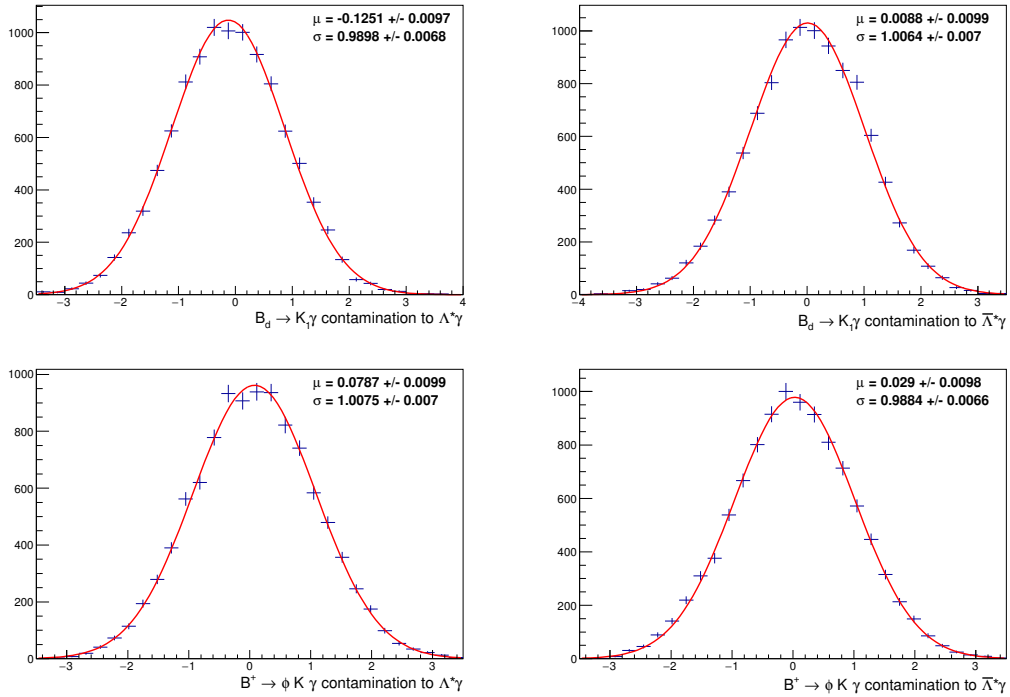

Figure B.11: Pull distributions for the partially reconstructed contamination for $\Lambda_b^0 \to \Lambda^{*0}\gamma$, for $B^+ \to$K˙1γ (top) and $B^+ \to \phi K\gamma$ (bottom). The distributions on the left correspond to contamination in the Λ_b^0 flavour while the distributions on the right correspond to contamination in the $\overline{\Lambda}_b^0$ flavour. The fit of the pull distributions to a Gaussian function is shown in a red line, with its parameters on the top right corner of each plot.

Appendix C

Comparison between background subtracted data and simulation

The Monte Carlo distributions of all the offline variables have been compared to the data distributions after the selection and the subtraction of the background. The following sections show this comparison for the three signal channels. For the $\Lambda_b^0 \to \Lambda^{*0}\gamma$ decay, the comparison is binned in terms of the resonance mass and the proton angle, due to the multiple contributions to the data sample.

$B^0 \to K^{*0}\gamma$ variables

In this section only the variables included in the BDT training are included. The number of tracks variable, used for the reweighing of the simulation samples, is also included.

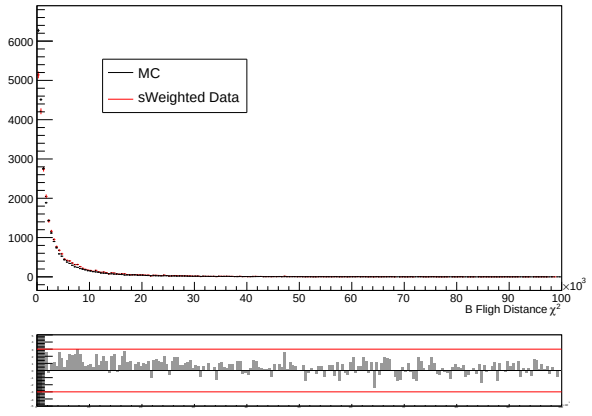

Figure C.1: Comparison of the B^0 flight distance χ^2 variable for simulation sample (black) and background-subtracted data (red). Residuals for a better comparison are included.

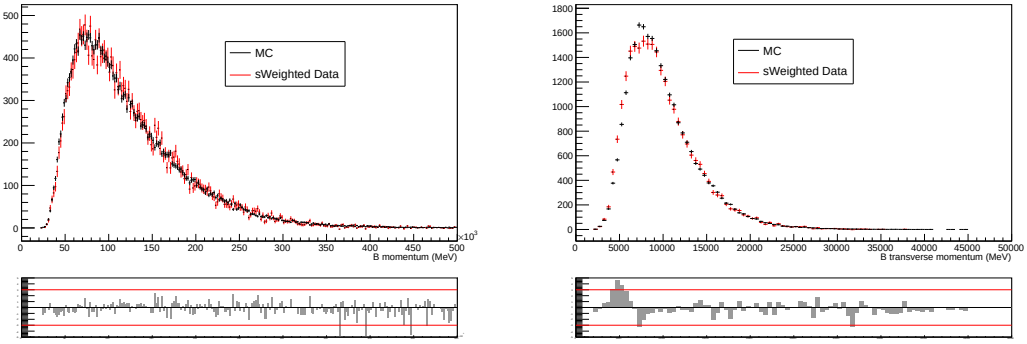

Figure C.2: Comparison of the B^0 momentum (left) and transverse momentum (right) for simulation sample (black) and background-subtracted data (red). Residuals for a better comparison are included.

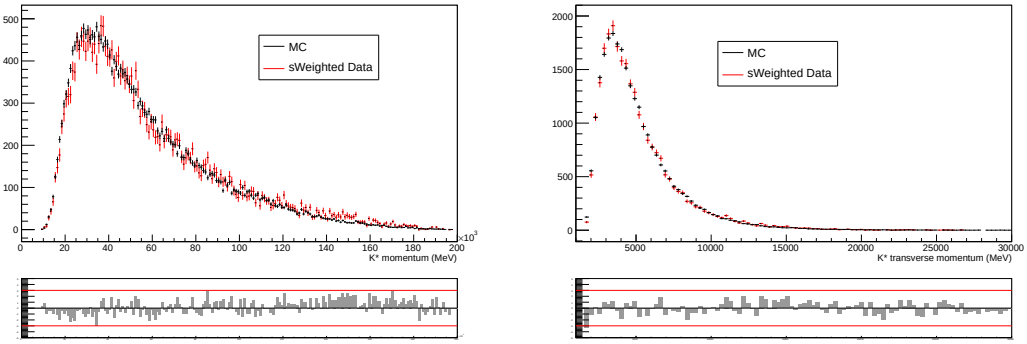

Figure C.3: Comparison of the K^* momentum (left) and transverse momentum (right) for simulation sample (black) and background-subtracted data (red). Residuals for a better comparison are included.

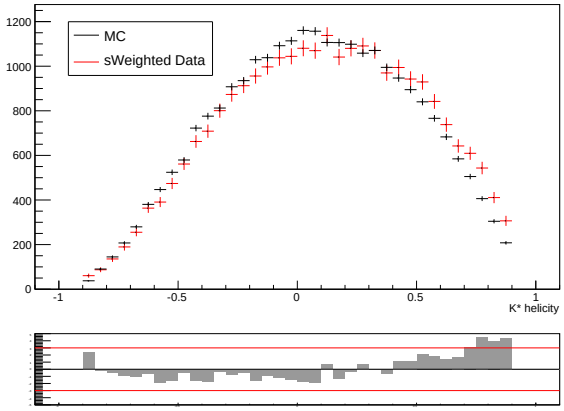

Figure C.4: Comparison of the helicity angle cosine for simulation sample (black) and background-subtracted data (red). Residuals for a better comparison are included. The discrepancies are mainly due to the technique to extract the background in the data sample.

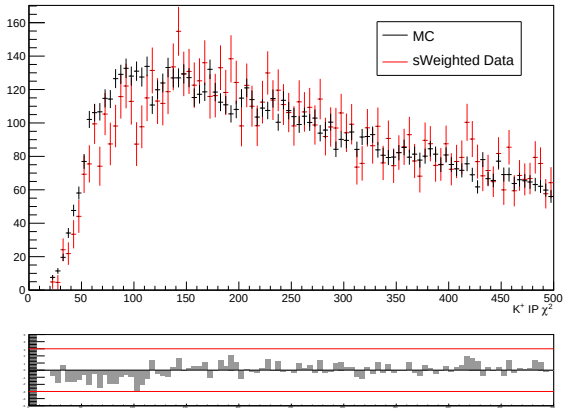

Figure C.5: Comparison of the kaon χ^2_{IP} for simulation sample (black) and background-subtracted data (red). Residuals for a better comparison are included.

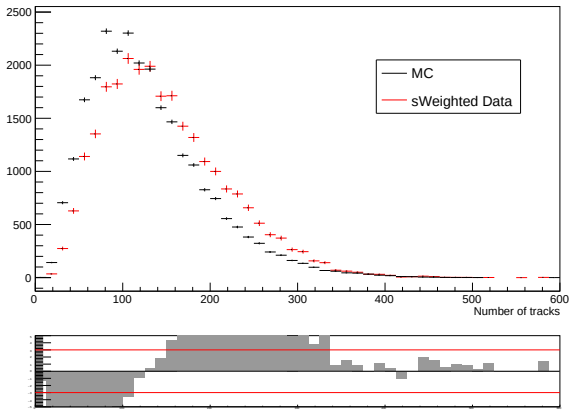

Figure C.6: Comparison of the number of tracks per event for simulation sample (black) and background-subtracted data (red). Residuals for a better comparison are included.

$B_s^0 \to \phi\gamma$ variables

In this section only the variables included in the BDT training are included. The number of tracks variable, used for the reweighing of the simulation samples, is also included.

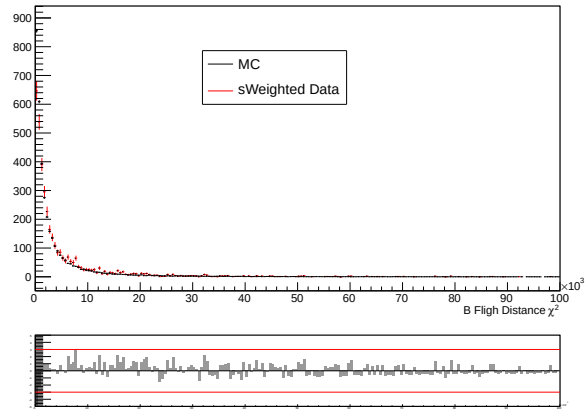

Figure C.7: Comparison of the B_s^0 flight distance χ^2 variable for simulation sample (black) and background-subtracted data (red). Residuals for a better comparison are included.

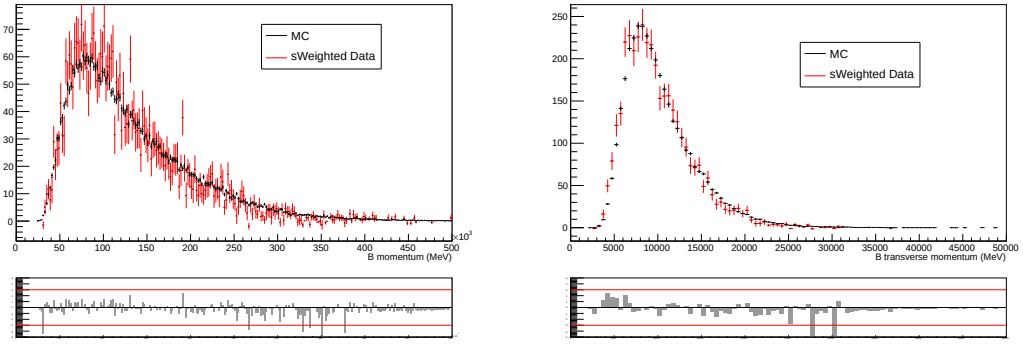

Figure C.8: Comparison of the B_s^0 momentum (left) and transverse momentum (right) for simulation sample (black) and background-subtracted data (red). Residuals for a better comparison are included.

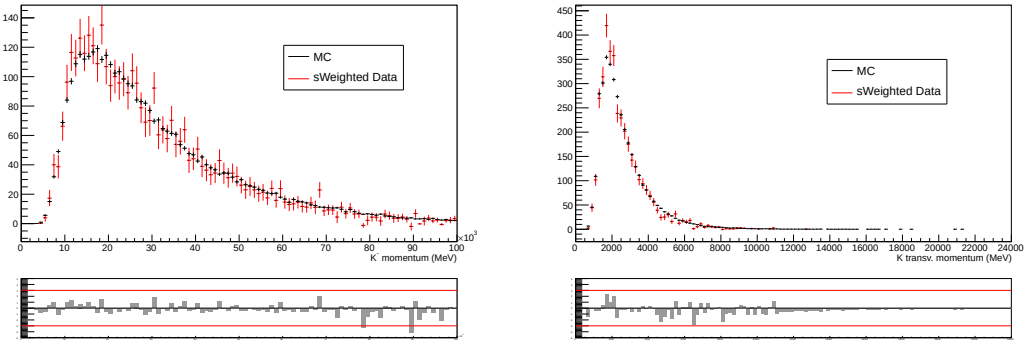

Figure C.9: Comparison of the kaon momentum (left) and transverse momentum (right) for simulation sample (black) and background-subtracted data (red). Residuals for a better comparison are included.

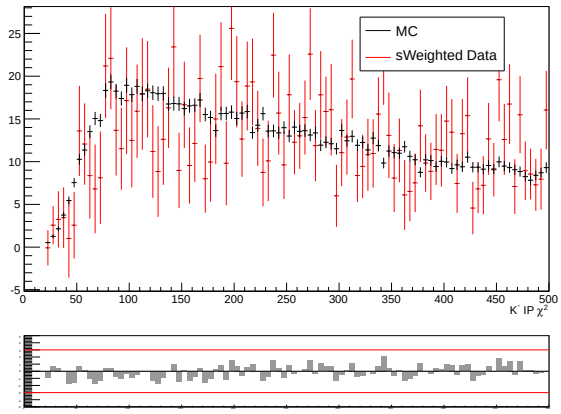

Figure C.10: Comparison of the kaon χ^2_{IP} variable for simulation sample (black) and background-subtracted data (red). Residuals for a better comparison are included.

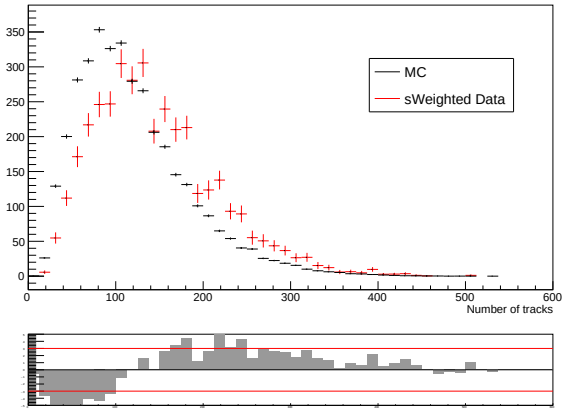

Figure C.11: Comparison of the number of tracks per event for simulation sample (black) and background-subtracted data (red). Residuals for a better comparison are included.

$\Lambda_b^0 \to \Lambda^{*0}\gamma$ variables

The same variables than in the previous cases are shown here as well as the variables used for the reweighing in the calculation of the systematic uncertainties. Due to the multiple contributions from different intermediate resonances, discrepancies in the data-MC comparison are expected and therefore a binning in intermediate resonance mass and proton angle is performed, in the same spirit than for the systematic uncertainties computation. Large error bars and few events per bin are expected. Only the comparison for one bin is presented here (the one corresponding to the resonance mass to be between 1610 MeV and 1660 MeV and the cosine of the proton angle to be between 1.9 and 2.3). The number of tracks variable, used for the reweighing of the simulation samples, is also

included. In this last case, the represented samples are the ones for the integrated angle and mass distribution.

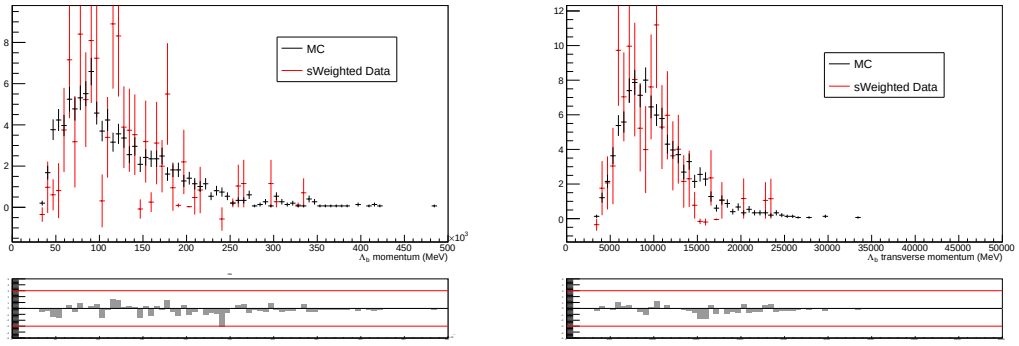

Figure C.12: Comparison of the Λ_b^0 momentum (left) and transverse momentum (right) for simulation sample (black) and background-subtracted data (red). Residuals for a better comparison are included.

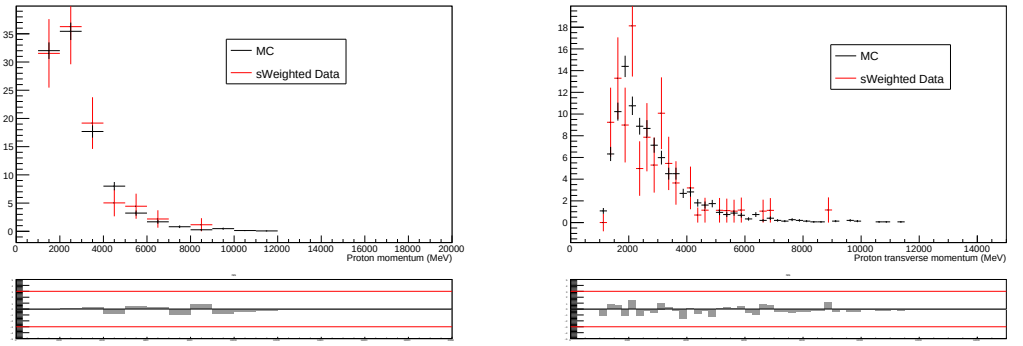

Figure C.13: Comparison of the proton momentum (left) and transverse momentum (right) for simulation sample (black) and background-subtracted data (red). Residuals for a better comparison are included.

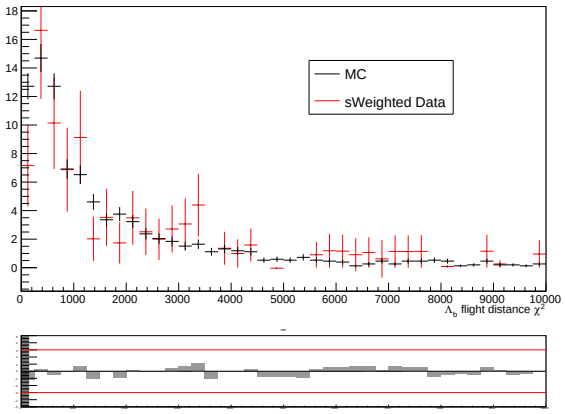

Figure C.14: Comparison of the Λ_b^0 flight distance χ^2 variable for simulation sample (black) and background-subtracted data (red). Residuals for a better comparison are included.

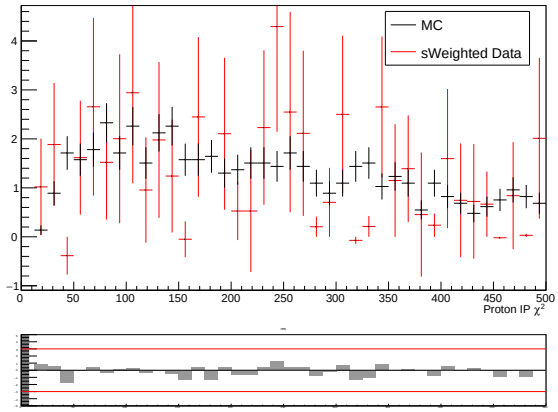

Figure C.15: Comparison of the proton χ^2_{IP} variable for simulation sample (black) and background-subtracted data (red). Residuals for a better comparison are included.

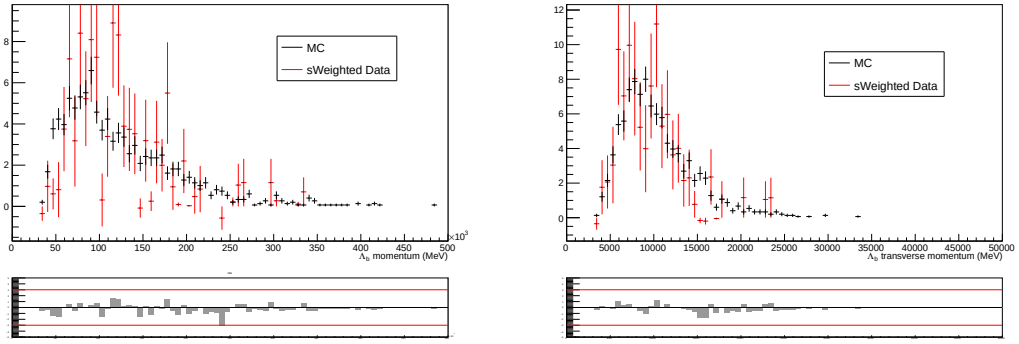

Figure C.16: Comparison of the Λ_b^0 momentum (left) and transverse momentum (right) for simulation sample (black) and background-subtracted data (red). Residuals for a better comparison are included.

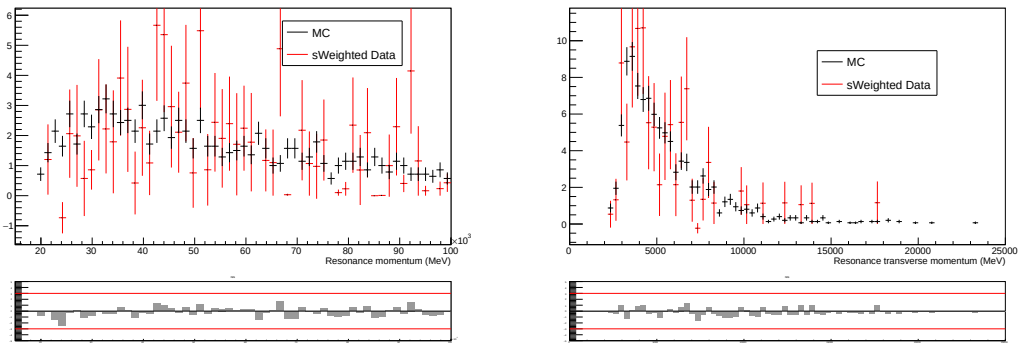

Figure C.17: Comparison of the intermediate resonance momentum (left) and transverse momentum (right) for simulation sample (black) and background-subtracted data (red). Residuals for a better comparison are included.

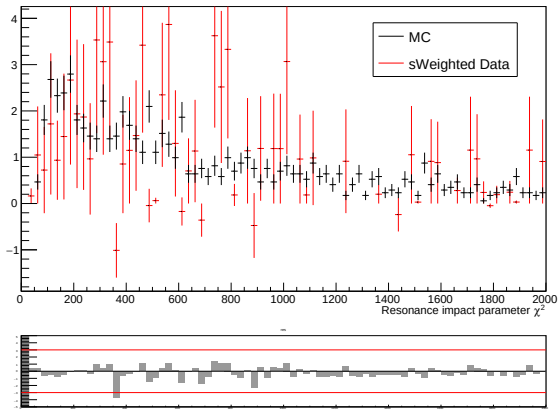

Figure C.18: Comparison of the intermediate resonance χ^2_{IP} variable for simulation sample (black) and background-subtracted data (red). Residuals for a better comparison are included.

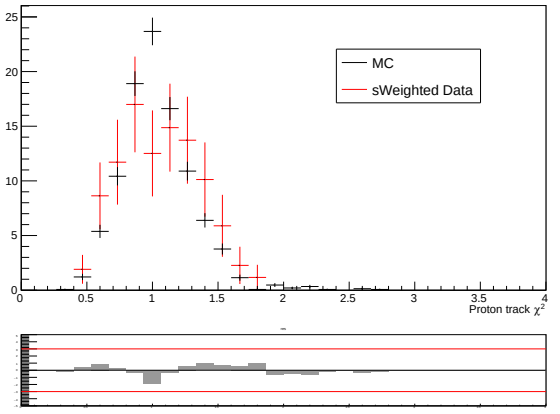

Figure C.19: Comparison of the proton track χ^2 variable for simulation sample (black) and background-subtracted data (red). Residuals for a better comparison are included.

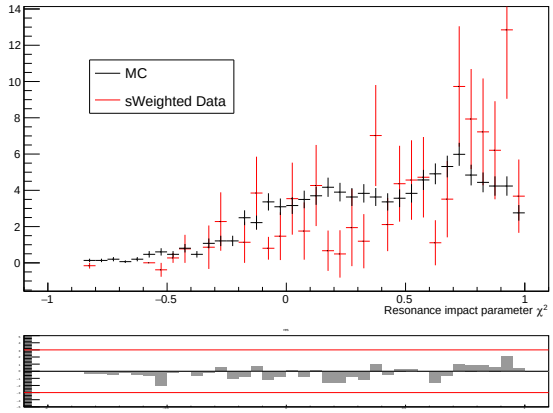

Figure C.20: Comparison of the helicity angle cosine variable for simulation sample (black) and background-subtracted data (red). Residuals for a better comparison are included.

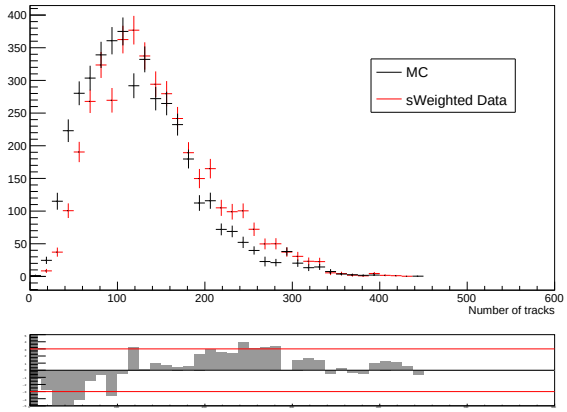

Figure C.21: Comparison of the number of tracks per event for simulation sample (black) and background-subtracted data (red). Residuals for a better comparison are included.